

Synthesis and analysis of carbon nanomaterials

Doctoral thesis
to obtain the doctorate degree (Dr. rer. nat.)
at the Faculty of Physics

by
Natalie Frese

Bielefeld University

April 2019

Content

1	Introduction	7
2	Methods	10
2.1	Helium ion microscopy	10
2.2	Atomic force microscopy	17
2.3	X-ray photoelectron spectroscopy	19
2.4	Raman spectroscopy	21
3	Results and Discussion	22
3.1	Cells	22
3.1.1	Stem cells	23
3.1.2	Neurons	25
3.1.3	Imaging of cell membranes	26
3.2	Carbon nanomembranes	34
3.2.1	Internally structured CNMs	37
3.2.2	CNM as a substrate for purple membrane	40
3.3	Carbon nanofoam	61
3.3.1	Low density carbon nanofoam	62
3.3.2	Comparison of carbon nanofoams	65
3.3.3	Inner structure of carbon nanofoams	68
3.3.4	Diamond-like carbon nanofoam	70
4	Summary	72
5	Publications	74
5.1	Cells	74
5.2	Carbon nanomembranes	105
5.3	Carbon foam	111
	Literature	143
	Acknowledgement	150

List of Publications

- (I) M. Wortmann, A. Hoffmann, N. Frese, A. Heide, J. Brikmann, N. Brandt, M. Menzel, A. Gölhäuser, E. Moritzer and B. Hüsgen: *Advanced Output of Silicone Molds in Vacuum Casting Processes by Polyamide 12 Powder Supplementation*. Polymer-Plastics Technology and Materials (2019, DOI: 10.1080/52740881.2019.1599944)
- (II) H. Haraguchi, N. Frese, A. Gölhäuser and H. Takei: *Protection of silver and gold LSPR biosensors in corrosive NaCl environment by short alkanethiol molecules; characterized by extinction spectrum, helium ion microscopy and SERS*. RSC Advances (2019, DOI: 10.1039/C8RA09778J)
- (III) M. Wortmann, N. Frese, A. Heide, B. Brockhagen, O. Strube, E. Moritzer, A. Gölhäuser and B. Hüsgen: *Entstehung und Untersuchung eines interpenetrierenden Polymernetzwerks aus Polyharnstoff und Silikonkautschuk beim Vakuumgießverfahren*. Tagungsband 3. Niedersächsisches Symposium Materialtechnik (2019, DOI: 10.21268/20190320-3)
- (IV) M. Wortmann, N. Frese, L. Sabantina, R. Petkau, F. Kinzel, A. Gölhäuser, E. Moritzer, B. Hüsgen and A. Ehrmann: *New Polymers for Needleless Electrospinning from Low-Toxic Solvents*. Nanomaterials (2019, DOI: 10.3390/nano9010052)
- (V) M. Wortmann, N. Frese, L. Hes, A. Gölhäuser, E. Moritzer and A. Ehrmann: *Improved abrasion resistance of textile fabrics due to polymer coatings*. Journal of Industrial Textiles (2018, DOI: 10.1177/1528083718792655)
- (VI) N. Frese, J. Scherr, A. Beyer, A. Terfort, A. Gölhäuser, N. Hampp and D. Rhinow: *Multicomponent patterned ultrathin carbon nanomembranes by laser ablation*. Applied Surface Science (2018, DOI: 10.1016/j.apsusc.2017.07.303)
- (VII) M. Schürmann, N. Shephard, N. Frese, K. Geishendorf, H. Sudhoff, A. Gölhäuser, U. Rückert, C. Kaltschmidt, B. Kaltschmidt and A. Thomas: *Technical feasibility study for production of tailored multielectrode arrays and patterning of arranged neuronal networks*. Plos One (2018, DOI: 10.1371/journal.pone.0192647)
- (VIII) M. Wortmann, N. Frese, A. Heide, J. Brikmann, O. Strube, R. Dalpke, A. Gölhäuser, E. Moritzer and B. Hüsgen: *Examination of Interpenetrating Polymer Networks of Polyurea in Silicone Molds Arising during Vacuum Casting Processes*. Polymer-Plastics Technology and Engineering (2017, DOI: 10.1080/03602559.2017.1410838)
- (IX) M. Wortmann, N. Frese, A. Heide, O. Strube, A. Gölhäuser, E. Moritzer and B. Hüsgen: *Untersuchung der Alterungsmechanismen von Silikon-Gießwerkzeugen beim Vakuumgießen*. Ingenieurspiegel (2017, 3, 52-54)
- (X) N. Frese, S. T. Mitchell, A. Bowers, A. Gölhäuser and K. Sattler: *Diamond-Like Carbon Nanofoam from Low-Temperature Hydrothermal Carbonization of a Sucrose/Naphthalene Precursor Solution*. C (2017, DOI: 10.3390/c3030023)
- (XI) X. Ma, R. Hartmann, D. Jimenez de Aberasturi, F. Yang, S. J. H. Soenen, B. B.

- Manshian, J. Franz, D. Valdeperez, B. Pelaz, N. Feliu, N. Hampp, C. Riethmüller, H. Vieker, N. Frese, A. Götzhäuser, M. Simonich, R. L. Tanguay, X. Liang and W. Parak: *Colloidal Gold Nanoparticles Induce Changes in Cellular and Subcellular Morphology*. ACS Nano (2017, DOI: 10.1021/acsnano.7b01760)
- (XII) N. Frese, S. T. Mitchell, C. Neumann, A. Bowers, A. Götzhäuser and K. Sattler: *Fundamental properties of high-quality carbon nanofoam: from low to high density*. Beilstein Journal of Nanotechnology (2016, DOI: 10.3762/bjnano.7.197)
- (XIII) M. Schürmann, N. Frese, A. Beyer, P. Heimann, D. Widera, V. Mönkemöller, T. Huser, B. Kaltschmidt, C. Kaltschmidt and A. Götzhäuser: *Helium Ion Microscopy Visualizes Lipid Nanodomains in Mammalian Cells*. Small (2015, DOI: 10.1002/smll.201501540)
- (XIV) S. T. Mitchell, N. Frese, A. Götzhäuser, A. Bowers and K. Sattler: *Ultralight carbon nanofoam from naphthalene-mediated hydrothermal sucrose carbonization*. Carbon (2015, DOI: 10.1016/j.carbon.2015.08.001)
- (XV) H. Vieker, N. Frese, and A. Götzhäuser: *Das Heliumionen-Mikroskop: Mikroskopie mit geladenen Teilchen*. Physik in unserer Zeit (2015, DOI: 10.1002/piuz.201401403)

List of Presentations

- (I) 2017, 25 – 27 May: *Assembly of proteins and oriented purple membrane on functionalized carbon nanomembranes*. 116th General Assembly of the German Bunsen Society for Physical Chemistry, Technical University Kaiserslautern, Germany (Poster)
- (II) 2016, 11 – 15 December: *Assembly of proteins and oriented purple membrane on functionalized carbon nanomembranes*. Pacific Rim Symposium on Surfaces, Coatings and Interfaces, Kohala Coast, USA (Poster)
- (III) 2016, 7 – 8 December: *Helium Ion Microscopy visualizes Lipid Nanodomains in Mammalian Cells*. NRW Nano-Conference 2016, Messezentrum Münster, Germany (Poster)
- (IV) 2016, 6 – 11 November: *Helium Ion Microscopy Imaging of Carbon Nanofoams from Hydrothermal Carbonization of Sucrose*. AVS 63rd International Symposium and Exhibition, Nashville, USA (Talk)
- (V) 2016, 3 – 6 November: *Helium Ion Microscopy visualizes Lipid Nanodomains in Mammalian Cells*. German Female Physics Conference, University of Hamburg, Germany (Poster)
- (VI) 2016, 6 – 11 March: *Assembly of proteins and oriented purple membrane on functionalized carbon nanomembranes*. DPG Conference, University of Regensburg, Germany (Poster)
- (VII) 2015, 15 – 18 October: *Characterization of Carbon Nanofoam*. German Female Physics Conference, University of Göttingen, Germany (Poster)
- (VIII) 2015, 15 – 20 März: *Helium Ion Microscopy of Biological Cells*. DPG Conference, Technical University Berlin, Germany (Talk)
- (IX) 2014, 9 – 14 November: *Helium Ion Microscopy of Biological Cells*. AVS 61st International Symposium and Exhibition, Baltimore, USA (Talk)
- (X) 2014, 22 – 24 July: *Helium Ion Microscopy of Biological Cells*. 5th Workshop on Focused Electron Beam Induced Processing, Goethe University, Frankfurt am Main, Germany (Poster)

List of Figures

1	The helium ion microscope ORION by Carl Zeiss SMT.	10
2	Schematic structure of a helium ion microscope.	12
3	Helium ion emission pattern of a trimer.	12
4	Secondary electron generation in the helium-ion microscope.	13
5	Detection of secondary electrons with the Everhart-Thornley detector.	14
6	Scheme of the scattering volumes in the HIM and SEM.	16
7	Scheme of the charge compensation in the HIM.	16
8	Measuring principle of AFM in contact mode.	18
9	Lennard-Jones-Potential.	18
10	Measuring principle of XPS.	20
11	Self renewal and differentiation of NCSCs.	24
12	A NCSC and neuronally differentiated NCSCs.	24
13	Hippocampal mouse neurons.	25
14	A cell imaged by HIM with and without floodgun.	26
15	Three different cell types imaged by HIM.	27
16	NCSC imaged by AFM.	28
17	Mechanism of the pit-like membrane feature formation in a model membrane.	28
18	HIM images of a critical point dried neuronally differentiated NCSC.	29
19	HIM images of freeze dried neuronally differentiated NCSC.	30
20	Neurons on a patterned surface.	32
21	Line width dependence of neuron adhesion on patterns.	33
22	Production of carbon nanomembranes.	35
23	Irradiation dose series of NBPT.	36
24	Internally patterned CNMs by direct laser patterning.	37
25	Internally patterned CNMs transferred to another substrate.	38
26	Internally patterned CNM transferred onto metal grid.	39
27	Hybrid structure consisting of a CNM and PM.	41
28	Absorption spectrum of wildtype PM.	42
29	HIM analysis of wildtype PM on CNM followed by rinsing with water or salt buffer.	42
30	Incubation series of wildtype PMs on CNMs.	44

31	Orientation of PMs on NBPT.	45
32	NTA functionalization of NBPT CNMs.	46
33	Fluorescence microscopy of functionalized NBPT CNMs.	46
34	XPS spectra of NTA functionalization of NBPT CNMs.	47
35	Absorption spectrum of His-tagged PM.	48
36	SEM images of wildtype PM and PM mutants on NTA NBPT CNMs.	49
37	Orientation of His-tagged PMs on NTA NBPT CNM.	49
38	Assembly of PM on CNM by electrophoresis.	51
39	AFM of assembled PMs on CNM by electrophoresis.	51
40	AFM/EFM of assembled PMs on CNM by electrophoresis.	52
41	AFM images of assembled and crosslinked PMs on CNM.	52
42	Functionalization of NBPT CNM.	54
43	Fluorescence microscopy of functionalized NBPT CNM.	55
44	IRRAS spectrum of NBPT CNM after functionalization.	56
45	XPS spectra of the NBPT CNM functionalization.	57
46	AFM/EFM images of His-tagged PMs on a functionalized NBPT CNM.	58
47	AFM/EFM images of His-tagged PM fusions on functionalized NBPT CNM.	59
48	AFM image of His-tagged PM fusions on functionalized NBPT CNM.	60
49	Production of carbon nanofoam via HTC.	61
50	HIM images of hydrothermal generated carbon nanofoam.	63
51	XPS spectrum of carbon nanofoam.	64
52	Raman spectrum of carbon nanofoam.	64
53	HIM images of different carbon nanofoams.	65
54	XPS spectra of different carbon nanofoams.	66
55	TEM images of foam samples.	67
56	HIM images of foam slices.	68
57	TEM and HIM images of broken micropearls.	69
58	HIM images of diamond-like foam.	70
59	XPS and Raman spectra of diamond-like foam.	71

1 Introduction

The electron configuration of carbon enables the formation of a wide variety of molecules [1]. Over the last years, many researchers have focused their research interest in producing and analyzing novel carbon structures. The diverse production techniques used in the synthesis of these nanostructures have produced a range of carbon materials with different sizes, shapes and properties [2]. This is possible because of the unique ability of carbon to occur with structures resulting from sp^1 , sp^2 , and sp^3 orbital hybridizations and combinations of these configurations [3].

In this thesis, different carbon-based nanomaterials including cell membranes, carbon nanomembranes and carbon nanofoams were analyzed and modified for future applications such as filter systems. To visualize the surfaces of these materials, a helium ion microscope (*HIM*) was used. *HIM* is an alternative microscopy method to the commonly used scanning electron microscope (*SEM*). Compared to the *SEM*, it has the decisive advantage that insulating carbon materials can be imaged at high resolution without the need to apply a conductive coating [4].

Membranes usually serve as selective barriers and are important for technical applications, such as filter systems or barrier coatings. A membrane consists of a thin layer, which separates two environments. It can be differentiated between biological and synthetic membranes. An example of a biological membrane is a cell membrane that surrounds a cell and separates it from the outside environment. Cell membranes consist of different lipids and proteins [5]. It is assumed that the various lipids are arranged in domains that have an important impact on elementary functions of the cell such as the regulation of ion channel function [6].

In the first part of this thesis, various cell membrane domains were investigated by *HIM* based on the results shown in my master thesis [7]. The cells were dried for imaging but not coated. By these means, structures in the cell membranes of human stem cells, stem cell differentiated neurons and mouse neurons in the nanometer range could be imaged. To find out the origin of these structures, atomic force microscopy (*AFM*) was performed on biological membranes. By generating a supported lipid bilayer as a model membrane the occurring structures in biological membranes have been investigated.

Furthermore, mouse neurons were used to form neural networks. A neuron usually consists of a cell body, the so-called soma, and neurites, which enable signal transmission [8]. In order to study the signal transmission in neural networks, the neurons were grown on structured surfaces. This allows the cell somata and neurites to be localized on the electrodes, resulting in an increased signal strength during signal transmission experiments [9]. In this thesis surfaces were structured, consisting of junctions for the cell bodies and ridges

for the neurites arranged in regular intervals. The HIM was used to visualize the adhesion mechanism of cell membranes to the structured substrate and the growth of neurons.

The second part of this thesis focuses on carbon nanomembranes (*CNMs*), their chemical modification and their use as substrates for cell membranes. A CNM consists of only one monolayer and is made by self-assembly of carbon-based molecules and subsequent crosslinking by electron-, UV- or EUV- irradiation. CNMs are synthetic membranes and their mechanical properties can be tailored. In addition, CNMs can be modified, for example by chemical surface functionalization [10]. The functionalization of the CNM opens up new application possibilities for biological membranes. The cell membrane of *Halobacterium salinarum*, the so-called purple membrane (*PM*), consists of patches which have a diameter of only a few micrometer and thus require a suitable carrier film for potential technical applications [11]. Since CNMs are only 1 nm thin and can be prepared free-standing, they represent a promising carriage substrate [12]. PM patches contain the protein bacteriorhodopsin, which pumps protons by light irradiation through the membrane [13]. To use this feature for technical applications the PM patches need to be applied on a CNM with the same orientation, because the proton pumping property works unidirectionally. This can be achieved for example by electrophoretic sedimentation, wherein the immobilization of the PMs is controlled by an electric field [14]. This technique is presented in this thesis. For analysis of the orientation of the immobilized patches, mainly the AFM was used. A chemical bond between PM and CNM was achieved by complex formation. For this purpose, a PM mutant was used, which is specifically modified on only one side with polyhistidin-tags. Other PM mutants are available that pump, for example, chlorides and are therefore interesting for applications such as light-driven seawater desalination [15].

For future applications of CNMs further treatment methods were investigated. This includes the patterning of the membranes at nanometer scale, which is shown in this thesis. For this purpose, self-assembled monolayers were structured by direct laser printing and then partially refilled with other molecules. Subsequent crosslinking with electron irradiation then leads to structured membranes. These internally structured membranes can be used, for example, as model membranes, biochips or for directed cell growth [16].

In the third part of this thesis hydrothermal carbonization was investigated as an alternative method to obtain nanomaterials from carbon precursor molecules. For this, biomass such as sucrose is heated in an autoclave under hydrothermal conditions [17]. Usually carbon nanofoam is the resulting material, which consists of a network of micropearls. Micropearls are carbon-based, filled spheres of only a few micrometer in diameter. To reveal the morphology and chemical composition, the samples were analyzed by HIM, Raman spectroscopy and

X-ray photoelectron spectroscopy (*XPS*). As shown in this thesis, the demonstrated porosity of the foams could be used as an alternative material in filter applications.

On the one hand, this thesis shows the ability of the HIM to image uncoated carbon-based materials such as cells, in particular cell membranes, carbon nanomembranes and carbon nanofoam with nanometer resolution. On the other hand, this thesis focuses on two methods, self-assembly and hydrothermal carbonization, to obtain carbon nanomaterials, which can be used for purification processes in further studies. The materials were analyzed by various analytical methods, such as HIM, XPS, Raman spectroscopy and AFM. In the field of analysis of carbon-based nanomaterials, as well as in the development of new applications or treatment methods for nanomaterial-based filter applications, progress has been made.

2 Methods

2.1 Helium ion microscopy

The ORION Plus helium ion microscope (*HIM*) shown in figure 1 and its successor, Nanofab, are produced in the USA by Carl Zeiss SMT (Oberkochen, Germany). The HIM is known for high-resolution imaging of biological samples, nanostructures and nanolithography [18, 19, 20]. This chapter about the operating principle of a HIM was previously described in my master thesis [7]. The principle is based on a scanning method, in which a sample surface is rastered by a helium-ion beam and the resulting particles released from the sample surface are then detected. This principle is comparable to the operation of a scanning electron microscope (*SEM*), with the difference that in the SEM a beam of electrons scans over a sample [21].



Figure 1: The helium ion microscope ORION by Carl Zeiss SMT [22].

As shown schematically in figure 2, the HIM consists of a column containing the ion source, lenses and apertures for focusing and deflecting the ion beam, a sample chamber equipped with secondary electron and backscattered ion detectors and a computer, which is used to control and display the measurements.

The realization of the ion source is based on the principle of the field ion microscope by Erwin Müller from the year 1951 and was optimized by patented work of ALIS (Peabody, Massachusetts) under the direction of Bill Ward [23]. ALIS was purchased by Carl Zeiss SMT in 2006 and fully integrated [24].

ALIS (*Atomic Level Ion Source*) is the name of the gas field ionization source, consisting of liquid nitrogen cooled tungsten needle in ultra high vacuum with three atoms at the tip apex, a so called trimer. When helium gas enters the ionization chamber at a pressure of 10^{-6} mbar and a high voltage is applied between the needle and the extractor electrode, ionization disks form at the atoms of the trimer where helium atoms ionize continuously through the tunnelling effect and accelerate to the extractor electrode [21, 25]. Figure 2 illustrates this effect. An electric field strength of $3 \text{ V}/\text{Å}$ at the tip atoms is sufficiently large to allow the ionization of the helium atoms without causing a detachment of atoms from the tip.

For imaging sample surfaces one atom of the trimer is selected to generate the helium ion beam, while the other two helium ion beams are blocked by a variable-size aperture [26]. A typical emission current is between $0.1 - 100 \text{ pA}$ at an acceleration voltage of 30 keV [25].

Since in this work only the secondary electron detector (*SE-detection*) was used for imaging, the following section is about the generation of secondary electrons, the detection of secondary electrons, advantages of the HIM with SE-detection compared to a SEM and the effective charge compensation in the HIM.

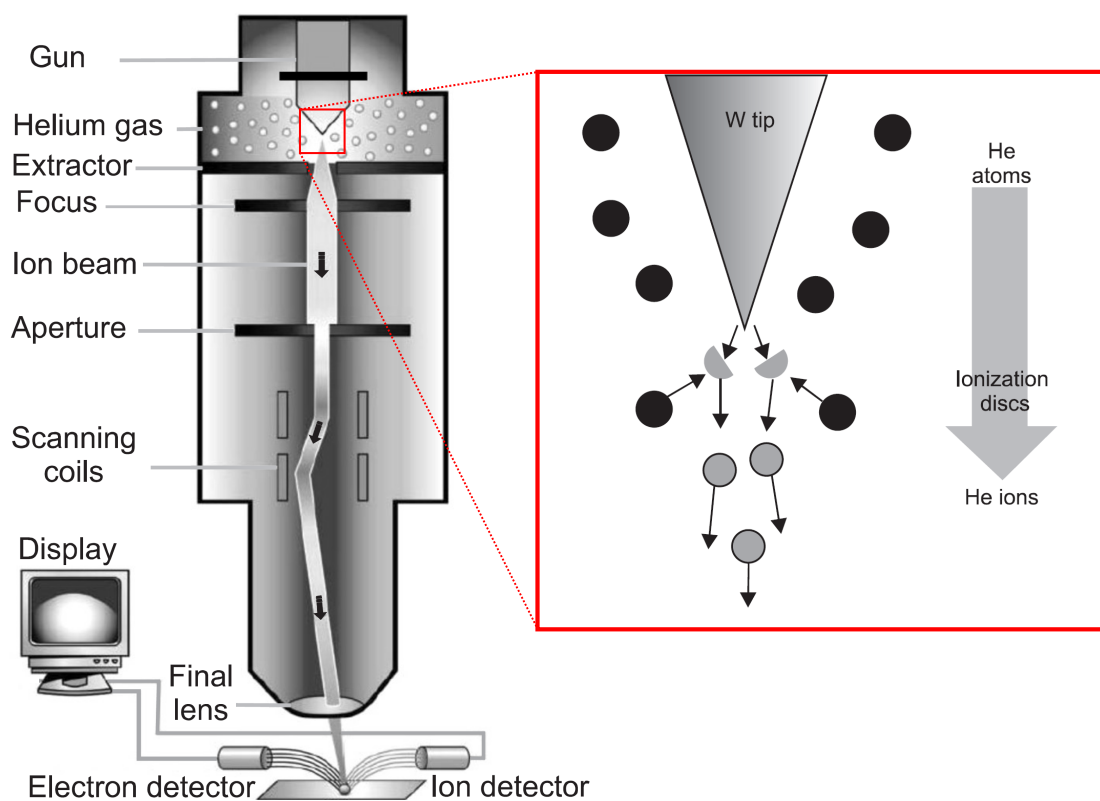


Figure 2: Schematic structure of a helium ion microscope [7, 27].

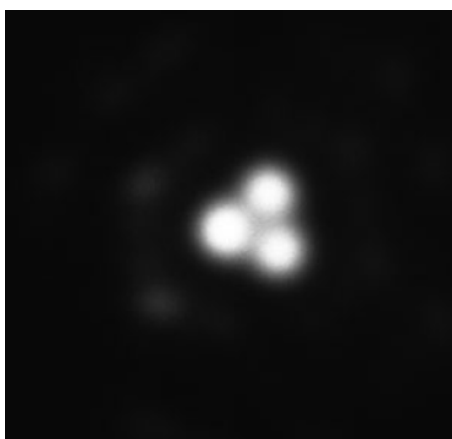


Figure 3: Helium ion emission pattern of a trimer in the Source-View-Mode [23].

Generation of secondary electrons

The images with the helium ion microscope are generated pixel by pixel. Starting at the top left edge of the image, the helium ion beam scans the first row, followed by the remaining rows. Each grid point of the helium ion beam corresponds to one pixel in the resulting image. The number of pixels per image is set in advance by the user, for example 1024 x 1024 pixels per image.

As shown schematically in figure 4, secondary electrons are generated at each pixel. Depending on the number of secondary electrons produced, the pixel is assigned a gray value. Therefore regions where more secondary electrons are produced per incident helium ion are assigned a higher gray scale level. In the resulting image these regions appear lighter than regions in which less secondary electrons are generated [22].

The number of generated secondary electrons depends on the material, topography, and electrical properties of the sample to be imaged, as well as the kinetic energy at which the helium ions strike the sample [28, 29]. Typically 3-8 secondary electrons are generated per helium ion with the rate of secondary electrons being greater for samples with high atomic numbers than for samples having low atomic numbers. Since most of the secondary electrons are generated directly by the helium-ion beam, the HIM images are rich in surface details [30].

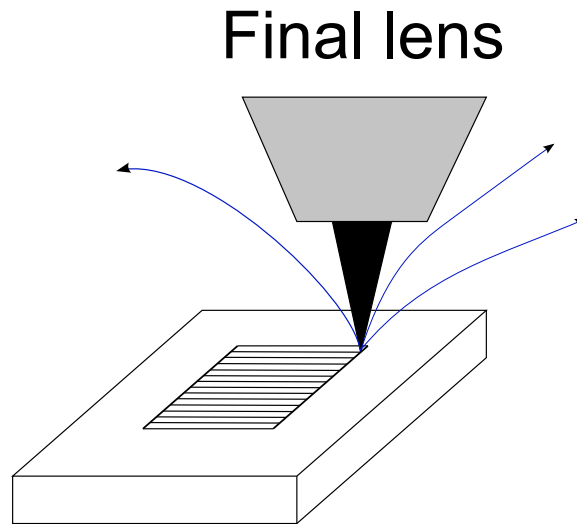


Figure 4: Secondary electron generation in the helium-ion microscope [7, 22].

Detection of secondary electrons

The number of secondary electrons generated by the helium ion beam is measured by an Everhart-Thornley detector. As shown in figure 5, the secondary electrons released from the sample are directed towards the detector with the aid of an Everhart-Thornley grid, to which a positive voltage of up to 500V can be applied. Once in the grid, the secondary electrons are accelerated to the scintillator and converted into photons by cathodoluminescence. Subsequently, the photons arriving at the photomultiplier are amplified and converted into a voltage pulse of maximum 2 V. From the resulting pulse amplitude, the gray value is calculated for the respective pixel. The raster motion of the helium-ion beam can be repeated line by line or imagewise to average the gray value per pixel from multiple scans to minimize noise [22].

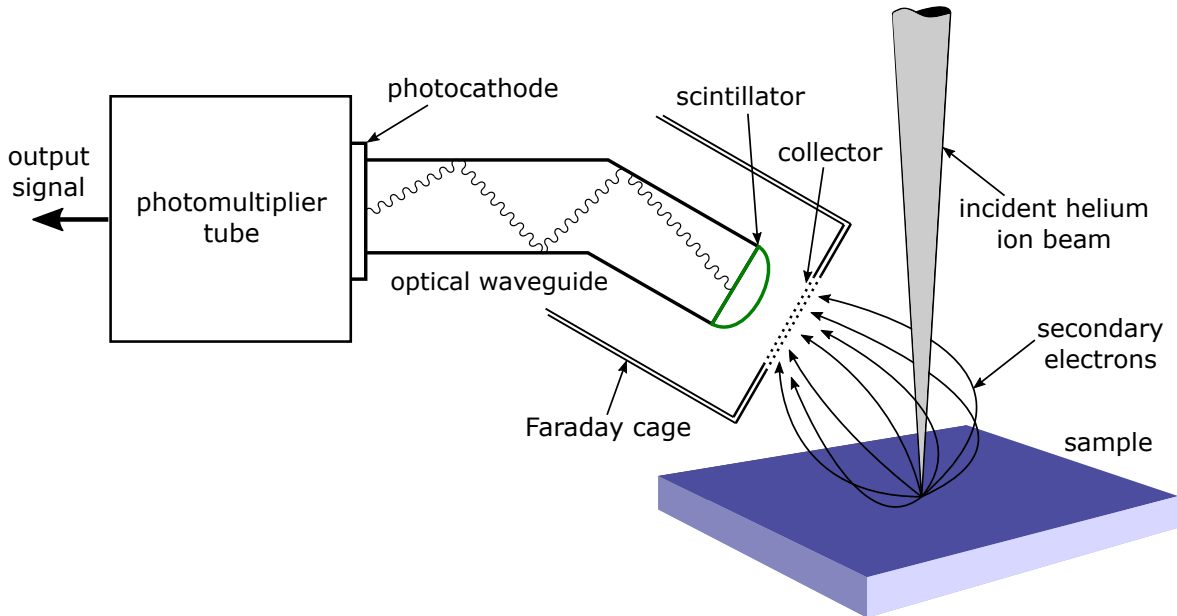


Figure 5: Detection of secondary electrons with the Everhart-Thornley detector. The secondary electrons are directed by the Everhart-Thornley grid in the direction of the detector and arrived there converted into photons. The photons are then converted in the photomultiplier into a voltage pulse, from which the respective gray value of the pixel is calculated [31].

Advantages of a HIM with SE-detection compared to a SEM

The helium-ion microscope and the scanning electron microscope are similar in their overall function, since in both devices a tungsten tip generates a beam of particles, which is guided in a rastering motion over the sample and through scattering processes released electrons are detected for each pixel and assigned a gray value. The minimum size of the ion beam spot on the sample surface in the HIM can be less than 0.25 nm, since the ion source consists of a single atom [32]. In contrast, in the SEM the minimum size of the electron beam spot on the sample surface is 0.8 nm. Together with the smaller wavelength of the helium ions compared to electrons, the resulting HIM images have a higher resolution and a greater depth of field compared to SEM images [21, 30].

Figure 6 schematically represents the scattering volumes, in which the beam-sample interactions take place, in the HIM and in the SEM. The depth of information (*SE escape depth*) is the region in which the secondary electrons have sufficient energy to leave the sample. For metallic samples, this depth of information is smaller than for insulating samples [33]. Importantly, most of the secondary electrons in the HIM are generated directly by the ion beam and not by further scattering processes. The reason for this is that the helium ions are heavier than electrons and thus penetrate deeper into the sample with less lateral scattering [25]. This results in an increased surface sensitivity for HIM compared to SEM. Since more secondary electrons are produced in the HIM per incident helium ion than for an electron, high-contrast images are possible in the HIM despite low emission currents [32]. Furthermore, the beam of noble gas ions minimizes the chemical, electrical and optical change of the sample [25].

Charge compensation

The artefact-inducing charge effects of insulating samples that occur during imaging with SE-detection can be stabilized by the use of an electron flood gun [34]. The sample is alternately scanned with the helium ion beam and irradiated with electrons, as shown in figure 7. The irradiation with electrons, as well as the scanning with the helium ion beam can be done line by line or imagewise. For an effective charge compensation, a balance between the ion beam, the secondary electron current and the electron beam of the electron gun is necessary. It should be noted that the HIM image can have a width of less than one micron, while the electron beam typically has a diameter of one millimeter [35]. In addition, the sample surface charge depends on the imaging settings, therefore optimal settings vary for each sample.

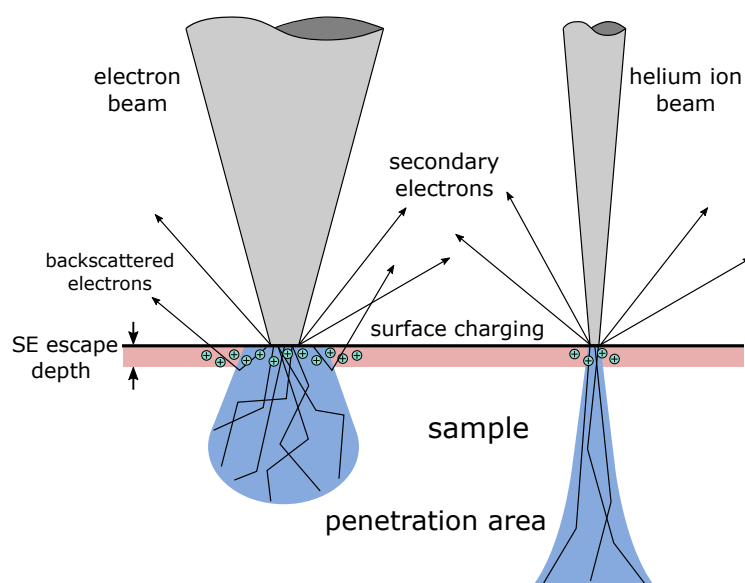


Figure 6: Scheme of the scattering volumes in the HIM and SEM [7, 33]. The secondary electron information depth indicates the region in which the secondary electrons have sufficient energy to leave the sample. Most of the secondary electrons in the HIM are generated directly by the ion beam and not by further scattering processes.

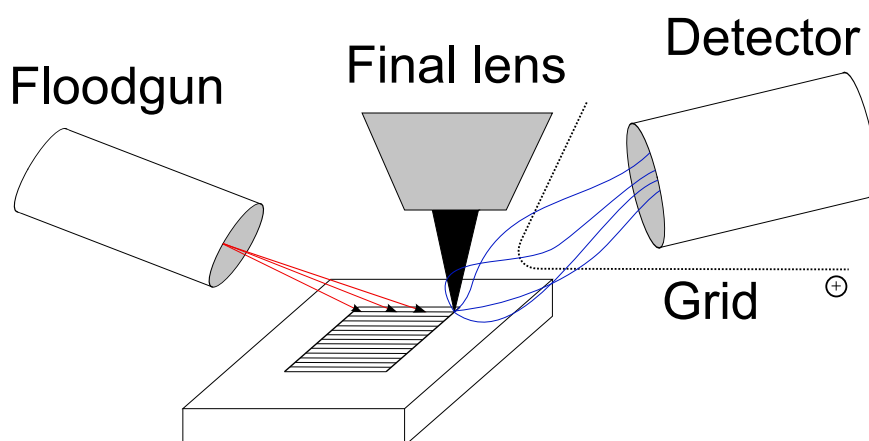


Figure 7: Scheme of the charge compensation in the HIM [7]. The charging of an electrically insulating sample surface by the ion beam (black) is stabilized by an additional electron beam (red). The number of secondary electrons released from the sample surface by the ion beam (blue) is detected for each pixel and assigned to a gray value.

2.2 Atomic force microscopy

The atomic force microscope (*AFM*) was developed 1986 by Binnig, Gerber and Quate for the topographical imaging of surfaces with a resolution in the subnanometer range [36]. This chapter about the operating principle of an AFM was previously described in my bachelor thesis [37]. The operation principle is based on the scanning of a sample surface line by line with the help of a fine probe. This principle can be realized in air, vacuum and liquids [36, 38, 39].

Between the scanning probe, consisting of a cantilever and a tip, and the sample surface long-range or short-range interactions can be used as imaging information. For the imaging of the surface topography, the interactions are usually detected optically by the deflection of the cantilever. The deflection can be measured by using a laser and diodes.

In general, a distinction is made between three different modes. The Lennard-Jones potential shown in figure 9 summarizes the forces acting on the various modes. In the contact mode, the tip of the sample surface is so close to the surface that the Pauli repulsion leads to the deflection of the cantilever (see figure 8). In the non-contact mode, the probe is excited next to the resonance frequency and approximates the sample surface until the resonant frequency of the probe shifts by a preset value due to penetration into the potential of the surface. This change is primarily explained by the Van-der-Waals interaction. In the semi-contact mode, the probe oscillates at a distance to the surface, as in non-contact mode, but touches it at regular intervals, so that both repulsive and attractive forces contribute [40]. For electrostatic force microscopy (*EFM*) measurements the same image is scanned two times. The first time in semi-contact mode and the second time with an adjustable height offset. The cantilever oscillates and the attractive and repulsive electrostatic forces are balanced by applying a voltage to the tip. The applied voltage indicates the electrostatic potential of the sample [41].

In this work, two different AFMs were used. The cells and model membranes were imaged using a NT-MDT Ntegra PNL in semi-contact mode and a cantilever with a spring constant of 0.03 N/m. The purple membranes were imaged using a Multimode 8 in semi-contact mode and a cantilever with a spring constant of 0.03 N/m. For electrostatic potential measurements of the purple membrane a conductive cantilever was used with a spring constant of 1 N/m.

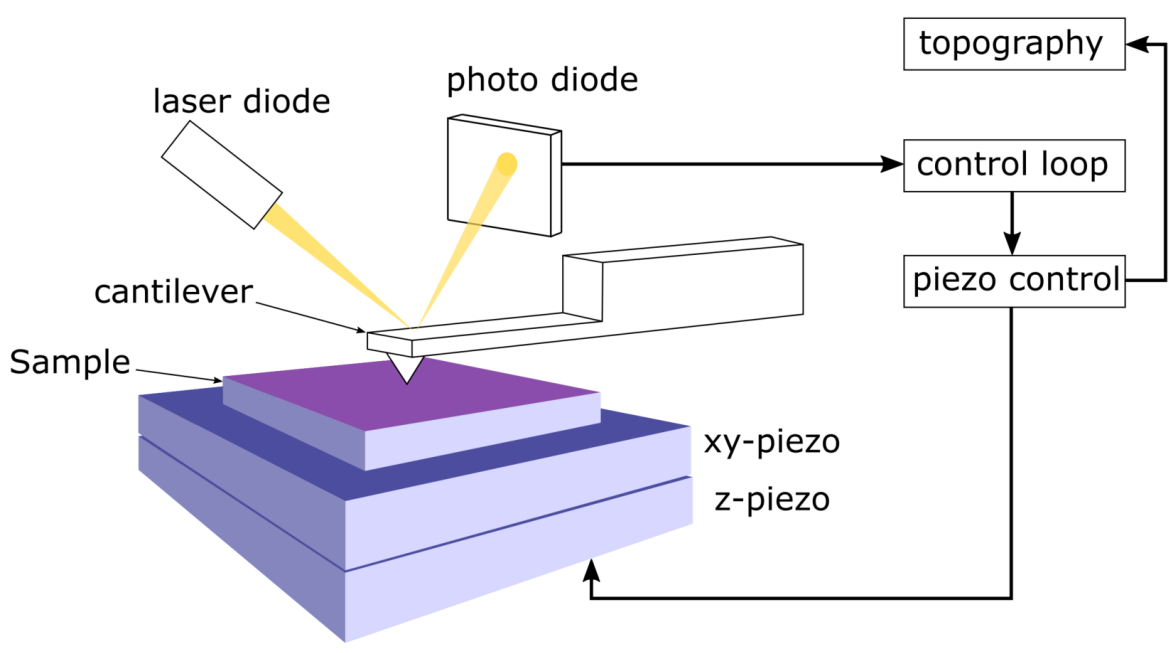


Figure 8: Measuring principle of an AFM in contact mode [42].

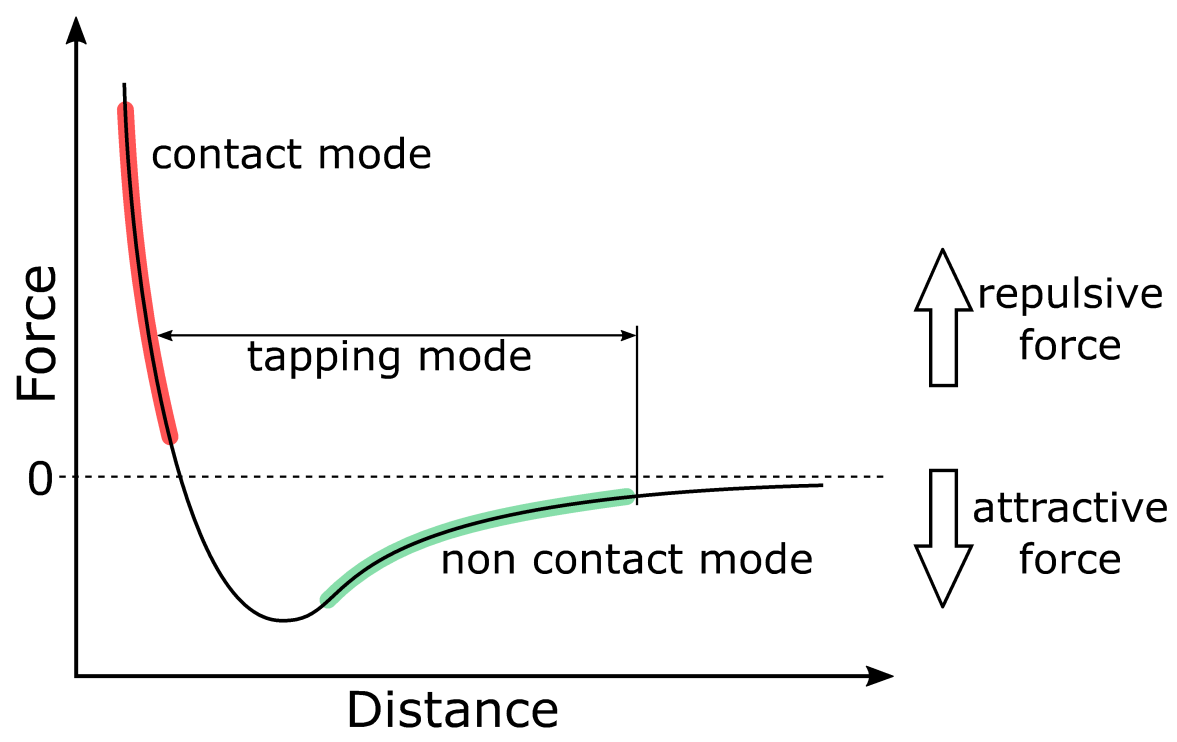


Figure 9: Lennard-Jones-Potential with marked areas for the three different AFM modes [42].

2.3 X-ray photoelectron spectroscopy

X-ray photoelectron spectroscopy (*XPS*) is a method to determine the chemical composition of material surfaces. XPS is based on the photoelectric effect, in which electrons are released from a surface by X-rays. By irradiating a surface with electromagnetic waves, whose energy is greater than the work function of the sample, electrons are excited from occupied initial states to unoccupied, unbound final states of the sample. From near-surface atoms of the sample, these photoelectrons are emitted and in the photoelectron spectrometer energy-dispersive detected. The analyzer used for the detection of the electrons is adjusted via electrostatic lenses, so that only electrons of a certain energy can pass through it [43].

The characteristic components of such an energy spectrum are emission lines of photoelectrons and Auger electron lines. For photoelectrons, a distinction is made between electrons emitted from core levels and those derived from the valence band. For XPS examinations, the positions of the core-level emission lines are usually of importance. The spectra are obtained by plotting the count rate against the measured kinetic energy of the electrons. It is also possible to convert the kinetic energy to the binding energy of the electrons with respect to the Fermi level [44].

Surface sensitivity is one of the most important properties of photoelectron spectroscopy. Crucial for this is the mean free path of photogenerated electrons in the material. This depends strongly on the kinetic energy of the electrons and varies only slightly between different materials. Usually the information depth is around 0.5-2 nm. The measuring principle is illustrated in figure 10 [45].

In this work the samples were analyzed in an Omicron Multiprobe UHV system at an pressure of 10^{-10} mbar. Monochromatic Al $K\alpha$ irradiation, a Sphera electron analyzer with a resolution of 0.9 eV and an emission angle of 20° were used.

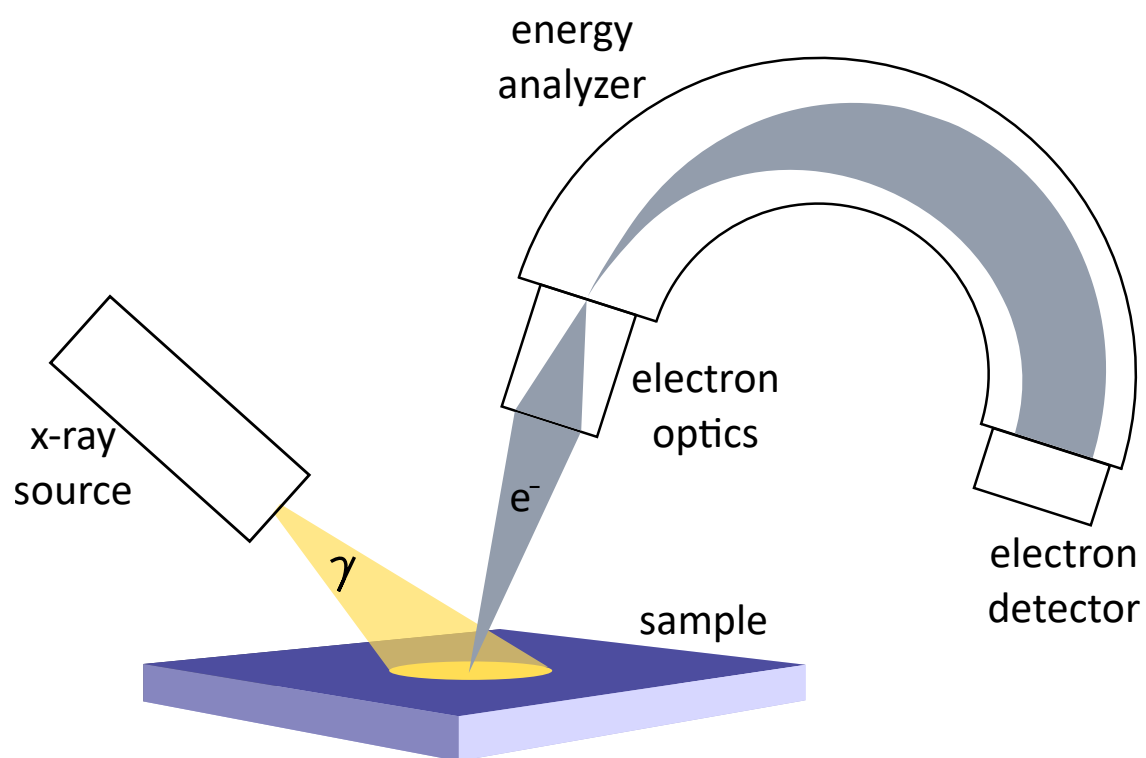


Figure 10: Measuring principle of XPS [45].

2.4 Raman spectroscopy

Raman spectroscopy is an analytical technique for the chemical characterization of samples discovered by Raman and Krishnan in 1928. The operating principle is based on the phenomenon of inelastic scattering of light. Raman and Krishnan used sunlight, which was focused on a sample and detected the scattered radiation, which had an altered frequency, with a lens and optical filters [46].

In modern systems, the sample is irradiated with a single frequency of radiation by using a laser beam. The incoming photon interacts with the molecule, which leads to polarization of the electron cloud. This state is named virtual state and is not stable. Therefore, the photon is reradiated with a frequency shift. The wavelengths of the reradiated light can be detected by a lens and filters. Raman scattering is a weak process as the scattered photons exhibit small frequency changes. Therefore, an effective filtering is essential [47].

Raman spectroscopy is a powerful method to characterize carbon materials as ordered and disordered structures can be distinguished. In this work carbon nanomembranes and carbon foams were analyzed by Raman spectroscopy. Therefore, a Raman spectrometer Labram ARAMIS was operated in the backscattering mode. A blue diode laser with a wavelength of 473 nm and a 10x microscope objective were used.

3 Results and Discussion

3.1 Cells

Biological samples including cells are characterized by nano-sized functional features. But as all biological samples, cells are not conductive. Therefore, they provide a good opportunity to use the high-resolution imaging of non-conductive samples by HIM as shown in this thesis.

Generally, a distinction is made between prokaryotic and eukaryotic cells. Prokaryotes are the simplest, single-celled organisms that, unlike eukaryotes, have no cell nucleus [48]. In this chapter eukaryotes were studied, therefore further sections focus on this cell type. The sections 3.1 - 3.1.2 were previously described in my master thesis [7].

Important cell structures are the organelles, the cytoplasm and the cell membranes. The organelles are embedded in the cytoplasm and include the cell nucleus containing the genome, mitochondria, the Golgi apparatus, centrioles and the endoplasmic reticulum. The mechanical stability of the cell is ensured by its cytoskeleton consisting of actin filaments, intermediate filaments and microtubules. The cytoskeleton extends through the entire cytoplasm and determines the shape of the cell. The filaments of the cytoskeleton form networks and contribute to the stabilization of the cell morphology. The filaments also stabilize cell protrusions. The cell is enveloped by the cell membrane, which separates the cell from its environment, thereby enabling the maintenance of the internal environment of the cell [49]. The vesicle transport by endocytosis or exocytosis between the extracellular matrix and the intracellular space enables controlled exchange of substances. Endocytosis is the invagination process in which a cell receives a vesicle derived from the extracellular matrix through the membrane, whereas in exocytosis a vesicle is delivered across the membrane into the extracellular matrix [50].

The cell membrane consists of a 5-6 nm thick double lipid layer, which is mainly composed of phospho- and sphingolipids, glycolipids and cholesterol [51]. Apart from cholesterol, the lipids have a hydrophobic side facing the center of the membrane and a hydrophilic side provided with a polar head group. The polar head group faces the cytoplasm on the one hand, and the extracellular space on the other hand [52]. The glycolipids have a carbohydrate residue that is important for interactions with the cell environment and cell stability [53]. The cholesterol, which belongs to the sterols, resides in the cell membrane. It increases the permeability and restricts the fluidity of the membrane [53].

The biological function of the membrane is mainly determined by a variety of different proteins [52]. The ratio of proteins to lipids varies depending on the type of membrane and cell. For example, while the cell membrane of a nerve cell contains 18 % proteins, the inner

mitochondrial membrane has a protein content of 76 %. According to the fluid mosaic model by Singer and Nicolson from 1972, the phase state of the lipids in cell membranes is fluid, allowing membrane proteins to move laterally freely [49]. A distinction is made between integral, lipid-anchored and peripheral membrane proteins. While integral membrane proteins span the double lipid layer, peripheral membrane proteins are superimposed on the surface of the inner or outer lipid layer. Integral membrane proteins include, for example, ion channels that are responsible for the generation and transmission of electrical signals between neuronal linked cells [54].

Lipid-anchored membrane proteins were originally thought to be peripheral membrane proteins but, in contrast to peripheral membrane proteins, are covalently linked to the hydrophobic lipid chains of the cell membrane. Since the lipid-anchored membrane proteins usually occur with membrane sphingolipids, they protrude from the cell membrane and assemble into microdomains. These microdomains are called lipid rafts [55]. A special type of raft-like domains are caveolae, which take part in endocytosis [56]. Their size is in the range of 10-200 nm, therefore these domains can not be imaged by confocal microscopy [57].

3.1.1 Stem cells

Stem cells can both reproduce and/or progress in differentiation. This means that the progeny of a stem cell are either stem cells themselves or more differentiated cells. Self renewal or differentiation of the stem cell depends on signals from the microenvironment of the respective niche [58].

The adult stem cells studied in this work can be transformed into cells with neuro-ectodermal and mesodermal phenotype, in particular into nerve, bone, fat and cartilage cells, as shown in figure 11 [59]. In general, a distinction is made between totipotent, pluripotent and multipotent cells. While research with human totipotent stem cells derived from embryonic tissue is possible only under strict conditions in Germany, research with adult human multipotent stem cells is considered ethically unobjectionable [58]. The multipotent stem cells studied in this work were obtained from the human respiratory mucosa of the nasal cavity, therefore named neural crest-derived stem cells (*NCSCs*). The advantage of these stem cells is, that they are easily accessible and can be isolated from patients of all ages while possessing a vast differentiation potential [59]. Figure 12 shows a NCSC in a) and neuronally differentiated NCSC in b) imaged by confocal laser scanning microscopy (*CLSM*).

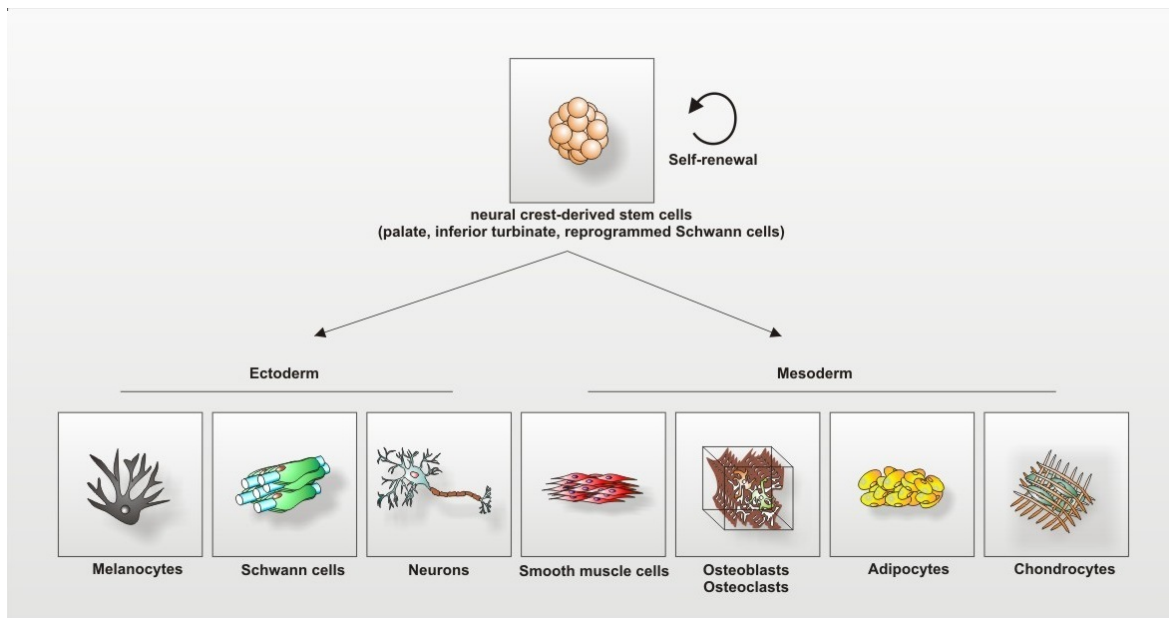


Figure 11: Self renewal and differentiation of NCSCs [60].

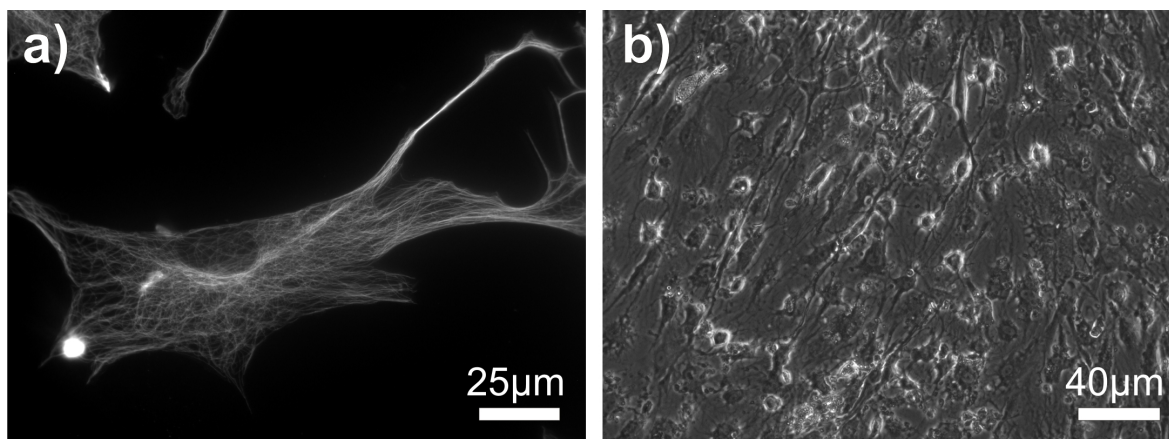


Figure 12: a) A NCSC and b) neuronally differentiated NCSCs.

3.1.2 Neurons

The human brain has more than 10^{11} neurons, which are linked together according to fixed rules and form a complex network. A neuron usually consists of a cell body, called soma, several dendrites and an axon, which is much longer than the dendrites [8].

While the dendrites act as signal inputs through spines, the axon has the ability to relay signals to other neurons. To establish a connection between neurons the so-called growth cone is of utmost importance. It is located at the end of the axon and equipped with finger-shaped membrane protrusions called filopodia, which scan surrounding areas. If the filopodia get in contact with unfavourable environment, the growth cone retreats. When the filopodia come into contact with a favourable environment such as a dendrite of another cell, the entire growth cone is directed in that direction, allowing to build synaptic connections [61].

The dendrites can form a multitude of branches and thus allow up to 10^5 signal inputs on a single neuron, whereby the cell body itself can also receive signals. The shape of the signal is the same for all neurons and consists of changes in the electrical potential across the cell membrane. In general, a spine that emerges from a dendrite forms a single synapse. A distinction is made between thin, mushroom, sessile and stubby spines. Spines serve to enlarge the surface and change its shape within seconds, which is essential for finding and stabilizing correct synaptic connections. Wiegert and Oertner describe spines as the elementary unit of memory [62].

The neurons studied in this work are hippocampal mouse neurons and are shown in figure 13 imaged by CLSM.

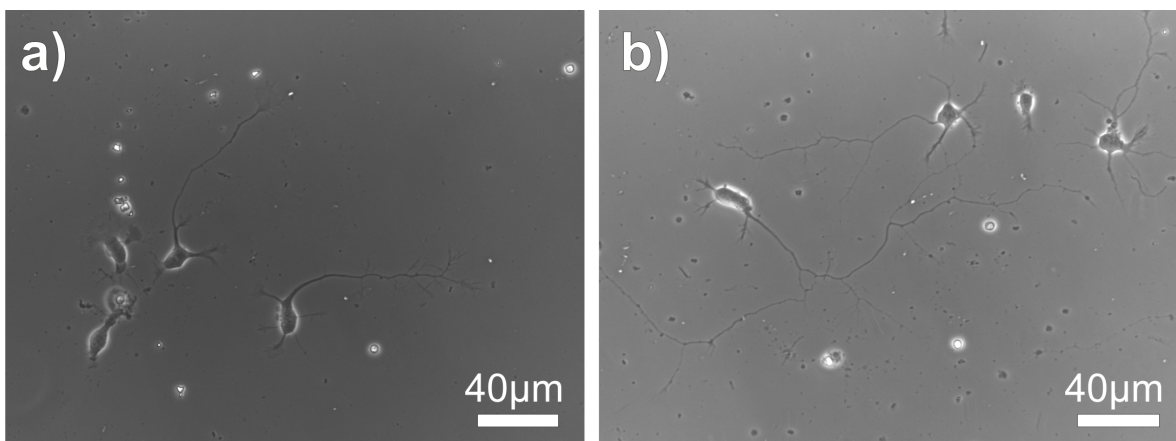


Figure 13: a) Hippocampal mouse neurons after 1 day in vitro and b) after 3 days in vitro.

3.1.3 Imaging of cell membranes

Figure 14 shows a silicon nitride membrane on a metal grid, on which HeLa cells were cultured. The HIM images in a) and b) show the same spot on the sample. In the middle of the images are two cells located on top of the freestanding membrane. Image a) was taken without simultaneous exposure by an electron floodgun and shows charging effects since the sample is not coated with metal. Hence, the membrane, which is not in contact with the metallic grid and the cells appear dark. In contrast to that image b) was taken with the floodgun, which can be used for charge stabilisation in the HIM. Therefore the charge effects are minimized and the cells and the freestanding membrane show a good contrast.

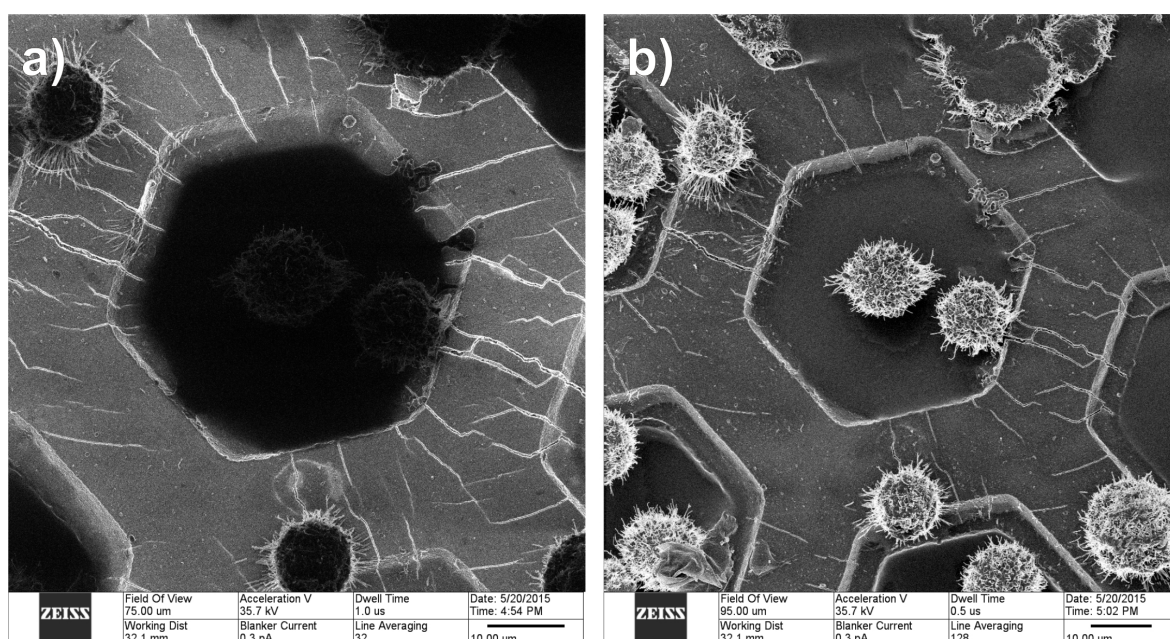


Figure 14: a) A cell imaged by HIM without floodgun and b) with floodgun.

HIM images of different cell types have shown that pits appear in all investigated cell membranes [63]. These pits could be areas where saturated fatty acids were located before the cells were critical point or freeze dried. Before drying of the cells their membranes were fixed with osmium tetroxide, which only crosslinks unsaturated fatty acids concentrated outside of the lipid nanodomains. In contrast to that non stabilized fatty acids inside the nanodomains will get lost during the subsequent drying process (e.g. the dehydration in ethanol) and the pits emerge. Figure 15 shows three of the investigated cell types: NCSCs, NCSC-derived human neurons, and hippocampal mouse neurons. The mean diameter of the pits is less than 20 nm and the main fraction of the domains lies closer than 50 nm to the next neighbor, which indicates the raft-like origin. Flask-like shaped pits originating from exocytosis or endocytosis for example would need to have a greater next neighbor distance. The pictures show the great ability to image uncoated cells at a high resolution with the HIM. In a common SEM

a metal coating would be necessary to image biological materials. Therefore, small features as the pits shown would be disturbed by the coating.

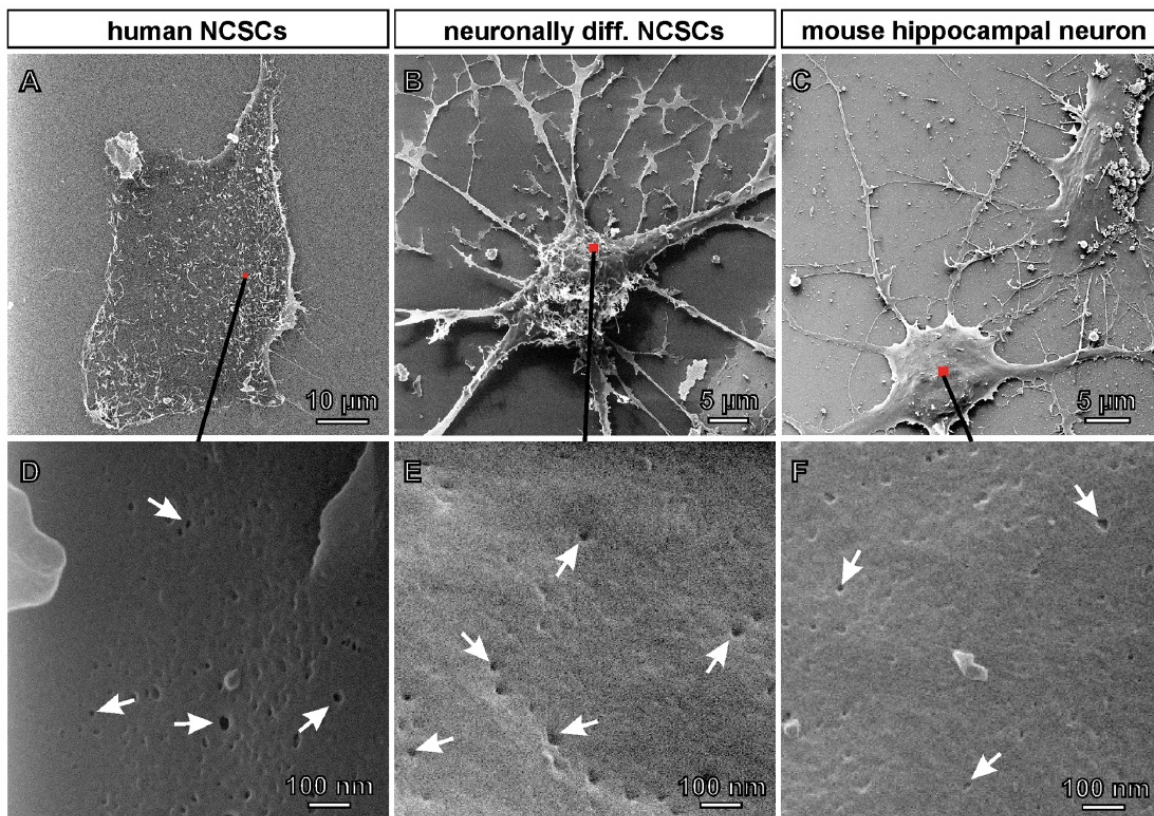


Figure 15: Three different cell types imaged by HIM. They all show pit-like structures in the cell membrane [63].

To elucidate the exact mechanism of nanodomain extraction another microscopy technique, the AFM, was applied to image the change in membranes after fixation and ethanol treatment. Figure 16 shows topographic AFM images of a NCSC fixed with aldehydes and osmium tetroxide (left) and of the same cell rinsed with 70 % ethanol (right) imaged under the same conditions. The fixed cell membrane appears smooth with a few groove-like membrane features (inset, left image). After treatment with ethanol the membrane becomes significantly rougher. Additionally, the small pit-like structures can be detected in the membrane (inset, right image). These images support the hypothesis that ethanol treatment after fixation leads to a pit formation in the cell membrane due to the loss of regions consisting mainly of saturated fatty acids.

To further support the above mentioned hypothesis a supported lipid bilayer was generated to work as a model membrane. AFM images of the following process are provided in figure 17. 1,2-dioleoyl-sn-glycerol-3-phosphocholine (*DOPC*) and 1,2-distearoyl-sn-glycerol-

3-phosphocholine (*DSPC*) on mica were used to mimic a biological cell membrane (B). After fixation (C) and treatment with ethanol (D), only DOPC areas were able to withstand the extraction process, which was proposed by the hypothesis. Further investigation by CLSM showed that labelled, saturated domains in the cell membranes showed no signal after treatment with ethanol. In summary these experiments lead to the conclusion that the pits in the cell membrane, which were first seen in the HIM, originate from lipid-raft like nanodomains. These nanodomains, especially their size and distribution, have an important impact on elementary functions of cells and can be visualized with nanometer precision by HIM.

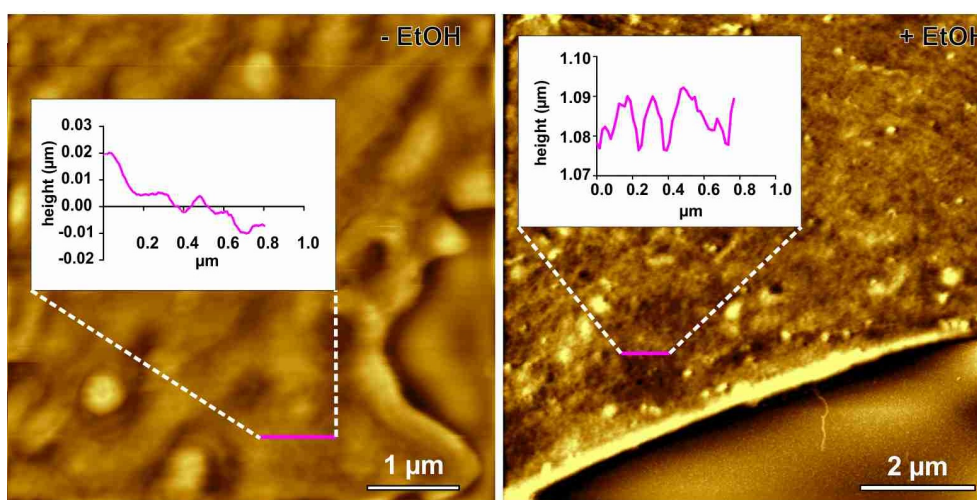


Figure 16: NCSC imaged by AFM before and after ethanol treatment.

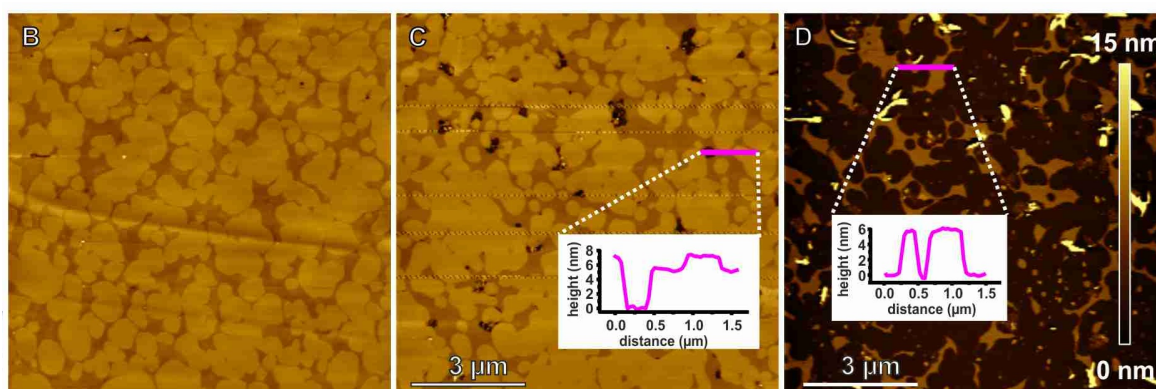


Figure 17: AFM images show the mechanism of the pit-like membrane feature formation in a model membrane [63]. DOPC and DSPC on mica were used to mimic a biological cell membrane (B). After fixation (C) and treatment with ethanol (D), only DOPC areas were able to withstand the extraction process.

High resolution HIM images of the membrane of a critical point dried neuronally differentiated NCSC are shown in figure 18. Figure 18 (A) shows the analyzed cell and (B) a close up of the somatic cell membrane. A neurite of the cell is imaged in (C), whereas (D) shows a close up of the cell membrane of the neurite.

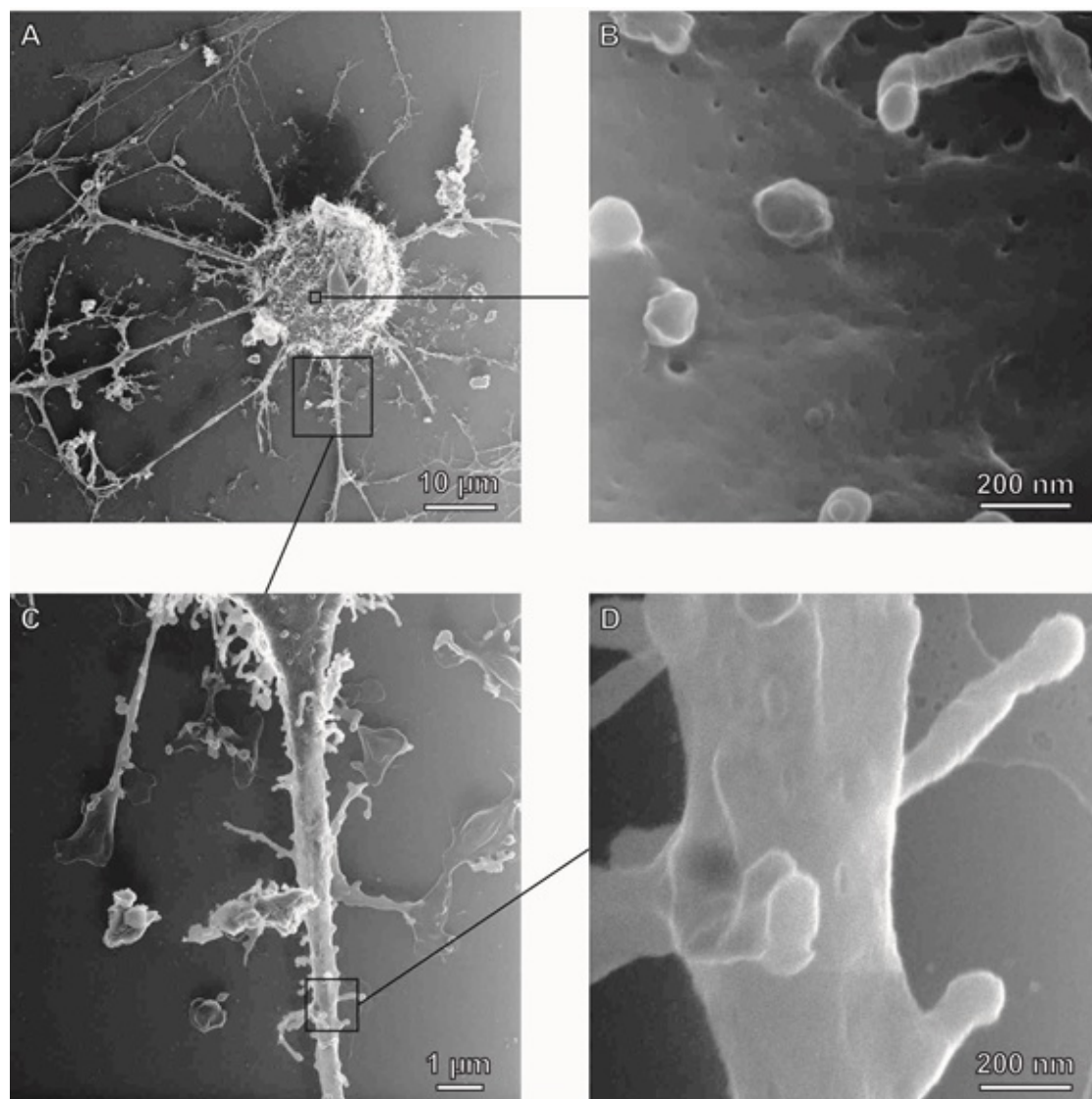


Figure 18: HIM images of a critical point dried neuronally differentiated NCSC [63].(A) HIM image of a neuronally differentiated and critical point dried NCSC. (B) The somatic membrane reveals pit-like nanodomains. (C) A neurite of the cell. (D) High magnification of the membrane of the neurite.

A different preparation method for imaging neuronally differentiated NCSCs by HIM is freeze drying after the fixation of the cells. This method does not require ethanol treatment compared to critical point drying. Figure 19 includes three images of the same cell membrane at different magnifications labelled with (A)-(C). The highest magnification in (C) reveals similar pit-like structures compared to critical point dried cells of the same cell type. This indicates that the unfixed nanodomains are also unstable in air. Preparation details and further information can be found in [63]. The presented images show that HIM of biological cells can be used to get a deeper understanding of the composition of cell membranes of different cell types and regions.

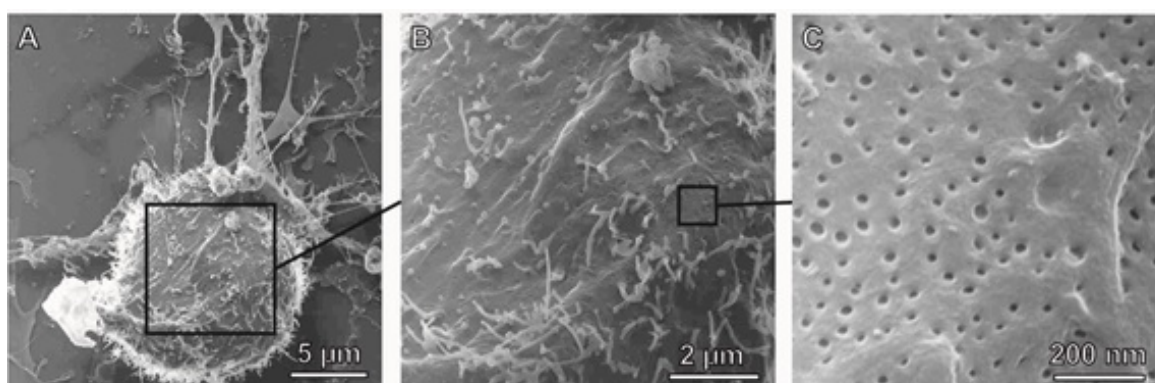


Figure 19: (A)-(C) HIM images of a freeze dried neuronally differentiated NCSC at different magnifications. The highest magnification in (C) shows that the cell membrane has similar sized and shaped nanodomains as membranes observed after critical point drying [63].

Cells on structured surfaces

In a following study it was investigated how mouse hippocampal neurons behave on multi-electrode arrays [64]. In particular, the process of neuron attachment and neurite guidance was investigated by HIM and light microscopy. Therefore, a structured poly lysine coating on glass was produced consisting of spots of a size allowing only one cell to adhere connected through lines for the neurite guidance. As figure 20 shows the neurons adhere to the substrate in a random manner after initial attachment (A). But after 3 days most of the neurons migrated toward the coated surface (dashed lines) whereas the dots seem to be more attractive since they provided enough space for the cell soma with a diameter of $30\ \mu\text{m}$ compared to the $3\ \mu\text{m}$ lines (B, C). The HIM image in (D) shows the tight adherence of a cell as seen by adhesion protrusions. The inset in (D) confirms that the axon is tightly bound to the surface as wanted.

To initially investigate which line width is needed to guide the axon but prevents the cell soma from adhering on the line, different line widths were tested. As seen in figure 21 the neuron on the pattern (dashed line) in (a) with the thin line of about $2.5\ \mu\text{m}$ adheres to the node whereas the neuron in (b) stays on the line since the soma fits onto the $6\ \mu\text{m}$ line. Hence, a pattern with $6\ \mu\text{m}$ lines is too wide for building a neuronal network where the somata stay on the nodes. Preparation details and additional information can be found in [64]. In summary the images shown in this chapter reveal the high potential of imaging biomaterials as cell membranes without coating via HIM to study their morphology or adhesion on different substrates.

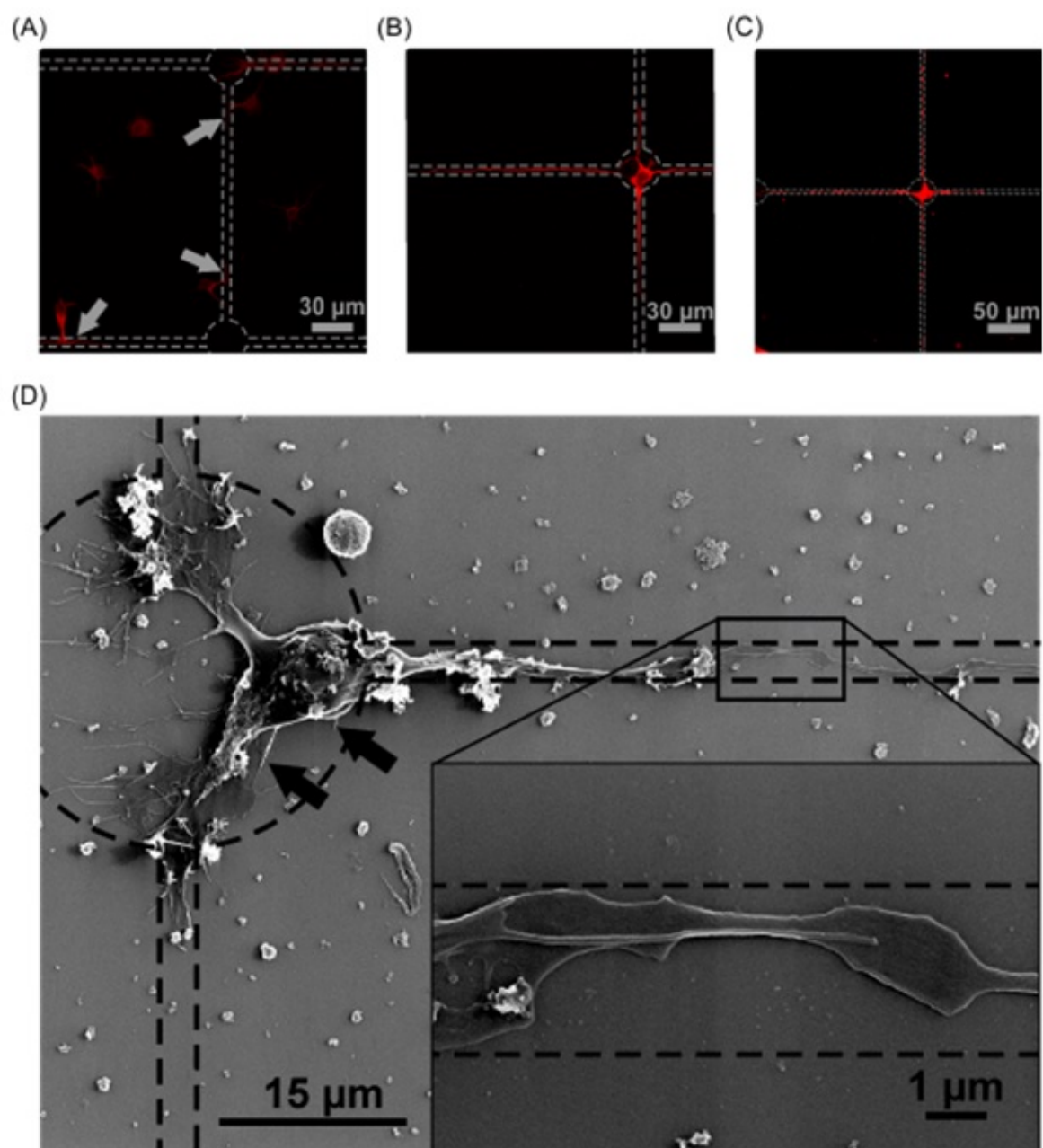


Figure 20: Neurons on a patterned surface [64]. (A), (B) and (C) show the migration of the neurons towards the pattern imaged by CLSM. (D) A single neuron is imaged by HIM.

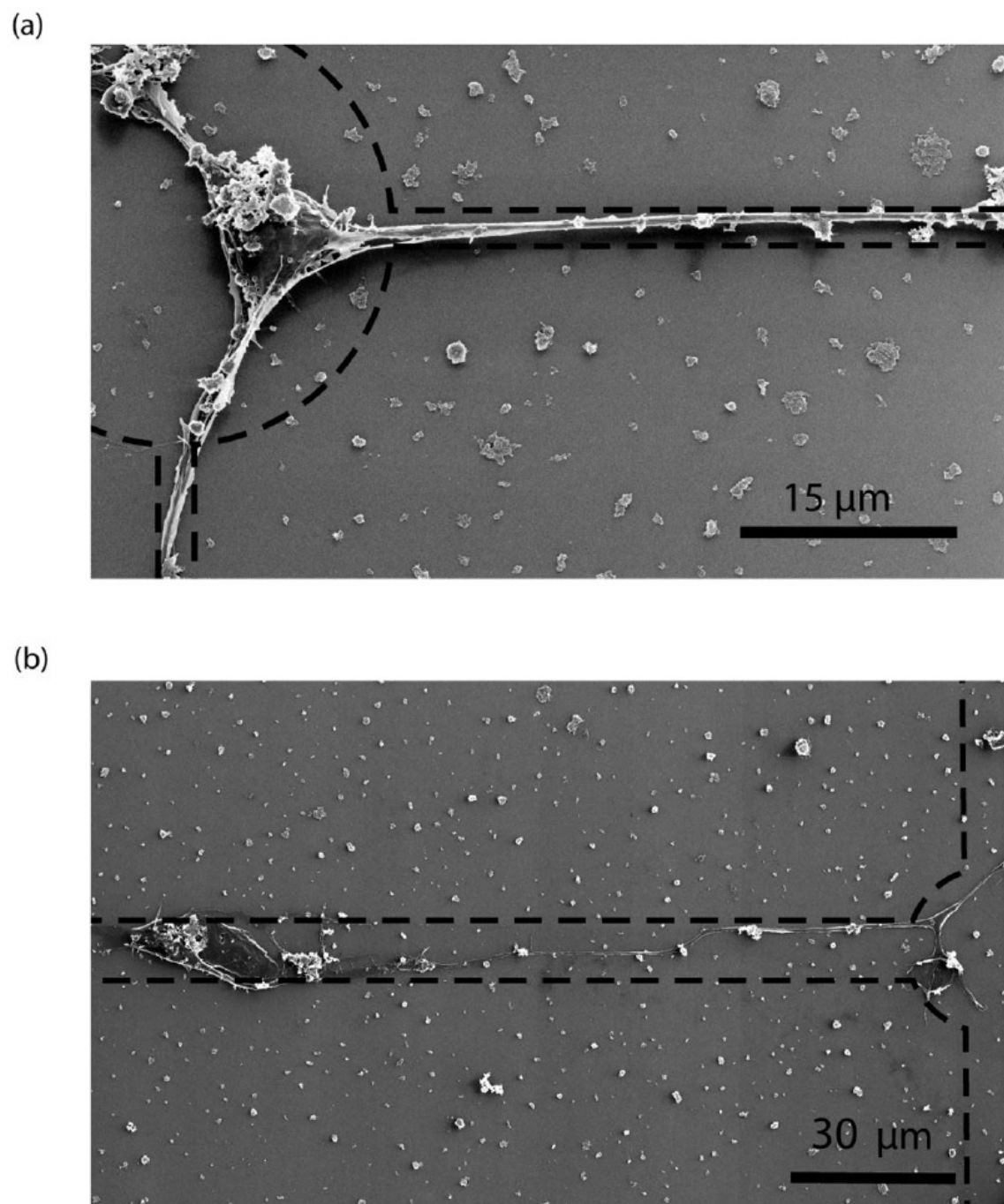


Figure 21: Line width dependence of neuron adhesion on patterns [64]. The line in (a) has a width of 2.5 μm and the line in (b) has a width of 6 μm.

3.2 Carbon nanomembranes

The production and characterization of two-dimensional functional membranes is a rapidly growing field of research within the nanosciences [65]. Molecular thin freestanding films have high potential as active or passive components in electrical and mechanical devices, biomimetic applications, water filters or diffusion barriers [66, 67, 68, 69].

Carbon nanomembranes (*CNMs*) are 1 nm thin carbon-based sheets. CNMs are prepared by irradiation-induced crosslinking of surface bound self-assembled monolayers (*SAMs*), which consist of aromatic molecules on a substrate. The crosslinking of neighboring molecules can be achieved via electron irradiation, UV- or EUV-radiation, since these methods induce the separation of C-H bonds. This process is shown in figure 22 a). By etching away the substrate, the CNM can be transferred to another substrate such as a metal grid [70]. Parts of the membrane are then freestanding. Figure 22 b) and c) show two HIM images of CNMs that were transferred onto metal grids with carbon lacey covered openings.

An advantage of CNMs is that their modular construction system allows chemical functionalization and modification of the membrane surface. Membranes can be tailored by the appropriate choice of precursor molecules and irradiation conditions. Through modification with chemical lithography complex architectures have been build as patterns of proteins or bifacial Janus membranes [71, 72]. In this work, CNMs have been used to produce internally structured membranes and as a support for biological membranes. Therefore, SAMs consisting of 4'-nitro-1,1'-biphenyl-4-thiol (*NBPT*) or 1,1'-biphenyl-4-thiol (*BPT*) on a Au(111)-substrate have been mostly used (see figure 22).

To study the crosslinking process during irradiation, NBPT on gold samples were exposed to synchrotron radiation with a wavelength of 13.5 nm at different doses as seen in figure 23. The spectra have been measured by XPS. The lowest dose is 300 mJ/cm² and the highest dose is 20000 mJ/cm². The spectra show the conversion of the terminal nitro groups into amino groups as seen by the chemical shift of the N1s binding energy from 405.5 eV to 399.2 eV. The resulting amino groups can be used for further functionalization. It can be seen that at the highest dose a nitro group peak is still present, which means that the CMN is not fully crosslinked. The membranes shown in the following sections have been crosslinked by electron irradiation via electron floodgun at an energy of 100 eV and a dose of 50 mC/cm² in a vacuum chamber at a pressure of 10⁻⁷ mbar.

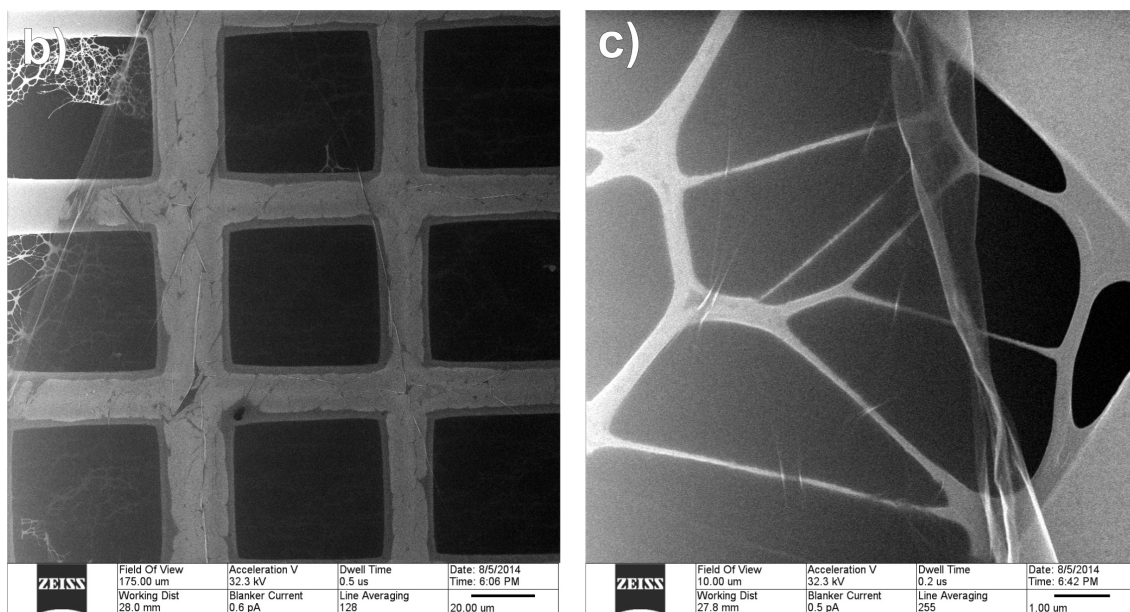
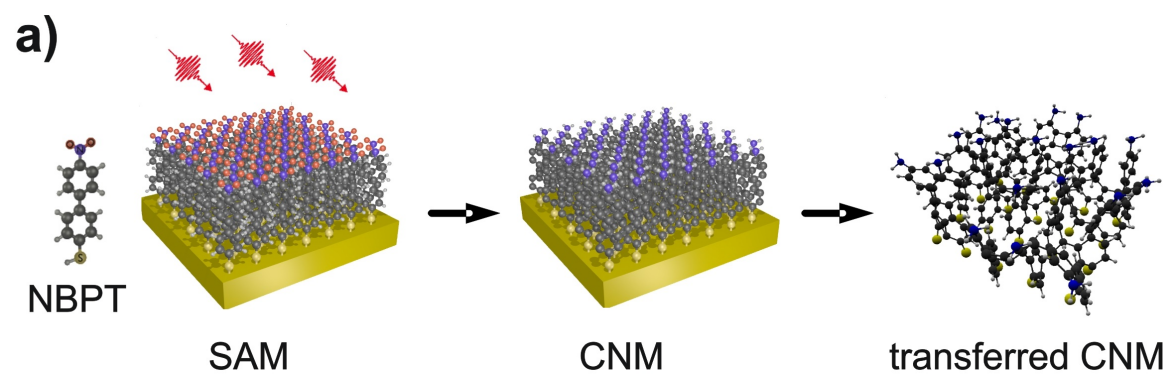


Figure 22: Production of carbon nanomembranes.

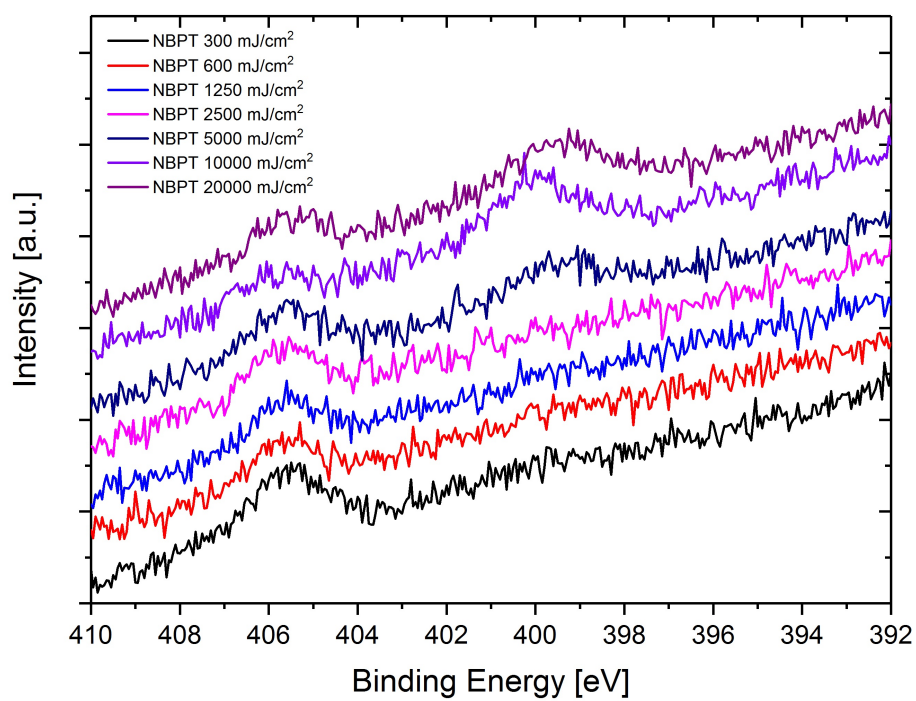


Figure 23: Irradiation dose series of NBPT on gold. XPS spectra show the N1s binding energy shift during irradiation.

3.2.1 Internally structured CNMs

In section 3.1.3 it is shown that a model membrane can help to understand biological membranes. Another type of model to study self-assembly or membranes are SAMs made of thiols on gold. But these monolayers are not stable in the absence of the substrate. Crosslinking of a SAM produces a CNM, which is mechanically stable even without a substrate [70]. Direct laser patterning of a SAM leads to the removal of molecules at the exposed areas. These gaps can be refilled with other aromatic molecules. Subsequent crosslinking converts these mixed SAMs to internally patterned CNMs [73]. A scheme of this process is shown in figure 24.

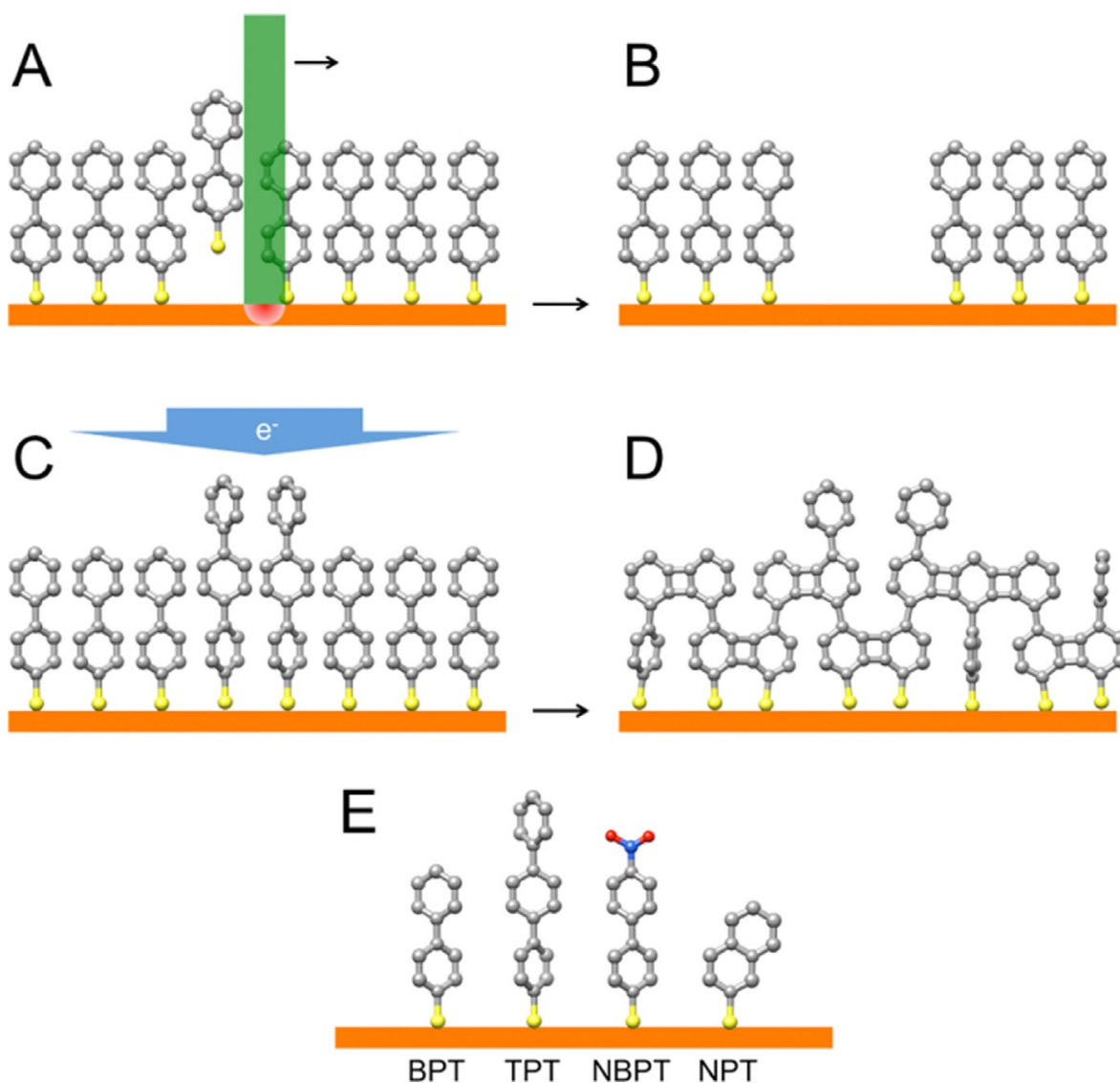


Figure 24: Internally patterned CNMs by direct laser patterning [73].

After crosslinking the internally patterned CNMs were transferred to different substrates and analyzed with a light microscope, HIM and SEM. Figure 25 includes two images of the same sample, an internally patterned CNM transferred on gold and converted from a NBPT SAM patterned with BPT SAM lines. The crosslinked NBPT regions are labelled as ABPT, since the nitro groups convert into amino groups. These groups can be used for further functionalization as shown in the following chapter. The structured functionalization could be used to build devices such as a biochip by chemical modification with proteins to detect markers in biological samples. This method could be particularly useful in the single cell analysis, because of the small amounts of sample material.

Figure 26 shows an freestanding ABPT/BPT CNM transferred onto a metal grid. In summary, this method leads to a membrane with distinct chemical domains comparable to biological membranes. Further details on the preparation and usage of internally patterned CNMs can be found in [73].

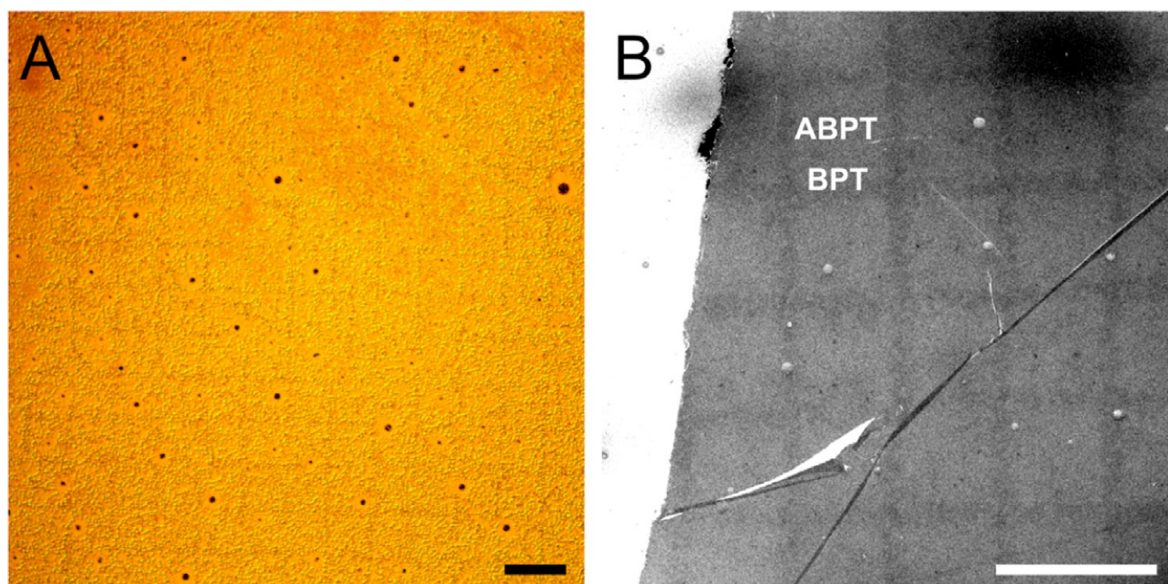


Figure 25: Internally patterned CNMs transferred to another substrate and imaged by (A) light microscopy and (B) helium ion microscopy [73]. Scale bars are 200 μm .

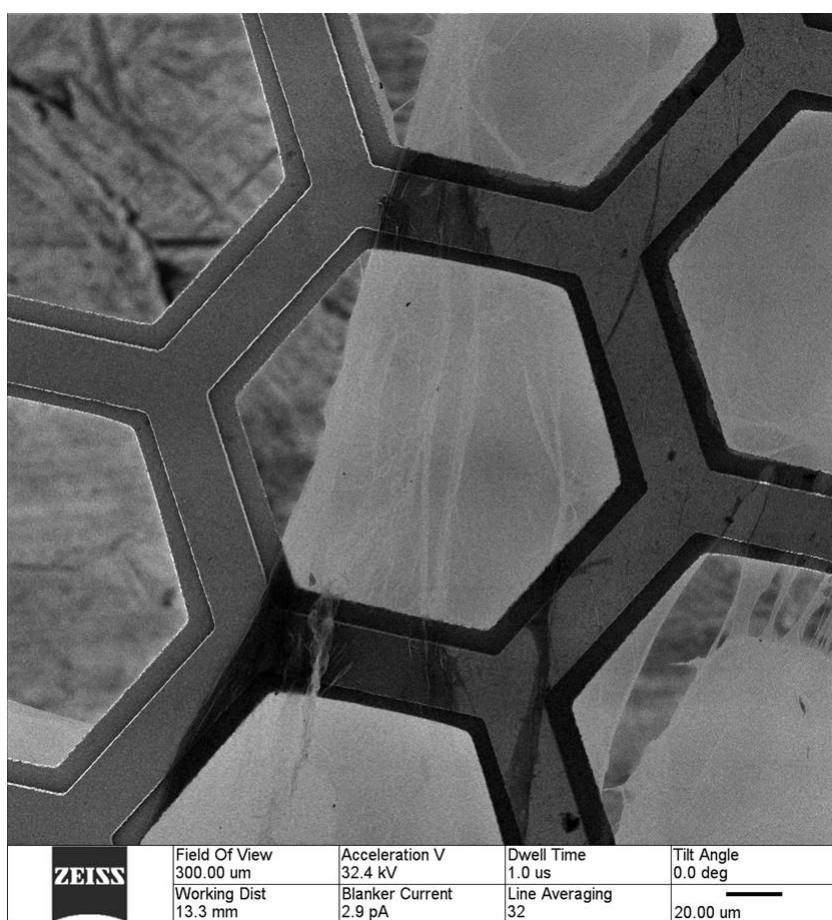


Figure 26: Internally patterned CNM transferred onto a metal grid.

3.2.2 CNM as a substrate for purple membrane

The goal of this project is to achieve a hybrid of biomolecular macromolecules on a surface by assembling CNMs and purple membranes (*PMs*). *PMs*, which are derived from *Halobacterium salinarum*, are membranes consisting of bacteriorhodopsin (*BR*) arranged in form of a hexagonal crystalline lattice and lipids [74]. *BR* is a light-driven proton pump, which generates a proton gradient and hence a free enthalpy, which enables energy consuming cell processes in the *Halobacterium salinarum* [13]. It consists of 7 alpha helices and one molecule of retinal, which changes its conformation and initiates a proton transfer when irradiated by photons [75]. Since *PMs* have a diameter of only a few micrometers and a thickness of 5 nm, they require a suitable carrier film for potential, technical applications such as a macroscopic proton pump [76].

CNMs are only 1 nm thin and can be prepared free-standing, therefore they are ideal carrier films. Since the migration of the protons through the membrane is unidirectional, the homogeneous orientation of the *PM* fragments on the CNM is mandatory for the functionality as a proton pump. The *PM* fragments itself include preoriented *BR* molecules, which can be genetically modified [77]. An assembly of *PMs* on a substrate is challenging as the two sides of the *PM* only slightly differ in charge and chemical composition.

Advance has been made with mutants where specific linker sides have been introduced on only one side of the membrane such as polyhistidine-tags. To obtain a binding of the mutated *PMs* on a carrier film, CNMs were chemically functionalized with molecules having a nitrilotriacetic acid (*NTA*) moiety as a head group, which is loaded with nickel. This functionalization leads to a complex formation with the polyhistidine-tags of the mutant during incubation of a *PM* solution on CNM. A scheme of a *PM*, which is bound to a CNM creating a hybrid structure connected through binding points is shown in figure 27.

A challenge concerning the assembly of *PMs* on CNM is the immobility of *PMs* in water due to fragment sizes in the micrometer range and thousands of *BR* molecules per fragment. Special techniques, such as concentration by drying or electrophoretic sedimentation, are needed to bring the two membranes, CNM and *PM*, into close contact to enable chelation. Additionally, *PM* fragments are irregular elliptical shaped, which hinders the formation of *PM* monolayers. The only way to form *PM* monolayers on CNMs might be recrystallization on the surface.

Since there is a limited availability of the C-terminal His-tagged *PM* mutant, initial ex-

periments were performed with wildtype PMs and NBPT CNMs without functionalization. NBPT CNMs were prepared as follows. 300 nm gold on mica substrates were cleaned in an ozone cleaner, rinsed with ethanol and dried in a stream of nitrogen. The cleaned samples were then immersed in 1 mmol solution of NBPT in degassed and dry dimethylformamide (*DMF*) and stored under nitrogen atmosphere. After 72 hours the samples were taken out of the solution and rinsed with DMF and ethanol. For crosslinking of the SAMs the samples were introduced into a high vacuum chamber (10^{-7} mbar) and irradiated with electrons at an energy of 100 eV and a dose of 50 mC/cm². After crosslinking the samples were stored under argon atmosphere until further use.

The wildtype PM solution in water was diluted in water to an optical density of $OD_{570} = 0.2$. Figure 28 shows the absorption spectrum of wildtype PM in water at a pH of 7 at room temperature. The longest wavelength absorption band occurs at 570 nm, which belongs to BR. This indicates intact BR proteins in the PM fragments.

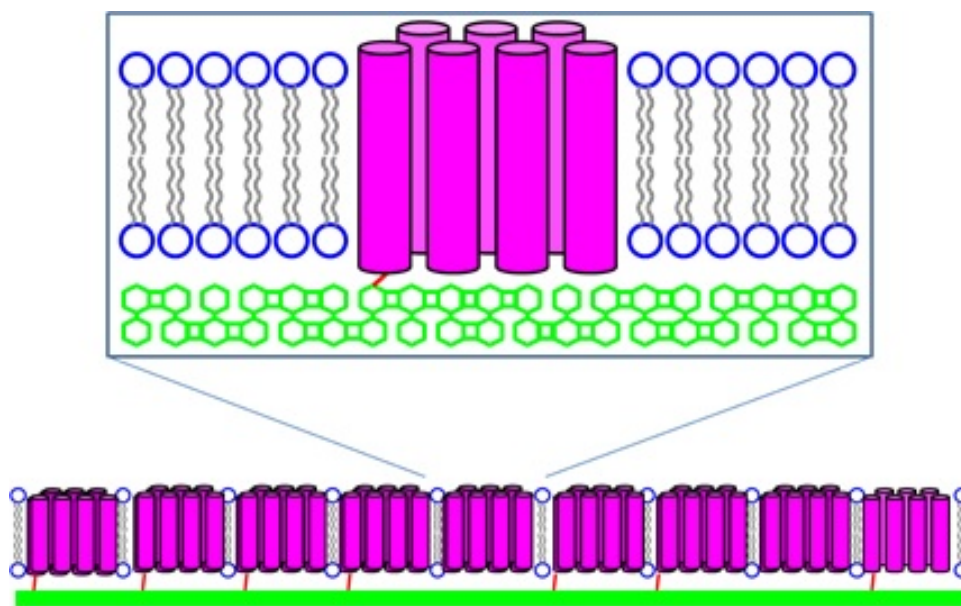


Figure 27: Hybrid structure consisting of a CNM (green) and a PM. The PM consists of BR (purple) and lipids (blue). The unidirectional assembly of PMs on CNMs is necessary for the potential use of their proton-pumping properties. The linkers are depicted as red lines.

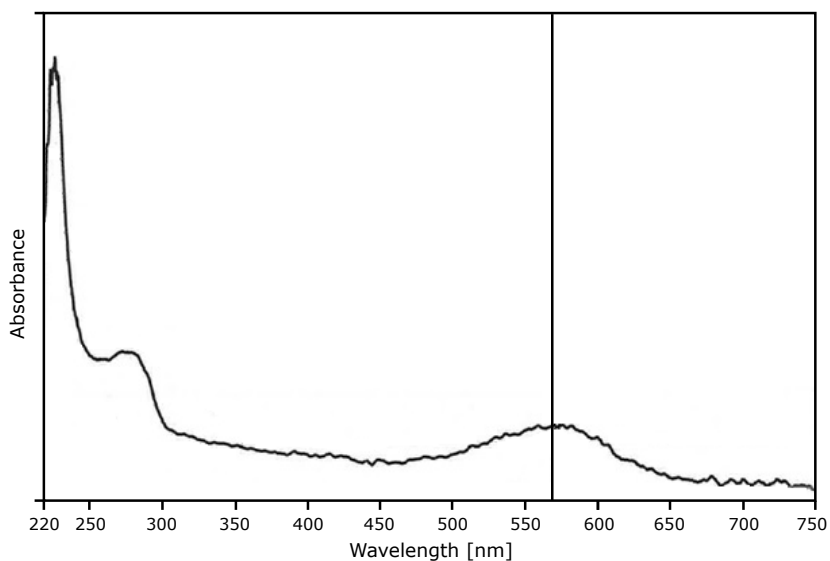


Figure 28: Absorption spectrum of wildtype PM in water at a pH of 7 and room temperature.

Figure 29 shows three HIM images of NBPT CNMs, on which wildtype PMs were incubated by drop casting with a) deionized (*DI*) water at a pH of 7, b) 300 mM potassium chloride at a pH of 8.2 and c) 5 mM calcium chloride, 300 mM potassium chloride, 10 mM Tris buffer at a pH of 8.2. After an incubation time of 40 minutes the samples were rinsed with the respective liquid for 1 minute each. The images reveal that the PMs incubated and rinsed with water were washed away by the rinsing. However, PMs incubated and rinsed in the presence of salt were not or only partially washed away.

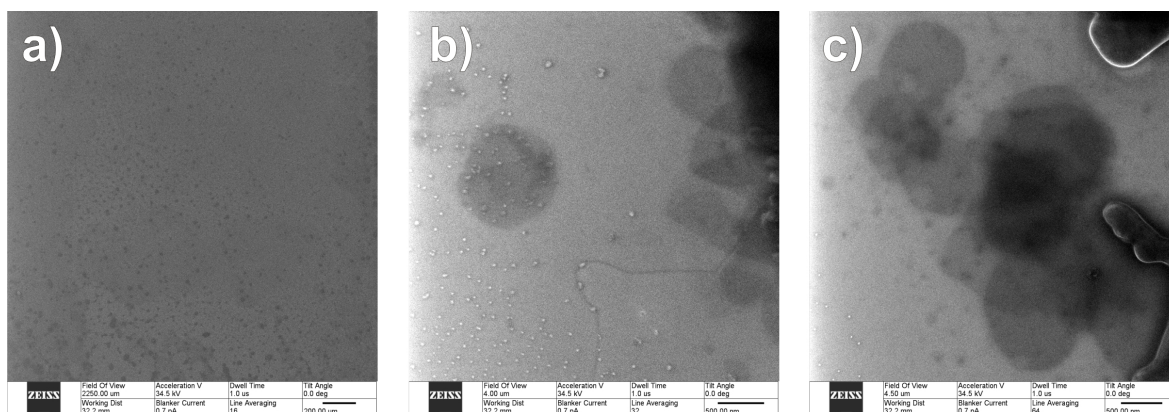


Figure 29: HIM images of NBPT CNMs, on which wildtype PMs were incubated by drop casting with a) deionized (*DI*) water at a pH of 7, b) 300 mM potassium chloride at a pH of 8.2 and c) 5 mM calcium chloride, 300 mM potassium chloride, 10 mM Tris buffer at a pH of 8.2. After 40 minutes of incubation the samples were rinsed with the respective liquid for 1 minute each.

This behavior changes when the wildtype PM is incubated, dried in air and then rinsed with the respective liquid. NBPT CNMs, which have been incubated for 40 minutes with wildtype PMs with and without a drying step between incubation and rinsing, were analyzed by CLSM. The samples, which have been dried between incubation and rinsing, show that the PM fragments could not be removed from the substrate by rinsing. The samples, which were directly rinsed show that PMs incubated and rinsed with DI-water can be almost fully removed, whereas incubation and rinsing with salt solutions result in patches on the surface. The highest amount of patches after 40 minutes of incubation and subsequent rinsing can be observed for 300 mM potassium chloride solution. This result and figure 29 reveal that drop casting of wildtype PMs on NBPT CNMs leads to overlapping PMs forming clusters on NBPT CNMs with single flat lying PM patches in-between.

An incubation series of wildtype PM on NBPT CNM is shown in figure 30. All samples were incubated with wildtype PM in a 300 mM potassium chloride solution and were not rinsed. Figure 30 shows AFM images of wildtype PMs on NBPT CNM after a) 1 hour of incubation, b) 4 hours of incubation, c) 12 hours of incubation and d) 24 hours of incubation. The images indicate that a longer incubation time leads to a higher coverage since a) shows a 50 % coverage whereas d) reveals a 80 % coverage.

Nonetheless, a monolayer consisting of PM patches on NBPT CNMs could not be achieved by drop casting. At this state the PM patches orient in a random way on the sample due to the size of the patches and van der Waals forces. This is shown by AFM/EFM images in figure 31). Therefore, the next sections focus on the functionalization of NBPT CNMs for the assembly of His-tagged PMs on modified NBPT CNMs.

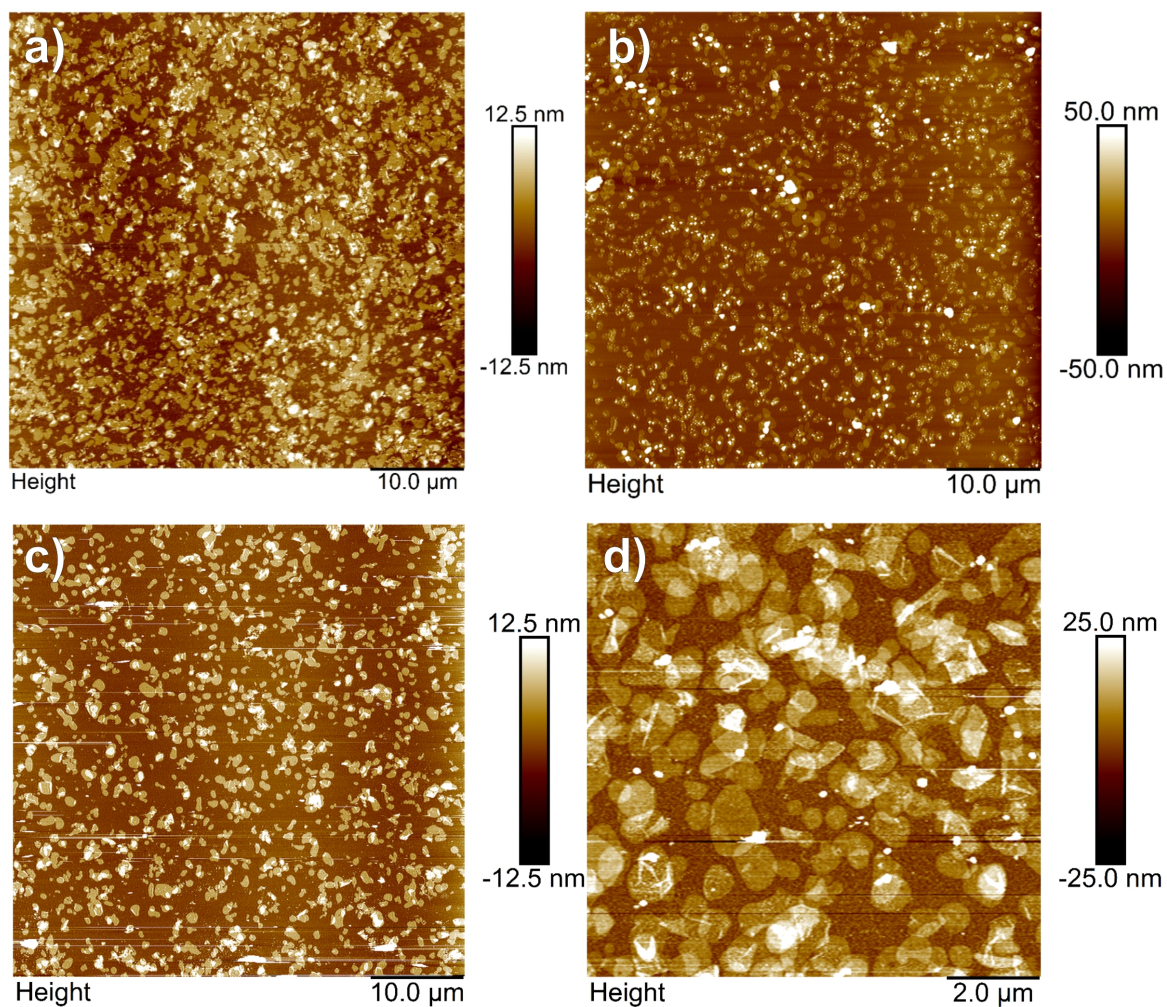


Figure 30: Incubation series of wildtype PMs on CNMs. AFM images of wildtype PMs on NBPT CNM after a) 1 hour of incubation, b) 4 hours of incubation, c) 12 hours of incubation and d) 24 hours of incubation without rinsing.

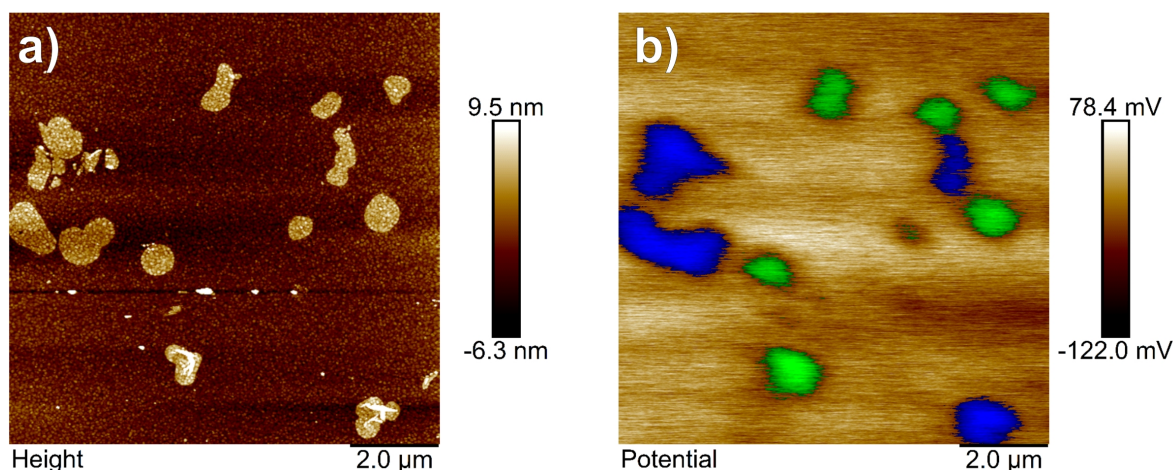


Figure 31: AFM/EFM measurements reveal the orientation of wildtype PMs on NBPT CNM. The EFM image in b) demonstrates that the orientation is random.

To achieve oriented PM patches bound to CNM, NBPT CNMs were functionalized to obtain NTA moieties as head groups of the CNM. These moieties can be loaded with nickel enabling complex building with molecules or particles, which are modified with His-tags, e.g. His-tagged PM mutants. The first promising functionalization of NBPT CNMs is depicted in figure 32. The images in figure 32 a)-c) schematically show the 2 step reaction to obtain NTA moieties as head groups of the NBPT CNM. For this purpose, 3-(Maleimido)propionic acid N-hydroxysuccinimide ester was dissolved in dried DMF (5 mg in 1 mL). 5 μ L of this solution was placed onto a NBPT CNM by drop casting and sandwiched with another substrate. The samples were stored protected from light and rinsed with DMF after 30 min. Subsequently the samples were dried in a stream of nitrogen. For the second functionalization step N-[N_{α} , N_{α} -Bis(carboxymethyl)-L-lysine]-12-mercaptododecanamide was solved in dried DMF (4 mg in 1 mL). 5 μ L of this solution was placed onto the substrate by drop casting, sandwiched with another substrate and stored protected from light. After 4 hours the samples were rinsed with DMF and dried in a stream of nitrogen.

The functionalized samples were tested with His-tagged green fluorescent proteins (*GFP*). Therefore, a functionalized sample was loaded with nickel by immersion in nickel sulfate for 30 minutes and dried in a stream of nitrogen. His-tagged GFP was adjusted to 0.2 mg/mL in PBS buffer. 10 μ L of this solution was placed on different samples and incubated for 10 minutes. After incubation each sample was washed with PBS buffer for 2.5 minutes and dipped in DI water. For imaging via fluorescence microscopy the samples were embedded in Mowiol. Figure 33 depicts fluorescence microscopy images of functionalized NBPT CNMs after the different substrate processing steps and with sequestered nickel incubated with His-tagged GFP molecules. Here, the prediction was that only functionalized NBPT CNM loaded with

nickel and incubated with His-tagged GFP should lead to a fluorescence signal, which was confirmed. The brightness of the signal is comparable to the reference signal, which is an indication for a successful functionalization. As expected, NBPT CNMs without functionalization or with functionalization but without nickel did not show a detectable fluorescence signal. Also functionalized NBPT CNM loaded with nickel, incubated with His-tagged GFP and immersed in ethylenediaminetetraacetic acid did not result in a fluorescence signal, which indicates a reversible binding of the GFP molecules.

Figure 34 shows XPS spectra of the nitrogen, oxygen, carbon and sulfur regions of the NBPT-CNM before chemical modification (blue) and after the coupling with NTA (red). The increase of the nitrogen, oxygen and carbon signal and the appearance of a carboxylic peak at around 289 eV indicate the successful coupling of the molecules to the NBPT-CNM.

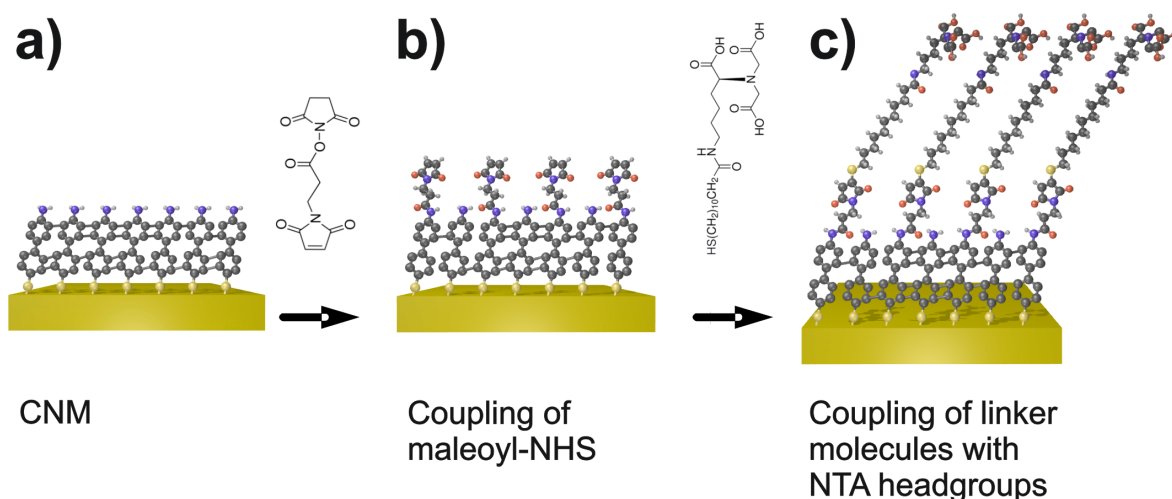


Figure 32: Functionalization of NBPT CNMs. a)-c) schematically show the 2 step reaction to obtain NTA moieties as head groups of the NBPT CNM.

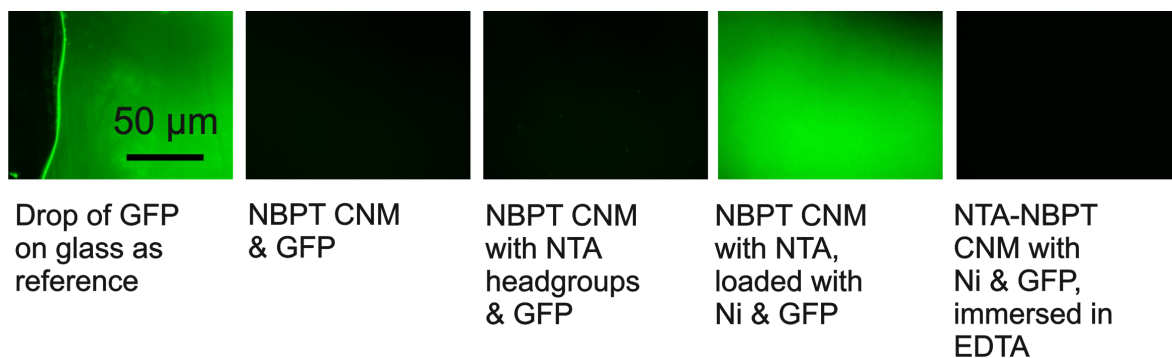


Figure 33: Fluorescence microscopy of functionalized NBPT CNMs incubated with His-tagged GFP molecules and different substrates for comparison.

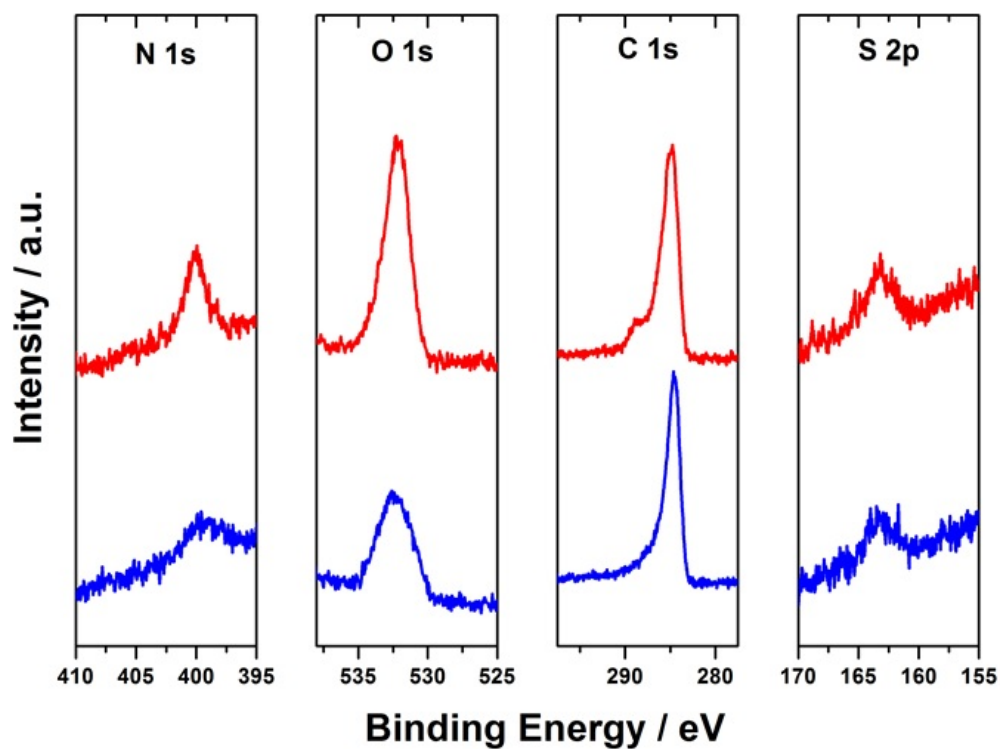


Figure 34: XPS spectra of NTA functionalization of NBPT CNMs. The spectra of the nitrogen, oxygen, carbon and sulfur regions of the NBPT-CNM before (blue) and after the two reaction steps (red). The increase of the nitrogen, oxygen and carbon signal and the appearance of a carboxylic peak at around 289 eV indicate the successful coupling of the molecules to the NBPT-CNM.

The functionalized NBPT CNMs were tested as a substrate for wildtype PMs and His-tagged PMs. The His-tagged PM solution in water was diluted in water to an optical density of $OD_{570} = 0.2$. Figure 35 shows the absorption spectrum of His-tagged PM in water at a pH of 7 and room temperature. The longest wavelength absorption band occurs at 570 nm and belongs to BR molecules. This indicates intact BR proteins in the PM fragments.

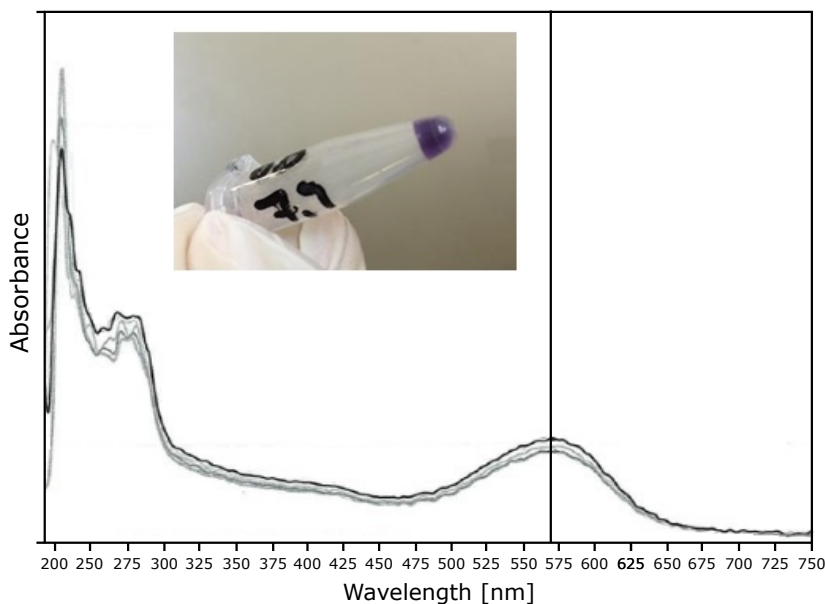


Figure 35: Absorption spectrum of His-tagged PM in water at a pH of 7 and room temperature.

Figure 36 shows SEM images of a) wildtype PMs and b) His-tagged PM mutants on functionalized NTA NBPT CNMs. For incubation a 300 mM potassium chloride was used without the addition of nickel. The images show no significant difference in the distribution of the PMs. On both images the PM patches form clusters. Some patches lie flat on the substrate, some are partially or fully stacked on top of each other.

Next, the functionalized samples were loaded with nickel to form complexes during incubation with His-tagged PMs to get an orientation of the PM patches. But experiments showed that His-tagged PMs on functionalized NBPT CNMs incubated with 300 mM potassium chloride and loaded with nickel do not lead to uniform orientation of the PMs. This can be seen in figure 37, which includes a) an AFM image and b) an EFM image of the same region. The EFM image reveals the orientation of the membrane patches. The membranes don't exhibit the expected uniform orientation. A reason for this behavior could be the fact that PM patches are immobile in solution. Once a membrane patch comes into contact with the surface, it does not matter if there are molecular sized tags on one or the other side of

the membrane. Therefore, a different technique is necessary to obtain an oriented assembly of PMs on CNMs. Only when the functional sides of the PMs come into close contact with the sample surface, the NTA/His-tag complex can be formed.

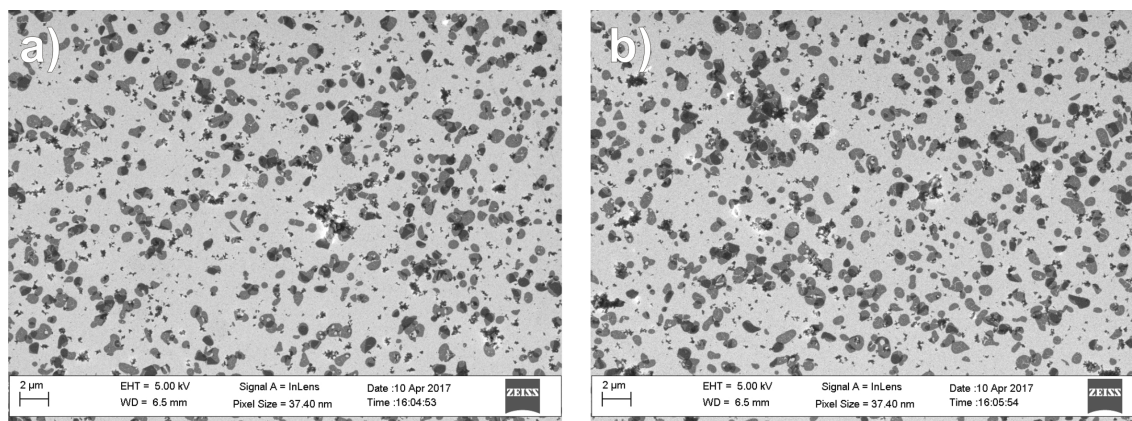


Figure 36: SEM images of a) wildtype PMs and b) His-tagged PM mutants on functionalized NTA NBPT CNMs. The images show no significant difference in the distribution of the PMs.

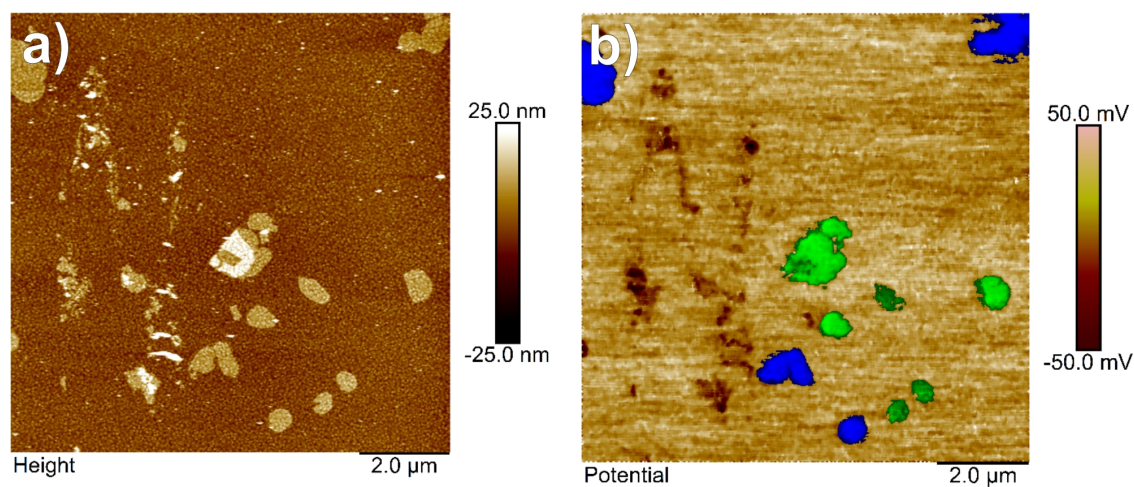


Figure 37: AFM/EFM images reveal the orientation of His-tagged PMs on NTA NBPT CNMs. a) shows the AFM image and b) the corresponding EFM image. The patches do not exhibit a uniform direction.

In summary, the immobility of PM prevents a uniform directed deposition on substrates by drop casting. Since the two sides of a PM patch are differently charged, electrophoresis has been applied during immobilization to force the patches to orient in the desired direction before reaching the substrate surface. This technique was realized by utilizing a capacitor. Therefore, the CNMs on gold substrates have been used as one of the capacitor plates. Immobilization takes place by filling PM solution between the capacitor plates and applying a voltage. Figure 38 shows a schematic structure of the electrophoresis setup.

First experiments were performed with wildtype PM on NBPT CNM on gold. Therefore, wildtype PM in water was diluted to an optical density of $OD_{570} = 0.001$. No buffer was used to obtain residual free surfaces. 5 μ L of the PM solution was pipetted between the capacitor plates and a voltage of 700 mV was applied to orient the patches on the NBPT CNM. After incubation the sample was dried and imaged by AFM/EFM. Figure 39 a) shows the edge of the drop on the NBPT CNM. Figure 39 b) shows a higher magnification of the PMs inside the drop. It can be seen that the patches do not form clusters as seen in previous experiments by drop casting. Most of the patches lie flat on the surface and cover a large area.

Figure 40 a) shows the wildtype PM inside the drop on NBPT CNM measured by AFM and figure 40 b) shows the same area on the sample measured by EFM, which reveals the orientation of the PM patches. All PM patches on the sample exhibit the same surface potential, which indicates that they all have the same orientation. Therefore, electrophoresis seems to be a promising technique to obtain a monolayer of unidirectional PM patches on CNM.

Thereafter, the samples were crosslinked with glutaraldehyde to achieve a monolayer of PM. Figure 41 shows two AFM images of the wildtype PM on NBPT CNM a) before and b) after crosslinking with 0.5 % glutaraldehyde and rinsing with water. The image b) indicates that the crosslinking worked since neighboring wildtype PM patches seem to form a monolayer. This technique has also been applied on silicon wafers and on gold on mica substrates, whereupon it also worked. The only requirement that has not been met by this technique is the formation of a stable bond between the PM layer and the substrate.

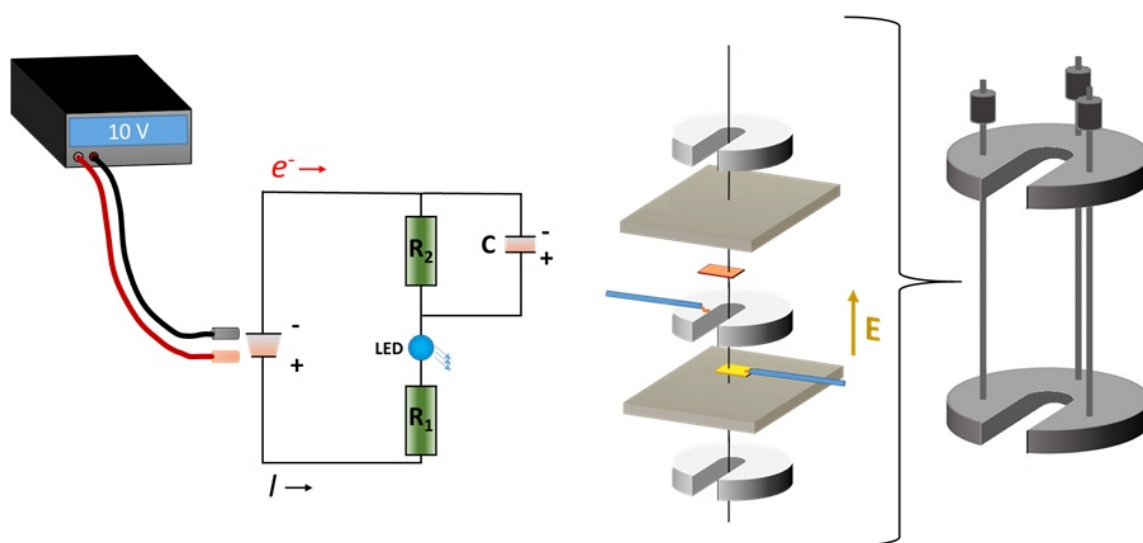


Figure 38: Assembly of PM on CNM by electrophoresis. CNM on gold substrates were used as one of the capacitor plates during experiments.

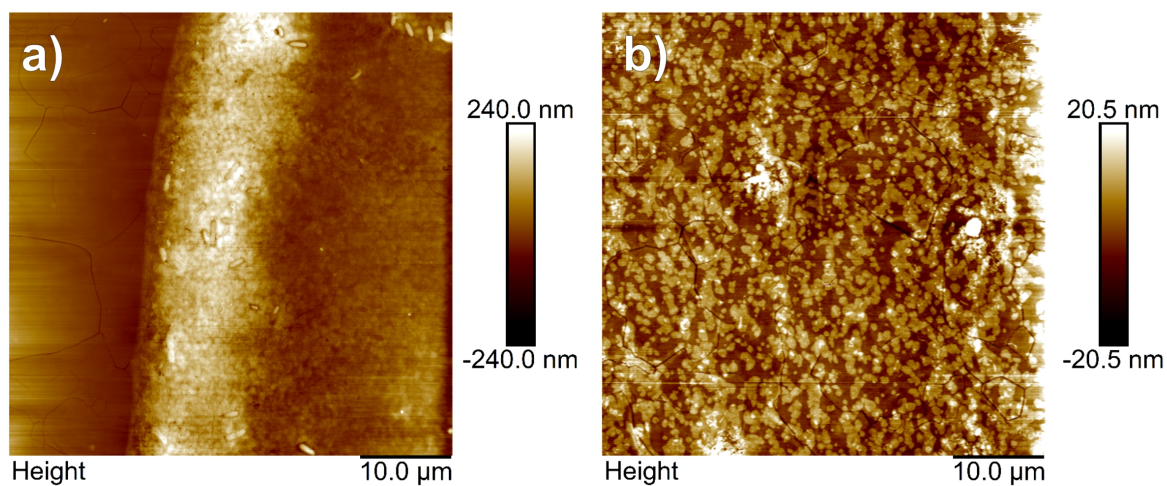


Figure 39: Assembly of wildtype PM on NBPT CNM by electrophoresis. CNM on gold substrates were used as one of the capacitor plates during experiments. a) shows the edge of the drop on the NBPT CNM. b) shows a higher magnification of the PMs inside the drop.

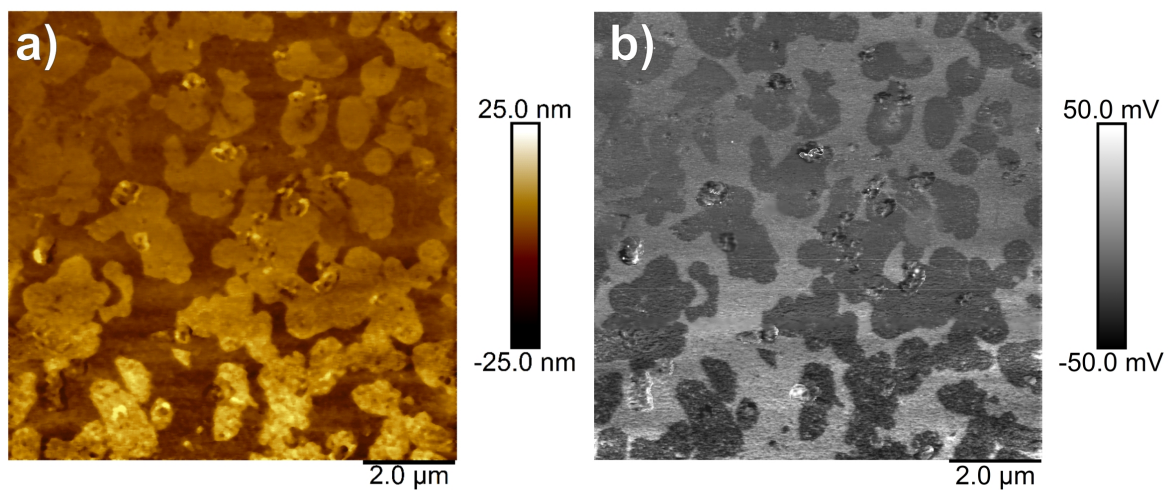


Figure 40: AFM/EFM of assembled wildtype PMs on NBPT CNM by electrophoresis. a) shows the wildtype PM inside the drop on a NBPT CNM measured by AFM and b) shows the same area on the sample measured by EFM.

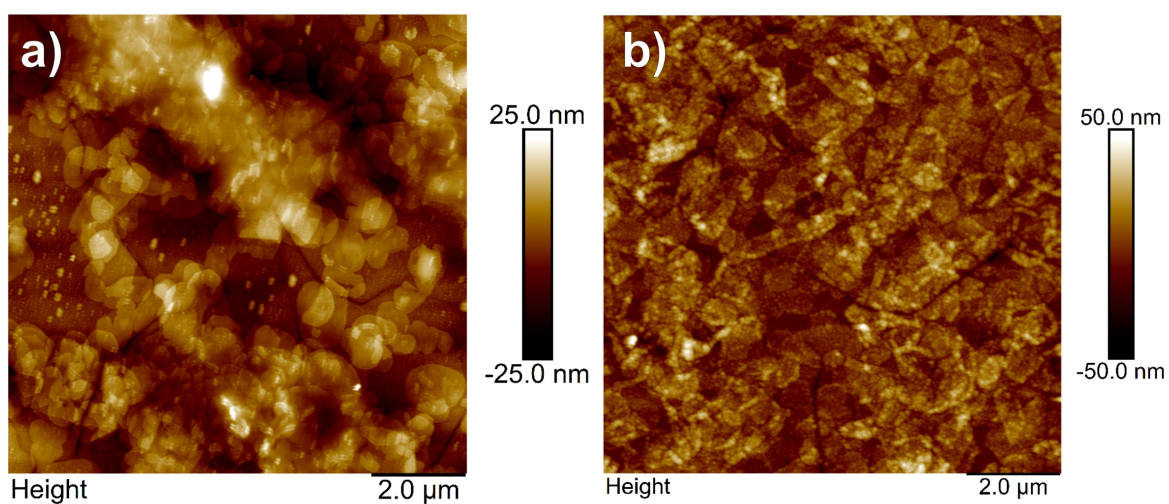


Figure 41: AFM images of assembled wildtype PMs on NBPT CNM by electrophoresis. a) before and b) after crosslinking with glutaraldehyde.

In order to obtain a stable bond between the PM patches and the NBPT CNM, the substrates were again functionalized to obtain NTA moieties as head groups but with a different functionalization than shown in the previous sections. The previous presented functionalization with NTA was tested with GFP after the CNM was only partially irradiated. However, the pattern of irradiation could not be identified in the CLSM. This is an indication that the functionalization did not work properly. Therefore, a further functionalization was tested, which is presented in the following sections.

The new functionalization route is shown in figure 42: The crosslinking of a) NBPT SAM on gold on mica leads to b) a NBPT CNM. This sample was placed into a dried flask. Then the flask was filled with 1 mL azidoacetyl chloride in 30 % diethyl ether, 8 mL dichloromethane and 0.3 mL diisopropylethylamine. The flask was cooled in an ice bath to slow down the reaction and to dissipate the heat of the reaction. After 24 hours the sample was rinsed with ethanol and isopropanol. The resulting molecules on gold are shown in c). Afterwards 5 μ L of a 1 mg of dibenzocyclooctyne-maleimide in 20 mL dried DMF solution was placed onto the sample and sandwiched with another sample. After 24 hours of incubation in the dark the sample was rinsed with ethanol and dried in a stream of nitrogen. The resulting molecules on gold are shown in d) and were further functionalized with 5 μ L of a 1 mg of N - [N $_{\alpha}$, N $_{\alpha}$ - Bis(carboxymethyl) - L - lysine] - 12 - mercaptododecanamide in 15 mL dried DMF solution by drop casting. The sample was sandwiched with another one and protected from light for 24 hours. The final molecule is shown in e).

The functionalization was tested with the His-tagged fluorescence protein mTurquoise. Figure 43 shows four fluorescence pictures imaged with a CLSM. In figure 43 a) a NTA NBPT CNM sample was loaded with nickel and incubated with the protein. This image shows the strongest fluorescence signal as expected. The edge of the drop can be seen on the right hand side. In b) a NTA NBPT CNM sample was loaded with nickel, incubated with the protein and eluted with imidazole. The samples in c) and d) were not loaded with nickel, incubated with the protein and d) additionally eluted with imidazole. The fluorescence signals in b), c) and d) exhibit a comparable fluorescence signal, which is weaker than the signal in a). This indicates that the functionalization was successful and the formed complexes with His-tagged proteins exhibit reversible bonds.

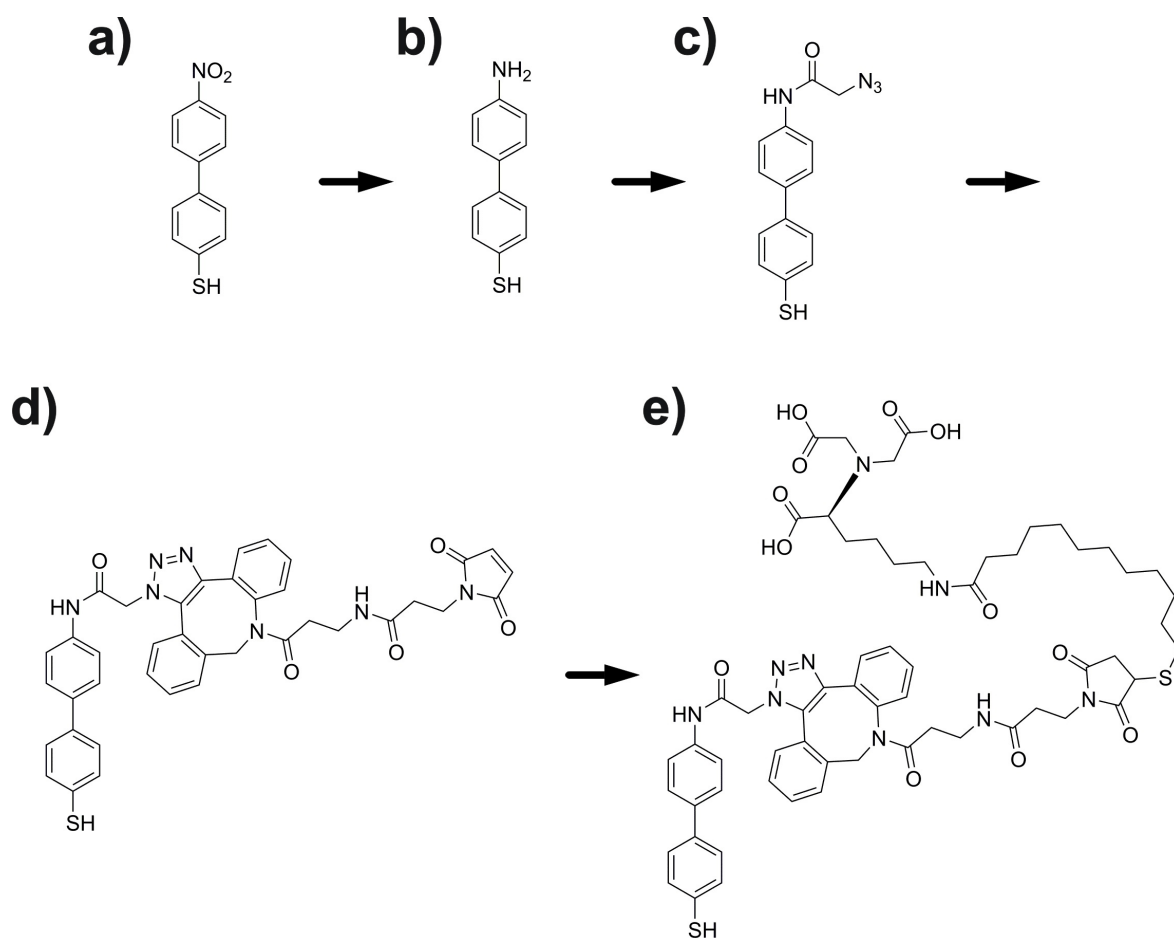


Figure 42: Functionalization of NBPT CNM.

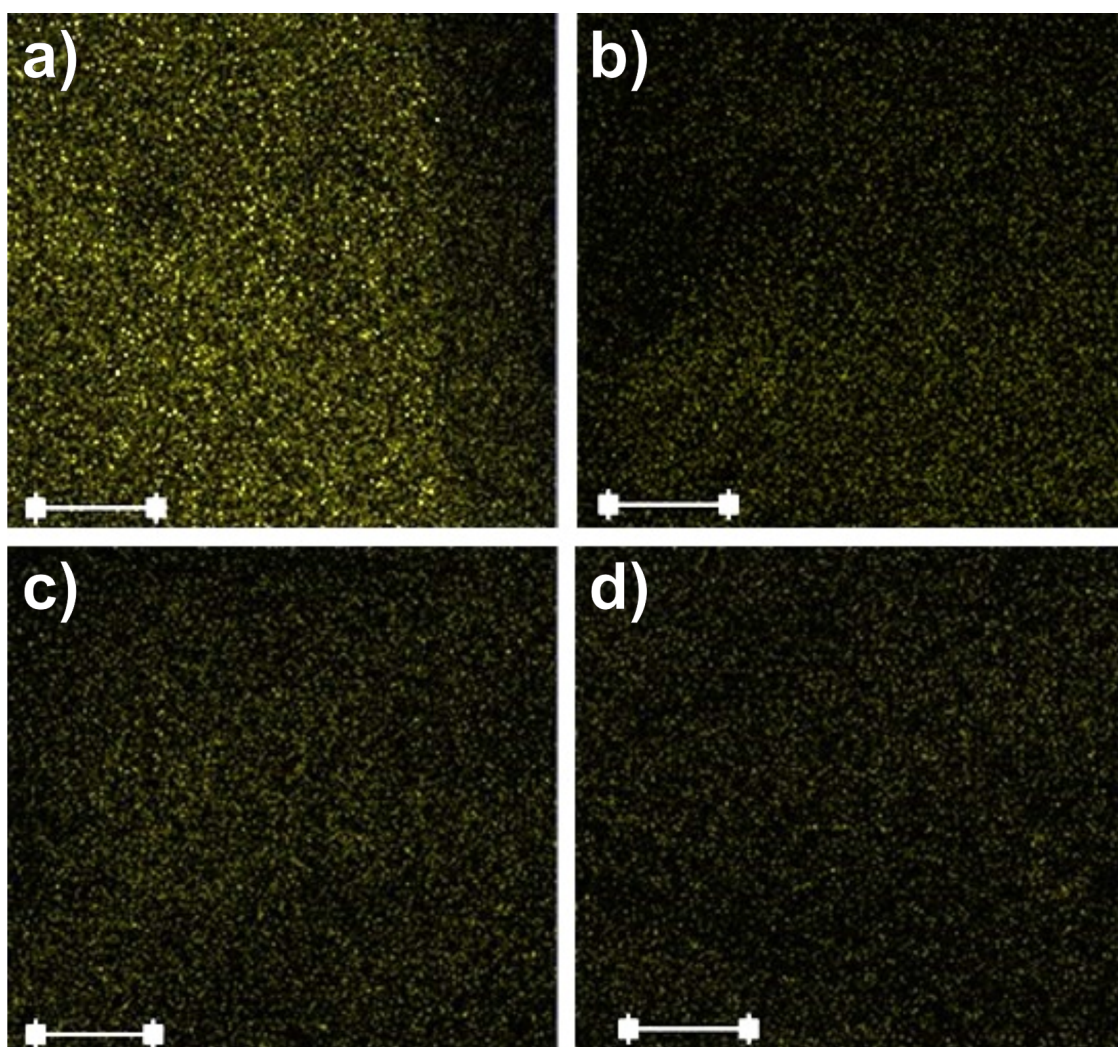


Figure 43: Fluorescence microscopy of NTA functionalized NBPT CNMs incubated with a fluorescence protein (mTurquoise). Scale bars are 100 μm . a) A functionalized NBPT CNM sample was loaded with nickel and incubated with the protein. The edge of the drop can be seen on the right hand side. In b) a functionalized NBPT CNM sample was loaded with nickel, incubated with the protein and eluted with imidazole. The samples in c) and d) were not loaded with nickel, incubated with the protein and d) additionally eluted with imidazole. The signal in a) shows the strongest fluorescence signal, which indicates that the functionalization was successful.

The functionalization was also tested via infrared reflection absorption spectroscopy (*IRRAS*) and XPS. Figure 44 shows the *IRRAS* spectrum of a NBPT CNM after the first functionalization step (see figure 42 c)). The peak at 2106 cm^{-1} , caused by the asymmetrical stretching vibration of the azido moiety, indicates that the first functionalization step was successful. In figure 45 XPS spectra of the NBPT SAM (green), NBPT CNM (blue) and NBPT CNM after the NTA functionalization (red) are shown. The conversion of the SAM to CNM can be traced by the chemical shift of the N1s binding energy from 405.5 eV to 399.2 eV, the broadening of the oxygen and carbon peak and additional sulfur species belonging to sulfur, which is not bound to gold any more after crosslinking. The functionalization (red) is indicated by a carbon shoulder around 289 eV referring to carboxyl groups of the NTA moieties. Also the increasing signal intensities of the nitrogen and oxygen peaks indicate a successful functionalization.

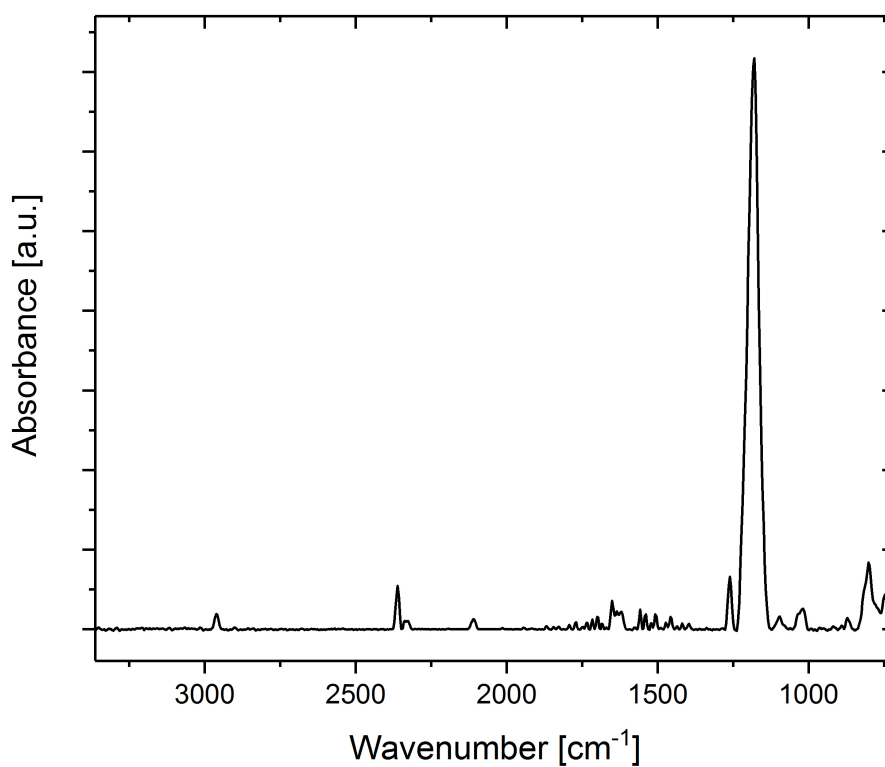


Figure 44: *IRRAS* spectrum of NBPT CNM after the first functionalization step (see figure 42 c)). The peak at 2106 cm^{-1} is caused by the stretching vibration of the azido moiety.

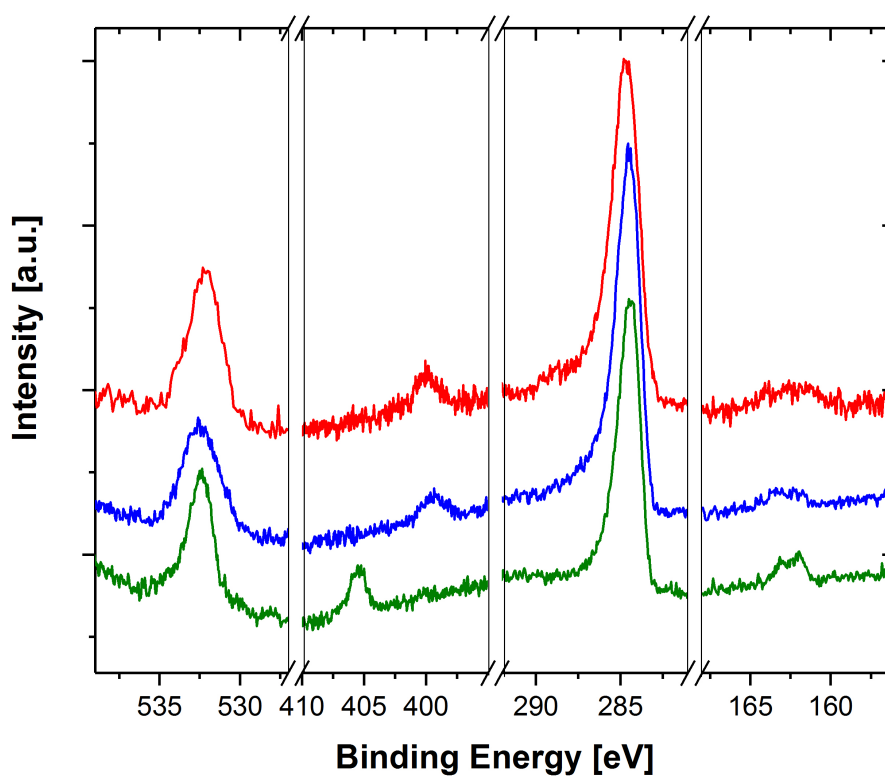


Figure 45: XPS spectra of the NBPT SAM (green), NBPT CNM (blue) and NBPT CNM after the NTA functionalization (red) are shown. The conversion of the SAM to CNM can be traced by the chemical shift of the N1s binding energy, the broadening of the oxygen and carbon peak and additional sulfur species belonging to sulfur, which is not bound to gold. The functionalization (red) is indicated by an additional shoulder in the carbon signal.

The previously described functionalized samples were used for electrophoresis experiments with His-tagged PM mutants to obtain bonds between the PM patches and the substrate. For this purpose, the substrates were loaded with nickel. Figure 46 shows AFM and EFM images of a sample, which was prepared by incubating a His-tagged PM solution with an optical density of $OD_{570} = 0.05$ for 3 minutes by electrophoresis at an applied voltage of 5 V. The substrate was used as one of the capacitor plates. Figure 46 a) shows an AFM image of PM mutants on the substrate and b) an EFM image of the area, which is marked by a red square in image a). The PMs show a comparable surface potential, which indicates a unidirectional assembly. Figure 46 c) shows an AFM image of another area of the sample and d) shows the corresponding EFM image. The EFM image also indicates a unidirectional assembly. But it can also be seen from all images that the substrate is not covered by a monolayer consisting of PMs.

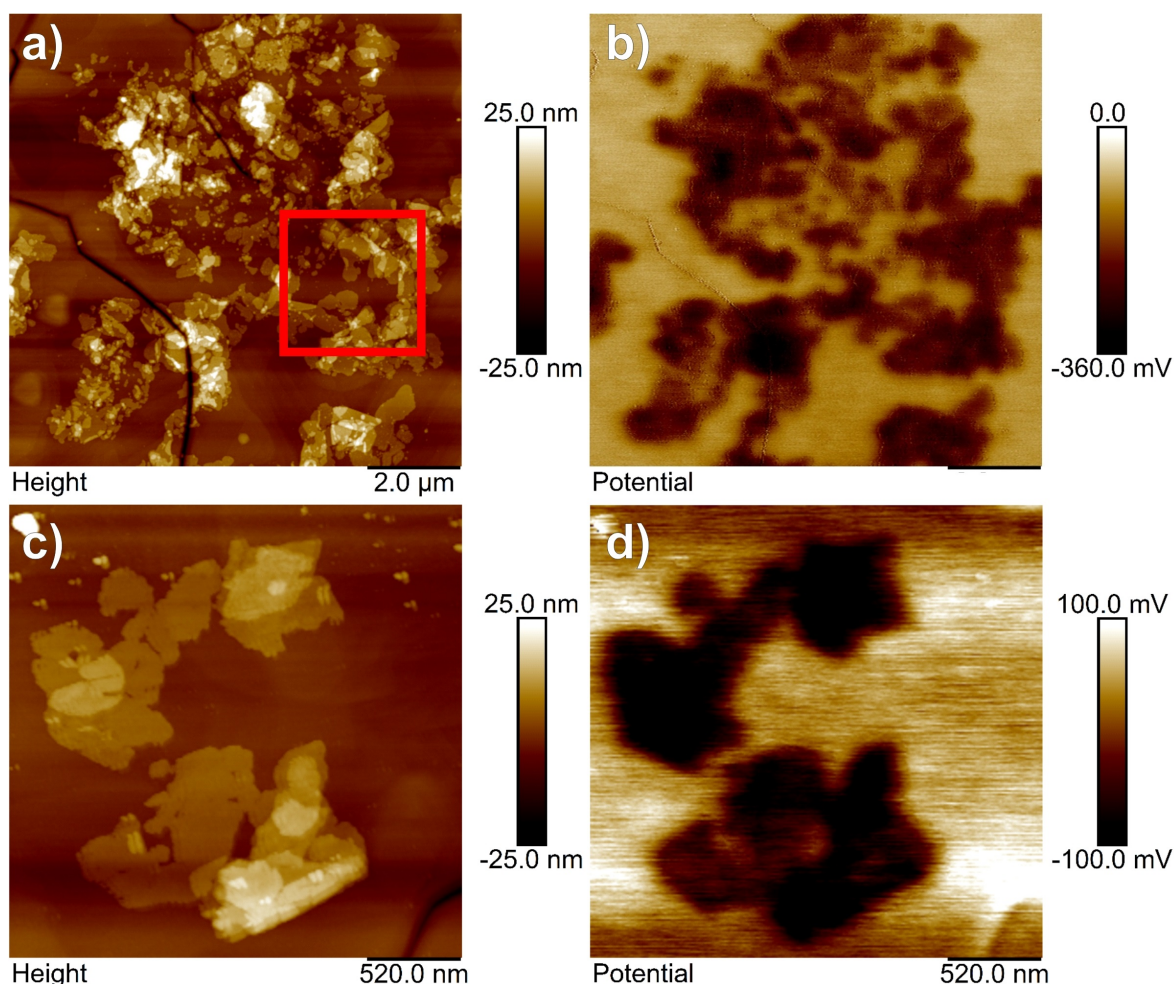


Figure 46: AFM/EFM images of His-tagged PMs on a functionalized NBPT CNM. a) AFM image of PM mutants on the substrate and b) EFM image of the in a) depicted area. c) AFM image of another area on the sample and d) the corresponding EFM image. The potential of the PMs indicate an unidirectional orientation.

To get closer to a monolayer the concentration of the PM solution was decreased to an optical density of $OD_{570} = 0.02$ and then incubated four times for 3 minutes, each time on the same sample. Afterwards 25 % glycerol was added to support the formation of PM monolayers and to prevent clustering. Figure 47 shows three AFM images of an exceptional area of PMs in a), b) and c). In these areas the patches seem to merge and form large monolayers with a thickness of around 5 nm. The EFM image shown in d) belongs to the area in c) and indicates a uniform orientation of these monolayers. Figure 48 shows another area, where the mutated PMs form large area fusions on the substrate. In summary, this experiment fulfils all the requirements of the project, as a large range of bound, fused and unidirectional PMs were assembled on CNMs. In future experiments the assembly could be attempted on free-standing CNMs to test the proton pumping properties of the PMs.

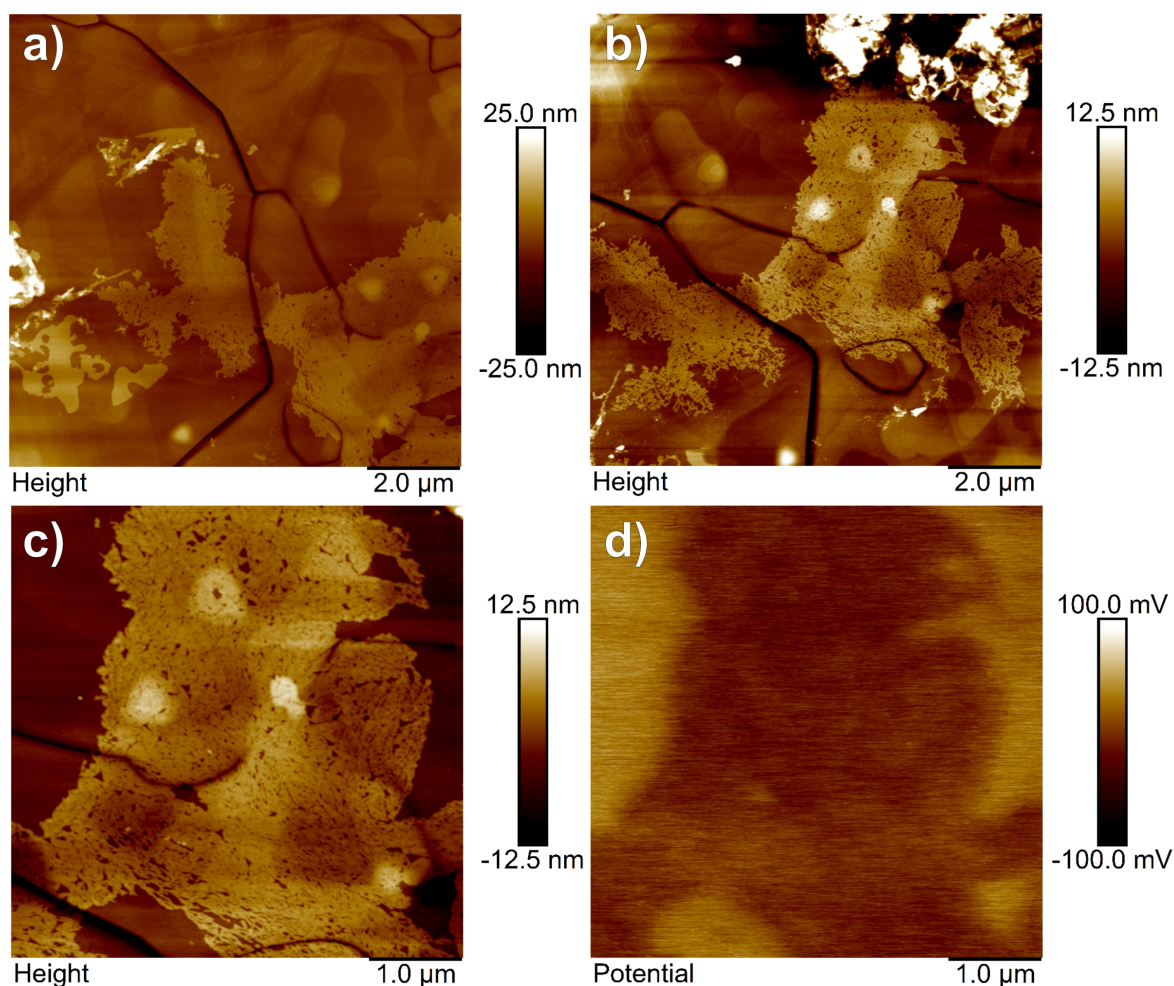


Figure 47: AFM/EFM images of His-tagged PMs on a functionalized NBPT CNM. a) and b) show AFM images of PM mutants on the substrate. c) Higher magnification AFM image and d) the corresponding EFM image. The potential of the PMs indicate an unidirectional orientation.

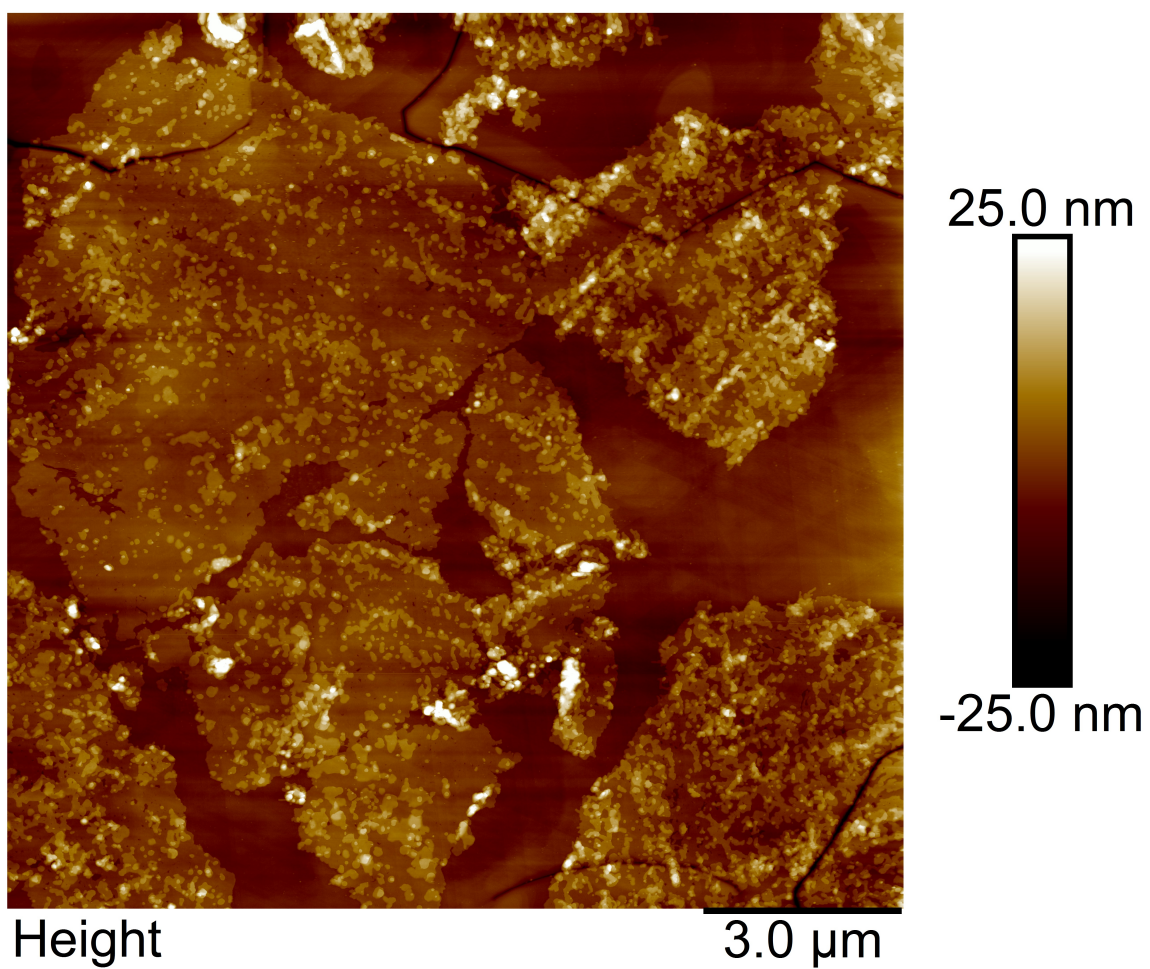


Figure 48: AFM image of His-tagged PM fusions on a functionalized NBPT CNM.

3.3 Carbon nanofoam

In the previous chapter self-assembly of carbon precursor molecules was used to produce carbon nanomembranes. A different approach to produce carbon nanomaterials is the so called hydrothermal carbonization (*HTC*). In this work a range of high-quality uniform nanoporous materials of graphitic nature such as carbon nanofoams, were produced by *HTC* of carbon precursor materials [78, 79, 80]. The samples were studied by mass density measurements, HIM, XPS, Raman spectroscopy and other techniques, which reveal structural and chemical information of the materials.

Carbon nanomaterials with a low weight are interesting for a variety of engineering applications. Such materials can exhibit thermodynamically stable crystalline and non-crystalline structures with different properties. This variety of structures is possible because of the ability of carbon to form diverse bonds. A distinction is made between sp^1 - (polymeric-type), sp^2 - (graphite-like) and sp^3 - (diamond-like) hybridized bonds [78]. Porous carbon materials are attractive for a number of different applications, such as storages, electrodes or for cleaning toxic environments [81, 82].

Figure 49 shows schematically the production of the foams [83]. A sucrose solution and a small amount of naphthalene were filled in an autoclave and heated to temperatures between 120 °C and 170 °C. Depending on the conditions, such as time or temperature, different foam morphologies were produced by this process. Most of the produced foams consist of spherical microparticles, which are arranged in a network.

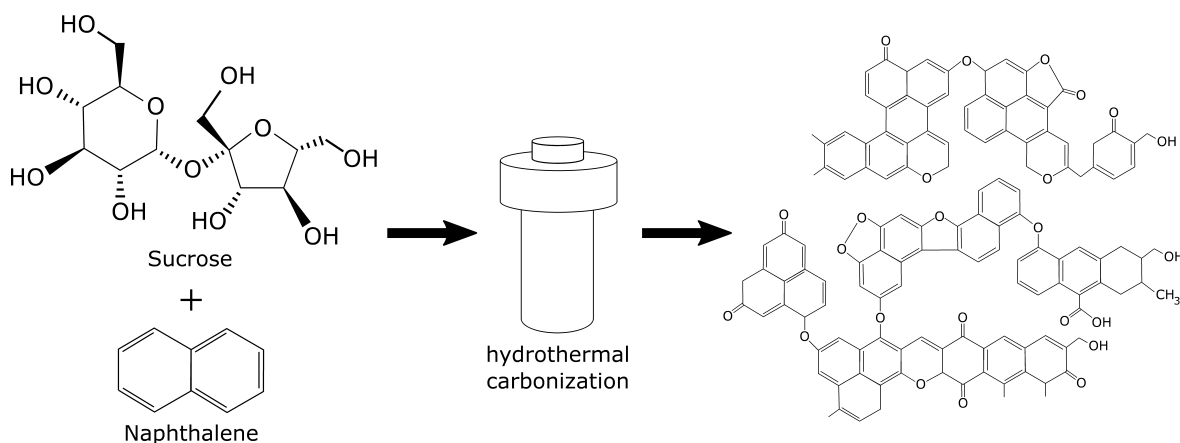


Figure 49: Production of carbon nanofoam via *HTC*. A sucrose solution and a small amount of naphthalene were filled in an autoclave and heated. Depending on the conditions, such as time or temperature, different forms of foams can be produced consisting of carbon networks [83].

3.3.1 Low density carbon nanofoam

The foam with the lowest density of 0.085 g/cm^3 has a black colour and was produced via HTC of a 5 molar sucrose solution and 3 mg of naphthalene, which acts as a nucleation seed, filled in a 130 mL autoclave. After heating the autoclave for 5 hours at $155 \text{ }^\circ\text{C}$ the foam was extracted, rinsed with hot water and dried. HIM images of the foam are shown in figure 50.

The image in figure 50 a) gives an overview of a piece of the foam. In b) the uniform structure of the foam can be observed. Single micropearls with diameters between $3 \text{ }\mu\text{m}$ and $15 \text{ }\mu\text{m}$ are connected and form a network. A single pearl is shown in c) and a close up of a part of this pearl is shown in d). The close up reveals an additional structure in the surface of the pearl with features around 25 nm in diameter. These features indicate that the single pearls are porous, which partly explains the low density of the sample.

The XPS C1s spectrum of the sample is shown in figure 51. Three peaks were fitted into the C1s region, labelled as C1, C2 and C3. The C1s peak at 285.0 eV can be attributed to aromatic and aliphatic carbons. The C2 peak at 286.2 eV and the C3 peak at 288.6 eV peak can be attributed to oxygenated carbons. In particular the C2 peak indicates the presence of C-OH bonds and the C3 peak indicates the presence of C=O and carboxyl groups on the surface of the sample.

The Raman spectrum of the sample is shown in figure 52. The two characteristic peaks, the G band at 1589 cm^{-1} and the D band at 1371 cm^{-1} can be seen. The peaks are not separated, which indicates that there is no phase separation between graphite-like and diamond-like regions and that the foams are structured as a network of carbons. Additionally the D band intensity indicates that the foam contains a few carbons in other hybridizations than sp^2 . The spectrum of the foam sample does not show peaks indicating naphthalene content, which points to complete carbonization of the naphthalene in the hydrothermal process.

Along with the XPS data, the foam sample might consist of an amorphous carbon core decorated with oxygenated groups on the surface. However, these experiments do not reveal whether the micropearls are filled with material or if they are hollow.

Experimental details and further information about low density carbon nanofoam can be found in [78].

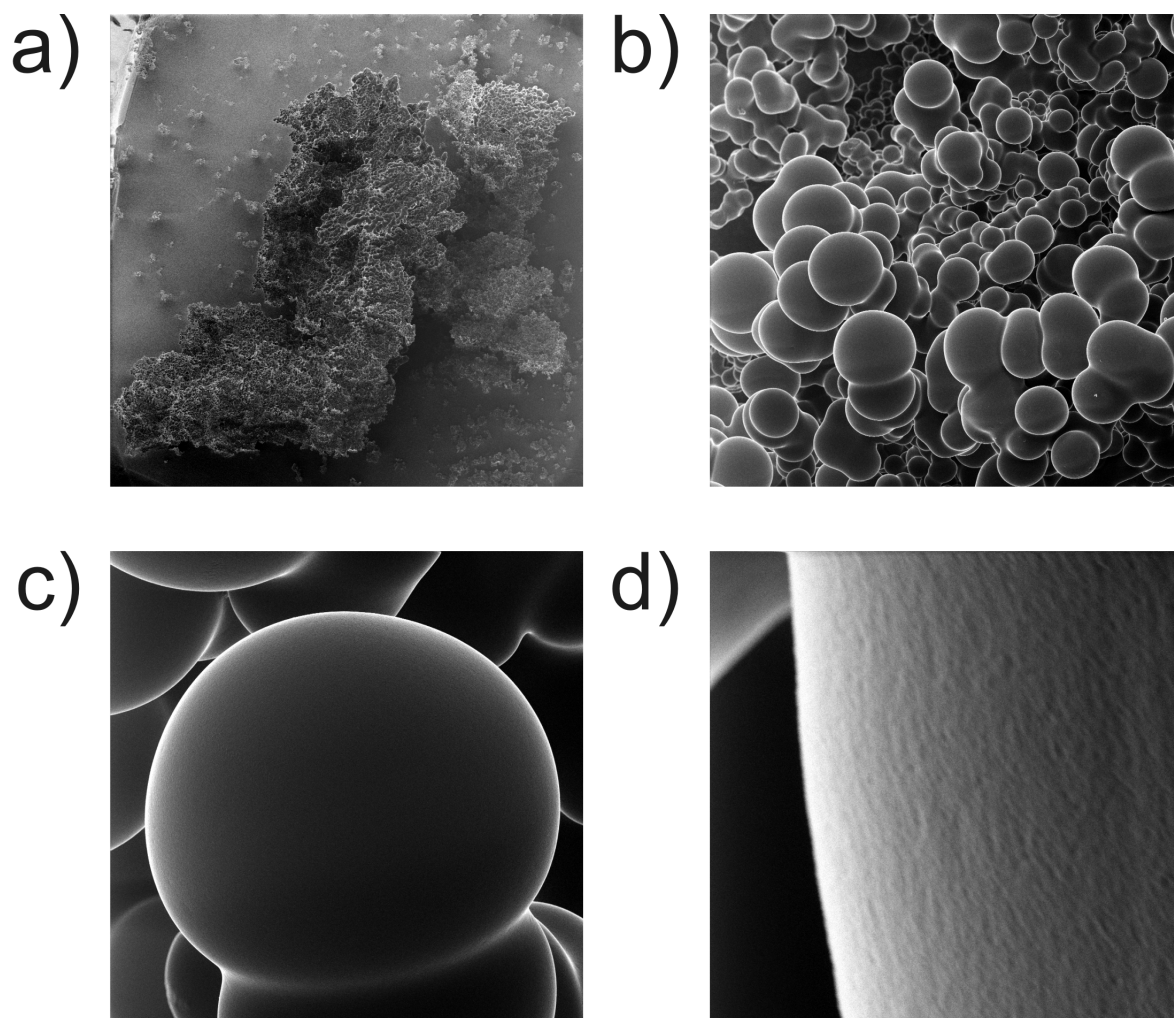


Figure 50: HIM images of hydrothermal generated carbon nanofoam. a) Overview of the carbon nanofoam. Field of view: 2 mm. b) Close up of the carbon nanofoam. Field of view: 75 μm . c) Single foam micropearl. Field of view: 15 μm . d) Close up of the micropearl. Field of view: 1 μm .

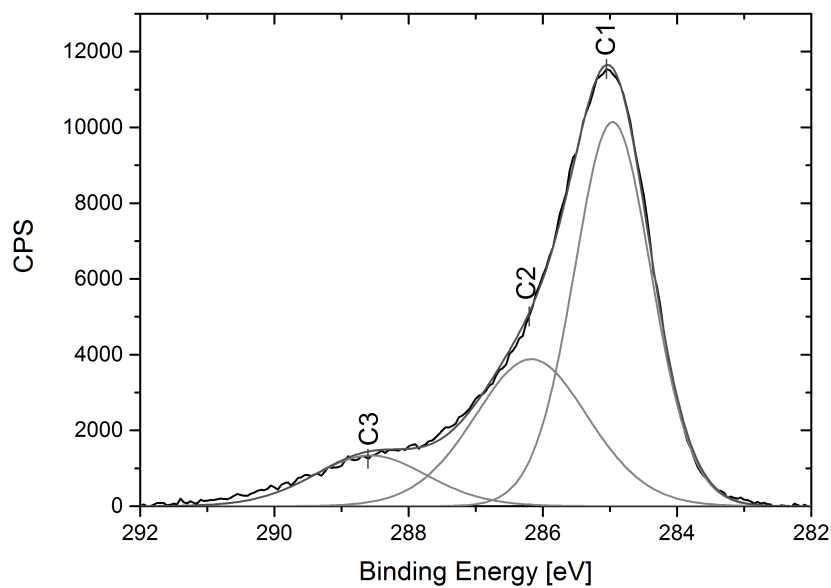


Figure 51: XPS spectrum of carbon nanofoam with a low density.

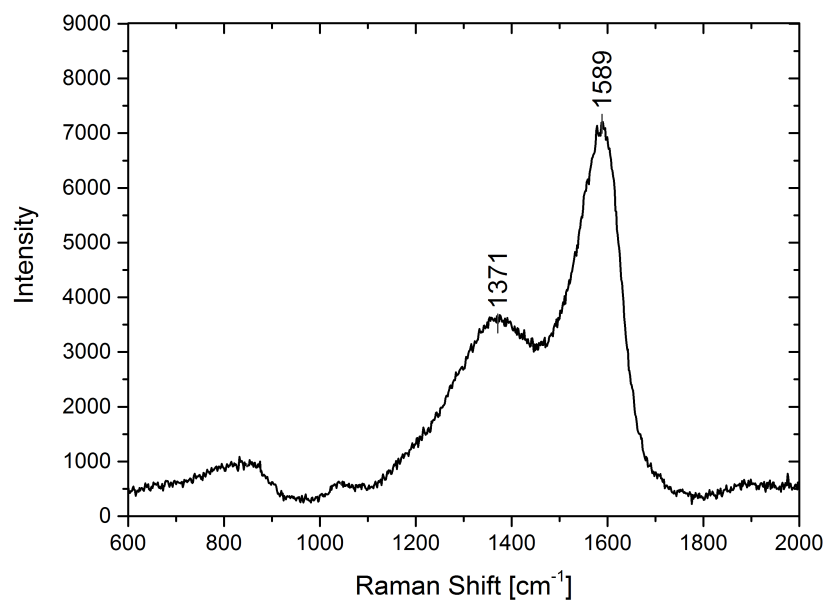


Figure 52: Raman spectrum of carbon nanofoam with a low density.

3.3.2 Comparison of carbon nanofoams

Carbon nanofoams consisting of a micropearl structure with higher densities were also produced. Figure 53 shows four HIM images of two different foam samples. Figure 53 a) and b) belong to a sample, which was produced by heating a 0.5 molar sucrose solution with 2 mg naphthalene at 160 °C for two days. The foam has a medium density of 0.104 g/cm⁻³. Figure 53 c) and d) belong to a sample, which was prepared at the same conditions except a higher heating temperature of 185 °C. The foam has a high density of 0.278 g/cm⁻³. The images reveal that a higher temperature leads to a foam consisting of bigger micropearls.

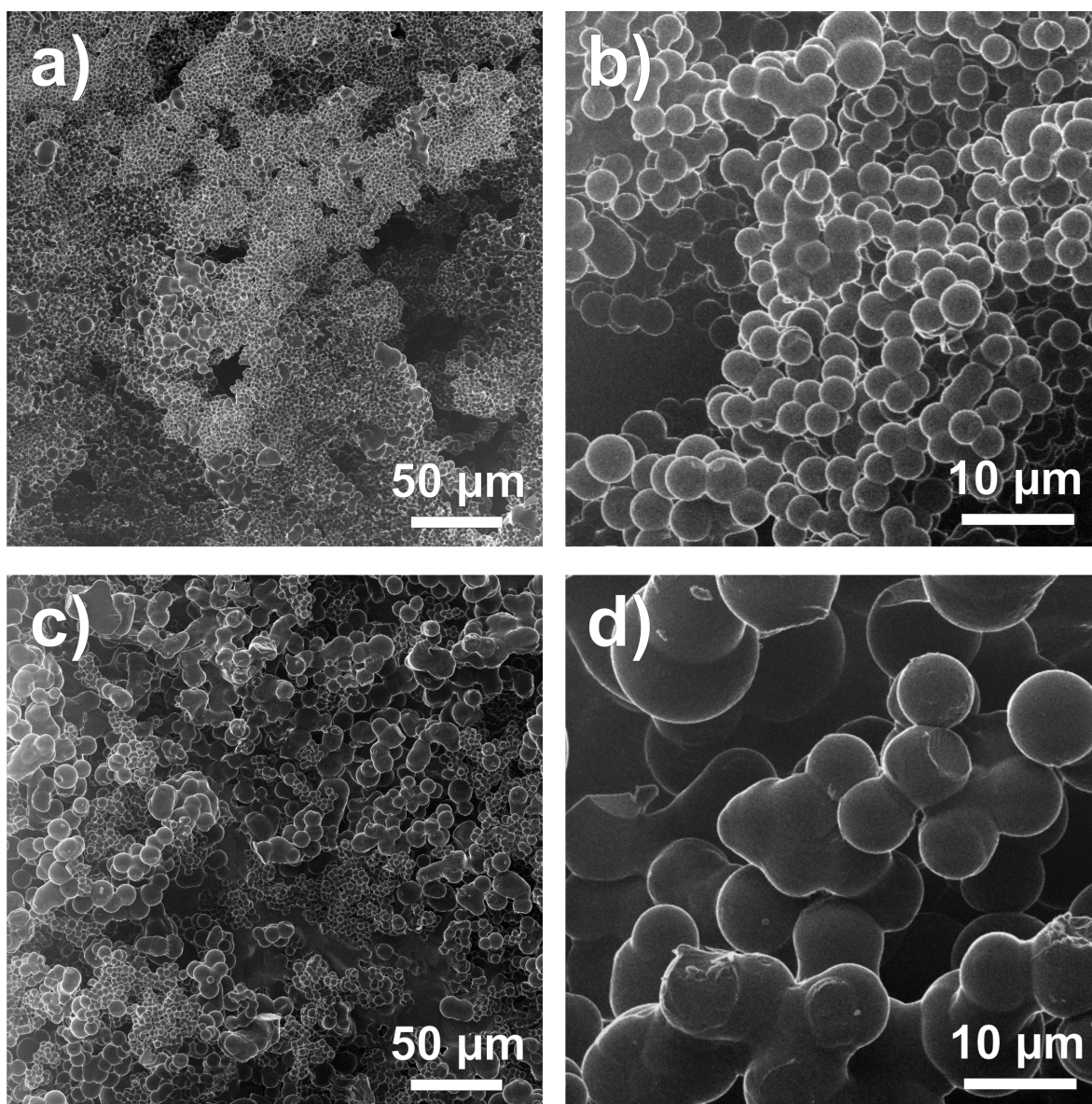


Figure 53: HIM images of different carbon nanofoams. The foam in a) and b) exhibits a density of 0.104 g/cm⁻³ whereas the foam in c) and d) has a density of 0.278 g/cm⁻³.

Figure 54 depicts XPS spectra of the medium and high density foam samples. The spectrum in figure 54 a) belongs to the medium density foam sample and the spectrum in figure 54 b) belongs to the high density foam sample. The peaks labelled with C1 at 284.4 eV correspond to sp^2 -type carbons and the C2 peaks correspond to sp^3 -type carbons. The C3 peaks correspond to the oxygenated groups on the surface.

A comparison of the spectra indicates that the higher density sample has a higher content of sp^3 -type carbons. The higher amount of sp^3 -type carbons could be caused by a higher amount of fusions between the micropearls, as seen in the HIM images in figure 53. These fusions create neck areas with a negative curvature. Therefore heptagons or sp^3 -type carbons are necessary to build these areas. Further details can be found in [79].

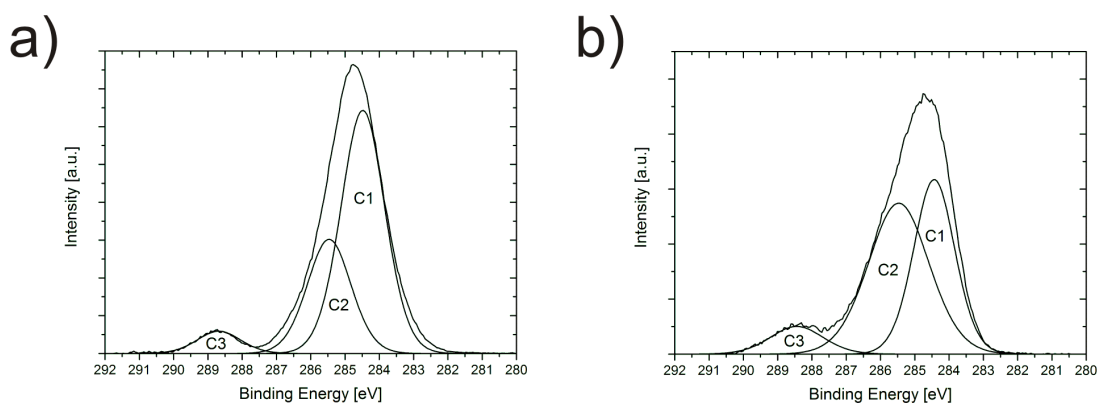


Figure 54: XPS spectra of different carbon nanofoams. a) corresponds to the medium density foam sample and c) corresponds to the high density foam sample.

The same samples were imaged by transmission electron microscopy (*TEM*) as shown in figure 55. The images in figure 55 a) and b) correspond to the medium density sample and the images in c) and d) correspond to the high density sample. A comparison of the images in a) and c) reveals that the micropearls in c) appear darker than the micropearls in a). This indicates the higher density of the sample in c) and d). The images in b) and d) show high resolution images of edges of the micropearls, which reveal a comparable crystallinity. Carbon nanomembranes, which are described in the previous chapter, were used as a substrate.

All in all, from the HIM images shown in figure 50, 53 and from the shown spectra it is not clear whether the micropearls are filled with material or hollow, as the used techniques only analyze surfaces.

To find out the inner structure, the micropearls were embedded in resin and cut into 200 nm slices with a microtome. Then the slices were imaged by HIM in the transmission mode, as shown in figure 56. The images in figure 56 a) and b) depict micropearls slices, which are fused to other pearls. From these images it can be seen that the pearls are filled with material and are not hollow. Furthermore, the micropearls seem to have a core-shell structure and neck areas consisting of carbon material with higher densities, which fits to the previous mentioned results.

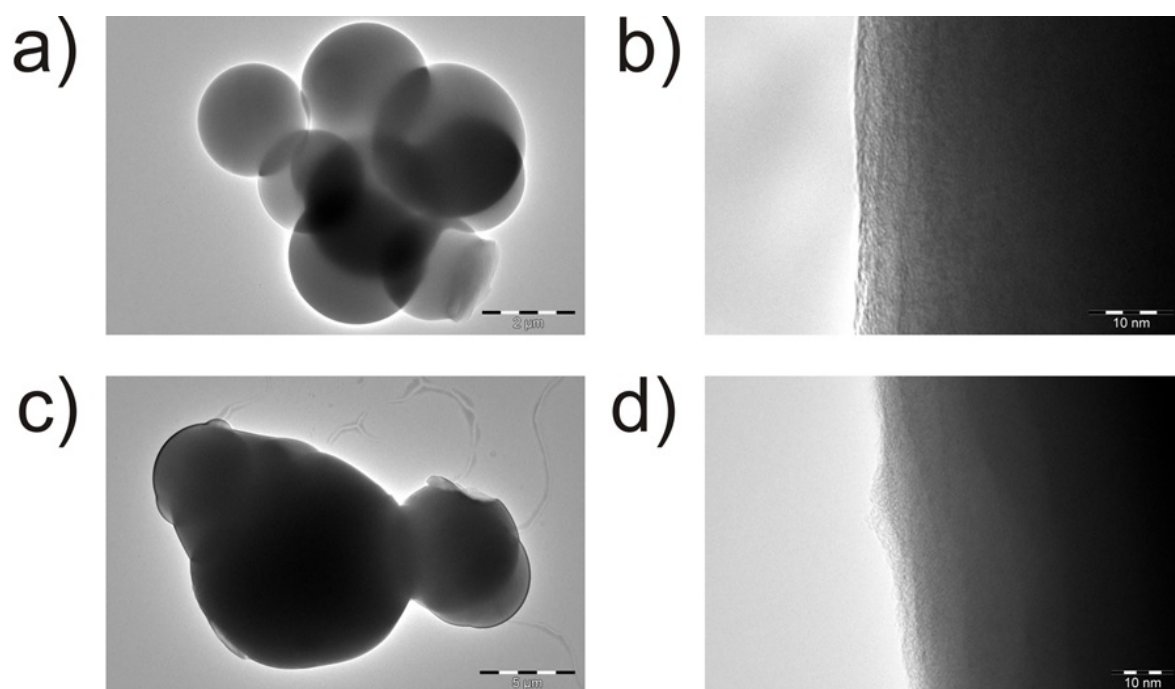


Figure 55: TEM images of foam samples. a) and b) correspond to the medium density sample and the images in c) and d) correspond to the high density sample.

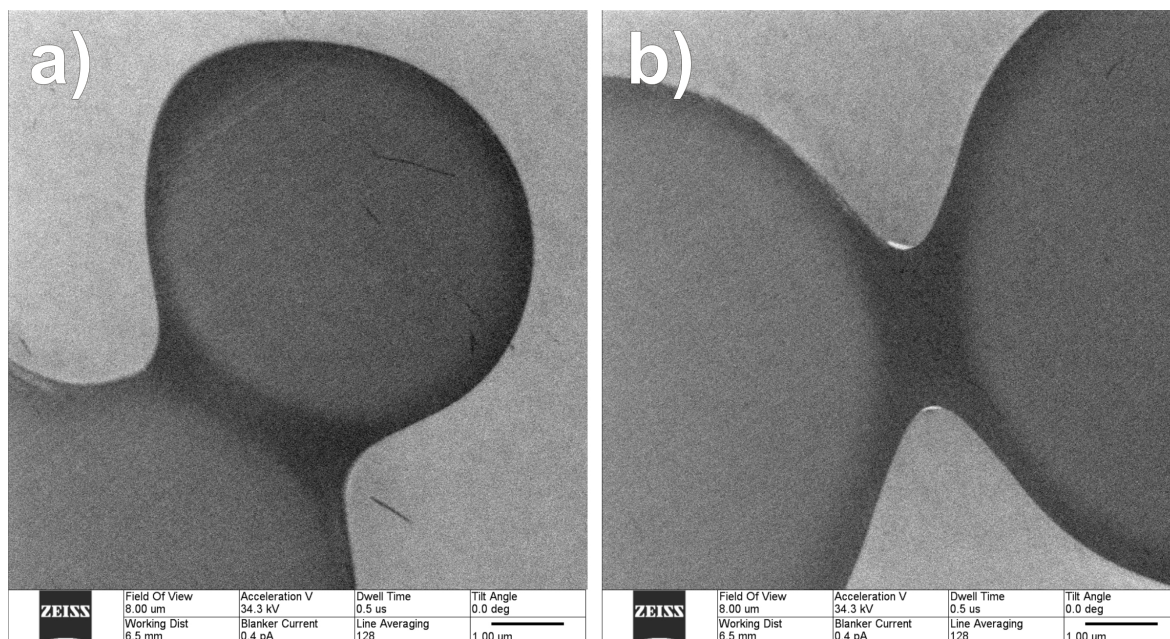


Figure 56: HIM images of foam slices.

3.3.3 Inner structure of carbon nanofoams

From the measurements shown it is unclear how the pearls grow during the HTC process and how the internal structure of a micropearls looks like. A simplified possible growth process is the following: The naphthalene in the solution acts as a nucleation seed, which makes low temperatures possible during the process. Then, single carbon atoms combine and form aromatic compounds. Afterwards, from the aromatic compounds graphene layers are formed. In a next step, these layers stack on top of each other and form the resulting micropearls, which then consist of layered or onion-like graphene structures. To confirm this suggestion experimentally broken foam micropearls were imaged by HIM and TEM, as shown in figure 57.

In figure 57 a) a TEM image of a broken micropearl placed on a carbon nanomembrane is shown. The close up of the broken part in b) indicates that the pearl consists of multiple carbon layers. The image in 57 c) shows a network of micropearls with two cracked pearls imaged by HIM. A close up of one of the pearls is shown in d), but it is not obvious how the internal structure is constructed. Therefore, further experiments are needed to determine the inner structure of the micropearls.

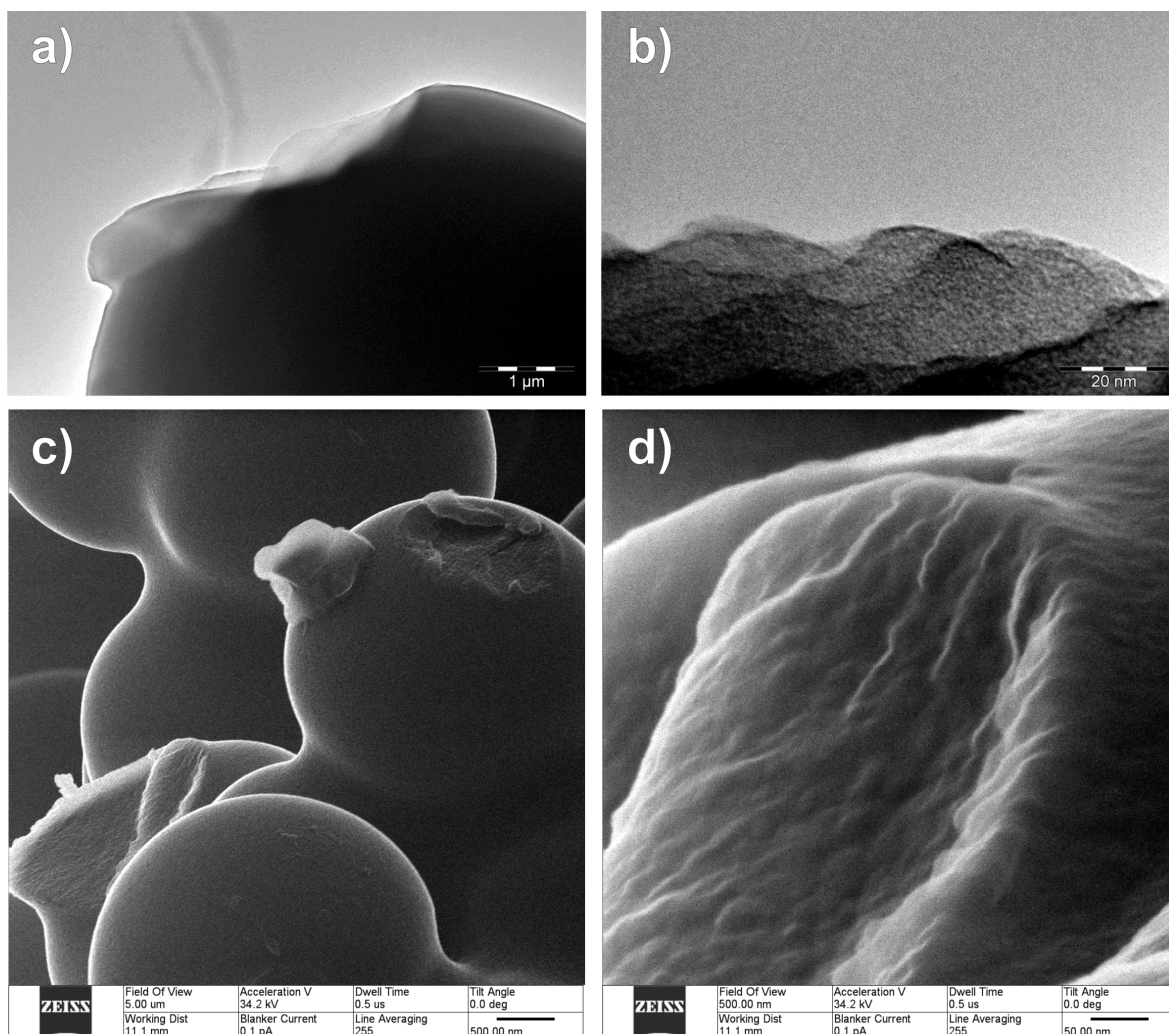


Figure 57: TEM images in a) and b) and HIM images in c) and d) of broken micropearls.

3.3.4 Diamond-like carbon nanofoam

A different form of foam was produced by heating a 2 M sucrose solution with 9 mg of naphthalene in a 130 mL autoclave at 130 °C for 72 h. The foam turned out brown due to the increased amount of naphthalene and has a density of 0.21 g/cm⁻³. The low density can be explained by the sponge-like surface of the sample, which indicates a porous structure of the sample. The surface morphology was analyzed by HIM images as shown in figure 58. Figure 58 a) shows a piece of the sample and in b) a close up of the foam piece is shown. Overall, the sample has a different structure compared to the samples shown in the previous sections. This sample consists of pieces in the 200-500 µm range instead of single and fused micropearls.

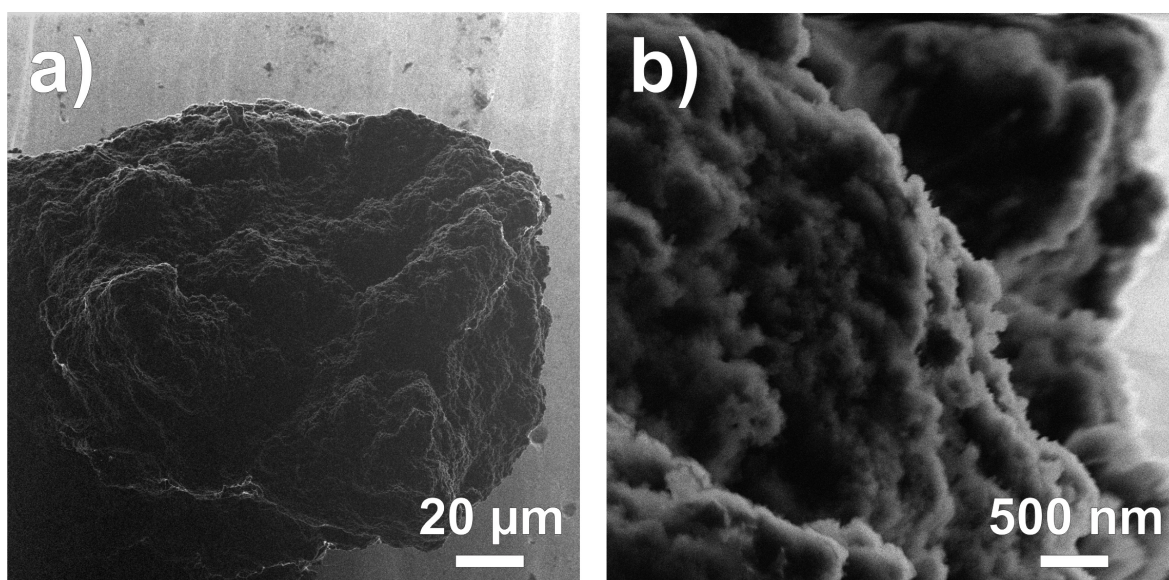


Figure 58: HIM images of diamond-like carbon foam. a) shows a piece of the diamond-like carbon foam and b) shows a close up of the surface. The morphology is different compared to the other produced samples, which are shown in the previous sections.

The C1s XPS spectrum of the sample is shown in figure 59 a) and also looks different compared to the previous shown C1s XPS spectra of the other carbon nanofoam samples. The spectrum consists of five peaks. C1 and C2 correspond to aromatic and aliphatic carbons, respectively. The C2 peak has a higher intensity than the C1 peak, which reveals a diamond-like composition of the sample surface. The other three peaks are assigned to oxygenated carbon groups.

The Raman spectrum shown in figure 59 b) consists of two main peaks, the D and the G peak. The G peak has a higher intensity and the peaks are not separated, which refers to carbonized materials. The existence of the D peak reveals that the sample consists of both,

sp^2 and sp^3 carbons.

In summary, the sample might have graphite carbon core and a diamond-like carbon surface, since XPS and Raman spectroscopy probe a different sample depth. Preparation details and further information can be found in [80].

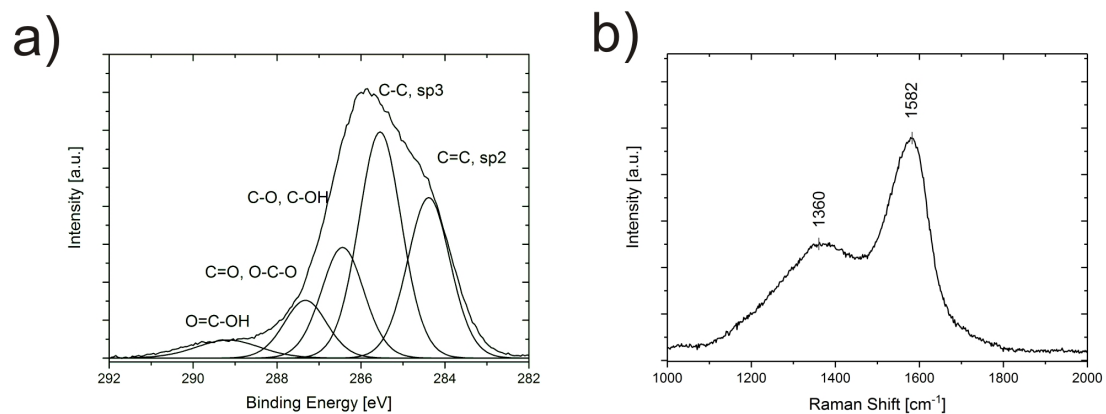


Figure 59: XPS and Raman spectra of diamond-like foam. a) shows the XPS C1s spectrum of the sample and b) the Raman spectrum.

4 Summary

This thesis focuses on the fundamental development, modification and investigation of carbon-based nanostructures, which promise great potential in research and industrial applications such as filter systems. The investigated materials are essentially carbon-based membranes and foams with different morphologies in the nanometer range used in combination with different biological materials. For material analysis HIM, AFM, XPS and Raman spectroscopy were applied.

The results of this thesis are divided into three parts. The first part is about the investigation of biological cells by HIM. The cells studied originate either from humans or from mice. It has been shown that through investigations with the HIM holes in the nanometer range could be found in the membrane of dried cells. The HIM opens up the possibility to image organic samples even without metallic coatings, therefore the cell membranes were imaged without a conductive coating. Charging effects were minimized by using an electron floodgun during imaging. Further experiments have shown that the holes are areas, which contain saturated fatty acids in untreated cells. This has been confirmed by the production and examination of model membranes. It was found that during the drying process the treatment with ethanol dissolves those areas, which include saturated fatty acids from the membrane. AFM measurements of cells before and after an ethanol treatment confirmed this result.

Further investigations on cells revealed the propagation of neurons on structured surfaces. These results are used as a preliminary study to structure self-made microelectrode arrays. HIM images have shown that after a few days in culture the neurons prefer the structured parts of the surface consisting of nodes connected by lines. Optimizing the line width prevented the cells from being placed on the lines. The cells now located on the nodes showed a good adhesion to the substrate. The dendrites and axons have grown as expected along the lines. These experiments show that the HIM is an excellent method for examining biological cells without coating. The purposeful attachment of neurons to chemically defined electrodes might be a novel way to grow guided neuronal networks.

The second part of this thesis focuses on CNM, which can be used as a different type of model membrane or as a substrate for biological samples. CNMs are produced by self-assembly of carbon-based precursor molecules. It has been shown that the membranes can be partly eroded by laser ablation. The subsequent replenishment of these regions with other carbon-based precursor molecules enabled the production of internal structured membranes through crosslinking by electron irradiation. The resulting membrane can be considered as a model of a biological cell membrane, as both are internally structured. A possible application for these

membranes is for example a biochip for single cell analysis. In further experiments cell growth could also be controlled by optimizing the choice of carbon-based precursor molecules in a structured CNM substrate. Therefore, the biocompatibility of the CNM was investigated. It has been shown that the molecules used in this thesis are suitable for the production of a CNM, which can be used as a substrate for cells. HIM images revealed that cells, which were immobilized on the CNMs, exhibited a good adhesion to the CNM and could even be immobilized on free-standing CNMs.

Not only cells were immobilized on CNMs, but also PM, which is the biological membrane of an Archaea, with the aim of producing a hybrid of CNM and PMs. This hybrid could, for example, be used for water purification in future applications. The hybrid was produced by the deposition of PMs on CNM while an electric field was applied in order to allow an oriented deposition of the PMs. Since protons can pass through the PM in one direction only, the unidirectional orientation of the patches is required to ensure a possible application of the hybrid as a proton pump. AFM and EFM images were used to confirm the orientation of the patches. A bond was achieved by a complex formation between functionalized CNM and PM mutants.

In the third part of this thesis carbon nanofoams were produced from carbon-based precursor molecules. The foams were produced by hydrothermal carbonization of carbon-based precursor molecules as sucrose. Most of the foams are made of micropearls, which are fused to network-like structures. Depending on the conditions, the size of the pearls could be tailored. Other carbon materials, which are not made of pearls, were also produced by variation of the precursor molecules.

In summary, this thesis shows that the HIM is an ideal microscopy technique for the analysis of carbon materials in the micrometer and nanometer range. Biological cells, carbon nanomembranes and carbon nanofoams were imaged and analyzed by HIM. The AFM was used for further examination of the biological and carbon membranes to determine the topology and electrostatic surface potential. XPS and Raman spectroscopy were used to investigate the molecular constitution and structure of the precursor molecules and obtained materials. The gained insights on carbon-based materials can be used as a basis for the development of new promising applications.

5 Publications

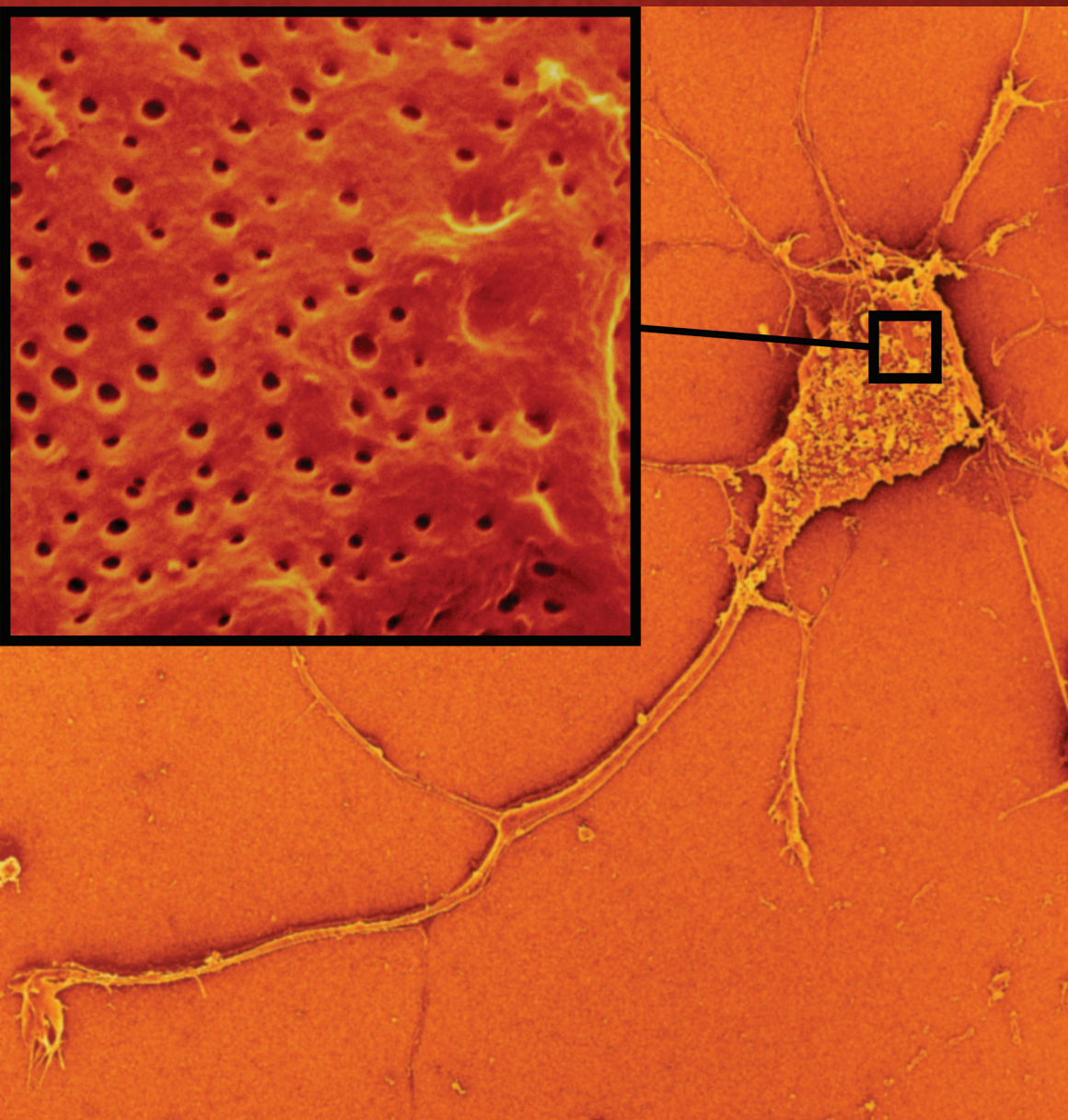
5.1 Cells

Volume 11 · No. 43 – November 18 2015

NANO MICRO

small

www.small-journal.com



43/2015

WILEY-VCH

Helium Ion Microscopy Visualizes Lipid Nanodomains in Mammalian Cells

B. Kaltschmidt, C. Kaltschmidt, A. Gölzhäuser, and co-workers

Helium Ion Microscopy Visualizes Lipid Nanodomains in Mammalian Cells

Matthias Schürmann, Natalie Frese, André Beyer, Peter Heimann, Darius Widera, Viola Mönkemöller, Thomas Huser, Barbara Kaltschmidt, Christian Kaltschmidt,* and Armin Götzhäuser*

Cell membranes are composed of 2D bilayers of amphipathic lipids, which allow a lateral movement of the respective membrane components. These components are arranged in an inhomogeneous manner as transient micro- and nanodomains, which are believed to be crucially involved in the regulation of signal transduction pathways in mammalian cells. Because of their small size (diameter 10–200 nm), membrane nanodomains cannot be directly imaged using conventional light microscopy. Here, direct visualization of cell membrane nanodomains by helium ion microscopy (HIM) is presented. It is shown that HIM is capable to image biological specimens without any conductive coating and that HIM images clearly allow the identification of nanodomains in the ultrastructure of membranes with 1.5 nm resolution. The shape of these nanodomains is preserved by fixation of the surrounding unsaturated fatty acids while saturated fatty acids inside the nanodomains are selectively removed. Atomic force microscopy, fluorescence microscopy, 3D structured illumination microscopy, and direct stochastic optical reconstruction microscopy provide additional evidence that the structures in the HIM images of cell membranes originate from membrane nanodomains. The nanodomains observed by HIM have an average diameter of 20 nm and are densely arranged with a minimal nearest neighbor distance of ≈ 15 nm.

M. Schürmann, Dr. P. Heimann, Dr. D. Widera,
Prof. B. Kaltschmidt, Prof. C. Kaltschmidt
Faculty of Biology
Bielefeld University
33501 Bielefeld, Germany
E-mail: c.kaltschmidt@uni-bielefeld.de

N. Frese, Dr. A. Beyer, V. Mönkemöller,
Prof. T. Huser, Prof. A. Götzhäuser
Faculty of Physics
Bielefeld University
33501 Bielefeld, Germany
E-mail: ag@uni-bielefeld.de

Dr. D. Widera
Reading School of Pharmacy
University of Reading
Reading RG6 6UB, UK

DOI: 10.1002/sml.201501540



1. Introduction

According to the classic liquid mosaic model, cell membranes represent a 2D lipid bilayer allowing for free lateral diffusion of membrane components.^[1] Since its initial postulation, the liquid mosaic model has been substantially modified based on various findings made with regard to inhomogeneities in cell membranes on the micro- and nanoscale.^[2,3] Such small detergent-resistant membrane nanodomains are called “lipid rafts” and are constituted mostly of sphingolipids with a much higher number of saturated bonds^[4] per molecule as compared to other common membrane lipids, e.g., phosphatidylcholine.^[5] A special type of raft-like nanodomains are the so-called “caveolae,” which are raft-like membrane invaginations stabilized by caveolin.^[3] Based on their size in the range of 10–200 nm,^[6] these membrane domains (lipid rafts and caveolae) can be

collectively termed membrane nanodomains.^[7] Due to their size of <200 nm, membrane nanodomains like lipid rafts of 200 nm cannot be assessed by confocal microscopy. In principle, transmission electron microscopy (TEM) could assess the size of such nanodomains. However, lipid rafts cannot be measured directly, because they cannot be distinguished from the surrounding cell membrane. Thus, mostly indirect methods have been applied to measure their size. Older studies based on the lateral diffusion of glycosylphosphatidylinositol-anchored (GPI-anchored) proteins suggested a size between 200 and 300 nm.^[8,9] However, modern, super-resolution-based approaches based on investigation of diffusion of GPI-anchored proteins point toward a smaller diameter of ≈ 20 nm.^[10] Similarly, single particle tracking of GPI-anchored proteins demonstrated a size of ≈ 26 nm.^[11] Further, Krager et al. used a biotinylated lipid raft reporter for TEM investigation of plasma membrane nano/microdomains and reported cluster sizes of 20–50 nm.^[12]

The size and density of membrane nanodomains are believed to play a substantial role in many membrane-related biological processes such as apoptosis,^[13] endocytosis, exocytosis, and immune response^[14] as well as in cancer.^[15] Moreover, membrane nanodomains play an important role in the biology of neurons, as they are involved in neurotransmitter signaling. Changes in neuronal membrane nanodomains may be associated with age-related neurological diseases including Parkinson and Alzheimer.^[16–19] Due to their nanoscale size below the diffraction limit of conventional light microscopy, membrane nanodomains have been mostly studied by indirect biophysical methods (reviewed in refs. [20] and [21]). Hell and co-workers utilized stimulated emission depletion (STED) microscopy to tune the optical resolution of a confocal laser beam from 250 nm down to 20 nm to directly monitor the diffusion and formation dynamics of membrane lipids in a living cell.^[10] In an extended approach, the same group applied coaligned dual-channel STED to quantify the diffusion of labeled lipids in cell membranes with a spatial resolution down to 20 nm.^[22] Despite STED's ability to image fast dynamic processes, a direct spatial imaging of these structures in living cells has not yet been accomplished. The extended spatial resolution of super-resolution optical microscopy is well complemented by combination with modern electron microscopy. During the last decades scanning electron microscopy (SEM) has become a widespread instrument to investigate the surface structure of biological samples with a resolution between 2 and 5 nm.^[23] However, since imaging by SEM inevitably introduces electric charge into the specimen it is necessary to render the sample conductive, which is routinely accomplished by coating the sample with a thin metal film. The drawback of this technique is that the metal coating might obscure small structural features.

Since the 2010s, helium ion microscopes have been commercially available. In helium ion microscopy (HIM), a focused beam of positive helium ions (He^+) is utilized to scan a sample surface, leading to the ejection of secondary electrons (SEs) that are then detected.^[24] Like in a scanning electron microscope, the local variation of the SE intensity is converted into a grayscale image. Soon after its introduction, the HIM evolved into a very useful tool in materials science.

Its small He^+ beam can be focused with a diameter below 0.3 nm, which leads to high-resolution images. In addition, a pronounced material contrast is generated due to a high variation of elemental cross-sections of He^+ ions, leading to additional information for chemically heterogeneous samples (a recent review on HIM is found in ref. [25]). An HIM can also provide sharp images from electrically insulating samples. This is achieved by a charge compensation, in which positive charges deposited by the He^+ beam are neutralized by an electron beam thus balancing the charge of the incoming He^+ ions and the outgoing SEs. Armed with this capability, the HIM successfully imaged complex biological specimen such as *Arabidopsis thaliana* sepal cuticle or the human cell line *HeLa* during mitosis with subnanometer resolution.^[26] Using HIM and its charge compensation, networks of collagen fibers in cartilage^[23] and polymerized fibrin fibers in a 3D matrix used for stem cell cultivation^[27] were visualized. Thus, the HIM is an ideal tool to explore the nanostructural details of biological membranes and membrane nanodomains.

Here, we investigate the ultrastructure of cell membranes with the helium ion microscope. We found that all mammalian cell types studied exhibit pit-like features with average diameters of 20 nm. We provide evidence that these pit-like membrane inhomogeneities represent membrane nanodomains within an ordered liquid phase. Moreover, our data suggest that these membrane nanodomains are lipid-raft-like domains and caveolae visualized using HIM with a resolution of 1.5 nm.

2. Results and Discussion

Because of their small size, well below the optical resolution limit, nanoscale membrane inhomogeneities cannot be assessed by conventional light microscopy. However, such nanodomains seem to play an important role in health and disease,^[18,19] making the study of their structure and composition particularly important. We have imaged different mammalian cell types, undifferentiated adult human neural crest-derived stem cells (NCSCs) from the human respiratory mucosa,^[28] NCSC-derived human neurons,^[29] and hippocampal mouse neurons with a helium ion microscope. **Figure 1A–C** shows images of NCSC-derived human neurons with and **Figure 1D–F** without an initial gold coating.

In both approaches, stem cells differentiated into neurons showed a round and defined cell body and numerous slender, branching, and long projections with small diameters representing neurites (**Figure 1A,D**). Remarkably, in specimens sputter-coated with gold (Au) with a typical thickness of ≈ 10 nm (**Figure 1A–C**), the cell membrane is covered with clustered Au, masking the cell surface. The evaluation of HIM images of uncoated, native-state cell membranes revealed numerous pit-like membrane inhomogeneities or domains with varying diameters that are rarely visible in coated cells (**Figure 1D–F**). This becomes particularly clear by comparing the high-magnification HIM images in **Figure 1C,F**, which show regions on the somata of the cells. We also performed HIM imaging on the neurites of stem cells differentiated into neurons, cf. **Figure S1** (Supporting Information). To verify the 3D appearance of the inhomogeneities, further HIM imaging

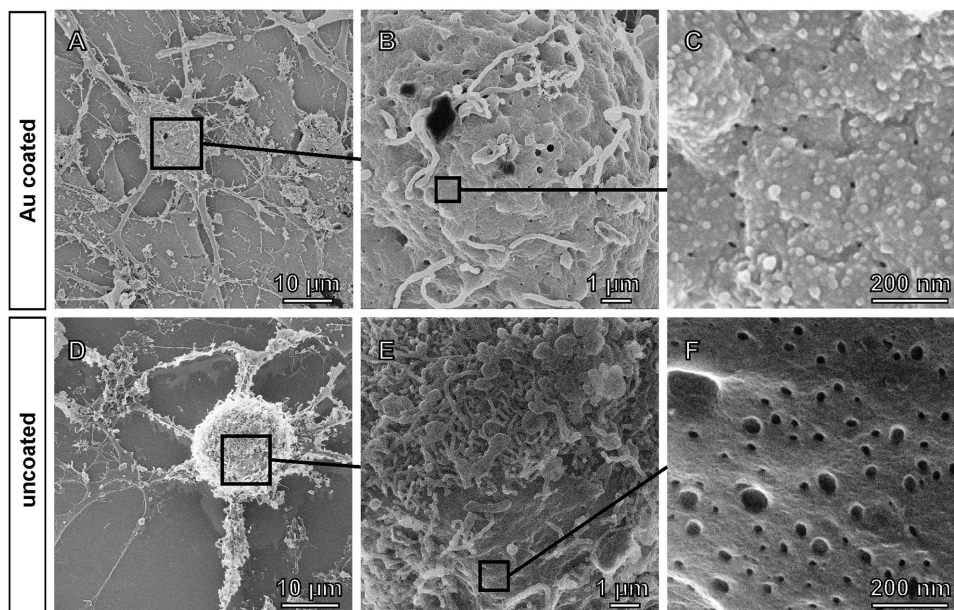


Figure 1. Helium ion microscopic image of critical point dried stem cells differentiated to the neuronal lineage with and without gold coating. A,D) Human neural crest-derived stem cells differentiated to neurons with a round and defined cell body and numerous thin, slender, branching, and long projections with small diameter representing neurites. B,E) Cell membrane of soma. C) In specimens sputter coated with gold (Au) with standard thickness of ≈ 10 nm the cell membrane is covered with clustered Au, masking the true cell surface. F) Helium ion microscopy allows high-resolution inspection of uncoated cell surface in the native state. Numerous nanodomains with a roundish circumference and of varying diameter become discernible.

of uncoated specimens was performed, cf. **Figure 2** and **Figure S2** (Supporting Information).

Human neurons are of limited availability and accessibility. Very recently, we successfully differentiated adult

human NCSCs into neurons with forebrain and midbrain characteristics.^[29] Therefore here we employed human stem cell-derived neurons as a model system to study human neuronal cells. In addition to these cells, we used different cell

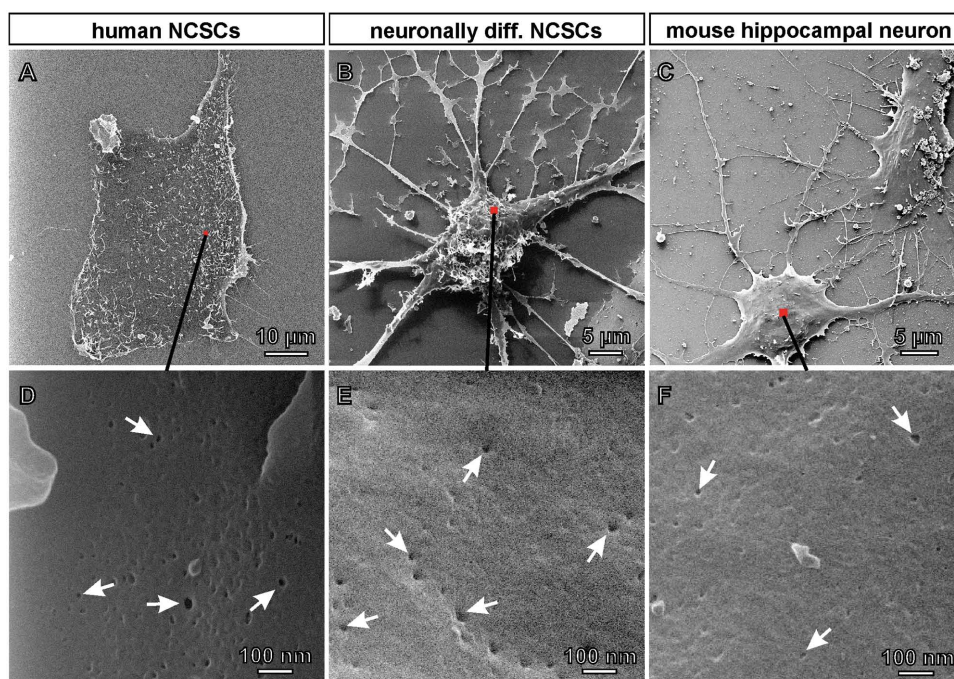


Figure 2. Pits in ultrastructure of membrane topology are present in different cell types derived from different species. HIM imaging was performed on critical point dried uncoated primary mouse hippocampal mouse neurons (4 d cultured), human NCSCs, and human NCSC-derived neurons. A–C) In the overview all cell types show their typical morphology, i.e., undifferentiated, adherent for A) NCSC and C) neuronal for primary mouse hippocampal neurons and B) neuronally differentiated human NCSC. D–F) Remarkably all images of the different cell membranes acquired at a high magnification showed unevenly distributed pit-like structures (arrows).

types for HIM imaging to exclude interspecies variations and potential impact of the differentiation method (Figure 2).

Adult human NCSCs were imaged either undifferentiated (Figure 2A) or differentiated into neurons (Figure 2B), which showed typical shape and diverse neurites closely resembling morphological features of primary neurons from embryonic mouse hippocampus cultured for 4 d (Figure 2C). Importantly, the cell surfaces of all three cell types (NCSCs, differentiated NCSCs, and primary neurons) showed anisotropically distributed pit-like structures (Figure 2D–F).

It is our hypothesis that the pit-like domains are a direct visualization of the shape of membrane nanodomains, including lipid rafts and caveolae. These nanodomains consist mainly of saturated fatty acids while the lipid bilayer outside of the nanodomains consists of unsaturated fatty acids. It is known that osmium tetroxide (OsO_4) used in the cell fixation and drying (see the Experimental Section) reacts with unsaturated fatty acids inside the lipid membrane to create cyclic ethers.^[30] If two unsaturated fatty acids are positioned in the right manner this is followed by a cross-linking of the membrane. On the other hand, saturated fatty acids in lipid membranes do not cross-link with OsO_4 as shown below. Thus, we conclude that the cell fixation with OsO_4 cross-links the lipid bilayer outside the nanodomains while the lipid bilayer inside the nanodomains is removed by the required subsequent rinsing with ethanol for the cell drying process. Therefore, imaging with HIM reveals the shape of the nanodomains as missing lipid bilayer domains, i.e.,

pit-like structures. In addition, we performed freeze drying of stem cells differentiated into neurons after fixation with aldehydes and OsO_4 . HIM imaging of these cells also shows nanodomains in the cell membranes, cf. Figure S3 (Supporting Information). It follows that the nanodomains are unstable not only in ethanol but also in air.

Support of our hypothesis was obtained by reproducing the proposed mechanism of selective cross-linking and ethanol-based removal with a lipid bilayer model system. For this purpose we generated supported lipid bilayers (SLBs) composed of a 1:1 mixture of 1,2-dioleoyl-sn-glycerol-3-phosphocholine (DOPC) and 1,2-distearoyl-sn-glycerol-3-phosphocholine (DSPC) on a mica surface (Figure 3). Such SLBs are widely used as models to investigate phospholipid membranes mimicking biological surfaces including cell membranes and can be accessed by AFM.^[31] Remarkably, the DOPC and DSPC lipid domains can be distinguished based on their height difference relative to the mica surface.^[32]

The separation of the two phases in the bilayer into a gel-like DSPC and more fluid DOPC domains is apparent as a height difference of about 1.5 nm (Figure 3C). Here, DSPC lipid domains (bright areas, ≈ 7 nm) can be clearly differentiated from DOPC domains (dark areas, 5.5 nm). After treatment with OsO_4 and subsequent EtOH extraction of lipids, ethanol extraction resistant DOPC domains remain detectable by their height and shape using AFM (Figure 3D). Importantly, DOPC domains in the bilayer cross-linked by the OsO_4 treatment are able to withstand the extraction

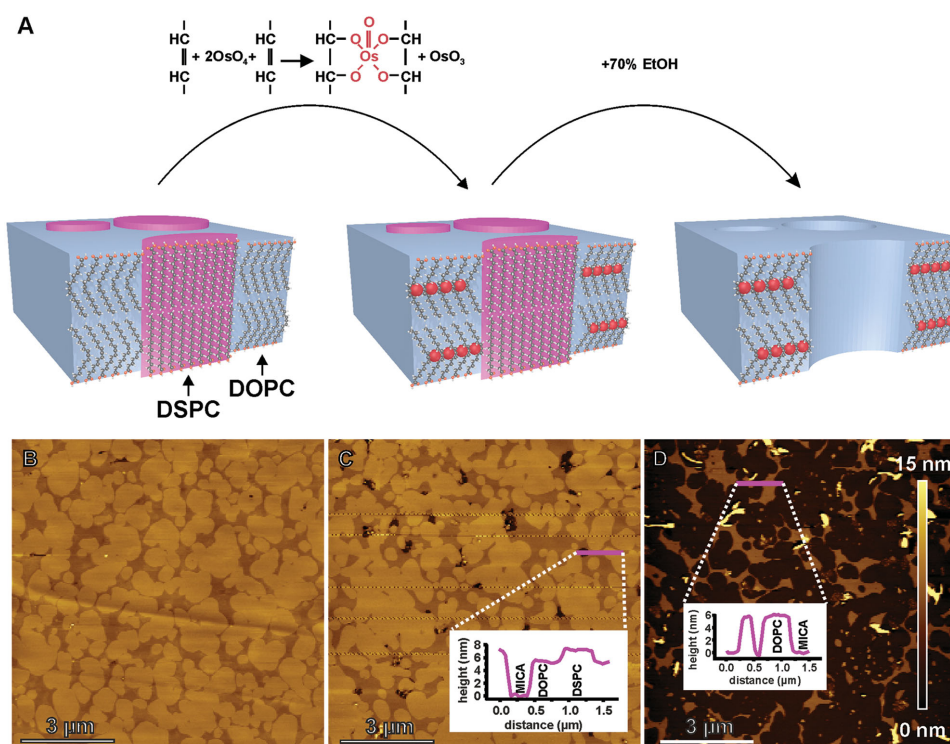


Figure 3. A proposed mechanism for the generation of pit-like membrane features in a synthetic model membrane. A) Scheme of the pit formation including the cross-linking of the unsaturated fatty acids via OsO_4 and the extraction of the lipid domains by ethanol. B–D) The experimental test of the hypothesized mechanism with a topographic AFM image of a synthetic lipid membrane. The artificial lipid bilayer showed a characteristic phase separation of the two lipids resulting in domains with a height of 5.5 nm for DOPC and 7 nm for DSPC. These height values were measured with respect to the mica substrate, cf. line profile (inset, C). The extraction of the saturated fatty acids domains with ethanol can be easily ascertained by their characteristic shape and height (inset, D).

process with ethanol, which clearly proves the effectiveness of the proposed mechanism of a spatially selective cross-linking and ethanol-based removal.

Further visualization of the proposed mechanism was obtained with mammalian cells by fluorescence-based imaging techniques. Therefore, we stained fixed NCSCs using aldehydes and OsO_4 followed by labeling of lipid domains using Alexa Fluor 488—coupled to cholera toxin fragment B (CTxB) (Figure 4). CTxB is known to efficiently label a fraction of raft-like lipid nanodomains in cells by binding to Ganglioside 1.^[6,33,34]

Figure 4 shows that domains of the cell membrane positive for CTxB can get extracted with 70% ethanol as visualized by a loss of the corresponding fluorescence signal only in the EtOH-treated specimen (Figure 4B) in comparison to the control sample, which was prepared in the same way except for the EtOH treatment (Figure 4A). The visualized extraction of CTxB-labeled membrane domains indicates that our

proposed mechanism of selective cross-linking and EtOH-based removal is not only effective in model membranes but also detectable in membranes of mammalian cells. Thus, we can infer that the pit-like membrane domains in the HIM images visualize the shape of lipid raft-like domains and/or caveolae.

Higher resolved fluorescence images reveal the distribution of the CTxB labels in the samples without EtOH treatment by 3D structured illumination microscopy (3D-SIM) and direct stochastic optical reconstruction microscopy (dSTORM), cf. Figure 4C,D, respectively. These images show that the CTxB labels are arranged in the form of nanodomains and are colocalized with actin which proves that the raft-like lipid nanodomains are present in the investigated mammalian cells.^[35]

Concluding from dSTORM that the nanodomains visualized in HIM are also visible with an independent method, we used the superior resolution of HIM to quantify

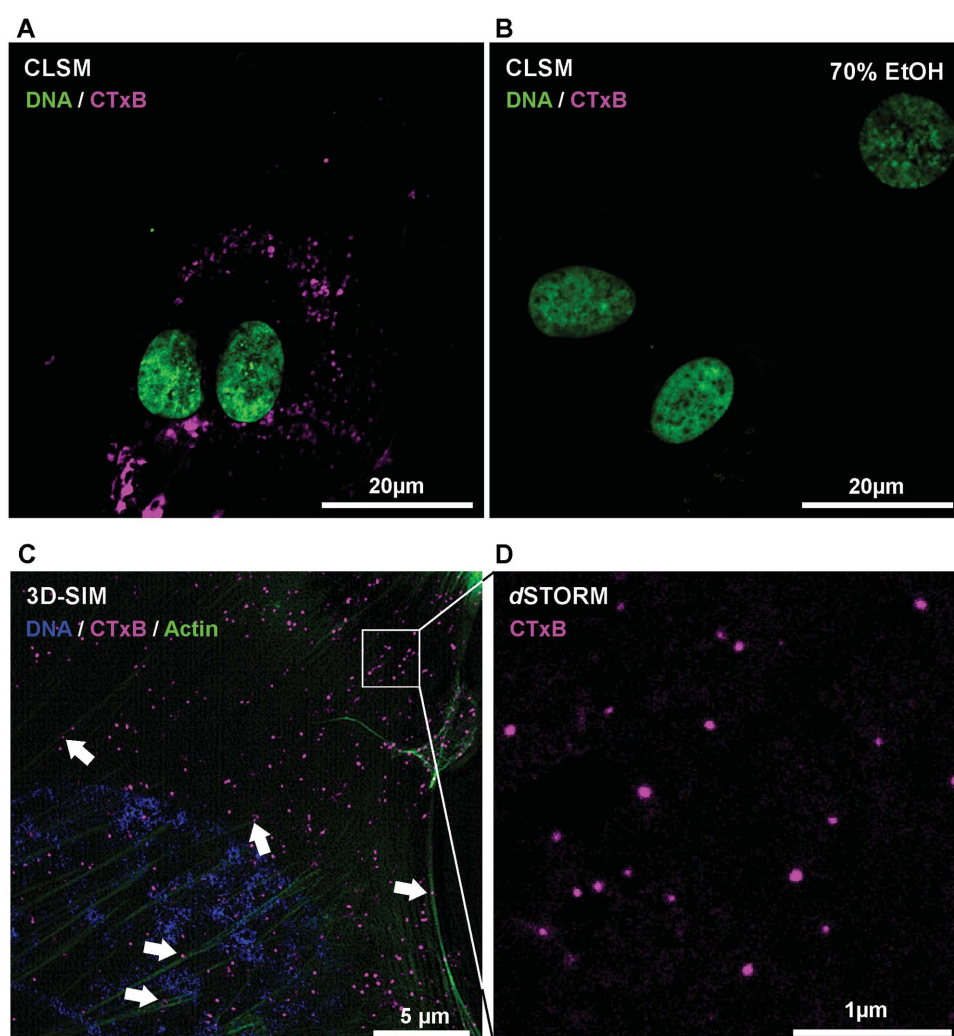


Figure 4. The domains in a fixed cell membrane labelled with cholera toxin subunit B (CTxB) can be extracted with ethanol suggesting a lipid raft-like and/or caveolae-nature. Confocal laser scanning microscopy (CLSM) images of cells fixed with aldehydes and OsO_4 were treated with B) ethanol or remained in A) PBS and subsequently stained with CTxB. The cells treated with ethanol show no positive signal for CTxB. C) 3D structured illumination microscopy (3D-SIM) and D) direct stochastic optical reconstruction microscopy (dSTORM) yielded images with a higher resolution. A homogenous but anisotropic distribution of CTxB labelled membrane nanodomains is found. In addition, colocalization of nanodomains and actin filaments is marked by arrows in (C).

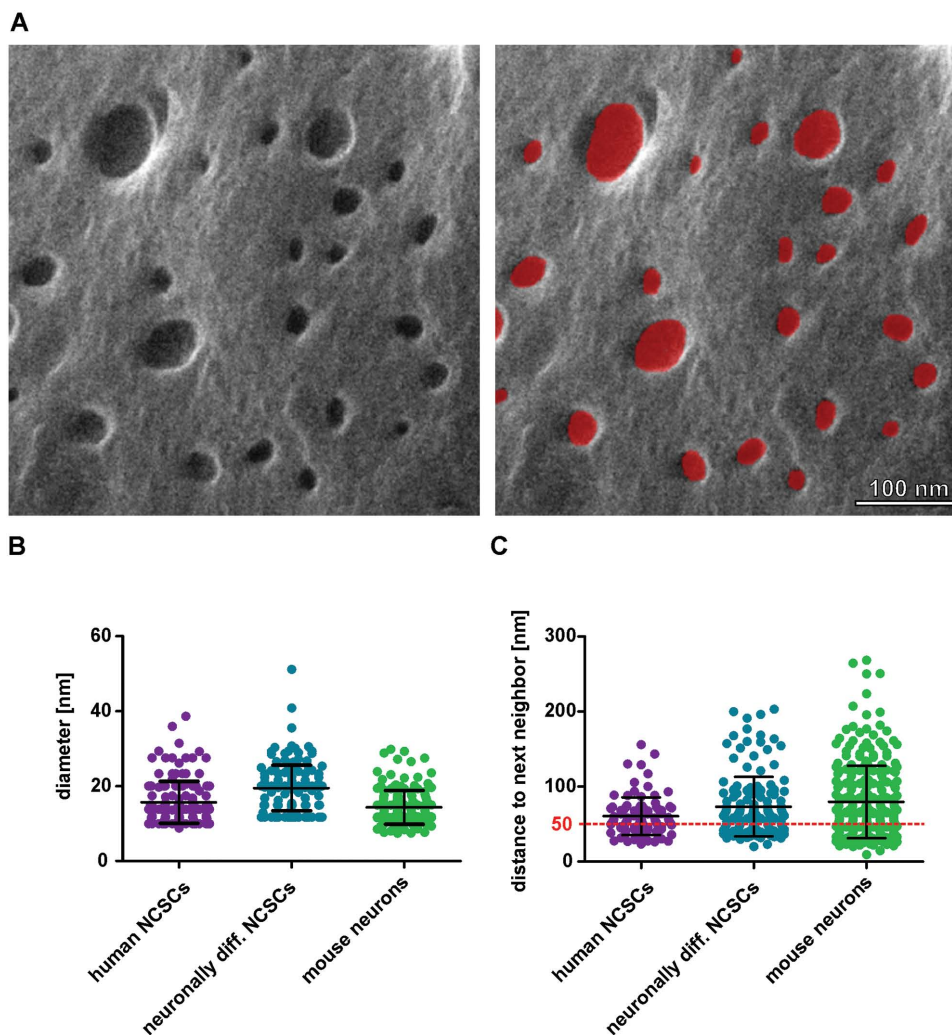


Figure 5. Measurement of the size and distribution of membrane pits with nm-accuracy by HIM. A) For measuring the properties of the pit-like structures (lipid-nanodomains) the corresponding regions were marked in the HIM image of an NCSC-derived human neuron soma. B) The resulting size was measured at the soma for three different cell types (two cells per type). The size distributions of cells from the same type were comparable. The mean diameter for all investigated cell types was shown to be ≤ 20 nm. C) Further measurements regarding the distance to the next neighboring domain showed that a main fraction of the domains lies closer than 50 nm to its next neighbor and hence is at least partly of raft-like origin.

lipid nanodomains. We therefore measured the diameters and mean nearest neighbor distances of pit-like structures (lipid nanodomains) in three different cell types: NCSCs, neuronally differentiated stem cells, and mouse hippocampal neurons.

For all three cell types we measured a mean diameter of ≤ 20 nm suggesting that most of the pit structures are raft-like (Figure 5B). This is in general accordance with the consensus size definition of lipid rafts, claiming raft diameters of 10–200 nm.^[6]

Due to the overlapping size of lipid raft-like membrane nanodomains (diameter of lipid rafts: 10–200 nm;^[6,36–38] diameter of caveolae: 50–120 nm with an open pore of 30–50 nm^[39,40]), the measurement of the pit diameter is not sufficient to distinguish between both nanodomains. Thus, in addition to the determination of the diameter (Figure 5A) we measured the mean distance between the respective neighboring nanodomains in NCSCs, stem cell-derived human neurons, and mouse hippocampal neurons. Caveolae are

invaginations of the cell membrane, which look in a section like a balloon, cf. Figure S6 (Supporting Information). Since the diameter of the caveolae is in the range of 50–120 nm it is impossible that the openings of two caveolae can lie closer to each other than 50 nm. Hence we conclude that the fraction of the pit-like structures revealed by HIM having distances to the neighboring domain < 50 nm represents at least partly lipid-raft-like membrane nanodomains and not caveolae (Figure 5C).

In summary, we present a strong line of evidence that pit-like structures revealed in helium ion microscopy images of mammalian cell membranes represent both lipid raft-like membrane nanodomains and caveolae. Since its first introduction, the concept of lipid rafts is still controversial and a matter of ongoing scientific debate.^[4,41] However, cholesterol and sphingolipid-rich nanodomains within the cell membrane seem to have tremendous impact on elementary functions of different cell types including signal transduction and regulation of the cell fate. The controversy of the lipid raft concept is partly driven by the fact

that they are difficult to visualize in cells. Our study allows for the first time a direct observation of lipid raft-like nanodomains that appear as pit-like structures in unstained and uncoated cell membrane. Thus, broad application of HIM in lipid raft research could crucially contribute to clarification of open questions on their size and (sub-) cellular distribution in different cell types. As helium ion microscopy is a versatile and “easy to use” method, it is expected to find numerous applications in biological and medical research, opening new opportunities for bioimaging with ions, especially if correlated with other state-of-the-art methods, such as super-resolution optical microscopy, cryoelectron microscopy, or nanomass spectrometry, thus pushing the limits in soft-matter research.

3. Experimental Section

Cell Culture: Human inferior turbinates were obtained by biopsy during routine surgery after an informed consent according to local (Bezirksregierung Detmold/Münster) and international guidelines. Cell isolation and cultivation was performed as described in ref. [28]. Briefly, inferior turbinates were mechanically and enzymatically dissociated and further cultivated in a serum-free medium (Dulbecco's modified eagle medium (DMEM)/Ham's F12 nutrient mixture (F12) containing B27 supplement, basic fibroblast growth factor (FGF-2) and epidermal growth factor (EGF)). For rapid expansion NCSCs were cultivated in medium supplemented with 10% human blood plasma as described in ref. [27]. Mouse hippocampal neurons were isolated and cultivated as described in ref. [42]. In particular, mouse hippocampal neurons were obtained by dissecting the hippocampi from mouse embryonic stage E17.5 followed by digestion in trypsin ethylenediaminetetraacetic acid (EDTA) (from PAA) for 30 min at 37 °C. Subsequently the tissue was mechanically dissociated by pipetting the solution through a Pasteur pipette. Afterward the cells were seeded on polyethyleneimine (PEI)-coated cover slips in DMEM containing 10% fetal calf serum (FCS) with a density of 1000 cells mm⁻². The medium was changed to neurobasal medium containing 1% B27 1 h and 24 h after seeding.

Neuronal Differentiation of Human Neural Crest Stem Cells: Adult human NCSCs were differentiated toward neuronal lineage as described in ref. [29].

HIM Imaging: The samples were imaged with the helium ion microscope ORION PLUS from Zeiss with an accelerating voltage between 35 and 40 eV and a beam current between 0.4 and 1.1 pA. The electron flood gun was used to compensate for charging of uncoated samples. For visualization with HIM the cells were fixed with 100 × 10⁻³ M sodium cacodylate (pH 7.2) containing 4% paraformaldehyde (PFA) and 4% glutaraldehyde for 1 h at 4 °C followed by lipid fixation in 100 × 10⁻³ M sodium cacodylate buffer containing 1.5% OsO₄ for 30 min at 4 °C. Fixed cells were then dehydrated in ethanol series and critical point dried via CO₂ of highest purity. The cover slips were either left in their native state or were sputtered with 10 nm of gold. Other specimens were freeze dried. For this purpose fixed specimens were washed in distilled water, which was sucked away resulting in a very thin film of water. Subsequently specimens were plunge frozen in liquefied propane at -190 °C. Shock frozen specimens were then transferred under N₂ atmosphere into a self-made freeze-drying apparatus (consisting in principle out of two heavy polished copper blocks having a distance of 5 mm) at -196 °C. The device was brought

into a high-vacuum chamber and dried for 15 h at 10⁻⁵ millibar. The resolution of the helium ion microscope was determined as the distance between two points on a keen edge on which the signal corresponds from 25% to 75% of the absolute signal of the edge. For this purpose the signal of ten scan lines that cross an extracted lipid domain was analyzed. The diameters of the pit-like features were determined by calculating equivalent circle areas from the pit-like feature areas that are exemplary red marked in Figure 5A. For this purpose, we created a mask by marking the nanodomains with the “mask editor” in Gwyddion and calculated equivalent disc areas by using the “grain functions” in Gwyddion. Furthermore the distances between the middle of every pit-like feature and their next neighboring feature were measured.

Transmission Electron Microscopy: Animals were transcardially perfused (with a permit of the local authorities) under deep anesthesia first for 40 s with heparin/procaine (blood isotonic) followed by 2% formaldehyde/4% glutaraldehyde fixative in 0.1 M phosphate buffer for 10 min. Dissected organs were further fixed for 2–4 h at 4 °C and postfixed with 2% OsO₄ plus 0.15% potassium hexacyanoferrate(III) in buffer and embedded in Araldite. Ultrathin sections (70 nm) were contrasted with uranyl acetate and lead citrate and viewed under a Zeiss EM109 electron microscope at 50 kV.

Liposome Preparation: Liposomes (DSPC, 18:0 and DOPC, 18:1; Sigma-Aldrich) were prepared by dissolving the two lipids in chloroform to obtain solutions at a 1:1 ratio. The solvent was removed by drying the mixture in a glass test tube under a nitrogen stream. Rehydration of the lipid film was accomplished in vesicle buffer consisting of 10 × 10⁻³ M HEPES, 150 × 10⁻³ M NaCl, and 4 × 10⁻³ M CaCl₂ at pH 7.4 obtaining a dispersion with an overall lipid concentration of 1 × 10⁻³ M. Small unilamellar vesicles (SUVs) were formed by sonication in a water bath of an ultrasonic cleaner which was heated to ≈60 °C slightly above the transition temperature of DSPC (55 °C) until the dispersion became only slightly hazy. To remove the lipid debris generated during the SUV formation the dispersion was centrifuged for 3 min at 2000g.

SLB Formation: The supported planar bilayer was formed by incubation of freshly cleaved mica with the SUV dispersion for 30 min at room temperature (RT). Subsequently the mica was washed three times with vesicle buffer. Following this primary washing steps the mica was further washed to remove excess liposomes and calcium prior to AFM imaging using rinsing buffer composed of 10 × 10⁻³ M HEPES, 150 × 10⁻³ M NaCl, and 4 × 10⁻³ M EDTA at a pH of 7.4.

AFM Imaging and Fixation of the Supported Planar Bilayer: AFM imaging was performed using the NT-MDT Ntegra device in tapping mode at RT in rinsing buffer as described above (SLB formation). The image acquisition was performed using a piezo scanner with a maximum scanning area of 71.3 μm and a 225 μm long V-shaped cantilever with a spring constant of ≈0.03 N m⁻¹. The AFM images were acquired with a scan rate of 0.3 Hz and a tip oscillating frequency of 12.2 kHz. Fixation of the supported planar lipid bilayer was performed by submerging the bilayer in 100 × 10⁻³ M sodium cacodylate buffer containing 1.5% OsO₄ for 30 min at RT. Extraction of the unfixed lipid with ethanol was executed by rinsing the bilayer with 70% ethanol for three times.

CTxB Staining and Confocal Fluorescence Imaging: For staining with Cholera Toxin subunit B NCSCs were plated on glass cover slips in DMEM containing 10% FCS and fixed as described above (HIM imaging). Subsequently the cells were either washed with

PBS or washed with 70% ethanol followed by rinsing with phosphate-buffered saline (PBS). Afterward the cells were stained with $1 \mu\text{g mL}^{-1}$ CTxB Alexa Fluor 488 conjugate (life technologies) and $1 \mu\text{g mL}^{-1}$ 4',6-diamidin-2-phenylindol (DAPI) in PBS for 10 min at RT. To visualize the fluorochromes confocal microscopy was applied (CLSM 780, Carl Zeiss).

Super-Resolution Imaging of Lipid Rafts: NCSCs were plated on glass cover slips in DMEM containing 13% FCS and fixed with 4% FPA in PBS for 20 min at RT. Cells were then stained for 30 min with $0.1 \mu\text{g mL}^{-1}$ CTxB AlexaFluor 647 conjugate (Life Technologies) and 165 nM Phalloidin AlexaFluor 488 conjugate (Invitrogen). Further NCSCs were stained with $0.1 \mu\text{g mL}^{-1}$ DAPI in PBS for 10 min. All staining steps were executed at RT. 3D-SIM images of NCSCs were acquired using a commercial 3D structured illumination microscope (3D-SIM, DeltaVision|OMXv4.0 BLAZE, GE Healthcare). To achieve even higher spatial resolution of lipid rafts we used 3D-SIM in combination with single molecule localization microscopy of conventional fluorophores (dSTORM) on the same setup by changing the illumination mode from structured illumination to ring-TIRF (total internal reflection fluorescence excitation), albeit at an angle just below the critical angle to obtain a highly inclined laminated optical sheet illumination mode.

To enable their controlled blinking, the CTxB-AlexaFluor 647 molecules were excited with a 642 nm laser. The 642 nm laser power was set to 100% of laser power so that the density of the blinking fluorophores appears as high as possible while still creating sufficient spatial separation between molecules for single molecule localization. Typical excitation laser power densities were $\approx 0.5 \text{ kW cm}^{-2}$. The acquisition time was 30 ms per frame and 12 000 frames were recorded using an sCMOS camera (total acquisition time ≈ 10 min). Raw data were preprocessed to reduce background signal and single pixel characteristics intrinsic to sCMOS cameras by subtracting the average of the image stack from each individual frame.

For the final reconstruction of a dSTORM image the 12 000 frames were analyzed by the open source reconstruction software rapidSTORM.^[43] Images were corrected for sample drift by assuming linear drift using the built-in drift correction of rapidSTORM and the localization precision was calculated for each detected fluorophore in rapidSTORM.

dSTORM images were analyzed to extract feature size using Fiji. Thresholding was done using the auto threshold function "moments." To extract the size distribution of lipid rafts, Fiji's particle analysis procedure was used with a minimum size of 200 nm² and a minimum circularity of 0.3.

Acknowledgements

M. Schumann and N. Frese contributed equally to this work. The authors thank H. Vieker and B. Völkel for technical help and valuable discussion. They also thank the Volkswagenstiftung for financial support.

- [1] S. J. Singer, G. L. Nicolson, *Science* **1972**, 175, 720.
- [2] M. J. Karnovsky, A. M. Kleinfeld, R. L. Hoover, R. D. Klausner, *J. Cell Biol.* **1982**, 94, 1.
- [3] R. G. Parton, K. Simons, *Science* **1995**, 269, 1398.
- [4] K. Simons, J. L. Sampaio, *Cold Spring Harb. Perspect. Biol.* **2011**, 3, a004697.
- [5] K. Simons, E. Ikonen, *Nature* **1997**, 387, 569.
- [6] L. J. Pike, *J. Lipid Res.* **2009**, 50, S323.
- [7] V. Horejsi, M. Hrdinka, *FEBS Lett.* **2014**, 588, 2392.
- [8] K. Jacobson, E. D. Sheets, R. Simson, *Science* **1995**, 268, 1441.
- [9] E. D. Sheets, G. M. Lee, R. Simson, K. Jacobson, *Biochemistry* **1997**, 36, 12449.
- [10] C. Eggeling, C. Ringemann, R. Medda, G. Schwarzmann, K. Sandhoff, S. Polyakova, V. N. Belov, B. Hein, C. von Middendorff, A. Schonle, S. W. Hell, *Nature* **2009**, 457, 1159.
- [11] A. Pralle, P. Keller, E. L. Florin, K. Simons, J. K. H. Horber, *J. Cell Biol.* **2000**, 148, 997.
- [12] K. J. Krager, M. Sarkar, E. C. Twait, N. L. Lill, J. G. Koland, *J. Lipid Res.* **2012**, 53, 2214.
- [13] K. S. George, S. Wu, *Toxicol. Appl. Pharmacol.* **2012**, 259, 311.
- [14] K. Simons, M. J. Gerl, *Nat. Rev. Mol. Cell Biol.* **2010**, 11, 688.
- [15] S. Staubach, F. G. Hanisch, *Expert Rev. Proteomics* **2011**, 8, 263.
- [16] M. Hashimoto, T. Takenouchi, E. Rockenstein, E. Masliah, *J. Neurochem.* **2003**, 85, 1468.
- [17] R. Ehehalt, P. Keller, C. Haass, C. Thiele, K. Simons, *J. Cell Biol.* **2003**, 160, 113.
- [18] A. M. Sebastiao, C.-M. Oliveira, A.-N. Lopes, R. B. Dias, J. A. Ribeiro, *Neuropharmacology* **2013**, 64, 97.
- [19] R. Marin, J. A. Rojo, N. Fabelo, C. E. Fernandez, M. Diaz, *Neuroscience* **2013**, 245, 26.
- [20] K. Simons, D. Toomre, *Nat. Rev. Mol. Cell Biol.* **2000**, 1, 31.
- [21] S. Sonnino, A. Prinetti, *Curr. Med. Chem.* **2013**, 20, 4.
- [22] F. Gottfert, C. A. Wurm, V. Mueller, S. Berning, V. C. Cordes, A. Honigsmann, S. W. Hell, *Biophys. J.* **2013**, 105, L01.
- [23] W. S. Vanden Berg-Foels, L. Scipioni, C. Huynh, X. Wen, *J. Microsc.* **2012**, 246, 168.
- [24] B. W. Ward, J. A. Notte, N. P. Economou, *J. Vac. Sci. Technol. B* **2006**, 24, 2871.
- [25] G. Hlavacek, V. Veligura, R. van Gastel, J. Poelsema, *J. Vac. Sci. Technol. B* **2014**, 32, 020801.
- [26] M. S. Joens, C. Huynh, J. M. Kasuboski, D. Ferranti, Y. J. Sigal, F. Zeitvogel, M. Obst, C. J. Burkhardt, K. P. Curran, S. H. Chalasani, L. A. Stern, B. Goetze, J. A. Fitzpatrick, *Sci. Rep.* **2013**, 3, 3514.
- [27] J. F. Greiner, S. Hauser, D. Widera, J. Müller, F. Qunneis, C. Zander, I. Martin, J. Mallah, D. Schuetzmann, C. Prante, H. Schwarze, W. Prohaska, A. Beyer, K. Rott, A. Hüten, A. Gözlhäuser, H. Sudhoff, C. Kaltschmidt, B. Kaltschmidt, *Eur. Cells Mater.* **2011**, 22, 403.
- [28] S. Hauser, D. Widera, F. Qunneis, J. Müller, C. Zander, J. Greiner, C. Strauss, P. Luningschorr, P. Heimann, H. Schwarze, J. Ebmeyer, H. Sudhoff, A.-M. J. Bravo, B. Greber, H. Zaehres, H. Scholer, C. Kaltschmidt, B. Kaltschmidt, *Stem Cells Dev.* **2012**, 21, 742.
- [29] J. Müller, C. Ossig, J. F. Greiner, S. Hauser, M. Fauser, D. Widera, C. Kaltschmidt, A. Storch, B. Kaltschmidt, *Stem Cells Transl. Med.* **2015**, 4, 31.
- [30] G. Lang, *Praxislehrbuch für die Biomedizinische Analytik*, Springer, Vienna **2013**, p. 53.
- [31] Redondo-L. Morata, M. I. Giannotti, F. Sanz, *Mol. Membr. Biol.* **2014**, 31, 17.
- [32] M. C. Giocondi, D. Yamamoto, E. Lesniewska, P. E. Milhiet, T. Ando, L. C. Grimellec, *Biochim. Biophys. Acta* **2010**, 1798, 703.
- [33] K. Badizadegan, A. A. Wolf, C. Rodighiero, M. Jobling, T. R. Hirst, R. K. Holmes, W. I. Lencer, *Int. J. Med. Microbiol.* **2000**, 290, 403.
- [34] B. J. Nichols, A. K. Kenworthy, R. S. Polishchuk, R. Lodge, T. H. Roberts, K. Hirschberg, R. D. Phair, J. Lippincott-Schwartz, *J. Cell Biol.* **2001**, 153, 529.
- [35] R. Raghupathy, A. A. Anilkumar, A. Polley, P. P. Singh, M. Yadav, C. Johnson, S. Suryawanshi, V. Saikam, S. D. Sawant, A. Panda, Z. Guo, R. A. Vishwakarma, M. Rao, S. Mayor, *Cell* **2015**, 161, 581.
- [36] J. B. Helms, C. Zurzolo, *Traffic* **2004**, 5, 247.

- [37] L. Rajendran, K. Simons, *J. Cell Sci.* **2005**, *118*, 1099.
- [38] D. V. Nicolau Jr., K. Burrage, R. G. Parton, J. F. Hancock, *Mol. Cell Biol.* **2006**, *26*, 313.
- [39] M. Westermann, H. Leutbecher, H. W. Meyer, *Histochem. Cell Biol.* **1999**, *111*, 71.
- [40] A. W. Cohen, R. Hnasko, W. Schubert, M. P. Lisanti, *Physiol. Rev.* **2004**, *84*, 1341.
- [41] S. Munro, *Cell* **2003**, *115*, 377.
- [42] C. Klenke, D. Widera, T. Engelen, J. Muller, T. Noll, K. Niehaus, M. L. Schmitz, B. Kaltschmidt, C. Kaltschmidt, *PLoS One* **2013**, *8*, e65280.
- [43] S. Wolter, U. Endesfelder, S. van de Linde, M. Heilemann, M. Sauer, *Opt. Express* **2011**, *19*, 7020.

Received: June 1, 2015
Revised: July 16, 2015
Published online: October 5, 2015

RESEARCH ARTICLE

Technical feasibility study for production of tailored multielectrode arrays and patterning of arranged neuronal networks

Matthias Schürmann^{1,2*}, Norman Shephard^{3,4}, Natalie Frese⁵, Kevin Geishendorf⁶, Holger Sudhoff², Armin Gölzhäuser⁵, Ulrich Rückert⁴, Christian Kaltschmidt¹, Barbara Kaltschmidt^{1,7}, Andy Thomas^{3,6*}

1 Cell Biology, Bielefeld University, Bielefeld, Germany, **2** Department of Otolaryngology, Head and Neck Surgery, Klinikum Bielefeld, Bielefeld, Germany, **3** Center for Spinelectronic Materials and Devices, Physics Department, Bielefeld University, Bielefeld, Germany, **4** Cognitronics and Sensor Systems, Cognitive Interaction Technology Center of Excellence, Bielefeld University, Bielefeld, Germany, **5** Physics of Supramolecular Systems and Surfaces, Physics Department, Bielefeld University, Bielefeld, Germany, **6** Leibniz Institute for Solid State and Materials Research Dresden (IFW Dresden), Institute for Metallic Materials, Dresden, Germany, **7** Molecular Neurobiology, Bielefeld University, Bielefeld, Germany

* matthias.schuermann@klinikumbielefeld.de (MS); a.thomas@ifw-dresden.de (AT)



OPEN ACCESS

Citation: Schürmann M, Shephard N, Frese N, Geishendorf K, Sudhoff H, Gölzhäuser A, et al. (2018) Technical feasibility study for production of tailored multielectrode arrays and patterning of arranged neuronal networks. PLoS ONE 13(2): e0192647. <https://doi.org/10.1371/journal.pone.0192647>

Editor: Dario Pisignano, Universita del Salento, ITALY

Received: July 3, 2017

Accepted: January 26, 2018

Published: February 23, 2018

Copyright: © 2018 Schürmann et al. This is an open access article distributed under the terms of the [Creative Commons Attribution License](https://creativecommons.org/licenses/by/4.0/), which permits unrestricted use, distribution, and reproduction in any medium, provided the original author and source are credited.

Data Availability Statement: All relevant data are within the paper and its Supporting Information files.

Funding: This work was supported by the Ministry of Innovation, Science and Research (MIWF) of North Rhine-Westphalia with an independent researcher grant and by the Cluster of Excellence Cognitive Interaction Technology 'CITEC' (EXC 277) at Bielefeld University, which is funded by the German Research Foundation (DFG; <http://www.dfg.de>).

Abstract

In this manuscript, we first reveal a simple ultra violet laser lithographic method to design and produce plain tailored multielectrode arrays. Secondly, we use the same lithographic setup for surface patterning to enable controlled attachment of primary neuronal cells and help neurite guidance. For multielectrode array production, we used flat borosilicate glass directly structured with the laser lithography system. The multi layered electrode system consists of a layer of titanium coated with a layer of di-titanium nitride. Finally, these electrodes are covered with silicon nitride for insulation. The quality of the custom made multielectrode arrays was investigated by light microscopy, electron microscopy and X-ray diffraction. The performance was verified by the detection of action potentials of primary neurons. The electrical noise of the custom-made MEA was equal to commercially available multielectrode arrays. Additionally, we demonstrated that structured coating with poly lysine, obtained with the aid of the same lithographic system, could be used to attach and guide neurons to designed structures. The process of neuron attachment and neurite guidance was investigated by light microscopy and charged particle microscopy.

Importantly, the utilization of the same lithographic system for MEA fabrication and poly lysine structuring will make it easy to align the architecture of the neuronal network to the arrangement of the MEA electrode. In future studies, this will lead to multielectrode arrays, which are able to specifically attach neuronal cell bodies to their chemically defined electrodes and guide their neurites, gaining a controlled connectivity in the neuronal network. This type of multielectrode array would be able to precisely assign a signal to a certain neuron resulting in an efficient way for analyzing the maturation of the neuronal connectivity in small neuronal networks.

dfg.de/). The authors received this funding were (UR, NS).

Competing interests: The authors have declared that no competing interests exist.

Introduction

The characteristic feature of a neuron is its capability to generate and propagate action potentials. In this manner, these electrically excitable cells fulfill their main purpose by transmitting and processing information in the neuronal networks drawn through the organism (Fig 1A).

To study the mechanisms underlying the function of neurons, measurements of the action potentials from cells cultured in vitro can be carried out by various techniques, such as patch clamp or multielectrode arrays (MEAs). Patch clamp is a well-established technique, since Neher and Sakmann have introduced it in 1976 [1]. Even though there were many improvements introduced to this technique in the last decades, it still requires a lot of experience to be executed properly. Even though the patch clamp technique provides quantitative electrophysiological measurements of single cells or even ion channels, the measurements on many different neurons at exactly the same time is very difficult. In contrast, an analysis of several extracellular potentials from nerve cells in a network is possible with the MEA technique, which is easier to operate.

A bird's eye view of a MEA is provided in Fig 1C, showing its general structure. Fig 1B schematically shows the function of a MEA with its core elements, the electrodes on top of the glass substrate and a neuron in close contact to the electrodes with a narrow gap between electrode and neuron. Titanium (Ti, dark grey) and di-titanium nitride (Ti₂N, orange) are used here as the conductive materials for the electrodes. The blue layer is made of silicon nitride and insulates the conductive pathways from the majority of the cells. Even though the neuron is not in direct contact with the electrode, the extracellular potential in the gap between the

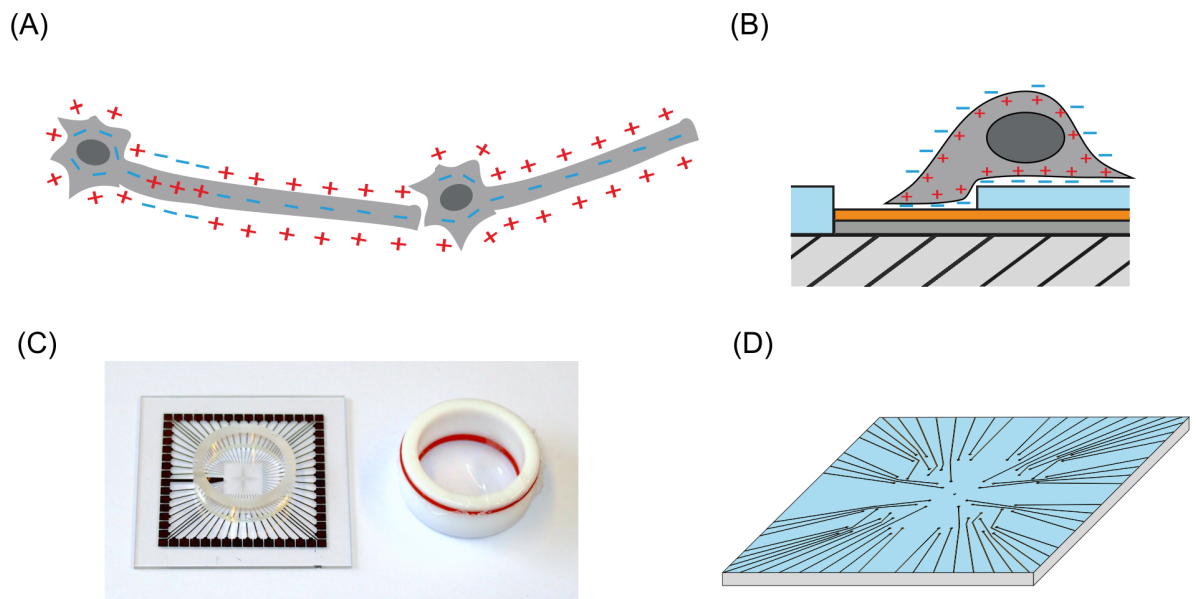


Fig 1. Schematic view on the multielectrode array technique. (A) Scheme of an action potential propagating along an axon of a neuron, which is connected to a neighboring neuron by a synapse. This composition represents the smallest unit of a neuronal 'network'. (B) Detection of an action potential by a MEA electrode. The hatched area is the underlying glass substrate. The dark grey and orange layers show the conducting path, which consist of a titanium layer (dark grey) and a di-titanium nitride layer (orange). The top layer (blue) is made of silicon nitride serving as an insulator. A neuron, which partly covers the MEA electrode, is depolarized. Capacitive coupling to the electrode surface, which is tightly covered by the cell membrane, transmits the extracellular potential. (C) Image of the multielectrode array. The 59 contact pads lead to the measuring electrodes in the center and one reference electrode. For cell cultures, a glass ring is glued to the top. To prevent contamination, e.g. with bacteria or fungi, a lid is placed on the glass ring and sealed with an O-ring. (D) A scheme of the electrodes and the conductive pathway in the center of the MEA layout with a triangular geometry.

<https://doi.org/10.1371/journal.pone.0192647.g001>

electrode and the neuronal membrane can be probed by the electrode [2, 3]. In most cases, the neurons do not cover the whole electrode (Fig 1B). Nevertheless it is known, that the detectable signal is proportional to the ratio of its overlap with the electrode-area [2]. Since this ratio is not accessible in most cases, MEA measurements only give access to information regarding the location and frequency of action potentials in neuronal networks. To make the MEAs suitable for cell culture experiments, a glass ring is glued on to the top of the MEA (Fig 1C).

Although the MEA technique was first described by Thomas et al in 1972 [4], this technique was rarely utilized until the 1990s. This was mainly due to the lack of micro structuring facilities and computer power. Today, several advantages of the MEA technology come into effect.

A benefit is that MEAs receive the action potentials in a non-invasive way, which allows the experimenter to investigate the development of a neuronal network without disturbance. This option is used in pharmaceutical research, where the effect of substances on a neuronal network can be examined without affecting the cells in culture. Alongside to drug discovery, basic research on the growth and development of neuronal networks can be accomplished with the MEA technique as well, reviewed by Stett and coworkers [5]. Another remarkable advantage of MEAs is the simultaneous analysis of multiple electrodes or neurons, respectively. This is necessary to enable studies of the interaction within in neuronal networks. Hence, MEAs were applied to study the development of networks from neural progenitor cells [6], the properties of inhibitory or excitatory neurons within a network [7], the growth of functional connectivity [8], or even the controlled development of hippocampal networks on patterned substrates [9]. In addition to the investigation of neuronal networks developed *in vitro* MEAs are broadly used to study neuronal networks developed *in vivo* under *ex-vivo* conditions, like organotypic hippocampal slices [10, 11], or even intact tissue, e.g. retina as described in [12]. A further advantage of MEA technique is the possibility to utilize one arbitrary electrode for electrical stimulation of the neuronal network and simultaneously examine the reaction of the neuronal network upon stimulation. Based on the mentioned properties, the MEA is a very good technique to study the development of neuronal networks by electrical stimuli as demonstrated by Jewett *et al.* [13]. In summary, the MEA is a convenient tool to investigate the development of growing neuronal networks with the possibility to record and stimulate electric signals from cells.

One major disadvantage of a standard MEA is that the position of the electrodes is fixed and cannot be adapted to the architecture of a specific neuronal network. To overcome this problem, the electrode density can be adapted to increase spatial resolution. When pursuing this strategy, it should be taken into account, that the signal generated by the extracellular potential is captured from every cell in the range of the electrode diameter. Thus, the diameter of electrodes should be scaled down with an increase in electrode density. These high resolution MEAs are used to analyze retinal ganglion cells [14] or other dense populations. New complementary metal-oxide-semiconductor (CMOS) based MEAs improve this technology by overcoming the major problem for high density MEAs, which lies in the limited number of contacts to external devices [15, 16]. Today, multiplexing allows an electrode amount of 26400 electrodes [17]. The analysis of the large data from these CMOS MEAs is still a topic of research [18, 19].

Another more elegant approach to analyze neuronal networks might be to prompt the neuron soma to adhere directly to the electrodes. It is established, that an adhesion promoting surface coating, e.g., with poly lysine, is necessary to enable the attachment and survival of neurons in culture [20]. Hence, an adhesion promoting, dot-like structure on top of the MEA electrodes would be preferable.

Patterning of coated surfaces to control neuronal adhesion via lithographic technique was first realized by [21]. In addition to photolithography, different methods of surface patterning

were developed. Corey and coworkers used laser ablation on poly lysine coated glass to locate neurons to a specific site [22]. Nowadays, the most common approach is the micro contact printing or soft lithography. During micro contact printing a polydimethylsiloxane stamp soaked with the cell adhesion molecule, is carefully pressed onto the sample surface [23]. More techniques are further described by Kane and colleagues [24]. Furthermore, structured poly lysine coating was already utilized to create artificial neuronal networks on MEAs [9]. This was accomplished with a rather coarse approach, not able to localize the cell soma to the electrodes.

In this study, we demonstrate a simple approach to produce tailored MEAs (cf. Fig 1D) with the aid of photolithographic devices and sputtering systems. Both devices are accessible as shared facilities of the science and engineering school in many universities and research institutions. Furthermore, we utilize the same lithographic device to create a structure of poly lysine, which is able to prompt the neurons somata to certain positions, and let their neurites extend in a systematic approach, which creates a defined network. The aim of this study is to determine the characteristics of a surface patterning regarding its geometry, which will support the localization of somata on the dots while preventing their localization on the connecting lines. Since we use the same laser lithographic device for structuring the MEA as well as the cell adhesive poly lysine pattern, an alignment of the electrode layout to the structure of the neuronal network can be easily accomplished. This kind of approach might answer one fundamental question in network simulations, e.g. the minimal required mechanism for one cell or synapse to work properly in neuronal networks.

Materials and methods

Multielectrode array fabrication

A square borosilicate glass (D263, Schott) with a side length of 49 mm and a thickness of 1.1 mm served as a substrate for the MEA. The glass was cleaned in an ultrasonic bath with acetone and subsequently with ethanol (Fig 2A). Afterwards, it was dried under a nitrogen stream. Positive Photoresist (AR-P 5350, AllResist) was spin-coated on the substrate for 60 seconds at 5000 rpm. In the following, the resist was cured on a hot plate for 4 minutes at 100°C (Fig 2B). The resist was exposed via a UV-laser lithographic system (DWL66, Heidelberg Instruments). The UV-lithography system was controlled via a computer aided design (CAD) file (.dxf file), which was drawn by a standard CAD program (AutoCAD). These exposed areas were dissolved with one part remover (AR 300–35, AllResist) diluted with two parts deionized H₂O (Fig 2C). Afterwards the sample was rinsed with H₂O for 30 seconds and dried with nitrogen. Subsequently, a 75 nm Ti layer was DC-sputtered on the surface via a self-build magnetron sputter deposition system (Fig 2D).

Patterned poly lysine surface coating

A poly lysine pattern was applied on top of a glass surface. First, the surface was cleaned with acetone in an ultrasonic bath for 15 minutes. Secondly, the sample was immersed in ethanol for about 30 seconds. Afterwards, the cleaned surface was treated with oxygen plasma for 30 seconds (self-build plasma etcher). Subsequently, the whole surface was coated via gas phase coating with 3-aminopropyltriethoxysilane (APTES, Sigma-Aldrich). For this purpose, the sample and an upwardly open vessel with 200 µL APTES were placed in a desiccator for 1 h, which was evacuated below 10 mbar. For the correct assembly of the APTES layer, the sample was deposited for 24 h in a normal lab atmosphere at room temperature. Afterwards, the sample was prepared for lithography with photoresist (AR-P 5350, AllResist) on a spin coater (5000 rpm, 60 seconds) and structured by UV-laser-lithography. Following this, the resist was

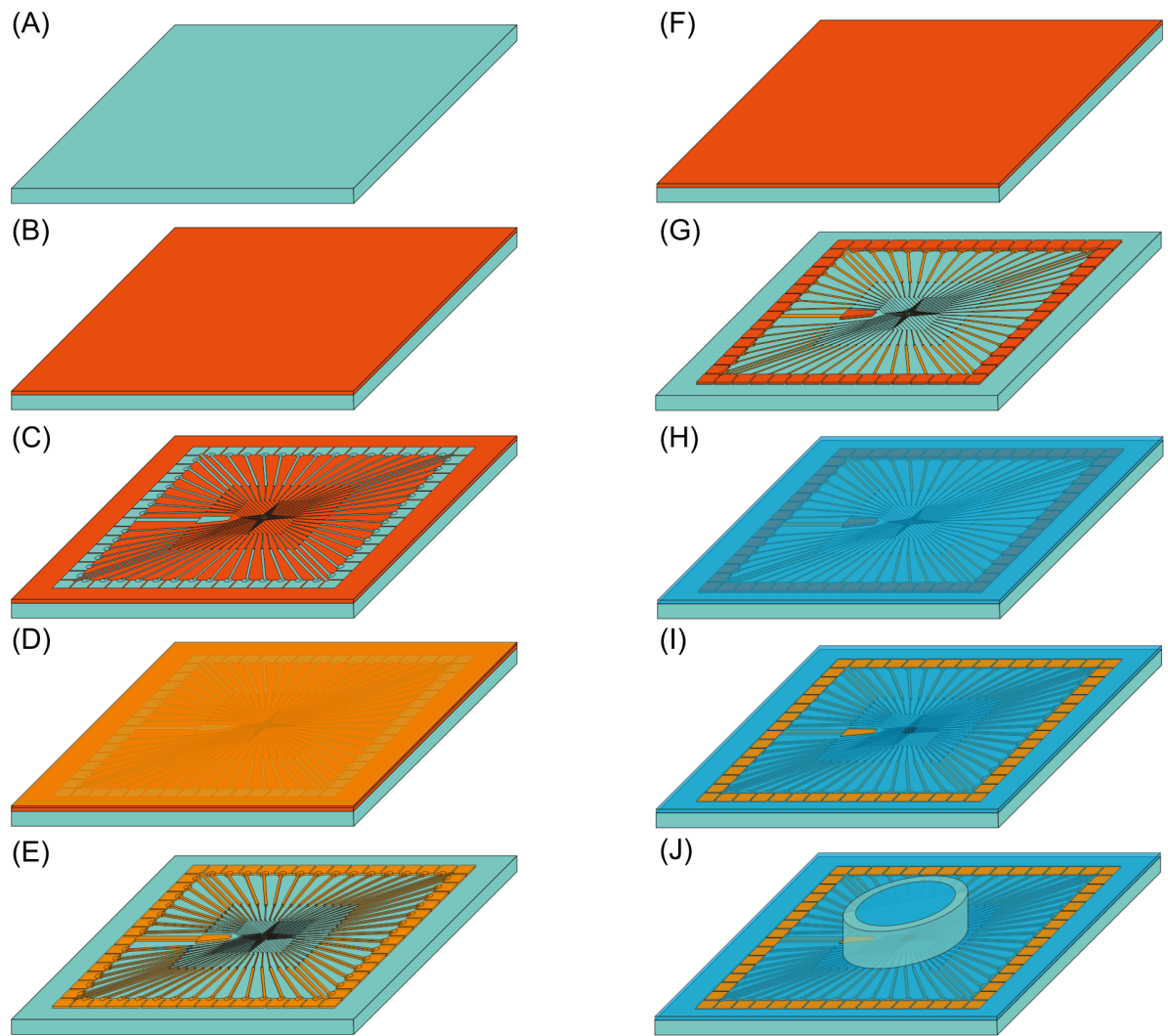


Fig 2. Fabrication strategy of our custom-made multielectrode array. (A) Cleaning of the glass substrate in acetone/ethanol in an ultrasonic bath. (B) Spin coating with positive photoresist, which is cured on a hot plate and then (C) exposed to a laser lithography system. Afterwards the exposed photoresist is removed with the dedicated chemical. (D) 100 nm thin layer of Ti is deposited via sputter deposition on the surface. Subsequently, a 25 nm layer of Ti_2N is deposited on top. (E) The excessive photoresist is removed in an ultrasonic bath in acetone. (F) and (G) show a second lithography step, processed like the first one, except the photoresist remains solely on the contact pads on the rim and the electrodes in the center. (H) 200 nm of silicon nitride is deposited via sputtering on top. (I) The remaining photoresist is removed in an ultrasonic bath. (J) For cell culture experiment a glass ring is glued to the top. Thereafter, a second 25 nm thick layer of di-titanium nitride was reactively sputtered on top. The excess photoresist was lift off in an ultrasonic bath with acetone. The sample was cleaned with ethanol afterwards. The processed sample consists of the glass substrate with Ti/ Ti_2N electrodes (Fig 2E). To insulate the conducting paths, a second lithography step was necessary. The sample was resist coated as stated before (Fig 2F). This time, a pattern was obtained, which covered the electrode in the middle and the contact pads at the rim of the MEA (Fig 2G). The alignment of the second lithography step was done manually with a micro camera within the UV-lithography system, which allows an accurate alignment of the structures. After resist development, a 200 nm insulating layer of silicon nitride was deposited on top via RF sputtering (radio-frequency sputtering, Fig 2H) and the photoresist was lift off (Fig 2I). Finally, a glass ring was glued to the top with silicone aquarium sealant to make the MEA suitable for cell culture experiments (Fig 2J).

<https://doi.org/10.1371/journal.pone.0192647.g002>

developed with one part AR 300–35 (AllResist) diluted with two parts deionized water. Finally, the sample was rinsed with deionized water and dried with nitrogen.

The sample surface, partly covered with the structured photoresist, was functionalized with a 6% glutaraldehyde (Sigma-Aldrich) solution in water. For this purpose, 300 μ L of the

solution was applied to the surface and the sample was stored at 4°C for 3 h. After washing with deionized water, the sample was coated with poly-d-lysine (PDL, MW = 1–5 kDa, Sigma-Aldrich) or fluorescein labeled poly-l-lysine (PLL-FITC, MW = 15–30 kDa, Sigma-Aldrich). For this purpose, 300 µL of a poly lysine solution (100 µg/ml in PBS, pH 8.0) was applied to the surface at 4°C for 16 h. Afterwards, the sample was washed several times with deionized water. Finally, the remaining photoresist was removed with acetone and ethanol in an ultrasonic bath. Because of this procedure, a checkered pattern with line widths of about 2.5 µm, 3 µm and 6 µm and dots of 30 µm diameters marking the nodes of the pattern were obtained (cf. [S1 Fig](#)).

Cell culture

Mouse hippocampal neurons were isolated and cultivated as described in [25], with approval of the Landesamt für Natur, Umwelt und Verbraucherschutz NRW, Germany (LANUV NRW, No. 8.87–50.10.43.08.105). In particular, mouse hippocampal neurons were obtained by dissecting the hippocampi from the cortex of a mouse in the embryonic stage E17.5. The hippocampi were enzymatically digested for 30 min at 37°C in 3 ml of a solution containing 0.05% trypsin and 0.02% EDTA. Afterwards, the trypsin was quenched with 1 ml Dulbeccos modified eagle medium (DMEM) containing 10% fetal calf serum (FCS), and the tissue was broken down mechanically by gently pipetting through a Pasteur pipette. Subsequently, the cell number in the obtained suspension was determined. Thereafter, the cell suspension was further diluted in DMEM containing 10% FCS and the cells were plated on the samples with a density of 3×10^4 cell/cm². The medium was changed to neurobasal medium containing 1% B27 1 h, 24 h after seeding and subsequently every third day.

Microscopy and sample preparation

Phase contrast images of living neuronal networks and structured collagen, and bright field images of MEA electrodes were obtained with a Zeiss Axiovert D1 microscope. The fluorescence imaging of the structured FITC-PLL coating was performed by confocal laser scanning microscopy (Zeiss LSM780). For the evaluation of the protein adsorption to the poly lysine pattern the substrates were incubated with a solution of DMEM containing 10% FCS and 1 µg/ml IgG Protein coupled with Alexa350 fluorophore at room temperature for 30 minutes. Afterwards, the samples were briefly rinsed with PBS, mounted with mowiol and examined using a confocal laser-scanning microscope (Zeiss LSM780). For immunocytochemistry, the cells were fixed with PBS containing 4% paraformaldehyde for 15 minutes. Subsequently, the neurons were permeabilized with 0.2% Triton X-100 in PBS for 10 minutes and incubated with a primary antibody against microtubule associated protein 2 (MAP2; rabbit, polyclonal, santa cruz, sc-20172) in phosphate buffered saline (PBS) at a concentration of 1 µg/ml at 4°C overnight. In the next step, the cells were incubated with PBS containing an appropriate secondary antibody coupled to Alexa647 at a concentration of 0.3 µg/ml at room temperature for 1 h. Finally, the slides were mounted with mowiol and examined using a confocal laser-scanning microscope (Zeiss LSM780). For helium ion microscopy (HIM) the samples were fixed in a solution of 4% glutaraldehyde and 4% paraformaldehyde in PBS at room temperature for 1 h. Subsequently, the samples were post-fixed with 1% osmiumtetroxide in PBS at room temperature for 30 minutes. After fixation, the samples were dehydrated in acetone and critical point dried via CO₂. Imaging was performed with the helium ion microscopy ORION PLUS from Zeiss [26] with an acceleration of 39.9 kV and a beam current of 0.2 pA. An electron flood gun was used to compensate the charging of the uncoated samples.

XRD and SEM

For an analysis of the sputtered electrode materials, x-ray diffraction (XRD, X'Pert Pro MPD, Philips) as well as scanning electron microscopy (SEM, Helios NanoLab DualBeam, FEI) were used. A layer stack of Ti and Ti₂N was sputtered on silicon, likewise to the conductive material for the MEA. The XRD reflexes are compared to calculated data from the ICSD (Inorganic Crystal Structure Database, Collection Code: 033715). To investigate the structure of the created layer stack, a fragment of the sample was severed to obtain a cross section image of the layers by SEM.

Electrophysiological measurement

The electrophysiological measurement was done with a MEA preamplifier (MEA1060 amplifier, MCS Reutlingen), as well as an external power supply (PS40W, MCS Reutlingen). We grab our signal over the 64-channel signal divider (SD64, MCS Reutlingen) and record one channel at a time via a multimeter with internal data acquisition (Keithley 2701/e, Keithley Instruments). The acquired data was read out with the aid of self-programmed data acquisition software. Finally, the signal was processed by a data analyzing software (OriginPro 2016) and fast-fourier filtered through a high pass with a cut off at 55 Hz. During noise measurements we compared the results between the self-built MEAs and commercial available MEAs (60MEA200/30iR-Ti, MCS Reutlingen) having the same electrode composition, metric and geometry.

Results

MEA fabrication and design

We fabricated MEAs in two different layouts, shown in Fig 3. We produced a standard layout often used in MEA set-ups with electrodes in a rectangular pattern. In Fig 3A, the CAD file for the first lithography step of a standard MEA layout with 59 electrodes is shown. The electrodes have 30 μm diameters and are spaced 200 μm from the neighboring electrodes. A conducting track links each electrode to one of 60 contact pads, which can be seen in Fig 1C. The one remaining contact pad is connected to the grounded reference electrode, needed to measure the potentials applied to the 59 measuring electrodes with respect to the ground. The conducting track is 10 μm wide and expands its width to 100 μm close to the contact pad. Fig 3B shows a microscopic image of the self-fabricated rectangular MEA. Fig 3C shows a MEA design based on a triangular layout. The baseline is 200 μm and the electrode diameter is 30 μm. Fig 3D shows a microscopic image of the produced triangular MEA. The flexibility to produce the proper MEA according to the experiment is a key feature of the CAD controlled laser lithographic system.

We used SEM for structure examination of the sputtered electrode layers, as well as XRD for analysis of the crystalline structure and the chemical composition of the two layers. The SEM image (Fig 4A) revealed a Ti₂N layer, exhibiting its typical columnar morphology on top of the homogenous Ti layer. Further examination of the layer stack system by XRD (Fig 4B) revealed the first (200) reflex of Ti₂N at 36.025° and the second (400) reflex at 76.425°. This is in accordance with the calculated reflectivity for tetragonal Ti₂N (calculated from ICSD using POWD-12++, (1997)). The Ti layer showed reflexes at 38.175° representing the (002) orientation of Ti.

To test the performance of our self-built MEAs, a neuronal culture from hippocampal mice neurons was cultured on the self-built rectangular MEA. The electrophysiological measurement in Fig 5A depicts a recording of the culture after 3 days *in vitro* (DIV3). Several spikes

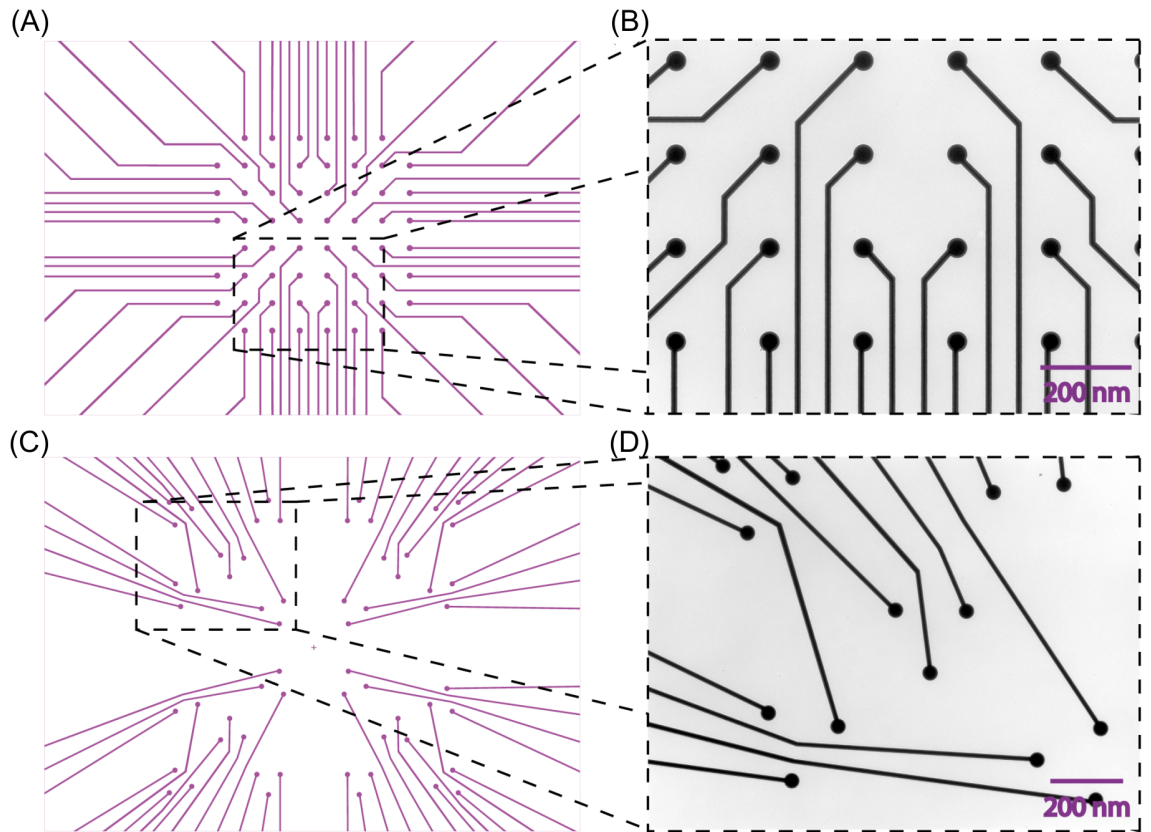


Fig 3. Design of multielectrode arrays. (A) and (C) show the central part of the CAD generated printout used to control the laser lithography system. The layout corresponds with the later conducting titanium and di-titanium nitride tracks with dot-like electrodes at the end. (A) Shows a standard rectangular layout with 200 μm distances between the electrodes. (B) The area in the black dashed box is shown as a bright field microscopic image of a MEA produced by this layout. Picture (C) is a custom-made design for a MEA. In this case, triangles with a base of 200 μm are used for the positioning of the electrodes. Image (D) shows the corresponding bright field microscopic image of the custom made MEA layout.

<https://doi.org/10.1371/journal.pone.0192647.g003>

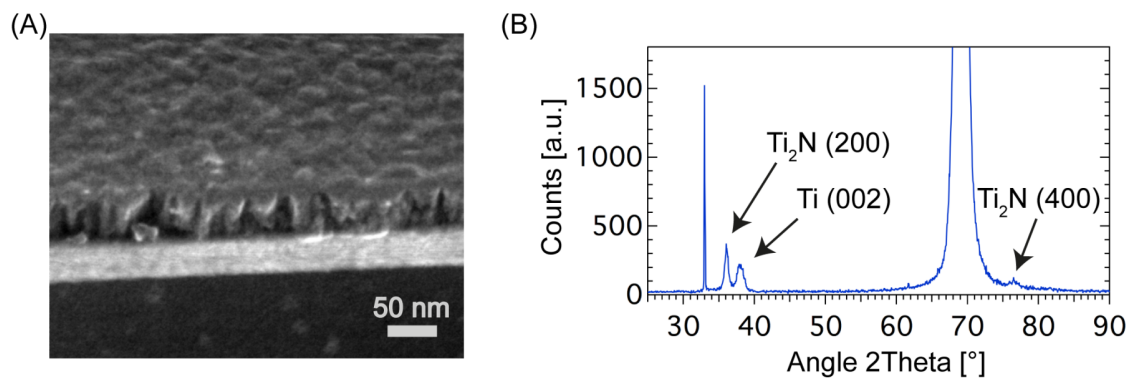


Fig 4. Electrode material characterization. (A) A SEM picture of a silicon substrate coated with layers of 40 nm titanium and 40 nm di-titanium nitride (Ti_2N). The Ti_2N crystals grow in characteristic columns. (B) X-ray diffraction (XRD) measurement from the same sample. Distinctive reflexes of Ti_2N and the underlying Ti layer are detectable.

<https://doi.org/10.1371/journal.pone.0192647.g004>

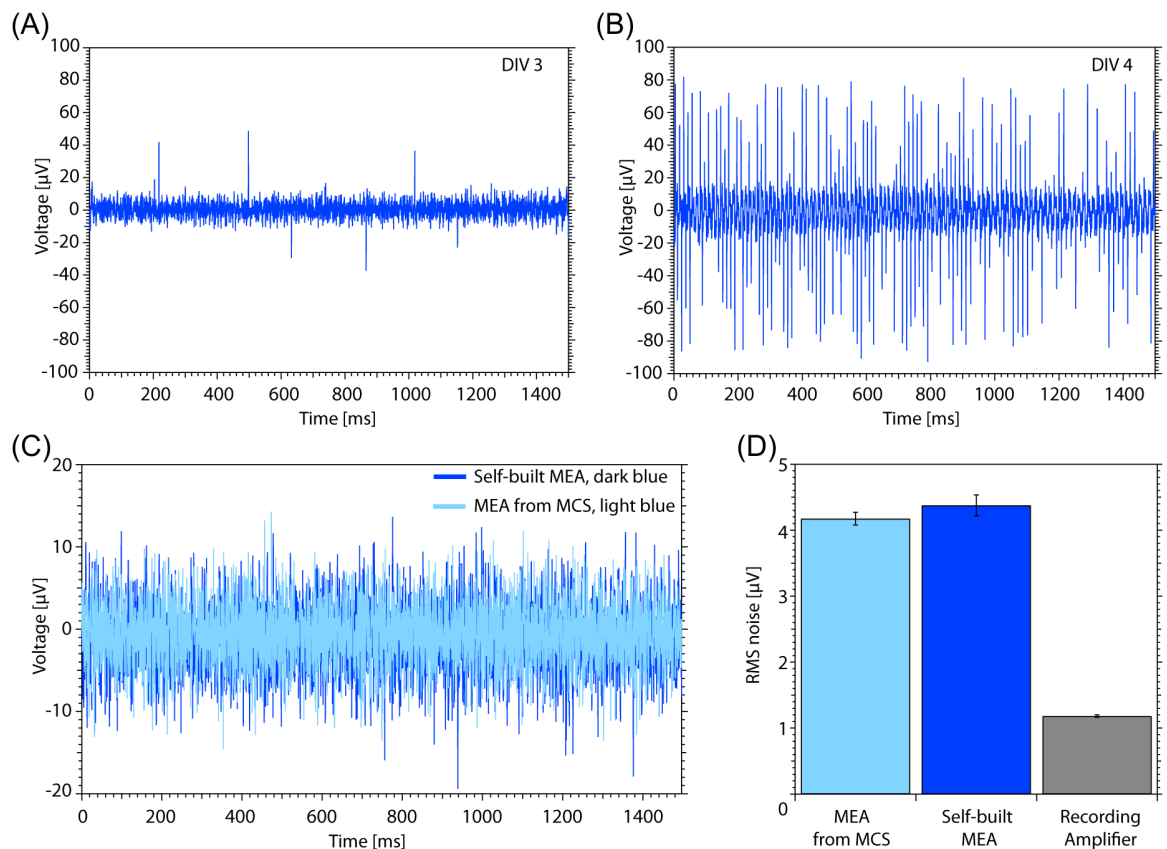


Fig 5. MEA measurements. (A) Measurement from a DIV3 neuron culture on the self-built MEA with rectangular layout show a few signals above the noise level. (B) A measurement on the same culture and electrode after DIV4. Accompanied with the progress in maturation, the spiking activity is visibly increasing. (C) Noise measurement of one electrode of the self-built MEA (dark blue) and a commercial available MEA from MCS, Reutlingen (light blue). (D) Comparison of the RMS noise values of the self-built MEA and the MEA from MCS (mean for 6 electrodes with standard deviation). The RMS noise of the self-built MEA is not significantly higher compared to the commercially available MEA from MCS. The noise measurement of the recording amplifier setup is below 1.2 μV and does not contribute significantly to the measured MEA noises.

<https://doi.org/10.1371/journal.pone.0192647.g005>

rise above the noise level with amplitudes of up to 40 μV . In Fig 5B, the same measurement performed after DIV4 is shown. The spiking activity is much higher than before. The noise measurement has been executed on plain MEAs without a neuronal culture, but with PBS in the culture chamber. In Fig 5C the noise of one electrode from our self-built MEA (dark blue) is compared to the commercially available one from the company MCS (light blue). We calculated the root mean square (RMS) noise for 6 arbitrary electrodes of each MEA and determined their mean (cf. Fig 5D). The commercially available MEA displays a RMS noise of $3.85 \pm 0.09 \mu\text{V}$, for our self-built MEA we calculated a RMS noise value of $4.04 \pm 0.15 \mu\text{V}$, demonstrating no significant difference to the commercially available MEA. The measured noise generated by the amplifying and recording setup does not contribute substantial to the overall noise.

Structured poly lysine coating

Usually, the MEA is coated homogenously with molecules supporting the adhesion and maturation of neurons to the substrate, e.g. poly lysine or polyethylenimine (PEI). Fig 6 shows

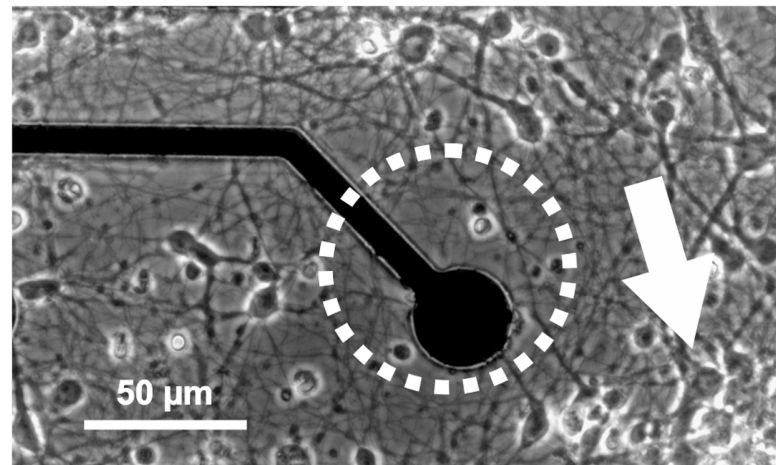


Fig 6. Hippocampal mouse neurons grown on custom made multielectrode array. Mouse neurons grown on a custom made MEA coated with PDL attach to the substrate in an anisotropic manner, with regions of higher (arrow) and lower (circle) cell density. Furthermore, the neurites exhibit no preferred direction of growth, resulting in an arbitrary neuronal connectivity.

<https://doi.org/10.1371/journal.pone.0192647.g006>

hippocampal mouse neurons grown on a custom made MEA coated with physically attached poly lysine. The cell density differs from region to region. In the dashed circle marks a low cell density area, at the arrow a cell cluster with high density can be observed.

The electrode seen in Fig 6 is not assigned to a single defined cell. A structured poly lysine coating as described in Fig 7 can be utilized to solve this problem. For this purpose, spots of lysine with a size allowing only one cell to adhere should be coated with poly lysine. In addition, small poly lysine lines are arranged between the spots, aiding the neurite guidance.

To understand the necessity of the covalent bonding of poly lysine, it must be taken into consideration that the coated sample has to be placed in acetone in an ultrasonic bath in order to remove the remaining photoresist (cf. Fig 7). Fig 8B shows a sample with poly lysine physically bound to the entire surface and cleaned in an ultrasonic bath in acetone. Compared to Fig 8C, where the same physically bound poly lysine surface is only rinsed with water, 8B shows nearly no adhered neurons on the sample, while the surface shown in 8C exhibits a well-developed neuronal network after DIV4. Hence, the physical bonding is not sufficient for an application in the utilized lithography process. To overcome this challenge, it is necessary to bind the poly lysine covalently to the sample surface (cf. Fig 8A).

To examine the quality of the surface coating, several imaging methods were utilized for verification. Initially, we obtained fluorescence images from the PLL-FITC coupled to the poly lysine (Fig 8A). The dot like structure was easily detectable and was measured to have a diameter of 30 μm , which is sufficient to promote the cell adhesion of a neuronal soma. Furthermore, thin lines of poly lysine connecting the single cell adhesion spots for neurite guidance have a width of approximately 2.5 μm .

To verify the adhesion promoting characteristics of the substrates, we tested its protein adsorption properties. For this purpose, we incubated the patterned substrates with a solution containing fluorescently labeled proteins. The poly lysine pattern demonstrated a much higher protein adsorption capability compared to the overall APTES background (Fig 9B).

Finally, we tested the developed substrates in a cell culture experiment (Fig 9C). The neuronal culture showed a high degree of arrangement on the substrate. The majority of the cell somata were located on the junctions of the checkered pattern, where poly lysine spots of

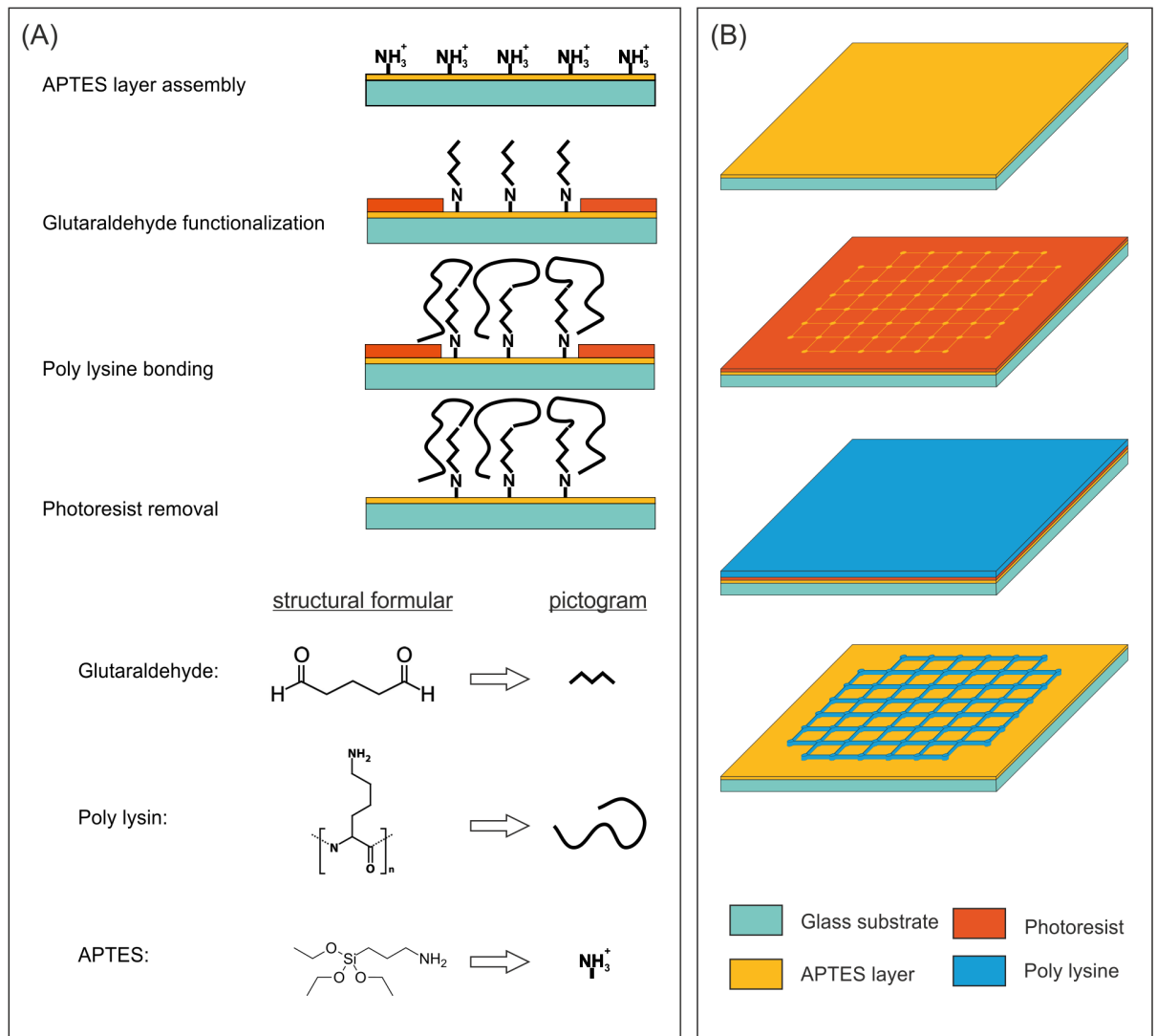


Fig 7. Poly lysine pattern fabrication for arranged neuron growth. (A) Provides the chemical process to gain a covalently bound poly lysine coating. The surface of the glass substrate is cleaned with acetone/ethanol in an ultrasonic bath. Afterwards the surface is etched with oxygen plasma to introduce hydroxyl groups to the surface. This surface is coated with a self-assembled layer of (3-Aminopropyl)triethoxysilane (APTES; yellow). After laser lithography, a layer of structured photoresist (orange) masks parts of the APTES layer. The next step is a treatment with glutaraldehyde to functionalize the surface. Following the washing of the sample with deionized water, the surface is treated with poly lysine and the sample is washed again. During this step, the poly lysine is covalently bound to the sample. Afterwards, the excess photoresist is removed with acetone in an ultrasonic bath. Finally, the substrate is decorated with a defined pattern made of poly lysine on an overall APTES grounding. (B) Schematically demonstrates the results of the chemical process for an applied pattern. After cleaning and plasma etching, the surface is coated with an APTES layer (yellow). Afterwards, the UV-laser lithography is performed; the orange layer is made of patterned photoresist. Glutaraldehyde and poly lysine are applied on top as described before. After washing the sample and removing the remaining photoresist with acetone in an ultrasonic bath, a pattern of covalently bound poly lysine remains on top of the sample.

<https://doi.org/10.1371/journal.pone.0192647.g007>

30 μm diameter provided enough space to allow their cell soma to attach. On the other hand, the thin lines of poly lysine connecting the spots provided enough space for the neurites to develop their mature morphology.

We further investigated the development of the neuronal network on the patterned substrates. For this purpose, we fixed neurons 18 hours, 3 days and 8 days after cell-seeding and stained the cells for MAP2, a marker for neuronal maturation. It appeared that the neurons

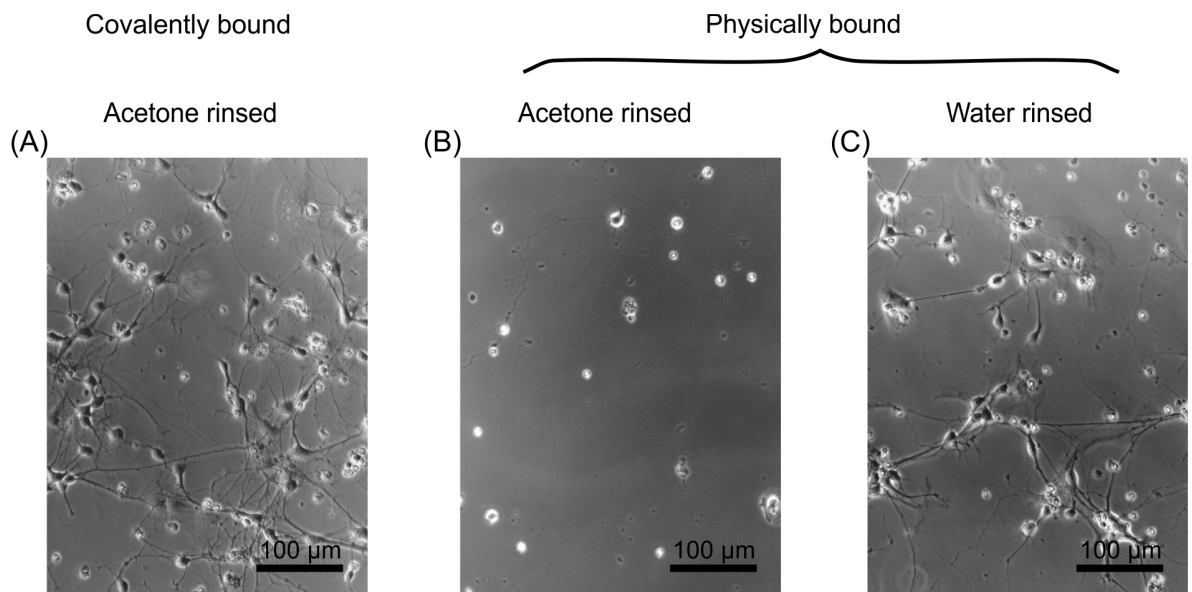


Fig 8. Hippocampal mouse neurons (DIV4) on differently coated substrates. (A) The substrate is furnished with covalently bound poly lysine. In (B) and (C) the poly lysine coating was solely physically adsorbed. The surfaces shown in (A) and (B) were cleaned in acetone in an ultrasonic bath while (C) was only rinsed with H₂O. In contrast to (A) and (C), (B) shows no poly lysine attached to the substrate to promote the cell adhesion and neurite outgrowth. Therefore, a covalent attachment of poly lysine is necessary to obtain a structured poly lysine coating after acetone treatment during the lithographic process.

<https://doi.org/10.1371/journal.pone.0192647.g008>

adhere to the substrate after initial attachment in a rather arbitrary manner (Fig 10A). However, they showed a high tendency to send out protrusion to the poly lysine pattern and allegedly started to migrate towards the coated surface. After three days in culture, most of the neurons had migrated towards the nodes at the junctions of the pattern (Fig 10B). The 30 µm dots seemed to be more attractive for the attachment of their soma compared to the thin lines with a width of about 3 µm. Presumably, the dots provided enough space to host the somata (which have a diameter of approximately 15 µm) without restricting its development in any

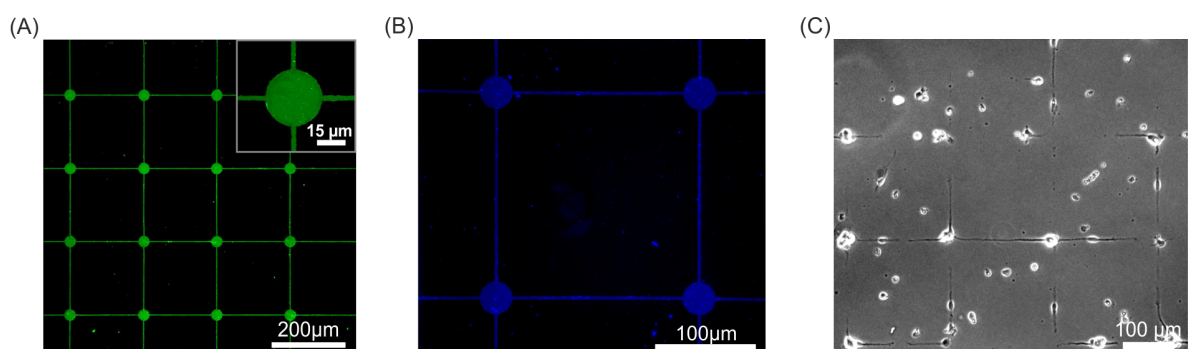


Fig 9. Covalent attachment of structured PDL is sufficient to induce an arranged attachment of neuronal cells and a directed outgrowth of their neurites. (A) Fluorescence microscopic image of structured poly lysine coupled to PLL-FITC. The homogenous distribution of the poly lysine is visualized as well as the 30 µm diameter of the dots and the 2.5 µm thickness of the lines connecting the dots (cf. inset). (B) Fluorescence microscopic image of the structured poly lysine coated surface with adsorbed fluorescently labeled proteins. The applied coating offers a much higher adhesiveness to proteins compared to the uncoated regions of the surface. (C) Phase contrast image of hippocampal mouse neurons grown for three days on the structured poly lysine coating. The neuronal somata tend to adhere to the circles marking the junctions of the checked pattern, while the lines connecting these circles guide the neurites.

<https://doi.org/10.1371/journal.pone.0192647.g009>

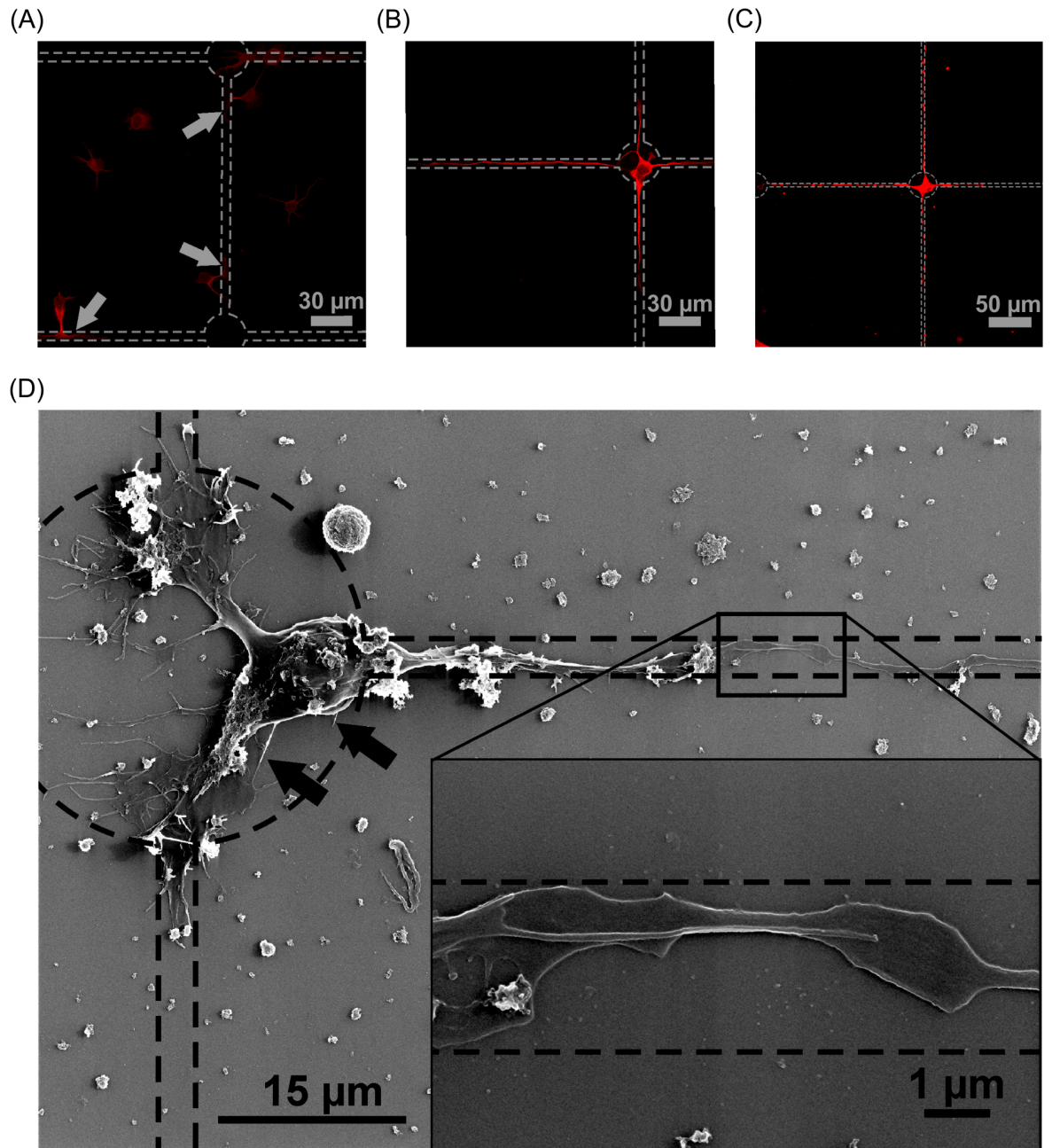


Fig 10. The processes involved in the controlled attachment and neurite outgrowth of the neurons on patterned substrate. Neurons are immuno-fluorescently labeled for the protein MAP2, a marker for neuronal maturation. The dashed lines indicate the poly lysine pattern. (A) 18 hours after cell-seeding the neurons have attached to the substrate in a rather arbitrary manner and are attracted by the poly lysine coated surface, notable by the protrusions attached to poly lysine (arrows). (B) After DIV3 the somata of the neurons are mainly located on the dots on the nodes of the checked poly lysine pattern (cf. Fig 9). Furthermore, their neurites are well developed and the translation of MAP2 is upregulated. (C) Even after DIV8 the somata stayed attached to the nodes and the neurites were further elongated, reaching into the neighboring node (arrowhead). (D) HIM image of a neuron seeded on an equal poly lysine pattern. The tight adherence of the soma is visible by adhesion protrusions (arrows). Investigation of the guided axon (inset) elucidated that the axon is tightly bound to the substrate by well-developed lamellar protrusion (arrowheads).

<https://doi.org/10.1371/journal.pone.0192647.g010>

direction (Fig 10D). Furthermore, the neurons showed an upregulation of MAP2 and a well-developed morphology of mature neurons with their neurites spanning over hundred micrometers. Even after DIV8 the soma of the neurons stayed attached firmly to the nodes, demonstrating the durability of the covalently bound coating. During the progress in neuronal maturation, the neurites further elongated to a length of up to 200 μm , reaching into the neighboring node.

The localization of a soma on the node after DIV3 could also be demonstrated on similar pattern by HIM (Fig 10D). The soma showed a well-developed native morphology and adhered firmly to the poly lysine node as demonstrated by the filopodia-like protrusions. High resolution images of the axon grown along the poly lysine lines show a tight adherence of the neurite to the substrate. This is manifested by lamellar extension arising from the axon (cf. inset Fig 10D). Furthermore, HIM demonstrated that thick lines with a width of approximately 6 μm provide enough area for neurons to adhere (Fig 11B). The neuron can be localized either on the lysine node or the lysine line with an elongated soma, as shown in Fig 11B. This is in

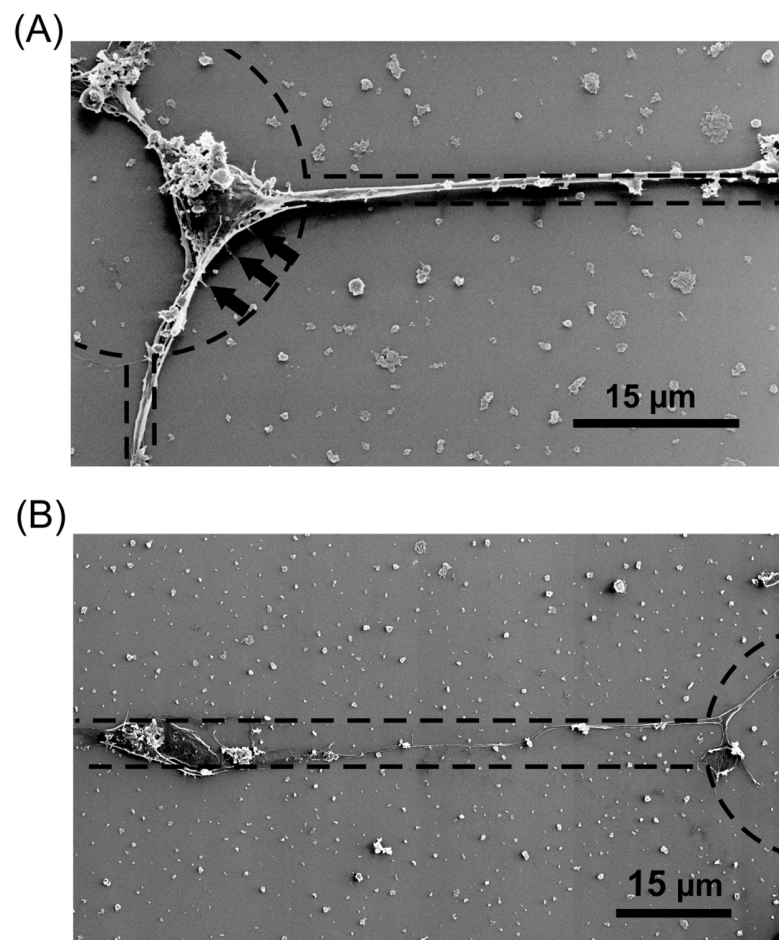


Fig 11. Line width dependence of neuronal soma adhesion to poly lysine lines. HIM image shows a neuron grown on lines with a width of about 2.5 μm (A) and 6 μm (B). The dashed lines indicate the poly lysine pattern. The neuron on the poly lysine pattern with thin line (A) is tightly adhered to the node of the checkered pattern as visualized by adherence promoting protrusion (arrows). In contrast to that the soma of a neuron adhered to a wider poly lysine line (B) stays fixed on the line and is not directed to migrate to the node of the checkered poly lysine pattern.

<https://doi.org/10.1371/journal.pone.0192647.g011>

strong contrast to cells seeded on substrates with line widths of about $2.5\ \mu\text{m}$ (Fig 11A), which prompted the soma to localize on the nodes, as already demonstrated.

Discussion

We demonstrate an opportunity to equip MEAs with chemical coating to enable electrophysiological measurements on an arranged neuronal network. The presented method for customized production of MEAs using laser UV-lithography offers a row of advantages. Compared to standard contact lithography, no photomask is needed for the laser lithography. This is advantageous in terms of the processing rate of our MEA production process, since several lithographic applications are required and a manual alignment of different masks would otherwise be necessary during every step. Besides, laser lithography works on several length scales. The smallest printable feature is approximately $1\ \mu\text{m}$ in size. The area printed during the first lithography step is about $39\ \text{mm}$ by $39\ \text{mm}$. The major advantage is easy adaptability of the CAD controlled laser lithographic system used in this study. This enables an easy alteration and high flexibility of the MEAs layout. This is of utmost importance in basic research where experimental setup changes frequently. In this context, layouts with two different electrode arrangements and an electrode diameter of $30\ \mu\text{m}$ with an electrode spacing of $200\ \mu\text{m}$ were chosen. For example, further downscaling of the electrodes can easily be achieved with the described methods, but the electrode spacing should be altered simultaneously, with respect to the range of the received signals.

In our MEA design, we used a layered system of Ti and Ti_2N as conductive materials. The biocompatible Ti_2N is deposited on top of the Ti and serves as passivation. This is necessary, since titanium tends to oxygenate to amorphous titanium oxide with insulating characteristics to a depth of about $3\ \text{nm}$ [27]. This will result in non-uniform electrical properties of the surface, which will tend to change upon contact with cell culture media [28], making it difficult to compare signals from different electrodes. Besides its protective function, Ti_2N is known to form a columnar microstructure, hence reducing the impedance of the electrodes. This will reduce their thermal noise in comparison to even Ti electrodes [29] and enhance charge transfer capability [30]. Silicon nitride is used as the insulating material on top of the MEA, its transparency making it suitable for microscopic investigation of the neurons cultured on the MEA. Furthermore, its hardness helps to protect the delicate conductive structure from scratches during cell culture processing. Electrophysiological measurements of the RMS noise from the self-built MEA and a commercial available MEA from Multichannelsystems shows no significant difference. Importantly, our electrophysiological measurements of cultivated neurons demonstrate the capability of the self-built MEA to distinguish between voltage peaks generated by action potentials and the overall noise. This is of particular interest, since the presented custom built MEAs cost around 10% of commercial available MEAs. Considering that many researchers nowadays have access to lithographic and sputtering devices, our approach offer a cost-effective alternative, which also can be tailored to the actual researcher needs.

The developed method for the patterning of adhesion molecules can be applied for direct attachment of neurons to the MEA electrodes. Buitengeweg *et al.* demonstrated that the localization of neurons on top of the electrodes will lead to an increase in the signal to noise ratio [3]. More importantly, since only one neuron is in the receiving range of an electrode, an assignment of a signal to one specific neuron would be feasible. To achieve this key point, cage-like shapes on top of MEA electrodes were applied [31]. A far more convenient method is to apply a pattern made of molecules promoting the adhesion of cells on the electrodes. This method was realized by micro contact printing [9] or photolithography [32] with the aid of the well characterized adhesion molecule poly lysine. Our approach utilized UV-laser lithography in

combination with the covalent binding of the poly lysine. The covalent binding will make the overall coating not only resistant to lithographic processing steps involving acetone (cf. Fig 8), but it will also allow the poly lysine structure to stay defined under cell culture conditions and more adhesive compared to physisorbed poly lysine [32]. In our experiments, this could be demonstrated by long lasting confinement of the soma to the nodes (cf. Figs 10C and 11A). This covalent binding can also be achieved with different adhesion promoting molecules, as long as they contain amine groups, like PEI [33] or poly ornithine [34]. In addition, proteins that can withstand the denaturing conditions of the coating process, could be used as well, e.g. collagen (cf. S2 Fig), which had been long known for promoting neuronal adhesion [35]. With the localization of a single neuronal cell on top of an electrode, it should be possible to count the generated action potentials of this particular neuron. This is of great interest, when the metabolism of a single neuron needs to be studied, which can be measured by Matrix-assisted laser desorption/ionization time-of-flight (MALDI-TOF) mass spectroscopy on arrayed dead cells [36] or even on living cells *in vitro* by fluorescence microscopic means [37].

To study the development of a neuronal network, a second task has to be managed: the guidance of the neurites. The structured coating of covalently bound poly lysine was already utilized to create artificial neuronal networks [32]. In this study, the chosen line width was too big (20 μm) and hence no localization of the soma to the nod was observable. The structuring of proper poly lysine pattern with micro contact printing [38] has its difficulty, because it is complicated to produce lines thin enough to fulfill the mentioned needs. In the study of Boehler *et al.* from 2012, [9] the rather low resolution of the utilized micro contact printing, resulted in a line width of only 10 μm , which made it impossible to locate the neuronal soma on the nodes of the intersecting lines. We decided to use UV-laser lithography, because thin lines can be easily structured by this technique. Neurite guidance can be accomplished with 2.5 μm wide lines of adhesion molecules connecting the electrodes. The thickness of this structure must be balanced between large enough to ensure neurite growth and small enough to prohibit the adhesion of soma on the lines. We could observe that poly lysine lines with a thickness of 6 μm were not sufficient to force the soma to be located on the nodes. This finding is in accordance to previous studies [39] focusing on the same issue.

Furthermore, we established a technique to align the cultured neuron on a surface with the aid of structured cell adhesion molecules to make the MEA suitable to study the development of neuronal networks on a single cell level. In the study of Boehler *et al.* from 2012, micro contact printing was utilized to create artificial neuronal networks on MEAs [9], but the difficult positioning of the micro contact stamp prohibited an exact alignment of the poly lysine structure to the MEA [9, 40–47]. An advantage of the UV-laser lithographic structuring of the poly lysine pattern described in this paper is the feasible alignment of the adhesive pattern to an electrode array structured with the same lithographic device. Furthermore, the method presented in this study, the CAD file for the MEA can be reused offhand for structuring the poly lysine pattern with few modifications. Hence, the adhesion pattern can be designed to match each self-built MEA individually. This can be utilized in future studies to perform research on well-defined neuronal networks with directed neurite maturation. Further designs might match to the self-built triangular MEAs, so that defined neural logics of three neurons can be studied. To focus on the interplay in simple networks, understanding of the basic rules of large neuronal networks can be accomplished. In this manner, Pershin *et al.* [48] demonstrated the formation of associative memory with three electronic neurons. Similar experiments could be executed with living neurons *in vitro*.

Since the presented strategy of axon guidance is biocompatible and, due to the covalent bonding, long lasting, it could be applied to support directional growth of axons, which is crucial for peripheral nerve regeneration. Therefore, findings from this work could be extended to

an *in vivo* situation to aid peripheral nerve regeneration after injury or to improve integration of electrodes from retinal implants or other neuroprosthetic devices.

Supporting information

S1 Fig. Structures with different line width. Confocal laser scanning microscopic image of PLL-FITC labeled poly lysine pattern. The three different line width of 6 μm (A), 3 μm (B) and 2.5 μm (C) are easily distinguishable.

(TIF)

S2 Fig. Layer of covalently attached structured collagen is visualized by phase contrast microscopy. Phase contrast image of collagen covalently attached to the surface with the same pattern design used for the poly lysine coated samples. The procedure to fabricate this collagen sample follows the method for the patterned poly lysine coating except the use of collagen instead of poly lysine. Despite the collagen sample in the image was threatened with acetone in an ultrasonic bath during fabrication, the collagen pattern is still on top. The dots have 30 μm diameter and the connecting lines are 2.5 μm wide.

(TIF)

Acknowledgments

We acknowledge support for the Article Processing Charge by the DFG and the Open Access Publication Fund of Bielefeld University.

Author Contributions

Conceptualization: Matthias Schürmann, Norman Shepherd, Christian Kaltschmidt, Andy Thomas.

Data curation: Matthias Schürmann, Norman Shepherd, Natalie Frese.

Formal analysis: Matthias Schürmann, Norman Shepherd, Andy Thomas.

Funding acquisition: Holger Sudhoff, Armin Götzhäuser, Ulrich Rückert, Barbara Kaltschmidt, Andy Thomas.

Investigation: Matthias Schürmann, Norman Shepherd, Natalie Frese, Kevin Geishendorf, Christian Kaltschmidt, Andy Thomas.

Methodology: Matthias Schürmann, Norman Shepherd, Natalie Frese, Kevin Geishendorf.

Project administration: Andy Thomas.

Supervision: Holger Sudhoff, Armin Götzhäuser, Ulrich Rückert, Christian Kaltschmidt, Barbara Kaltschmidt, Andy Thomas.

Validation: Matthias Schürmann, Norman Shepherd, Holger Sudhoff, Armin Götzhäuser, Ulrich Rückert, Christian Kaltschmidt, Barbara Kaltschmidt, Andy Thomas.

Visualization: Matthias Schürmann, Norman Shepherd, Natalie Frese, Kevin Geishendorf.

Writing – original draft: Matthias Schürmann, Norman Shepherd, Natalie Frese, Holger Sudhoff, Armin Götzhäuser, Ulrich Rückert, Christian Kaltschmidt, Barbara Kaltschmidt, Andy Thomas.

Writing – review & editing: Matthias Schürmann.

References

1. Neher E, Sakmann B. Single-channel currents recorded from membrane of denervated frog muscle fibres. *Nature*. 1976; 260(5554):799–802. Epub 1976/04/29. PMID: [1083489](#).
2. Buitengeweg JR, Rutten WL, Marani E. Modeled channel distributions explain extracellular recordings from cultured neurons sealed to microelectrodes. *IEEE transactions on bio-medical engineering*. 2002; 49(12 Pt 2):1580–90. Epub 2003/01/29. <https://doi.org/10.1109/TBME.2002.805555> PMID: [12549740](#).
3. Buitengeweg JR, Rutten WL, Marani E. Geometry-based finite-element modeling of the electrical contact between a cultured neuron and a microelectrode. *IEEE transactions on bio-medical engineering*. 2003; 50(4):501–9. Epub 2003/05/02. <https://doi.org/10.1109/TBME.2003.809486> PMID: [12723062](#).
4. Thomas CA Jr., Springer PA, Loeb GE, Berwald-Netter Y, Okun LM. A miniature microelectrode array to monitor the bioelectric activity of cultured cells. *Experimental cell research*. 1972; 74(1):61–6. Epub 1972/09/01. PMID: [4672477](#).
5. Stett A, Egert U, Guenther E, Hofmann F, Meyer T, Nisch W, et al. Biological application of microelectrode arrays in drug discovery and basic research. *Analytical and bioanalytical chemistry*. 2003; 377(3):486–95. Epub 2003/08/19. <https://doi.org/10.1007/s00216-003-2149-x> PMID: [12923608](#).
6. Stephens CL, Toda H, Palmer TD, DeMarse TB, Ormerod BK. Adult neural progenitor cells reactivate superbursting in mature neural networks. *Experimental neurology*. 2012; 234(1):20–30. Epub 2011/12/27. <https://doi.org/10.1016/j.expneurol.2011.12.009> PMID: [22198136](#).
7. Becchetti A, Gullo F, Bruno G, Dossi E, Lecchi M, Wanke E. Exact distinction of excitatory and inhibitory neurons in neural networks: a study with GFP-GAD67 neurons optically and electrophysiologically recognized on multielectrode arrays. *Frontiers in neural circuits*. 2012; 6:63. Epub 2012/09/14. <https://doi.org/10.3389/fncir.2012.00063> PMID: [22973197](#).
8. Downes JH, Hammond MW, Xydias D, Spencer MC, Becerra VM, Warwick K, et al. Emergence of a small-world functional network in cultured neurons. *PLoS computational biology*. 2012; 8(5):e1002522. Epub 2012/05/23. <https://doi.org/10.1371/journal.pcbi.1002522> PMID: [22615555](#).
9. Boehler MD, Leondopoulos SS, Wheeler BC, Brewer GJ. Hippocampal networks on reliable patterned substrates. *Journal of neuroscience methods*. 2012; 203(2):344–53. Epub 2011/10/12. <https://doi.org/10.1016/j.jneumeth.2011.09.020> PMID: [21985763](#).
10. Singec I, Knoth R, Vida I, Frotscher M. The rostral migratory stream generates hippocampal CA1 pyramidal-like neurons in a novel organotypic slice co-culture model. *Biology open*. 2015; 4(10):1222–8. Epub 2015/09/06. <https://doi.org/10.1242/bio.012096> PMID: [26340944](#).
11. Kleczkowska P, Kawalec M, Bujalska-Zadrozny M, Filip M, Zablocka B, Lipkowski AW. Effects of the Hybridization of Opioid and Neurotensin Pharmacophores on Cell Survival in Rat Organotypic Hippocampal Slice Cultures. *Neurotoxicity research*. 2015; 28(4):352–60. Epub 2015/08/20. <https://doi.org/10.1007/s12640-015-9553-9> PMID: [26286504](#).
12. Reinhard K, Tikidji-Hamburyan A, Seitter H, Idrees S, Mutter M, Benkner B, et al. Step-by-step instructions for retina recordings with perforated multi electrode arrays. *PloS one*. 2014; 9(8):e106148. Epub 2014/08/29. <https://doi.org/10.1371/journal.pone.0106148> PMID: [25165854](#).
13. Jewett KA, Taishi P, Sengupta P, Roy S, Davis CJ, Krueger JM. Tumor necrosis factor enhances the sleep-like state and electrical stimulation induces a wake-like state in co-cultures of neurons and glia. *The European journal of neuroscience*. 2015; 42(4):2078–90. Epub 2015/06/04. <https://doi.org/10.1111/ejn.12968> PMID: [26036796](#).
14. Jones IL, Russell TL, Farrow K, Fiscella M, Franke F, Muller J, et al. A method for electrophysiological characterization of hamster retinal ganglion cells using a high-density CMOS microelectrode array. *Frontiers in neuroscience*. 2015; 9:360. Epub 2015/11/04. <https://doi.org/10.3389/fnins.2015.00360> PMID: [26528115](#).
15. Berdondini L, Overstolz T, de Rooij N, Koudelka-Hep M, Martinoia S, Seitz P, et al., editors. High resolution electrophysiological activity imaging of in-vitro neuronal networks. *Microtechnologies in Medicine & Biology 2nd Annual International IEEE-EMB Special Topic Conference on*; 2002: IEEE.
16. Eversmann B, Jenkner M, Hofmann F, Paulus C, Brederlow R, Holzapfl B, et al. A 128/spl times/128 CMOS biosensor array for extracellular recording of neural activity. *IEEE Journal of Solid-State Circuits*. 2003; 38(12):2306–17.
17. Muller J, Ballini M, Livi P, Chen Y, Radivojevic M, Shadmani A, et al. High-resolution CMOS MEA platform to study neurons at subcellular, cellular, and network levels. *Lab on a chip*. 2015; 15(13):2767–80. Epub 2015/05/15. <https://doi.org/10.1039/c5lc00133a> PMID: [25973786](#).
18. Muthmann JO, Amin H, Sernagor E, Maccione A, Panas D, Berdondini L, et al. Spike Detection for Large Neural Populations Using High Density Multielectrode Arrays. *Frontiers in neuroinformatics*. 2015; 9:28. Epub 2016/01/07. <https://doi.org/10.3389/fninf.2015.00028> PMID: [26733859](#).

19. Maccione A, Gandolfo M, Zordan S, Amin H, Di Marco S, Nieuw T, et al. Microelectronics, bioinformatics and neurocomputation for massive neuronal recordings in brain circuits with large scale multielectrode array probes. *Brain research bulletin*. 2015; 119(Pt B):118–26. Epub 2015/08/02. <https://doi.org/10.1016/j.brainresbull.2015.07.008> PMID: 26232511.
20. Yavin E, Yavin Z. Attachment and culture of dissociated cells from rat embryo cerebral hemispheres on polylysine-coated surface. *The Journal of cell biology*. 1974; 62(2):540–6. Epub 1974/08/01. PMID: 4609989.
21. Kleinfeld D, Kahler KH, Hockberger PE. Controlled outgrowth of dissociated neurons on patterned substrates. *The Journal of neuroscience: the official journal of the Society for Neuroscience*. 1988; 8(11):4098–120. Epub 1988/11/01. PMID: 3054009.
22. Corey JM, Wheeler BC, Brewer GJ. Compliance of hippocampal neurons to patterned substrate networks. *Journal of neuroscience research*. 1991; 30(2):300–7. Epub 1991/10/01. <https://doi.org/10.1002/jnr.490300204> PMID: 1798054.
23. Xia Y, Whitesides GM. Soft lithography. *Annual review of materials science*. 1998; 28(1):153–84.
24. Kane RS, Takayama S, Ostuni E, Ingber DE, Whitesides GM. Patterning proteins and cells using soft lithography. *Biomaterials*. 1999; 20(23–24):2363–76. Epub 1999/12/30. PMID: 10614942.
25. Klenke C, Widera D, Engelen T, Müller J, Noll T, Niehaus K, et al. Hsc70 is a novel interactor of NF- κ B p65 in living hippocampal neurons. *PloS one*. 2013; 8(6):e65280. <https://doi.org/10.1371/journal.pone.0065280> PMID: 23762333
26. Schürmann M, Frese N, Beyer A, Heimann P, Widera D, Mönkemöller V, et al. Helium ion microscopy visualizes lipid nanodomains in mammalian cells. *Small*. 2015; 11(43):5781–9. <https://doi.org/10.1002/sml.201501540> PMID: 26436577
27. Lausmaa J. Surface spectroscopic characterization of titanium implant materials. *Journal of Electron Spectroscopy and Related Phenomena*. 1996; 81(3):343–61.
28. Hiromoto S, Hanawa T, Asami K. Composition of surface oxide film of titanium with culturing murine fibroblasts L929. *Biomaterials*. 2004; 25(6):979–86. Epub 2003/11/15. PMID: 14615162.
29. Ryyänen T, Kujala V, Ylä-Outinen L, Korhonen I, Tanskanen J, Kauppinen P, et al. All titanium micro-electrode array for field potential measurements from neurons and cardiomyocytes—a feasibility study. *Micromachines*. 2011; 2(4):394–409.
30. Janders M, Egert U, Stelzle M, Nisch W, editors. Novel thin film titanium nitride micro-electrodes with excellent charge transfer capability for cell stimulation and sensing applications. *Engineering in Medicine and Biology Society, 1996 Bridging Disciplines for Biomedicine Proceedings of the 18th Annual International Conference of the IEEE*; 1996: IEEE.
31. Erickson J, Tooker A, Tai Y-C, Pine J. Caged neuron MEA: A system for long-term investigation of cultured neural network connectivity. *Journal of neuroscience methods*. 2008; 175(1):1–16. <https://doi.org/10.1016/j.jneumeth.2008.07.023> PMID: 18775453
32. Kim YH, Baek NS, Han YH, Chung M-A, Jung S-D. Enhancement of neuronal cell adhesion by covalent binding of poly-d-lysine. *Journal of neuroscience methods*. 2011; 202(1):38–44. <https://doi.org/10.1016/j.jneumeth.2011.08.036> PMID: 21907237
33. Ruardij TG, Goedbloed MH, Rutten WL. Adhesion and patterning of cortical neurons on polyethylenimine-and fluorocarbon-coated surfaces. *IEEE transactions on biomedical engineering*. 2000; 47(12):1593–9. <https://doi.org/10.1109/10.887940> PMID: 11125594
34. Rüegg U, Hefti F. Growth of dissociated neurons in culture dishes coated with synthetic polymeric amines. *Neuroscience letters*. 1984; 49(3):319–24. PMID: 6493615
35. Letourneau PC. Possible roles for cell-to-substratum adhesion in neuronal morphogenesis. *Developmental biology*. 1975; 44(1):77–91. PMID: 1132590
36. Urban PL, Jefimovs K, Amantonico A, Fagerer SR, Schmid T, Mädler S, et al. High-density micro-arrays for mass spectrometry. *Lab on a chip*. 2010; 10(23):3206–9. <https://doi.org/10.1039/c0lc00211a> PMID: 20938499
37. Kurishita Y, Kohira T, Ojida A, Hamachi I. Rational design of FRET-based ratiometric chemosensors for in vitro and in cell fluorescence analyses of nucleoside polyphosphates. *Journal of the American Chemical Society*. 2010; 132(38):13290–9. <https://doi.org/10.1021/ja103615z> PMID: 20812684
38. Jun SB, Hynd MR, Dowell-Mesfin N, Smith KL, Turner JN, Shain W, et al. Low-density neuronal networks cultured using patterned poly-l-lysine on microelectrode arrays. *Journal of neuroscience methods*. 2007; 160(2):317–26. <https://doi.org/10.1016/j.jneumeth.2006.09.009> PMID: 17049614
39. Withers GS, James CD, Kingman CE, Craighead HG, Banker GA. Effects of substrate geometry on growth cone behavior and axon branching. *Journal of neurobiology*. 2006; 66(11):1183–94. <https://doi.org/10.1002/neu.20298> PMID: 16858695

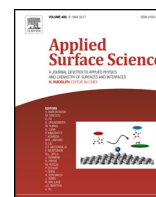
40. Samhaber R, Schottdorf M, El Hady A, Broking K, Daus A, Thielemann C, et al. Growing neuronal islands on multi-electrode arrays using an accurate positioning- μ CP device. *Journal of neuroscience methods*. 2016; 257:194–203. Epub 2015/10/04. <https://doi.org/10.1016/j.jneumeth.2015.09.022> PMID: 26432934.
41. Marconi E, Nieus T, Maccione A, Valente P, Simi A, Messa M, et al. Emergent functional properties of neuronal networks with controlled topology. *PLoS one*. 2012; 7(4):e34648. Epub 2012/04/12. <https://doi.org/10.1371/journal.pone.0034648> PMID: 22493706.
42. Jungblut M, Knoll W, Thielemann C, Pottek M. Triangular neuronal networks on microelectrode arrays: an approach to improve the properties of low-density networks for extracellular recording. *Biomedical microdevices*. 2009; 11(6):1269–78. Epub 2009/09/17. <https://doi.org/10.1007/s10544-009-9346-0> PMID: 19757074.
43. Jun SB, Hynd MR, Dowell-Mesfin N, Smith KL, Turner JN, Shain W, et al. Low-density neuronal networks cultured using patterned poly-L-lysine on microelectrode arrays. *Journal of neuroscience methods*. 2007; 160(2):317–26. Epub 2006/10/20. <https://doi.org/10.1016/j.jneumeth.2006.09.009> PMID: 17049614.
44. Nam Y, Branch DW, Wheeler BC. Epoxy-silane linking of biomolecules is simple and effective for patterning neuronal cultures. *Biosensors & bioelectronics*. 2006; 22(5):589–97. Epub 2006/03/15. <https://doi.org/10.1016/j.bios.2006.01.027> PMID: 16531038.
45. Nam Y, Chang JC, Wheeler BC, Brewer GJ. Gold-coated microelectrode array with thiol linked self-assembled monolayers for engineering neuronal cultures. *IEEE transactions on bio-medical engineering*. 2004; 51(1):158–65. Epub 2004/01/16. <https://doi.org/10.1109/TBME.2003.820336> PMID: 14723505.
46. James CD, Spence AJ, Dowell-Mesfin NM, Hussain RJ, Smith KL, Craighead HG, et al. Extracellular recordings from patterned neuronal networks using planar microelectrode arrays. *IEEE transactions on bio-medical engineering*. 2004; 51(9):1640–8. Epub 2004/09/21. <https://doi.org/10.1109/TBME.2004.827252> PMID: 15376512.
47. James CD, Davis R, Meyer M, Turner A, Turner S, Withers G, et al. Aligned microcontact printing of micrometer-scale poly-L-lysine structures for controlled growth of cultured neurons on planar microelectrode arrays. *IEEE transactions on bio-medical engineering*. 2000; 47(1):17–21. Epub 2000/01/26. PMID: 10646274.
48. Pershin YV, Di Ventra M. Experimental demonstration of associative memory with memristive neural networks. *Neural Networks*. 2010; 23(7):881–6. <https://doi.org/10.1016/j.neunet.2010.05.001> PMID: 20605401

5.2 Carbon nanomembranes



Contents lists available at ScienceDirect

Applied Surface Science

journal homepage: www.elsevier.com/locate/apsusc

Full Length Article

Multicomponent patterned ultrathin carbon nanomembranes by laser ablation



Natalie Frese^a, Julian Scherr^b, André Beyer^a, Andreas Terfort^b, Armin Götzhäuser^a, Norbert Hampp^c, Daniel Rhinow^{d,*}

^a University of Bielefeld, Faculty of Physics, Universitätsstr. 25, D-33615, Bielefeld, Germany

^b Goethe-University Frankfurt, Department of Chemistry, Max-von-Laue-Str. 9, D-60438, Frankfurt, Germany

^c Philipps-University Marburg, Department of Chemistry, Hans-Meerwein-Str. 4, D-35032, Marburg, Germany

^d Max Planck Institute of Biophysics, Department of Structural Biology, Max-von-Laue-Str. 3, D-60438, Frankfurt, Germany

ARTICLE INFO

Article history:

Received 5 May 2017

Received in revised form 25 July 2017

Accepted 31 July 2017

Available online 5 August 2017

Keywords:

Two-dimensional materials

Scanning electron microscopy

Helium ion microscopy

X-ray photoelectron spectroscopy

Self-assembly

Laser patterning

ABSTRACT

Carbon nanomembranes (CNMs) are a class of two-dimensional materials, which are obtained by electron beam-induced crosslinking of aromatic self-assembled monolayers (SAMs) on solid substrates. CNMs made from a single type of precursor molecule are uniform with homogeneous chemical and physical properties. We have developed a method for the fabrication of internally patterned CNMs resembling a key feature of biological membranes. Direct laser patterning is used to obtain multicomponent patterned SAMs on gold, which are subsequently crosslinked by electron irradiation. We demonstrate that the structure of internally patterned CNMs is preserved upon transfer to different substrates. The method enables rapid fabrication of patterned 2D materials with local variations in chemical and physical properties on the micrometer to centimeter scale.

© 2017 Elsevier B.V. All rights reserved.

1. Introduction

A technologically interesting feature of biological membranes is the formation of complex patterns by two-dimensional self-assembly of biomolecular building blocks in a 5 nm thin lipid matrix [1]. Self-assembled monolayers (SAMs) of thiols on gold have been studied extensively as model systems for self-assembly and pattern formation in two dimensions [2,3]. A variety of techniques has been used to pattern SAMs including UV lithography [4,5], microcontact printing [6], dip pen lithography [7], electron beam lithography [8,9], and direct laser patterning [10–15]. Direct laser patterning (DLP) of SAMs enables rapid fabrication of multicomponent surface structures with lateral dimensions in the micrometer to centimeter range [13], which is particularly useful for the fabrication of protein-surface [16] and cell-surface interfaces [17]. However, patterned thiol SAMs are not stable in the absence of the gold support, which precludes their transfer as a continuous membrane to another substrate.

It has been shown that SAMs of aromatic thiols can be crosslinked by irradiation with low-energy electrons [18]. Upon removal of the gold substrate, 1 nm thin free-standing carbon nanomembranes (CNMs) were obtained [19–21]. Depending on the aromatic precursor molecule, thickness and mechanical properties of CNMs can be tuned [22]. Owing to their low thickness, CNMs have been successfully applied as support films for transmission electron microscopy of biological specimens [23,24]. Furthermore, chemically patterned CNMs have been used as templates for the fabrication of nanostructures such as polymer carpets [25] or bio-hybrid assemblies [26].

CNMs made from a single precursor molecule are in principle uniform. Selective electron beam-induced crosslinking of aromatic SAMs, followed by exchange of thiols in the non-exposed areas and subsequent crosslinking of the heterogeneous SAM has been applied to fabricate chemically patterned CNMs [27]. A disadvantage of this method is the fact that crosslinked areas cannot be patterned multiple times. In this work, we used DLP to fabricate internally patterned CNMs and transferred them to different substrates. DLP enables rapid fabrication of chemically patterned aromatic SAMs, which are subsequently crosslinked to form internally patterned ultrathin CNMs with locally varying chemical and physical properties. Internally patterned CNMs were analyzed by X-

* Corresponding author.

E-mail address: daniel.rhinow@biophys.mpg.de (D. Rhinow).

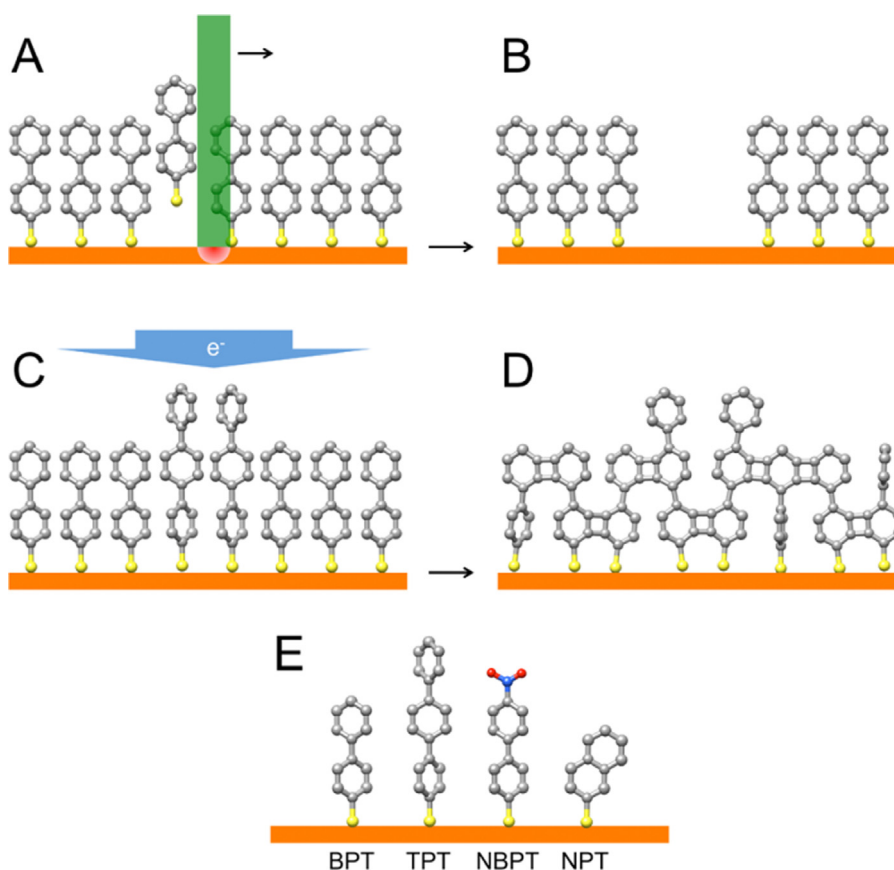


Fig. 1. Fabrication of internally patterned CNMs by direct laser patterning. (A) A SAM of aromatic thiols is formed on a gold surface. The SAM consists of BPT molecules. A focused laser beam ($\lambda = 532$ nm) is used to impart thermal energy to a confined area on the gold substrate causing desorption of aromatic thiols (B). (C) The gaps are filled with a second thiol, in this case TPT. Irradiation with low-energy electrons causes crosslinking of the aromatic thiols. (D) Internally patterned CNM. (E) Aromatic thiols used for the fabrication of patterned CNMs. BPT: 1'-Biphenyl-4-thiol; TPT: [1'',4',1',1]-terphenyl-4-thiol; NBPT: 4'-nitro-1,1'-biphenyl-4-thiol; NPT: naphthalene-2-thiol. Owing to the generation of hydrogen radicals during crosslinking, the nitro groups of NBPT are converted to amino groups (4'-amino-1,1'-biphenyl-4-thiol: ABPT) [29].

ray photoelectron microscopy (XPS), scanning electron microscopy (SEM) and helium ion microscopy (HIM).

2. Materials and methods

2.1. Chemicals

1,1'-Biphenyl-4-thiol (BPT), [1'',4',1',1]-terphenyl-4-thiol (TPT), and naphthalene-2-thiol (NPT) were purchased from Sigma-Aldrich (St. Louis, USA), 4'-nitro-1,1'-biphenyl-4-thiol (NBPT) was purchased from Taros Chemicals. Gold on silicon with titanium adhesion layer was purchased from Georg Albert PVD (Silz, Germany). Gold substrates suitable for subsequent transfer of patterned CNMs were made by depositing 200 nm of gold onto polished (100) silicon wafers. SAMs were formed by immersion in 10 mM solutions of aromatic thiols in organic solvents at room temperature. We used acetone (BPT, TPT, NPT), heptane (BPT), toluene (BPT, TPT), and dimethylformamide (NBPT) as solvents.

2.2. Direct laser patterning

DLP of aromatic thiols on gold was accomplished with a frequency-doubled Nd:YVO₄ diode pumped solid state laser (Explorer XP 532-5, Newport, USA) emitting 6 ns pulses (FWHM) with a 50 kHz repetition rate at a wavelength of $\lambda = 532$ nm. Photons of this wavelength are absorbed by the gold surface only. The laser beam was focused to a spot diameter of 15 μ m. In previous work, the optimum energy deposited to the sample was deter-

mined to 111 MW/cm² [11]. The energy deposited to the sample was adjusted with a polarizing beam splitter coupled to a polarizer. To optimize the patterning result, SAMs were patterned with decreasing laser power. After laser irradiation, patterned SAMs were immersed in a solution of the second thiol at room temperature.

2.3. Transfer of patterned CNMs

Damage-free transfer of CNMs was accomplished as described previously [20]. For the transfer of the patterned CNM, the film was protected with a double-layer of poly(methylmethacrylate) (PMMA) by spin-coating. Then the gold was exfoliated by angular dipping of the silicon wafer into water. The floating film on water was transferred to different solutions using a piece of silicon wafer. The gold was etched by placing the thin gold film on an aqueous iodine solution (10 wt% potassium iodide, 2.5 wt% iodine in water). Afterwards the PMMA-protected patterned CNM was placed on an aqueous potassium iodide solution (10 wt% potassium iodide in water). Finally, the film was transferred to a substrate (silicon or gold), the PMMA was removed by immersion in acetone for 2 h, and the substrate was dried in a stream of nitrogen.

2.4. Scanning electron microscopy (SEM)

Samples were analyzed in a Zeiss Auriga at an acceleration voltage of 5 kV using the in-lens detector for secondary electrons.

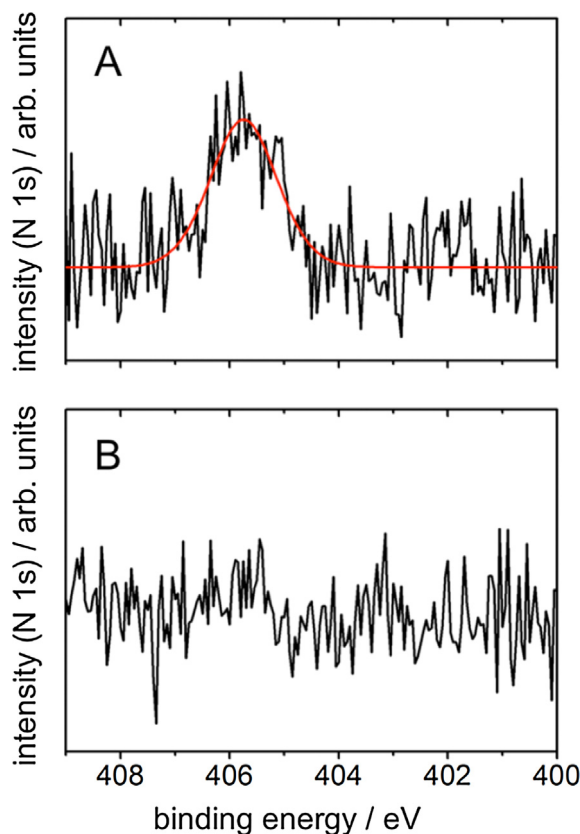


Fig. 2. Incorporation of NBPT into a BPT SAM with and without DLP. (A) XP spectrum obtained from a BPT SAM after laser irradiation and subsequent immersion in a solution containing NBPT for 72 h. The spectrum reveals the N 1s peak at 405.7 eV indicating the incorporation of NBPT. (B) XP spectrum of a BPT sample, which was immersed in a solution containing NBPT for 72 h. The N 1s peak is absent.

2.5. Helium ion microscopy (HIM)

Samples were imaged in a Zeiss Orion Plus at acceleration voltages between 30 and 36 kV and currents between 0.4–4 pA. An electron floodgun was used to mitigate electrostatic charging while secondary electrons were detected with an Everhart-Thornley detector.

2.6. X-ray photoelectron spectroscopy (XPS)

Samples were analyzed in an Omicron Multiprobe UHV system using monochromatic Al K α irradiation, a Sphera electron analyzer with a resolution of 0.9 eV and an emission angle of 20°.

3. Results and discussion

Fig. 1 illustrates the use of DLP to fabricate internally patterned CNMs consisting of crosslinked aromatic SAMs on a gold surface. This approach enabled us to fabricate patterned CNMs from a variety of aromatic precursor molecules (Fig. 1E).

To confirm that laser irradiation leads to spatially selective desorption of aromatic thiols by photothermal cleavage of the gold-sulfur bond (Fig. 1A and B), we analyzed the incorporation of NBPT into a BPT SAM with and without prior laser irradiation.

Fig. 2A shows XP spectra of a BPT SAM, which was irradiated with a focused laser beam ($\lambda = 532$ nm) and subsequently immersed in a solution containing NBPT. The XP spectrum reveals the N 1s signal at a binding energy of 405.7 eV, indicating the incorporation of NBPT molecules into gaps formed by photothermal desorption of BPT molecules. Our experiments are in accordance with previous

results obtained with DLP of NBPT SAMs [28]. Without prior laser irradiation, immersion of a BPT SAM on gold in a solution containing NBPT does not lead to incorporation of NBPT as confirmed by XPS (Fig. 2B). This demonstrates that self-exchange of aromatic thiols at room temperature is negligible at the time scale of a few days.

It is of critical importance that the structure of patterned SAMs is preserved after electron beam-induced crosslinking. We analyzed a patterned BPT SAM, consisting of TPT lines written into a BPT SAM, by HIM before (Fig. 3A) and after (Fig. 3B) crosslinking with electrons. Fig. 3C shows an SEM image of the same sample after crosslinking. Our experiments reveal that structure and chemical contrast of patterned aromatic thiol SAMs are preserved after crosslinking by electron irradiation.

Our experiments reveal that structure and chemical contrast of patterned aromatic thiol SAMs are preserved after crosslinking by electron irradiation. Furthermore, our analysis enables a direct comparison of HIM and SEM as tools for imaging patterned SAMs. SEM is suitable for the analysis of patterned SAMs as thiols produce chemical contrast in the secondary electron image in dependence of chain length, terminal groups, and acceleration voltage [30–33]. Recently, HIM has been used to analyze monolayers on solid substrates [34,35]. Interestingly, the same pattern appears with different contrast in HIM and SEM SE images. The TPT lines appear with a dark center and a bright rim in the HIM image (Fig. 3B), whereas in the SEM image TPT lines appear uniformly darker than the BPT matrix. This could be explained by the fact that in the SEM most secondary electrons (SE) are generated in the gold substrate and their contrast is determined by a stronger attenuation in TPT, as compared to BPT. Conversely, contrast in the HIM images is largely determined by SE generated in the organic film and is more influenced by the film's thickness and topography. On the other hand, it may also be that local heating of the gold substrate during DLP causes subtle rearrangements in the gold, which cause changes in SE contrast in HIM images only, owing to the high sensitivity of HIM towards surface chemistry. More work on charge-particle interaction in molecular films is needed to understand the subtle differences in the contrasts of HIM and SEM images.

The formation of mechanically stable membranes was confirmed by successful transfer of internally patterned CNMs to other substrates. Fig. 4A shows wetting patterns on a patterned CNM after transfer to a gold substrate, observed by light microscopy upon exposing the sample to humid air. Although quantitative description of wetting patterns is difficult, wetting is a fast method to visualize chemical patterns by light microscopy. Areas containing ABPT and BPT can be clearly distinguished in HIM (Fig. 4B) and SEM (Fig. 4C) SE images of the same sample.

It has been shown earlier that DLP can be used to fabricate patterned SAMs of arbitrary complexity [13]. We applied DLP to fabricate internally patterned CNMs consisting of three different types of aromatic molecules (Fig. 4D). Fig. 4D shows a SEM image of a transferred patterned CNM consisting of patterns of BPT, TPT, and NPT, which demonstrates that DLP enables the fabrication of multicomponent patterned CNM. In difference to SE images of crosslinked patterned SAMs, acquired before transfer to other substrates (Fig. 3B and C), transferred membranes produce identical contrast in HIM and SEM images (Fig. 4B and C). The mechanisms behind contrast generation in HIM SE images of monolayers on solid substrates require further elucidation.

4. Conclusions

We have demonstrated that DLP is a versatile tool for the fabrication of internally patterned CNMs. Like biological membranes, patterned CNMs consist of distinct chemical domains, which cause

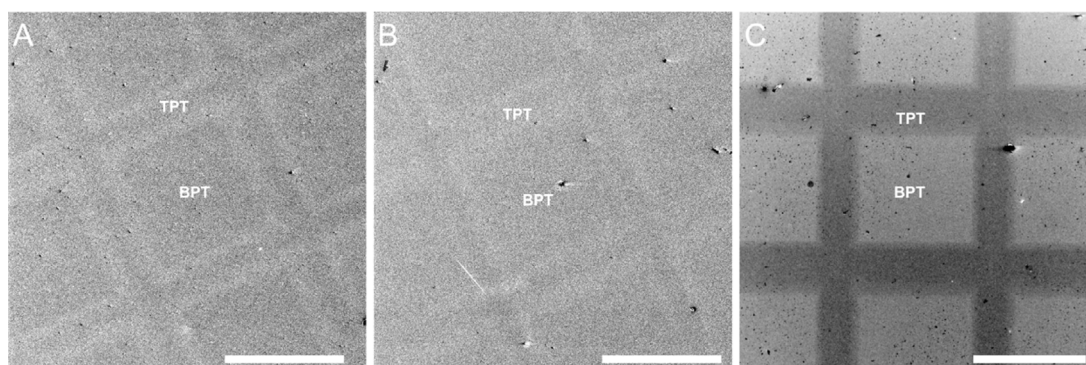


Fig. 3. Analysis of patterned aromatic SAMs by HIM and SEM. Secondary electron (SE) HIM images of a patterned SAM before (A) and after (B) crosslinking by electron irradiation. Apart from a small loss in contrast, the patterns are preserved. (C) SE SEM image of the sample after crosslinking. Scale bars are 100 μm .

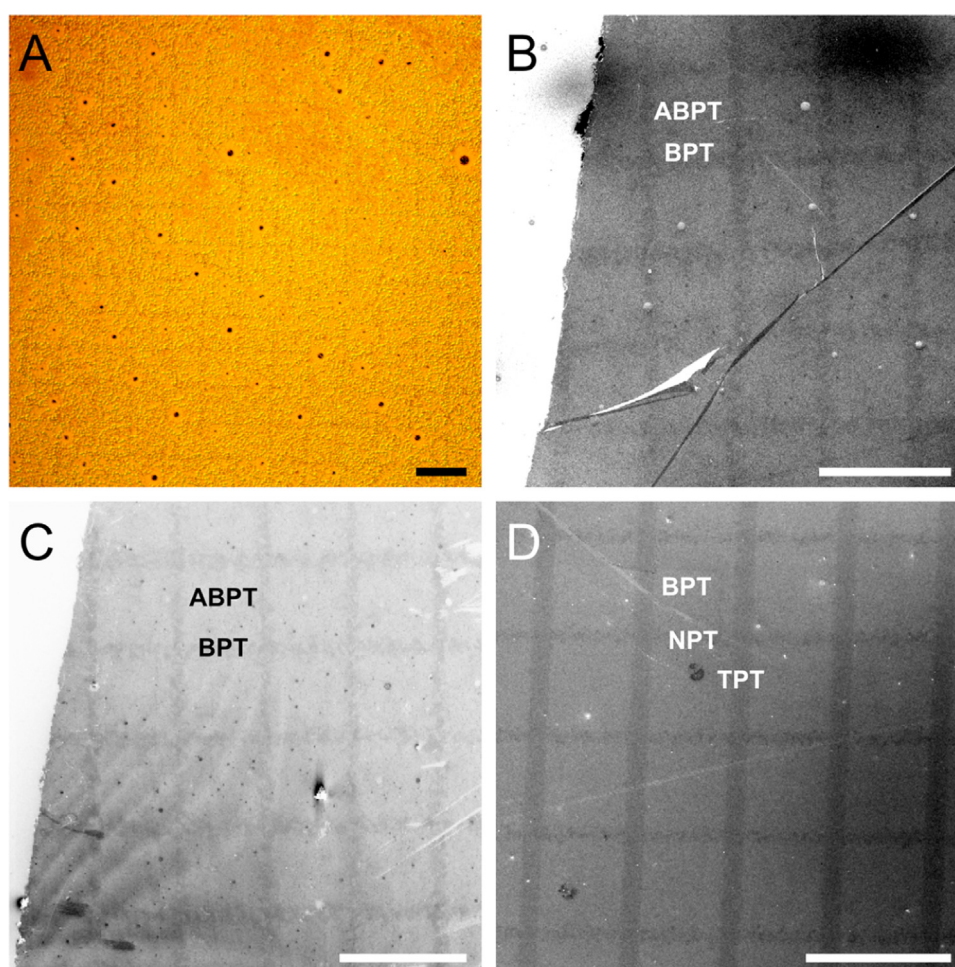


Fig. 4. Structural analysis of patterned CNMs transferred to different substrates. (A) Wetting patterns observed by light microscopy after transfer to a gold substrate. The CNM has been obtained by crosslinking of a NBPT SAM containing lines of BPT. Upon crosslinking, NBPT molecules were converted to amino-terminated molecules (ABPT) [29]. (B) The same sample imaged by HIM and SEM (C). Shown are SE images acquired at the edge of internally patterned CNMs. BPT lines appear darker than the ABPT matrix. (D) SEM image of a patterned CNM, consisting of three aromatic precursor molecules, after transfer to a silicon substrate. Scale bars are 200 μm .

local variation of physical and chemical properties. Future work should address the analysis of mechanical properties of patterned CNM. This could be accomplished by methods, which enable local determination of mechanical properties, such as atomic force microscopy. Combining DLP of SAMs on a solid substrate with subsequent crosslinking resembles a universal scheme for the rapid fabrication of chemically patterned 2D materials with patterns from the biologically relevant micrometer up to the centimeter

scale thus widening the spectrum of available nanomembranes [36] with technologically interesting properties.

Acknowledgements

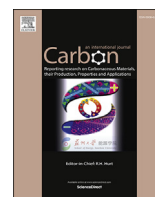
We thank Werner Kühlbrandt for support and a critical reading of the manuscript. This work was funded by German Research Council (DFG) Cluster of Excellence “Macromolecular Complexes”

Frankfurt, DFG grant GO 918/14-1 to AG, DFG grant HA 2906/9-1 to NH, DFG grant TE 247/14-1 to AT, and DFG grant RH 134/1-1 to DR.

References

- [1] K. Jacobson, O.G. Mouritsen, R.G. Anderson, Lipid rafts: at a crossroad between cell biology and physics, *Nat. Cell. Biol.* 9 (2007) 7–14.
- [2] J.C. Love, L.A. Estroff, J.K. Kriebel, R.G. Nuzzo, G.M. Whitesides, Self-assembled monolayers of thiolates on metals as a form of nanotechnology, *Chem. Rev.* 105 (2005) 1103–1169.
- [3] F. Schreiber, Structure and growth of self-assembling monolayers, *Prog. Surf. Sci.* 65 (2000) 151–256.
- [4] J.Y. Huang, D.A. Dahlgren, J.C. Hemminger, Photopatterning of Self-Assembled Alkanethiolate Monolayers on Gold – a Simple Monolayer Photoresist Utilizing Aqueous Chemistry, *Langmuir* 10 (1994) 626–628.
- [5] M.E. Anderson, M. Mihok, H. Tanaka, L.P. Tan, M.W. Horn, G.S. McCarty, P.S. Weiss, Hybrid approaches to nanolithography: photolithographic structures with precise controllable nanometer-scale spacings created by molecular rulers, *Adv. Mater.* 18 (2006) 1020–1022.
- [6] A. Kumar, G.M. Whitesides, Features of gold having micrometer to centimeter dimensions can be formed through a combination of stamping with an elastomeric stamp and an alkanethiol ink followed by chemical etching, *Appl. Phys. Lett.* 63 (1993) 2002–2004.
- [7] R.D. Piner, J. Zhu, F. Xu, S.H. Hong, C.A. Mirkin, Dip-pen nanolithography, *Science* 283 (1999) 661–663.
- [8] M.J. Lercel, G.F. Redinbo, F.D. Pardo, M. Rooks, R.C. Tiberio, P. Simpson, H.G. Craighead, C.W. Sheen, A.N. Parikh, D.L. Allara, Electron-beam lithography with monolayers of alkylthiols and alkylsiloxanes, *J. Vac. Sci. Technol. B* 12 (1994) 3663–3667.
- [9] A. Golzhauser, W. Eck, W. Geyer, V. Stadler, T. Weimann, P. Hinze, M. Grunze, Chemical nanolithography with electron beams, *Adv. Mater.* 13 (2001) 803–806.
- [10] M.R. Shadnam, S.E. Kirkwood, R. Fedosejevs, A. Amirfazli, Direct patterning of self-assembled monolayers on gold using a laser beam, *Langmuir* 20 (2004) 2667–2676.
- [11] D. Rhinow, N.A. Hampp, Forming microstructured alkanethiol self-assembled monolayers on gold by laser ablation, *IEEE Trans. Nanobiosci.* 5 (2006) 188–192.
- [12] T. Balgar, S. Franzka, E. Hasselbrink, N. Hartmann, Laser-assisted fabrication of submicron-structured hydrophilic/hydrophobic templates for the directed self-assembly of alkylsiloxane monolayers into confined domains, *Appl. Phys. A* 82 (2006) 15–18.
- [13] D. Rhinow, N.A. Hampp, Solid-supported multicomponent patterned monolayers, *Adv. Mater.* 19 (2007) 1967–1972.
- [14] L. Iversen, O. Younes-Metzler, K.L. Martinez, D. Stamou, Chemically specific laser-induced patterning of alkanethiol SAMs: characterization by SEM and AFM, *Langmuir* 25 (2009) 12819–12824.
- [15] D. Rhinow, N.A. Hampp, Patterned self-assembled monolayers of alkanethiols on copper nanomembranes by submerged laser ablation, *Appl. Phys. A* 107 (2012) 755–759.
- [16] A. Schroter, S. Franzka, N. Hartmann, Photothermal laser fabrication of micro- and nanostructured chemical templates for directed protein immobilization, *Langmuir* 30 (2014) 14841–14848.
- [17] J.H. Slater, J.S. Miller, S.S. Yu, J.L. West, Fabrication of multifaceted micropatterned surfaces with laser scanning lithography, *Adv. Funct. Mater.* 21 (2011) 2876–2888.
- [18] W. Geyer, V. Stadler, W. Eck, M. Zharnikov, A. Gölzhäuser, M. Grunze, Electron-induced crosslinking of aromatic self-assembled monolayers: negative resists for nanolithography, *Appl. Phys. Lett.* 75 (1999) 2401–2403.
- [19] W. Eck, A. Küller, M. Grunze, B. Völkel, A. Gölzhäuser, Freestanding nanosheets from crosslinked biphenyl self-assembled monolayers, *Adv. Mater.* 17 (2005) 2583–2587.
- [20] A. Turchanin, A. Beyer, C.T. Nottbohm, X.H. Zhang, R. Stosch, A. Sologubenko, J. Mayer, P. Hinze, T. Weimann, A. Golzhauser, One nanometer thin carbon nanosheets with tunable conductivity and stiffness, *Adv. Mater.* 21 (2009) 1233–1237.
- [21] A. Turchanin, A. Golzhauser, Carbon nanomembranes from self-assembled monolayers: functional surfaces without bulk, *Prog. Surf. Sci.* 87 (2012) 108–162.
- [22] P. Angelova, H. Vieker, N.E. Weber, D. Matei, O. Reimer, I. Meier, S. Kurasch, J. Biskupek, D. Lorbach, K. Wunderlich, L. Chen, A. Terfort, M. Klapper, K. Mullen, U. Kaiser, A. Golzhauser, A. Turchanin, A universal scheme to convert aromatic molecular monolayers into functional carbon nanomembranes, *ACS Nano* 7 (2013) 6489–6497.
- [23] D. Rhinow, M. Buenfeld, N.E. Weber, A. Beyer, A. Golzhauser, W. Kuhlbrandt, N. Hampp, A. Turchanin, Energy-filtered transmission electron microscopy of biological samples on highly transparent carbon nanomembranes, *Ultramicroscopy* 111 (2011) 342–349.
- [24] D. Rhinow, J. Vonck, M. Schranz, A. Beyer, A. Golzhauser, N. Hampp, Ultrathin conductive carbon nanomembranes as support films for structural analysis of biological specimens, *Phys. Chem. Chem. Phys.* 12 (2010) 4345–4350.
- [25] I. Amin, M. Steenackers, N. Zhang, R. Schubel, A. Beyer, A. Golzhauser, R. Jordan, Patterned polymer carpets, *Small* 7 (2011) 683–687.
- [26] A. Turchanin, A. Tinazli, M. El-Desawy, H. Grossann, M. Schnietz, H.H. Solak, R. Tampe, A. Golzhauser, Molecular self-assembly, chemical lithography, and biochemical tweezers: a path for the fabrication of functional nanometer-scale protein arrays, *Adv. Mater.* 20 (2008) 471–477.
- [27] A. Beyer, A. Godt, I. Amin, C.T. Nottbohm, C. Schmidt, J. Zhao, A. Golzhauser, Fully cross-linked and chemically patterned self-assembled monolayers, *Phys. Chem. Chem. Phys.* 10 (2008) 7233–7238.
- [28] A. Schroter, S. Franzka, J. Koch, B.N. Chichkov, A. Ostendorf, N. Hartmann, Femtosecond-laser processing of nitrobiphenylthiol self-assembled monolayers, *Appl. Surf. Sci.* 278 (2013) 43–46.
- [29] W. Eck, V. Stadler, W. Geyer, M. Zharnikov, A. Golzhauser, M. Grunze, Generation of surface amino groups on aromatic self-assembled monolayers by low energy electron beams – A first step towards chemical lithography, *Adv. Mater.* 12 (2000) 805–808.
- [30] G.P. Lopez, H.A. Biebuyck, G.M. Whitesides, Scanning electron-Microscopy can form images of patterns in self-assembled monolayers, *Langmuir* 9 (1993) 1513–1516.
- [31] A.G. Bittermann, S. Jacobi, L.F. Chi, H. Fuchs, R. Reichelt, Contrast studies on organic monolayers of different molecular packing in FESEM and their correlation with SFM data, *Langmuir* 17 (2001) 1872–1877.
- [32] N.H. Mack, R. Dong, R.G. Nuzzo, Quantitative imaging of protein adsorption on patterned organic thin-film arrays using secondary electron emission, *J. Am. Chem. Soc.* 128 (2006) 7871–7881.
- [33] C. Srinivasan, T.J. Mullen, J.N. Hohman, M.E. Anderson, A.A. Dameron, A.M. Andrews, E.C. Dickey, M.W. Horn, P.S. Weiss, Scanning electron microscopy of nanoscale chemical patterns, *ACS Nano* 1 (2007) 191–201.
- [34] G. Hlawacek, V. Veligura, S. Lorbek, T.F. Mocking, A. George, R. van Gastel, H.J.W. Zandvliet, B. Poelsema, Imaging ultra thin layers with helium ion microscopy: utilizing the channeling contrast mechanism, *Beilstein J. Nanotechnol.* 3 (2012) 507–512.
- [35] A. George, M. Knez, G. Hlawacek, D. Hagedoorn, H.H.J. Verputten, R. van Gastel, J.E. ten Elshof, Nanoscale patterning of organosilane molecular thin films from the gas phase and its applications: fabrication of multifunctional surfaces and large area molecular templates for site-selective material deposition, *Langmuir* 28 (2012) 3045–3052.
- [36] J.A. Rogers, M.G. Lagally, R.G. Nuzzo, Synthesis, assembly and applications of semiconductor nanomembranes, *Nature* 477 (2011) 45–53.

5.3 Carbon foam



Ultralight carbon nanofoam from naphthalene-mediated hydrothermal sucrose carbonization



Shelby Taylor Mitchell ^a, Natalie Frese ^b, Armin Götzhäuser ^b, Amanda Bowers ^a, Klaus Sattler ^{a,*}

^a Department of Physics and Astronomy, University of Hawaii, 2505 Correa Road, Honolulu, HI 96822, USA

^b Faculty of Physics, University of Bielefeld, D-33501 Bielefeld, Germany

ARTICLE INFO

Article history:

Received 5 May 2015

Received in revised form

27 July 2015

Accepted 2 August 2015

Available online 7 August 2015

ABSTRACT

We report experimental studies of carbon nanofoam produced using a hydrothermal autoclave reactor with a sucrose solution and a small added amount of naphthalene. The foam has an average density of 85 mg/cc and is uniform in its appearance. He-ion microscopy (HeIM), Raman spectroscopy and X-ray photoelectron spectroscopy (XPS) were used to characterize the foam samples. These show good consistency in the micro/nanostructure as well as in the elemental constitution. The vibrational and electron core-level studies suggest an open cellular structure with curved graphene walls and basal-plane oxide groups. We conclude that naphthalene-assisted hydrothermal processing of sucrose is a useful method to produce high-quality carbon nanofoams.

© 2015 Elsevier Ltd. All rights reserved.

1. Introduction

Nanofoams from various materials have been synthesized in recent years. Among these are nanofoams from chemical elements such as copper [1], silicon [2], nickel [3], gold [4], and silica [5]. Also, various types of polymeric nanofoams have been produced since their first synthesis in 1994 [6]. In addition, nanocomposite foams have been investigated [7] which are interesting due to their superior mechanical and thermal properties. Cu-nanofoams were studied with respect to their possible use in energy applications [1].

There is an intense interest in nanocarbon for a variety of engineering applications. Nanocarbon materials are thermodynamically stable in different polymorphs which can adopt a wide range of crystalline and non-crystalline structures with very interesting properties. This is because of carbon's ability to form sp^1 - (polymeric-type), sp^2 - (graphite-like), and sp^3 - (diamond-like) hybridized bonds. Noncrystalline carbons usually are intermediate between diamond and graphite since they contain variable amounts of sp^3 - and sp^2 -type atoms. Hybrid graphite-diamond structures have been theoretically developed [8], in particular for the understanding of glassy carbons, carbon blacks, and diamond-like carbon films [9]. The properties of these materials depend very

strongly on the sp^3/sp^2 ratio [10]. Mass densities typically range from $\sim 3.5 \text{ gcm}^{-3}$ for diamond to about 1 gcm^{-3} for noncrystalline carbon films.

Carbon nanofoam (CNFM) was first produced in 2002 by high-repetition-rate laser ablation of a glassy carbon target in an Argon atmosphere [11]. The foams were found to have very low densities and high electrical resistivity. Carbon nanofoam has been considered as a potential hydrogen storage material [12] and as cathode materials for metal-air batteries [13]. It was found that this material contains both sp^2 and sp^3 bonded carbon atoms. It was suggested that the foams consist of graphite-like sheets with hyperbolic curvature, similar to the structure of "schwarzite". Surprisingly, ferromagnetism was found for some of the foams up to 90 K, with a narrow hysteresis curve and a high saturation magnetization [14]. Also, catalytic applications have been reported using carbon nanofoams [15]. Atomistic simulations of carbon nanofoams reveal a low-density nanoporous material [16]. A nanofoam-related structure has also been suggested for carbon nanotube aerogels [17]. Such carbon structures with complex topology related to the coexistence of both sp^2 and sp^3 hybridized atoms, have attracted considerable interest in recent years [18].

Porous carbon materials are usually produced by chemical [19,20] or physical [21] routes. Among these, the mesoporous and nanoporous carbons are attractive materials for a number of different applications, such as methane gas storage [22], hydrogen storage [23], as electrodes in supercapacitors [24,25], and as

* Corresponding author.

E-mail address: sattler@hawaii.edu (K. Sattler).

matrixes incorporating metal particles for highly efficient catalysts [26,27]. Porous carbon frameworks are also considered for capacitive deionization [28], as sensors for metal ions [29] or as hosts for the confinement of molecules [30].

In this work we report on the study of carbon nanofoams produced by hydrothermal processing of sucrose. Hydrothermal carbonization (HTC), most often applied to biomass processing [31], is an aqueous-phase route to produce carbon materials. High temperature/high pressure (HTHP) synthesis has been shown to lead to the production of a variety of carbon nanomaterials [32]. Separation of carbon species in structural and chemical pure form is usually required but is often difficult to achieve. Our method of hydrothermal processing reveals samples with uniform microstructure as recorded by helium ion microscopy (HeIM). Raman spectra show the typical carbon G and D peaks, no structure in the 2D and 2G overtone range, but two peaks in the 700–1200 cm^{-1} range. The deconvoluted XPS spectra show three C1s peaks which we assign to sp^2/sp^3 hybrid, C–OH, and C=O positioned carbon atoms. In the O1s energy range, we identify three spectral features, corresponding to oxygen bonded to aromatic (sp^2), aliphatic (sp^3), and to carbon atoms in C=O bonds, with the latter presumably from oxygen attached to carbons to the graphene-type basal-plane of the cellular walls.

2. Instruments and methods

2.1. Hydrothermal synthesis

A 130 ml stainless steel autoclave was filled with a 5-molar sucrose solution, and 3 mg of naphthalene was added. The autoclave then was tightly sealed and connected to the heating supply. Subsequently the autoclave was kept at 155 °C for 5 h. After cooling and opening, we extracted the foam which had formed in the container. Then we separated the foam from the remaining sucrose solution by rinsing the samples in hot water. After drying the samples, their mass density was determined using a high-precision balance and a pre-defined volume container. The density was determined for several samples from the same experimental run. The determined value gives an average of three measurements with a standard deviation of 0.8%.

2.2. Helium ion microscopy

Helium ion microscopy images were obtained using the ORION PLUS (Carl Zeiss) with an acceleration voltage of 34.9 eV and a beam current of 0.6 pA. Secondary electrons were detected and an electron flood gun was used to compensate charging of the uncoated samples. The foam was attached to the HeIM sample holder using conductive carbon pads.

The helium ion microscope is a powerful instrument for structure research [33]. It produces a high-brightness, low-energy-spread, subnanometer-size beam for imaging. A beam of He ions with a diameter of typically less than one atom is focused onto the substrate under investigation and the image is provided either by ionoluminescence [34], Rutherford backscattering of the ions, or secondary electron emission [35]. The high resolution is possible due to the small subsurface ion beam spread [36]. Due to its very high brightness it is particularly suitable for the imaging of low-mass elements such as carbon. Besides imaging, elemental analysis can be achieved with the He-ion microscope [37]. In this work we use the secondary electron emission setup for imaging of our samples.

2.3. Raman spectroscopy

Raman spectra were recorded using a micro Raman spectrometer (LabRAM ARAMIS) operated in the backscattering mode. Measurements were performed with a blue diode laser at 473 nm, a 10 \times microscope objective and a thermoelectrically cooled CCD detector. The foam was mounted on conductive carbon tape.

In Raman spectroscopy, vibrational modes are studied by measuring the energy of photons scattered from a sample which is exposed to laser light. Raman spectra of bulk carbon materials typically consist of a graphitic or G-band, and disorder from defects and from the surface results in the D-band. By determining the ratio between these two bands ($I_D:I_G$), a quantitative measure of defect density can be obtained. In addition, this intensity ratio can be used to determine the degree of graphitization of a sample.

2.4. X-ray photoelectron spectroscopy (XPS)

X-ray photoelectron spectroscopy was performed in a multi-chamber UHV system (Multiprobe, Omicron) at a chamber pressure below 10^{-9} mbar. Monochromatic Al K α irradiation, an electron analyzer (Sphera) with a resolution of 0.9 eV, and an emission angle of 20° were used. The foam was attached to the XPS sample holder by conductive carbon tape. For deconvolution of XP peaks a Shirley background and symmetric Voigt functions were employed.

XPS measures surface composition by determining the binding energy of photoelectrons ejected when a material is irradiated by X-rays. The surface sensitivity of XPS is derived from the small (<10 nm) inelastic mean free path of the ejected photoelectrons. This allows the elemental composition of the near surface region to be quantified.

In addition to compositional analysis, XPS can also provide information on the chemical environment of atoms based on the peak-fitting of the spectral envelopes. This capability stems from the fact that, although a photoelectron's binding energy is largely determined by the element from which it originates, binding energies are also influenced by the local chemical environment (e.g., for carbon atom: C–C, C=C, C–O, C=O).

XPS has been used for a large variety of carbon materials, such as nanostructured carbon films [38], carbon nanowall films [39], diamond-like carbon films [40], amorphous carbon [41], tetrahedral amorphous carbon films [42], nanoporous carbon [43], carbon black [44], activated carbon [45], or carbon nanotubes [46]. The XPS is an excellent instrument for chemical structure analysis [47], in particular for the study of the chemical states with emphasis on the sp^2/sp^3 hybridization ratio [41].

3. Results

3.1. Density

The density of the foam was obtained from averaging the data using various foam samples of the same batch. This resulted in an average density of 0.085 g cm^{-3} . This value is distinctively below the densities of diamond (3.515 g cm^{-3}), graphite (2.267 g cm^{-3}), amorphous carbon (1.8–2.1 g cm^{-3}), or carbon nanotubes (1.6 g cm^{-3}) [48].

Various types of 'ultralight carbons' have been fabricated with densities typically between 100 and 300 mg cm^{-3} . Among these are carbon aerogels [49–51], nanoporous carbons [52], amorphous carbon nanoparticles [53,54], carbon nanotube scaffolds [55], and carbon foams [56,57]. The densities of these carbon materials are significantly different from 'heavy carbons' such as pristine graphite (2.26 g cm^{-3}), DVD grown carbon films (2.14 g cm^{-3} [58]), or carbon nanotube forests (1.6–0.38 g cm^{-3} [59]). Some

techniques allow the production of carbons in a wide density range (0.20–1.4 g cm⁻³ [60]).

3.2. Microscopy

Fig. 1a shows a He-ion microscopy image of a foam sample with a 2 mm field of view. It can be seen that the structure of the material is quite uniform, at this level of magnification. Fig. 1b shows an image of the sample with a 75 micron-sized field of view. At this level of magnification, the sample consists of particles with diameters between ~3 and 15 microns. The particles tend to be spherical, with an eccentricity close to zero, but are often coalesced forming larger species. In Fig. 1c, one of the micropearls is shown enlarged, with a 15 micron field of view. It has a perfectly spherical shape with a sharp edge. On this recorded length scale, the surface of the pearl shows perfectly smooth appearance. However, with further magnification and refocusing of the He ion beam (Fig. 1d, with 1 micron field of view), additional structure can be observed with features as small as ~25 nm in diameter. This may be the diameter of the cavities in the cellular structure of the foam. However, HelM does not seem to resolve fully the individual pores of the foam. In this respect we note that pore sizes for nanoporous carbons are typically between 0.5 nm and 2 nm [61].

3.3. Raman spectroscopy

Raman spectroscopy is a powerful technique for the characterization of carbon nanomaterials and can be used to distinguish between ordered and disordered atomic structure. The typical features for carbon in Raman spectra are the G band at wavenumbers around 1580 cm⁻¹ and the D band at around 1350 cm⁻¹. The G band is usually assigned to E_{2g} phonons of C sp² atoms, and the D band is due to the breathing mode of k-point phonons of A_{1g} symmetry [62]. The G band may also contain signatures from polycyclic aromatic hydrocarbons (PAHs), often the precursors in the growth of graphitic particles [63]. Carbon stretch vibrations in benzene result in a peak at 1588 cm⁻¹ [64], and PAH signatures are at similar wavenumbers.

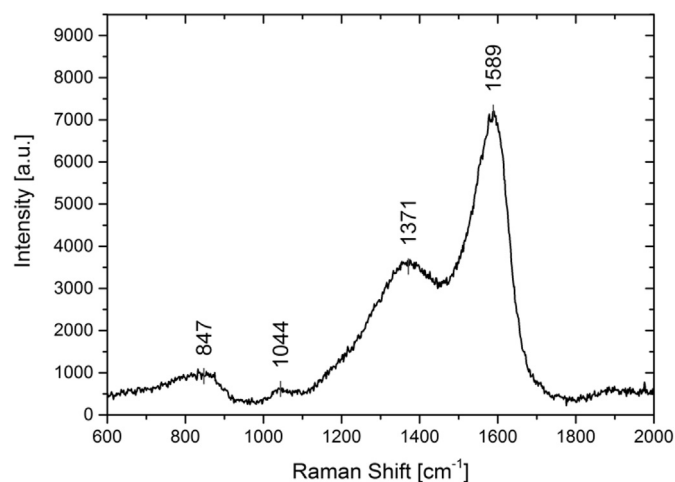


Fig. 2. Raman spectrum in the wavenumber range 750 cm⁻¹ to 2300 cm⁻¹.

Fig. 2 shows the Raman spectrum of our foam sample. We identify the two characteristic peaks, the G band at 1589 cm⁻¹ and the D band at 1371 cm⁻¹. The G band appears with much higher intensity than the D band. Such intense G band indicates the significant presence of a graphitic wall structure, presumably with single- or few-layer thickness. The wavenumber of the observed G band (1589 cm⁻¹) is slightly shifted to a higher value compared to that of the graphite G band (1580 cm⁻¹), which may result from high curvature of a graphene wall structure. The relatively low D-band intensity indicates that the nanofoam samples contain few carbons in hybridizations other than sp². We further note that the overtone of the D band, the 2D band, is usually located at about 2700 cm⁻¹ [65]. In our sample, the 2D band is not present in the extended spectrum.

3.4. XPS

XPS is a powerful method to investigate the character of the near-surface region of carbonaceous materials. It is a surface sensitive method in which the core level chemical shifts are measured. This is valuable for understanding the local environment of an atom, for example in finding whether a carbon allotrope is sp³ or sp² bonded. Apart from the chemical shift, the XPS investigation can provide useful information such as elemental composition, degree of disorder, compound formation, and surface functional groups.

Using XPS, the identity and concentration of oxygen-containing functional groups can, in principle, be obtained from spectral deconvolution of the C1s and O1s XPS regions. Unambiguous spectral deconvolution is, however, often complicated by the presence of different species (e.g., C–H, C–O, C=O, COOH) with similar binding energies. The C1s and the O1s spectral envelopes are typically broad and featureless due to both the proximity of the binding energies associated with different oxygen-containing functional groups and the limited resolution of typical energy analyzers.

In Fig. 3a and b, narrow-scan XPS spectra are provided for the C1s and O1s peak distributions, respectively. The two energy ranges cover the typical features present in the analysis of nanocarbon materials.

For the distribution in Fig. 3a we used three-curve fitting. We label the three peaks as C1, C2 and C3, and find the maxima and % areas at 285.0 eV (57.0%), 286.2 eV (32.0%), and 288.6 eV (11.0%), respectively. We assign the C1 peak to C–C bonds in a mixed sp²/

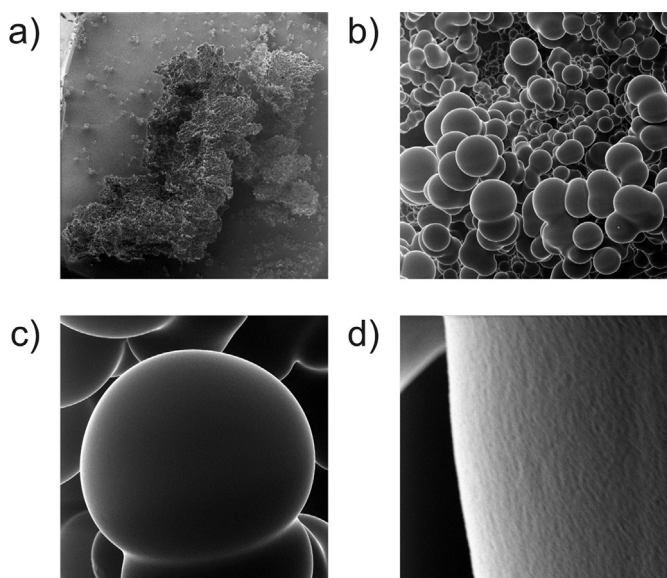


Fig. 1. Helium-ion microscopy (HelM) images of carbon nanofoam, Fields of view: (a) 2 mm, (b) 75 μm, (c) 15 μm, showing a single micropearl, and (d) 1 μm, showing a micropearl with internal structure.

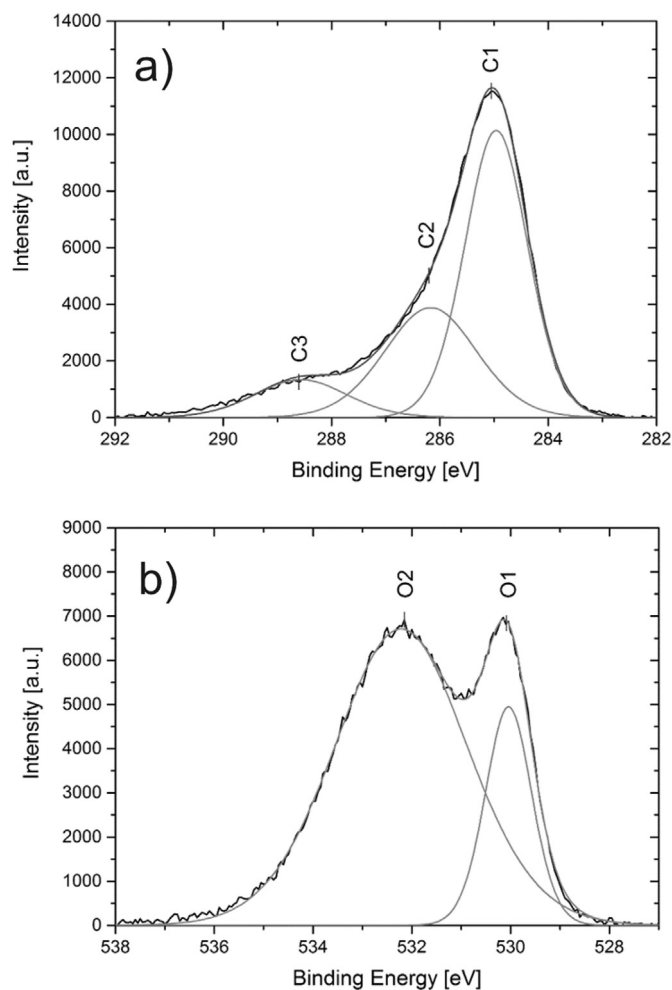


Fig. 3. XPS spectra showing the spectral regions of (a) C1s atomic carbon orbitals, and (b) O1s atomic oxygen orbitals.

sp^3 hybridization state since this peak is located between the graphite-type peak at about 284.3 eV and the diamond peak at about 285.5 eV. The C1 peak, with 57.0% area, gives the dominant contribution to the C1s region. The C2 and C3 peaks are assigned to carbon atoms in C–O and C=O bond configurations, respectively. The C–O peak has about half the area of the C–C peak, and the C=O peak a much smaller fraction.

The spectrum in Fig. 3b gives the distribution of the O1s core level energy with the oxygen atom in different bond environments. Application of two fitting curves gives the best results. Two peaks are identified, at 530.0 eV (O1) and at 532.2 eV (O2) with areas of 20.6% and 79.4%, respectively. We assign the broad peak, at 532.2 eV, to carbons in C–O bonds at sp^2 and sp^3 hybridized carbons, i.e. with the carbon atoms located in a diamond-graphite hybrid environment. The fact, that both, sp^2 - and sp^3 -related peaks are not separated in the O1s distribution suggests that there is no phase separation between sp^2 and sp^3 regions in the sample, a result which we also had obtained considering the location of the C1s C–C peak at 285.0 eV.

It has been reported that oxygen atoms in carbon materials with adsorbed water yield a peak in the 536–537 eV range (536 eV [96], 537.1 eV [66]). Since no such peak is found in our XPS spectrum, we conclude that the water from the sucrose/naphthalene solution has been completely extracted in drying the samples.

4. Discussion

We first discuss the Raman results. We find for our foam sample that the D and G bands are distinctively separated, different from the broad distribution of one unresolved peak observed for amorphous carbon [67]. This reveals that the foams have an ordered atomic structure.

In a survey, values for the G-band position between $\sim 1554\text{ cm}^{-1}$ and $\sim 1595\text{ cm}^{-1}$ have been given for a range of graphene-, nano-tube-, and fullerene-type carbon allotropes [68]. The G peak is positioned at 1581 cm^{-1} [68] in pristine graphite. However, it is usually shifted to higher values for the various nanocarbon materials. It was, for example, detected at 1593 cm^{-1} for carbon nanopearls [69], at 1591 cm^{-1} for carbon nanospheres [70] and 1595 cm^{-1} for graphene nanosheets [71]. The upshift of the Raman band has been attributed to highly-curved structures and small sizes of carbon species [68]. In our study of the carbon nanofoams we find the G band at 1589 cm^{-1} , which suggests that the nanofoam has a wall structure composed of curved graphene walls.

Numerous studies have shown that the D-band lies at $\sim 1350\text{ cm}^{-1}$ and is quite insensitive to the type of nanocarbons considered. It has been located at this value for porous carbon scaffolds (1350 cm^{-1} , [72]), disordered nanocarbons (1350 cm^{-1} , [73]), nanopearls (1350 cm^{-1} , [69]), carbon nanotubes (1349 cm^{-1} , [74]), and others. It was found at slightly higher values (1358 cm^{-1} , [75]) for cluster-assembled carbons, and at a lower value (1337 cm^{-1} , [70]) for carbon nanospheres. For the nanofoam sample in this study we find a value of 1371 cm^{-1} for the D band position which is consistent with the nanoporous structure of the foam having a curved and strained wall structure.

The characteristic Raman band has been observed at $\sim 1332\text{ cm}^{-1}$ for diamond films [76] and for nanocrystalline diamond [77]. In the case of phase separation, separate diamond and graphite areas would be present in the foam. However, no corresponding feature is found in the foam spectrum. We conclude that no indication for a phase separation of sp^2 and sp^3 regions is found.

We note that our foam samples show some structure in the Raman spectrum for wave numbers $\sim 1850\text{--}2140\text{ cm}^{-1}$, the range where features due to carbon chains are usually observed [73]. In this wavenumber range one expects a band originating from vibrations of carbon triple bonds, associated with the presence of conjugated polyacetylenic bonds with a distribution of chain lengths. The slightly enhanced intensity for wavenumbers $\sim 1850\text{--}2140\text{ cm}^{-1}$, displayed in Fig. 2, indicates that carbon triple bonds are included in the cell structure of the foam.

We don't have any indication for a 2D peak in our sample; if present, its intensity is below the noise level. The 2D band, located near 2700 cm^{-1} , gives a very strong peak for pristine graphene. However it is substantially reduced in finite graphene nanosheets [78]. Also, its intensity is sensitive to the degree of order in the sample. When exposed to Ar^+ -ion bombardment, this band significantly decreases, as shown in a study where the distance between ion impact-produced point defects was changed from 24 nm to 2 nm [79]. This reveals, that increasing degree of disorder leads to a suppression of the 2D band. Therefore, this band is usually not present in defective carbons such as graphene oxide and graphene aerogels [80]. Another property influencing the occurrence and height of the 2D peak is the curvature of the graphene network. It has been shown that the 2D peak becomes significantly lower when the diameter of a nanotube is reduced from 20 nm to 3 nm [81]. These results indicate that the nanofoams in our study have a strongly-curved defective graphene-type wall structure.

The nanofoam samples show features in the Raman spectrum in the wavenumber range of $800\text{--}1100\text{ cm}^{-1}$, as seen in Fig. 2 at

847.5 cm^{-1} and 1043.9 cm^{-1} . Two peaks in this range, at 860 cm^{-1} and 1100 cm^{-1} , have previously been observed for carbon onions [82]. A 1150 cm^{-1} mode has also been found for nanocrystalline diamond [83]. A peak at 1190 cm^{-1} was observed for amorphous hydrogenated carbon films produced by plasma deposition [84]. We conclude that our observed band at 847.5 cm^{-1} may originate from structures similar to carbon onions. The 1043.9 cm^{-1} band is well below the band for nanocrystalline diamond. Therefore there is no indication for a diamond-graphite phase separation in our samples.

Five bands characterize the Raman spectrum of naphthalene (C_{10}H_8); at 513.8 cm^{-1} , 763.8 cm^{-1} , 1021.6 cm^{-1} , 1382.2 cm^{-1} , and 1464.5 cm^{-1} [85]. The Raman spectrum of our foam sample does not show any sharp peaks at these wave numbers which points to complete carbonization of the naphthalene in the hydrothermal process of the sucrose/naphthalene solution.

Next we discuss the XPS results. Deconvolution of the C1s envelope for the nanofoams yields three peaks, labeled as C1, C2, and C3 in Fig. 3a. We attribute the C1 component to C–C bonds, the C2 and C3 peaks to C–O and C=O bonds, respectively.

We consider the location of the C1 core line. There is a general agreement (within ± 0.2 eV) about the binding energy of 284.3 eV for the 1s electron of a carbon atom in pristine graphite [86]. This binding energy is also found for a variety of C-based materials such as graphite oxide [87], multiwall carbon nanotubes [88], amorphous carbon films [89], carbon blacks [66], thin films of C_{60} [90], graphene [91], graphene oxide [92], and others. The location of this peak has been shown to be quite insensitive to strong changes in the carbon material's crystalline order. It was found, that with intense Ar^+ ion radiation of highly-oriented pyrolytic graphite (HOPG), the position of the C1 peak remained almost unchanged while the width (FWHM) changed significantly, from 0.6 eV to 1.5 eV [93]. Yet, small shifts to higher binding energies of 284.6 eV [94], 284.7 eV [95], and 284.8 eV [96] have been observed for various graphene oxide materials. In our studies of carbon nanofoams we also find an upward shift of the binding energy and observe the C–C peak at 284.96 eV. This indicates that the cellular walls of the foam in this study have structures related to graphene oxide.

This shift in binding energy may be explained by the presence of highly-curved and strained graphene walls in the foam structure. In fact, a value of 284.92 eV has been observed for strongly-curved single-wall carbon nanotubes [88]. The observed peak position is slightly below the sp^3 -originated C1s peak, which was found in the range of 285.2 eV–285.8 eV for diamond [97], hydrogenated amorphous carbon films [89], CVD diamond [89], and other diamond-like structures [98]. Therefore we suggest that the foam sample is characterized by a hybrid sp^2 - sp^3 structure of cavities with curved graphene sidewalls and with sp^3 bonds providing the links for the 3-dimensional graphene-like network. Hybrid graphene-diamond structures have been previously suggested by several research groups, with respect to their structural [99,100] and electronic [8] properties, and to their phase stability [101].

Another area of discussion is the width of the observed XPS peaks. For highly oriented pyrolytic graphite (HOPG) the crystals have close-to perfect atomic structures and the C1s peak is narrow, with a FWHM of 0.45 eV [93]. In defect-free graphite the electronic environment is the same for all carbon atoms. Consequently, the XPS spectrum of HOPG shows a narrow peak. The width of the peak is related to the heterogeneity of the electronic environment of the carbon atoms. Differences in the nearest-neighbor configuration will slightly shift the binding energy and cause a broadening of the observed peak. For the foam sample we determine a full-width at half maximum (FWHM) of 1.4 eV. We explain this by the

heterogeneity of the hybrid structure containing sp^2 - and sp^3 -type carbon atoms without a major phase separation.

The C2 peak in the C1s distribution, at 286.2 eV, has an area of 32.0%. It has been assigned to C–OH bonds in a number of studies of graphene oxide with reported values of 286.4 eV [102] and 286.2 eV [96]. It is typically found in the range of 285.5 eV–287.5 eV with carbon samples prepared under various conditions [103]. The peak receives its relatively large width from the coexistence of carbons in sp^2 and sp^3 configurations.

The C3 peak, at 288.6 eV, has a relative area of 11.0% and can be associated with C=O and carboxyl (COOH) groups [98,99]. These two functional groups usually are strong features in graphene oxide [104]. The C3 peak in our sample is well below the peaks at 290.6 eV and 291.6 eV usually assigned to shake-up satellite ($\pi \rightarrow \pi^*$) and plasmon excitations, respectively [105]. In shake-up events the emission process is accompanied by the promotion of an electron in one of the highest occupied orbitals into one of the lowest unoccupied orbitals. This leads to a photoelectron emitted from the solid with lower kinetic energy and the appearance of a higher binding energy for the C1s state. The lack of a plasmon excitation feature shows the insulating character of the foam sample. Both excitations, characteristic for HOPG, do not appear to be present in our foam sample or are too weak to give a measurable signal in the XPS spectrum. In fact, these features, related to the perfect crystal structure of HOPG, disappear when HOPG is exposed to Ar^+ ion radiation, i.e. with increasing degree of disorder [86].

One of the main objectives in the synthesis of new carbon materials is to find allotropes composed of carbon atoms in combined hybridized states, such as sp-sp^3 , $\text{sp}^2\text{-sp}^3$, or $\text{sp-sp}^2\text{-sp}^3$. Also, carbon atoms may exist in intermediate states sp^n , where n is a fractional number, with $1 < n < 2$ for cyclo(N)carbons and $2 < n < 3$ for closed-frame structures [106]. On the other hand, two phases may coexist side by side in different areas of a sample. For example, self-formed C_{60} inclusions were found in hydrogenated carbon films [107]. In this respect, it is interesting to ask if there is phase separation between different hybridizations in the foam sample. For example, clusters of sp^3 -bonded carbons could be incorporated in a graphitic framework. If nanodiamond-type clusters were constituents of the sample, one should observe a narrow C1s peak according to these species. The 1s core level peak of pristine nanodiamonds was observed at 289.07 eV [108], which is about 3 eV above the sp^3 peak in bulk diamond. Since no such peak is seen in our XPS spectra, we can exclude that nanodiamond areas are part of the foam structure. The spectra rather indicate that the foam scaffold is made of mixed sp^2/sp^3 bonding in a graphite-diamond hybrid network.

Information provided by analysis of the O1s spectra can complement the information from the analysis of C1s spectra. We note that, because the O1s photoelectron kinetic energies are lower than those of the C1s, the O1s sampling depth is smaller, and therefore the O1s spectra are slightly more surface specific.

In Fig. 3b we display the O1s binding energy distribution in the 525 eV–545 eV region. The spectrum shows two main features; a broad peak with relative peak area of 79.4% centered at 532.2 eV and a narrow peak centered at 530.0 eV with 20.6 area%. The observed maxima are very close to those found for oxygen-treated carbon materials [109]. A peak at ~ 533 eV is usually assigned to oxygen atoms bonded to carbon through aromatic sp^2 orbitals. A peak at ~ 531 eV is usually attributed to oxygen bonded to carbon through aliphatic sp^3 orbitals. The assumption of the coexistence of two different oxygen functionalities in our sample is supported by the very broad O1s peak at 532.2 eV, with a FWHM of about 3 eV.

The O1 peak, at 530.0 eV, is narrow and rarely seen in carbon nanomaterials. However, it was observed in the studies of a single layer graphene on Cu foil [110] with oxygen atoms adsorbed to the

surface of the layer. In another study, this peak was found at 530.6 eV for graphene oxide and was assigned to oxygen atoms in C=O bonds [111]. It is commonly observed, that the basal plane of graphene in graphene oxide is functionalized mostly with epoxide and hydroxyl groups, and the edges with carbonyl and carboxyl groups. Therefore, for the foam samples in this study, we ascribe the peak at 530.0 eV to oxygen atoms bonded to the basal plane of graphene oxide walls forming the cavities of the nanoporous foam structure.

We note that the type of oxygen functionalities present at the carbon surface affects the electrochemical response of the carbon material. It has been found that microporous carbon materials cannot be fully wetted in aqueous solutions because of their hydrophobic character [112]. Higher oxygen content affects the electric field in the surface by changing local polarity, which leads to an increase of the interaction with water molecules [61]. The prospects of future applications of carbon nanofoams may depend on the type of oxygen functionalization in the foams, and basal-plane-attached oxygen atoms may play a significant role in determining the electrochemical properties.

It is not possible to directly determine if the micropores seen in the images of Fig. 1b are hollow with a thin graphite skin or if they are solid with a cellular structure of cavities on the nanometer scale. Both topologies could describe the ultralow density of the foam. However, since we don't observe any water or sucrose signatures in Raman and XPS spectra, the cellular structure with open channels to the periphery of the foam seems to better describe the foam morphology. These structures presumably have on the nanoscale the topology of "negative-curvature" carbons (NCCs) with graphene-thin walls, similar to 'schwartzites', with sp^2 and sp^3 carbons forming an aperiodic space structure. N-gons larger than hexagons may also contribute to the curved graphitic structure [113]. Basal-plane hydrogenation and oxidation of the graphene wall leads to out-of-plane corrugation and strain, as found in materials such as graphene oxide and graphane [114]. Similar structures seem to describe the walls of the nanofoams in this study.

5. Conclusion

We have shown with our investigations that a small amount of naphthalene added to an aqueous sucrose solution, processed in a hydrothermal reactor, leads to the formation of carbon nanofoam. No traces of sucrose and naphthalene are detected in the foam and we conclude that the sucrose/naphthalene solution has completely been carbonized. The obtained foam has a continuous structure and has ultralow mass density. He-ion microscopy studies show an assembly of micron-sized carbon pearls as the structure of the foam on the micrometer length scale. With further magnification, features on as small as ~25 nm are observed. A porous structure on the nanometer length scale is required in order to explain the ultralow density of the foam. Raman and XPS studies of the foam sample reveal the characteristic spectroscopic features of nanocarbons. In addition, detailed analysis shows that signatures from aromatic and aliphatic bonds are not separated but lead to combined peaks. This observation helps to better understand the topologically complex carbon foam structure. It indicates that there is no phase separation between graphite- and diamond-like regions and that the foams are structured as a network of carbons in a hybrid sp^2/sp^3 orbital configuration. Further, the Raman and XPS results suggest that on the nanometer scale the foams appear to be composed of a curved graphene scaffold with oxygen functional groups at the basal-plane of graphene. Neither water, sucrose, or naphthalene signatures are seen in the spectra which suggests that the foam morphology does not contain closed cavities but has channels open to the periphery of the sample. Such an open cellular structure might be useful for

future applications of the material as a hydrogen gas or biomedical liquid storage medium.

Acknowledgement

The authors thank Christof Neumann for technical help with the Raman spectrometer.

References

- [1] H. Jo, et al., Novel method of powder-based processing of copper nanofoams for their potential use in energy applications, *Mater. Chem. Phys.* 145 (1–2) (2014) 6–11.
- [2] M. Castro, et al., Pattern-wavelength coarsening from topological dynamics in silicon nanofoams, *Phys. Rev. Lett.* 112 (9) (2014).
- [3] Y.J. Fu, et al., Template-free synthesized Ni nanofoams as nanostructured current collectors for high-performance electrodes in lithium ion batteries, *J. Mater. Chem. A* 1 (34) (2013) 10002–10007.
- [4] M. Caro, et al., Radiation induced effects on mechanical properties of nanoporous gold foams, *Appl. Phys. Lett.* 104 (23) (2014).
- [5] A. Kurek, et al., Silica Nanofoam (NF) supported single- and dual-site catalysts for ethylene polymerization with morphology control and tailored bimodal molar mass distributions, *Macromolecules* 46 (23) (2013) 9197–9201.
- [6] S. Jayaraman, et al., High T(G)polyimide nanofoams derived from pyromellitic dianhydride and 1,1-bis(4-aminophenyl)-1-phenyl-2,2,2-trifluoromethane, *Abstr. Pap. Am. Chem. Soc.* 207 (1994), p. 20-POLY.
- [7] S. Tabandeh, F.A. Taromi, H. Nazockdast, Flexible polyurethane nano-composite foam: synthesis and properties, *Polym. Sci. Ser. B* 56 (5) (2014) 681–685.
- [8] F.J. Ribeiro, et al., Structural and electronic properties of carbon in hybrid diamond-graphite structures, *Phys. Rev. B* 72 (21) (2005).
- [9] C.Z. Wang, K.M. Ho, Structure, dynamics, and electronic-properties of diamond-like amorphous-carbon, *Phys. Rev. Lett.* 71 (8) (1993) 1184–1187.
- [10] O.S. Panwar, et al., XPS and XAES studies of as grown and nitrogen incorporated tetrahedral amorphous carbon films deposited by pulsed unfiltered cathodic vacuum arc process, *Appl. Surf. Sci.* 221 (1–4) (2004) 392–401.
- [11] A.V. Rode, et al., Electronic and magnetic properties of carbon nanofoam produced by high-repetition-rate laser ablation, *Appl. Surf. Sci.* 197 (2002) 644–649.
- [12] R. Blinc, et al., Carbon nanofoam as a potential hydrogen storage material, *Phys. Status Solidi B Basic Solid State Phys.* 244 (11) (2007) 4308–4310.
- [13] C.N. Chervin, et al., Carbon nanofoam-based cathodes for Li-O₂ batteries: correlation of pore solid architecture and electrochemical performance, *J. Electrochem. Soc.* 160 (9) (2013) A1510–A1516.
- [14] A.V. Rode, et al., Unconventional magnetism in all-carbon nanofoam, *Phys. Rev. B* 70 (5) (2004).
- [15] J. Garcia-Martinez, T.M. Lancaster, J.Y. Ying, Synthesis and catalytic applications of self-assembled carbon nanofoams, *Adv. Mater.* 20 (2) (2008) 288–292.
- [16] C. Mathioudakis, P.C. Kelires, Atomistic simulations of low-density nanoporous materials: carbon nanofoams, *Phys. Rev. B* 87 (19) (2013).
- [17] S. Charnvanichborikarn, et al., Nanoporous Cu-C composites based on carbon-nanotube aerogels, *J. Mater. Chem. A* 2 (4) (2014) 962–967.
- [18] Z. Zhu, et al., Topologically protected conduction state at carbon foam surfaces: an Ab initio Study, *Phys. Rev. Lett.* 112 (2) (2014).
- [19] B.B. Chang, et al., Synthesis of sulfonated porous carbon nanospheres solid acid by a facile chemical activation route, *J. Solid State Chem.* 221 (2015) 384–390.
- [20] L.Q. Duan, et al., Fabrication and electrochemical performance of nanoporous carbon derived from silicon oxycarbide, *Microporous Mesoporous Mater.* 202 (2015) 97–105.
- [21] S.I. Kim, et al., Making porous conductive carbon films with unbalanced magnetron sputtering, *Jpn. J. Appl. Phys.* 54 (1) (2015).
- [22] X.Y. Zhu, Y.P. Zhao, Atomic mechanisms and equation of state of methane adsorption in carbon nanopores, *J. Phys. Chem. C* 118 (31) (2014) 17737–17744.
- [23] S. Leyva-Garcia, et al., New insights on electrochemical hydrogen storage in nanoporous carbons by in situ Raman spectroscopy, *Carbon* 69 (2014) 401–408.
- [24] R.S. Kalubarme, C.J. Park, P.M. Shirage, Two-dimensional mesoporous carbon electrode for high energy density electrochemical supercapacitors, *J. Nanosci. Nanotechnol.* 15 (2) (2015) 1253–1260.
- [25] J. Yin, et al., Meso- and micro-porous composite carbons derived from humic acid for supercapacitors, *Electrochim Acta* 136 (2014) 504–512.
- [26] L. Zhong, et al., Pd nanoparticles embedded in mesoporous carbon: a highly efficient catalyst for Suzuki-Miyaura reaction, *Catal. Today* 243 (2015) 195–198.
- [27] Y.B. Wang, H.Y. Zhao, G.H. Zhao, Iron-copper bimetallic nanoparticles embedded within ordered mesoporous carbon as effective and stable heterogeneous Fenton catalyst for the degradation of organic contaminants, *Appl. Catal. B Environ* 164 (2015) 396–406.

- [28] Y. Liu, et al., Porous carbon spheres via microwave-assisted synthesis for capacitive deionization, *Electrochim Acta* 151 (2015) 489–496.
- [29] D.L. Xiao, et al., Porous carbon quantum dots: one step green synthesis via L-cysteine and applications in metal ion detection, *RSC Adv.* 5 (3) (2015) 2039–2046.
- [30] F. Barroso-Bujans, et al., Intercalation and confinement of poly(ethylene oxide) in porous carbon nanoparticles with controlled morphologies, *Macromolecules* 47 (24) (2014) 8729–8737.
- [31] K. Tekin, S. Karagoz, S. Bektas, A review of hydrothermal biomass processing, *Renew. Sustain. Energy Rev.* 40 (2014) 673–687.
- [32] A. Bazargan, et al., A review: synthesis of carbon-based nano and micro materials by high temperature and high pressure, *Ind Eng. Chem. Res.* 52 (36) (2013) 12689–12702.
- [33] N.P. Economou, J.A. Nottle, W.B. Thompson, The history and development of the helium ion microscope, *Scanning* 34 (2) (2012) 83–89.
- [34] S.A. Boden, et al., Ionoluminescence in the helium ion microscope, *Microsc. Microanal.* 18 (6) (2012) 1253–1262.
- [35] K. Ohya, T. Yamanaka, Modeling secondary electron emission from nanostructured materials in helium ion microscope, *Nucl. Instrum. Methods Phys. Res. Sect. B Beam Interact. Mater. Atoms* 315 (2013) 295–299.
- [36] S. Sijbrandij, et al., Analysis of subsurface beam spread and its impact on the image resolution of the helium ion microscope, *J. Vac. Sci. Technol. B* 28 (6) (2010). C6F6–C6F9.
- [37] S. Sijbrandij, et al., Elemental analysis with the helium ion microscope, *J. Vac. Sci. Technol. B* 26 (6) (2008) 2103–2106.
- [38] P. Kerber, et al., Study of surface cleaning methods and pyrolysis temperatures on nanostructured carbon films using X-ray photoelectron spectroscopy, *J. Vac. Sci. Technol. A* 30 (6) (2012).
- [39] A. Achour, et al., Electrochemical anodic oxidation of nitrogen doped carbon nanowall films: X-ray photoelectron and Micro-Raman spectroscopy study, *Appl. Surf. Sci.* 273 (2013) 49–57.
- [40] M. Tagawaa, et al., Synchrotron radiation photoelectron spectroscopy and near-edge X-ray absorption fine structure study on oxidative etching of diamond-like carbon films by hyperthermal atomic oxygen, *Appl. Surf. Sci.* 256 (24) (2010) 7678–7683.
- [41] R. Haerle, et al., sp(2)/sp(3) hybridization ratio in amorphous carbon from C 1s core-level shifts: X-ray photoelectron spectroscopy and first-principles calculation, *Phys. Rev. B* 65 (4) (2002).
- [42] B.K. Tay, et al., Investigation of tetrahedral amorphous carbon films using X-ray photoelectron and Raman spectroscopy, *Surf. Interface Anal.* 28 (1) (1999) 231–234.
- [43] S.K. Gordeev, et al., Study of bonding in nanoporous carbon by X-ray photoelectron spectroscopy, *Mol. Mater.* 13 (1–4) (2000) 355–360.
- [44] M. Manickam, M. Takata, Electrochemical and X-ray photoelectron spectroscopy studies of carbon black as an additive in Li batteries, *J. Power Sources* 112 (1) (2002) 116–120.
- [45] K.V.V. Rao, et al., X-Ray Photoelectron spectroscopy studies on activated carbon prepared from rind of citrus nobilis, *Asian J. Chem.* 22 (6) (2010) 4377–4381.
- [46] S. Oida, F.R. McFeely, A.A. Bol, X-ray photoelectron spectroscopy study on Fe and Co catalysts during the first stages of ethanol chemical vapor deposition for single-walled carbon nanotube growth, *J. Appl. Phys.* 109 (6) (2011).
- [47] S. Takabayashi, et al., Chemical structural analysis of diamondlike carbon films with different electrical resistivities by X-ray photoelectron spectroscopy, *Jpn. J. Appl. Phys.* 47 (5) (2008) 3376–3379.
- [48] D.R. Lide, in: D.R. Lide (Ed.), *CRC Handbook of Chemistry and Physics*, 86 ed, CRC Press, Boca Raton (FL), 2005.
- [49] J.Z. Feng, J. Feng, C.R. Zhang, Thermal conductivity of low density carbon aerogels, *J. Porous Mater.* 19 (5) (2012) 551–556.
- [50] J. Marie, et al., Highly porous PEM fuel cell cathodes based on low density carbon aerogels as Pt-support: Experimental study of the mass-transport losses, *J. Power Sources* 190 (2) (2009) 423–434.
- [51] B. Zhou, et al., Preparation of low density and high mesoporosity carbon aerogels by an organic/inorganic hybrid method, *New Carbon Mater.* 26 (2) (2011) 117–122.
- [52] L.J. Peng, J.R. Morris, Structure and hydrogen adsorption properties of low density nanoporous carbons from simulations, *Carbon* 50 (3) (2012) 1394–1406.
- [53] R.B. dos Santos, F.D. Mota, R. Rivelino, A theoretical evaluation of the effect of water on the electronic properties of low density amorphous carbon nanoparticles, *Carbon* 50 (8) (2012) 2788–2795.
- [54] Y.N. Feng, et al., Pore size controllable preparation for low density porous nano-carbon, *J. Nanosci. Nanotechnol.* 13 (10) (2013) 7012–7015.
- [55] S.J. Shin, et al., Robust nanoporous alumina monoliths by atomic layer deposition on low-density carbon-nanotube scaffolds, *Carbon* 73 (2014) 443–447.
- [56] S. Chaurasia, et al., Laser interaction with low-density carbon foam, *Pramana Journal Phys.* 75 (6) (2010) 1191–1196.
- [57] A. Zani, et al., Ultra-low density carbon foams produced by pulsed laser deposition, *Carbon* 56 (2013) 358–365.
- [58] T. Urakawa, et al., Mass density control of carbon films deposited by H-assisted plasma CVD method, *Surf. Coatings Technol.* 228 (2013) S15–S18.
- [59] H. Sugime, et al., Growth kinetics and growth mechanism of ultrahigh mass density carbon nanotube forests on conductive Ti/Cu supports, *ACS Appl. Mater. Interfaces* 6 (17) (2014) 15440–15447.
- [60] R. Brandt, J. Fricke, Acetic-acid-catalyzed and subcritically dried carbon aerogels with a nanometer-sized structure and a wide density range, *J. Non-Cryst. Solids* 350 (2004) 131–135.
- [61] M.J. Bleda-Martinez, et al., Chemical and electrochemical characterization of porous carbon materials, *Carbon* 44 (13) (2006) 2642–2651.
- [62] A.C. Ferrari, J. Robertson, Interpretation of Raman spectra of disordered and amorphous carbon, *Phys. Rev. B* 61 (20) (2000) 14095–14107.
- [63] H. Hepp, K. Siegmann, K. Sattler, New aspects of growth mechanisms for polycyclic aromatic-hydrocarbons in-diffusion flames, *Chem. Phys. Lett.* 233 (1–2) (1995) 16–22.
- [64] J. Schwan, et al., Tetrahedral amorphous carbon films prepared by magnetron sputtering and dc ion plating, *J. Appl. Phys.* 79 (3) (1996) 1416–1422.
- [65] M. Sarno, et al., A study of the key parameters, including the crucial role of H-2 for uniform graphene growth on Ni foil, *J. Mol. Catal. A Chem* 366 (2013) 303–314.
- [66] D. Pantea, et al., Electrical conductivity of conductive carbon blacks: influence of surface chemistry and topology, *Appl. Surf. Sci.* 217 (1–4) (2003) 181–193.
- [67] M. Chhowalla, et al., Evolution of sp(2) bonding with deposition temperature in tetrahedral amorphous carbon studied by Raman spectroscopy, *Appl. Phys. Lett.* 76 (11) (2000) 1419–1421.
- [68] S. Gupta, A. Saxena, Nanocarbon materials: probing the curvature and topology effects using phonon spectra, *J. Raman Spectrosc.* 40 (9) (2009) 1127–1137.
- [69] C.N. Hunter, et al., Tribological properties of carbon nanopearls synthesized by nickel-catalyzed chemical vapor deposition, *Tribol. Lett.* 30 (3) (2008) 169–176.
- [70] D. Yuan, et al., Preparation of monodisperse carbon nanospheres for electrochemical capacitors, *Electrochem. Commun.* 10 (7) (2008) 1067–1070.
- [71] G. Wang, et al., Facile synthesis and characterization of graphene nanosheets, *J. Phys. Chem. C* 112 (22) (2008) 8192–8195.
- [72] M.T. Johnson, K.T. Faber, Catalytic graphitization of three-dimensional wood-derived porous scaffolds, *J. Mater. Res.* 26 (1) (2011) 18–25.
- [73] M.A. Pimenta, et al., Studying disorder in graphite-based systems by Raman spectroscopy, *Phys. Chem. Chem. Phys.* 9 (11) (2007) 1276–1291.
- [74] L. Ci, R. Vajtai, P.M. Ajayan, Vertically aligned large-diameter double-walled carbon nanotube arrays having ultralow density, *J. Phys. Chem. C* 111 (26) (2007) 9077–9080.
- [75] D. Bolgiaghi, et al., Pulsed laser deposition of glass-like cluster assembled carbon films, *Carbon* 43 (10) (2005) 2122–2127.
- [76] A.A. Zakhidov, et al., Carbon structures with three-dimensional periodicity at optical wavelengths, *Science* 282 (5390) (1998) 897–901.
- [77] J. Birrell, et al., Interpretation of the Raman spectra of ultrananocrystalline diamond, *Diam. Relat. Mater.* 14 (1) (2005) 86–92.
- [78] G.X. Wang, et al., Facile synthesis and characterization of graphene nanosheets, *J. Phys. Chem. C* 112 (22) (2008) 8192–8195.
- [79] L.G. Cancado, et al., Quantifying defects in graphene via Raman spectroscopy at different excitation energies, *Nano Lett.* 11 (8) (2011) 3190–3196.
- [80] M.A. Worsley, et al., High surface area, sp(2)-cross-linked three-dimensional graphene monoliths, *J. Phys. Chem. Lett.* 2 (8) (2011) 921–925.
- [81] E.F. Antunes, et al., Influence of diameter in the Raman spectra of aligned multi-walled carbon nanotubes, *Carbon* 45 (5) (2007) 913–921.
- [82] D. Roy, et al., Characterisation of carbon nano-onions using Raman spectroscopy, *Chem. Phys. Lett.* 373 (1–2) (2003) 86–92.
- [83] A.C. Ferrari, J. Robertson, Origin of the 1150-cm⁻¹ Raman mode in nanocrystalline diamond, *Phys. Rev. B* 63 (12) (2001).
- [84] J. Schwan, et al., Raman spectroscopy on amorphous carbon films, *J. Appl. Phys.* 80 (1) (1996) 440–447.
- [85] S. Fukura, et al., Factors determining the stability, resolution, and precision of a conventional Raman spectrometer, *Appl. Spectrosc.* 60 (8) (2006) 946–950.
- [86] G. Speranza, N. Laidani, Measurement of the relative abundance of sp(2) and sp(3) hybridised atoms in carbon based materials by XPS: a critical approach. Part I, *Diam. Relat. Mater.* 13 (3) (2004) 445–450.
- [87] S. Stankovich, et al., Stable aqueous dispersions of graphitic nanoplatelets via the reduction of exfoliated graphite oxide in the presence of poly(sodium 4-styrenesulfonate), *J. Mater. Chem.* 16 (2) (2006) 155–158.
- [88] T.I.T. Okpalugo, et al., High resolution XPS characterization of chemical functionalised MWCNTs and SWCNTs, *Carbon* 43 (1) (2005) 153–161.
- [89] J. Filik, et al., XPS and laser Raman analysis of hydrogenated amorphous carbon films, *Diam. Relat. Mater.* 12 (3–7) (2003) 974–978.
- [90] N. Swami, H. He, B.E. Koel, Polymerization and decomposition of C-60 on Pt(111) surfaces, *Phys. Rev. B* 59 (12) (1999) 8283–8291.
- [91] S. Park, et al., Aqueous suspension and characterization of chemically modified graphene sheets, *Chem. Mater.* 20 (21) (2008) 6592–6594.
- [92] C. Mattevi, et al., Evolution of electrical, chemical, and structural properties of transparent and conducting chemically derived graphene thin films, *Adv. Funct. Mater.* 19 (16) (2009) 2577–2583.
- [93] G. Speranza, N. Laidani, Measurement of the relative abundance of sp(2) and sp(3) hybridised atoms in carbon based materials by XPS: a critical approach. Part II, *Diam. Relat. Mater.* 13 (3) (2004) 451–458.
- [94] S.F. Pei, H.M. Cheng, The reduction of graphene oxide, *Carbon* 50 (9) (2012) 3210–3228.
- [95] Y.P. Zhang, C.X. Pan, TiO₂/graphene composite from thermal reaction of graphene oxide and its photocatalytic activity in visible light, *J. Mater. Sci.* 46 (8) (2011) 2622–2626.

- [96] H.A. Becerril, et al., Evaluation of solution-processed reduced graphene oxide films as transparent conductors, *ACS Nano* 2 (3) (2008) 463–470.
- [97] Y. Kawabata, J. Taniguchi, I. Miyamoto, XPS studies on damage evaluation of single-crystal diamond chips processed with ion beam etching and reactive ion beam assisted chemical etching, *Diam. Relat. Mater.* 13 (1) (2004) 93–98.
- [98] R. Sharma, et al., Effect of substrate bias on SE, XPS and XAES studies of diamond-like carbon films deposited by saddle field fast atom beam source, *Appl. Surf. Sci.* 220 (1–4) (2003) 313–320.
- [99] H.R. Karfunkel, T. Dressler, New hypothetical carbon allotropes of remarkable stability estimated by modified neglect of diatomic overlap solid-state self-consistent field computations, *J. Am. Chem. Soc.* 114 (7) (1992) 2285–2288.
- [100] A.T. Balaban, D.J. Klein, C.A. Folden, Diamond graphite hybrids, *Chem. Phys. Lett.* 217 (3) (1994) 266–270.
- [101] K. Umemoto, et al., Carbon foam: spanning the phase space between graphite and diamond, *Phys. Rev. B* 64 (19) (2001).
- [102] K. Haubner, et al., The route to functional graphene oxide, *Chemphyschem* 11 (10) (2010) 2131–2139.
- [103] F.C. Tai, et al., Correlation between I-D/I-G ratio from visible Raman spectra and sp²/sp³ ratio from XPS spectra of annealed hydrogenated DLC film, *Mater. Trans.* 47 (7) (2006) 1847–1852.
- [104] A. Kaniyoor, et al., Wrinkled graphenes: a study on the effects of synthesis parameters on exfoliation-reduction of graphite oxide, *J. Phys. Chem. C* 115 (36) (2011) 17660–17669.
- [105] C. Moreno-Castilla, M.V. Lopez-Ramon, F. Carrasco-Marin, Changes in surface chemistry of activated carbons by wet oxidation, *Carbon* 38 (14) (2000) 1995–2001.
- [106] E.A. Belenkov, V.A. Greshnyakov, Classification schemes for carbon phases and nanostructures, *New Carbon Mater.* 28 (4) (2013) 273–283.
- [107] J.G. Buijnsters, et al., Direct spectroscopic evidence of self-formed C(60) inclusions in fullerene-like hydrogenated carbon films, *Appl. Phys. Lett.* 92 (14) (2008).
- [108] S. Talapatra, et al., Irradiation-induced magnetism in carbon nanostructures, *Phys. Rev. Lett.* 95 (9) (2005).
- [109] J.L. Hueso, et al., XPS investigation of the reaction of carbon with NO, O₂, N₂ and H₂O plasmas, *Carbon* 45 (1) (2007) 89–96.
- [110] A. Siokou, et al., Surface refinement and electronic properties of graphene layers grown on copper substrate: an XPS, UPS and EELS study, *Appl. Surf. Sci.* 257 (23) (2011) 9785–9790.
- [111] D. Yang, et al., Chemical analysis of graphene oxide films after heat and chemical treatments by X-ray photoelectron and Micro-Raman spectroscopy, *Carbon* 47 (1) (2009) 145–152.
- [112] S. Biniak, A. Swiatkowski, M. Pakula, Electrochemical studies of phenomena at active carbon-electrolyte solution interfaces, in: L.R. Radovic (Ed.), *Chemistry and Physics of Carbon*, Vol. 27, 2001, pp. 125–225.
- [113] H. Terrones, M. Terrones, Curved nanostructured materials, *New J. Phys.* 5 (2003).
- [114] K. Xue, Z.P. Xu, Strain effects on basal-plane hydrogenation of graphene: a first-principles study, *Appl. Phys. Lett.* 96 (6) (2010).



Fundamental properties of high-quality carbon nanofoam: from low to high density

Natalie Frese^{1,2}, Shelby Taylor Mitchell¹, Christof Neumann², Amanda Bowers¹, Armin Gölzhäuser² and Klaus Sattler^{*1}

Full Research Paper

[Open Access](#)**Address:**

¹Department of Physics and Astronomy, University of Hawaii, 2505 Correa Road, Honolulu, HI 96822, USA and ²Physics of Supramolecular Systems and Surfaces, Bielefeld University, Universitätsstraße 25, 33615 Bielefeld, Germany

Email:

Klaus Sattler* - sattler@hawaii.edu

* Corresponding author

Keywords:

carbon nanofoam; helium ion microscopy; hydrothermal carbonization; nanocarbons

Beilstein J. Nanotechnol. **2016**, *7*, 2065–2073.

doi:10.3762/bjnano.7.197

Received: 16 July 2016

Accepted: 06 December 2016

Published: 27 December 2016

This article is part of the Thematic Series "Physics, chemistry and biology of functional nanostructures III".

Guest Editor: A. S. Sidorenko

© 2016 Frese et al.; licensee Beilstein-Institut.

License and terms: see end of document.

Abstract

Highly uniform samples of carbon nanofoam from hydrothermal sucrose carbonization were studied by helium ion microscopy (HIM), X-ray photoelectron spectroscopy (XPS), and Raman spectroscopy. Foams with different densities were produced by changing the process temperature in the autoclave reactor. This work illustrates how the geometrical structure, electron core levels, and the vibrational signatures change when the density of the foams is varied. We find that the low-density foams have very uniform structure consisting of micropearls with $\approx 2\text{--}3\ \mu\text{m}$ average diameter. Higher density foams contain larger-sized micropearls ($\approx 6\text{--}9\ \mu\text{m}$ diameter) which often coalesced to form nonspherical μm -sized units. Both, low- and high-density foams are comprised of predominantly sp^2 -type carbon. The higher density foams, however, show an advanced graphitization degree and a stronger sp^3 -type electronic contribution, related to the inclusion of sp^3 connections in their surface network.

Introduction

Nanofoams are of considerable current interest due to their unique structure, which lies between two and three dimensions, allowing for many new types of materials with promising new functions for future technologies. Since many material functions rely on molecule–surface interactions and low-dimensional properties, materials with large surface areas and a quantum-confined nanoscale nature are of particular interest. Such conditions are provided by porous materials with nanometer dimensions. The main questions to be answered are related to

the synthetic methods for formation, the foam morphologies, and the electronic and vibronic properties.

Nanofoam materials derived from various chemical elements have been investigated. In particular, foams from transition metals and noble metals have attracted attention, and interesting applications have been developed. Nickel nanofoam has been used for glucose sensing [1] and also been suggested for high-performance supercapacitor electrodes [2]. Copper

nanofoms containing both micropores and nanopores have been produced for potential use in energy applications [3], and furthermore, copper nanofom substrates were used for the production of electrocatalysts [4]. Gold nanofoms have been found to show excellent catalytic properties [5]. Hydrogen thermoporometry was used to determine the pore architecture of gold and titania nanofoms [6]. Nanofoms from low-mass elements are interesting with respect to possible energy harvesting applications, e.g., high hydrogen storage capacity of 10 wt % in Be nanofom has been predicted [7]. Besides cellular structures, other scaffolds have been suggested in some cases, for example, for gold. Foms of connected gold nanowires have been designed in molecular dynamics computer simulations [8]. Also, for materials such as glass compounds, nanofom with a three-dimensional scaffold of interconnected nanowires have been produced [9]. A few studies of semiconductor and insulator nanofoms have also been reported. A sol–gel process was used to produce silicon nanofom and acousto-optic characteristics were probed [10]. Silica nanofom was used as a support material for highly active single- and dual-site catalysts [11]. Macroporous structured materials with cavities of about 100 nm in diameter have been reported for silica [12], and polyhedral nanofom shells with open cells have been produced [13]. A labyrinth internal structure has been found for tantalum oxide nanofoms [14]. All these studies show that functional nanofom materials can be produced from various chemical elements and compounds and that these foms are promising materials for future technologies. However, many questions about the relationship between fom morphologies and corresponding formation parameters are not answered. This is in particular true for nanofoms of carbon, which can occur in many different structural forms.

Among the chemical elements, carbon has the largest variety of possible electronic configurations. Therefore, many researchers have focused their interest in the study of novel carbon structures. A variety of production techniques have resulted in a large number of carbon materials with different sizes and structural properties. In particular, nanocarbons have been the focus since their properties depend critically on the synthetic methods, and as a consequence, many exciting developments have been reported [15].

The unique ability of carbon to occur in the form of sp^1 , sp^2 , and sp^3 hybridizations and combinations between these configurations results in a wide range of morphologies. Among these are the complex carbon materials with nanometer-sized porous structures such as carbon aerogels [16] and carbon sponges [17]. Carbon nanofoms have first been produced using pulsed laser ablation of glassy carbon in argon atmosphere [18] and later, as graphite in liquid nitrogen [19]. Pulsed-laser deposi-

tion has also been used for the fabrication of carbon nanofom electrodes [20]. Carbon nanotube fom in the form of aligned layered carbon nanotube structures infiltrated with pyrolytic carbon is considered useful in water treatment and oil spill cleanup [21]. Carbon nanofom paper [22] is proposed for energy storage applications. Carbon nanofom composites may be used for electrochemical capacitor electrodes [23] with potential application in high energy density electrochemical supercapacitors.

A promising formation method for high-quality carbon nanofom is the low-temperature hydrothermal carbonization of sucrose [24]. In order to produce advanced carbon nanomaterials, there is a need for further development of this method since it is environmentally friendly without the use of toxic chemicals. Using this technique, the foms tend to be composed of micrometer-sized spheres of predominantly sp^2 carbon that forms a three-dimensional open scaffold. These so-called micropearls are usually detected as individual units which are weakly connected, forming the fom structure. Their interaction is not strong enough for coalescence to occur. The hydrothermal process allows for the variation of growth parameters which may lead to further fom morphologies. The study of the parameter–morphology relationship can help to better understand the hydrothermal carbonization process, and in addition, to tune the growth toward particular materials structures. Such studies can considerably expand the possibility of production of nanomaterials by hydrothermal carbonization.

In this paper, we probe two carbon nanofom materials with different densities produced by naphthalene-assisted hydrothermal sucrose carbonization. Structural, compositional, and vibrational information is obtained by helium ion microscopy (HIM), XPS (X-ray photoelectron spectroscopy), and Raman spectroscopy, respectively. We find significant differences between low- and high-density foms. The low-density foms consist of small, individual micropearls with only a few being interconnected. The high-density foms are formed by much larger micropearls where most of them are coalesced into larger units. Both the signatures in the XPS and the Raman spectra are different for the two types of foms. We discuss the foms assuming a 3D-graphene-type network with open cavities forming the micropearl structures.

Experimental

Hydrothermal reactor

Two stainless steel autoclaves, each with a volume of 130 mL, were used for these studies; a setup which is similar to that applied in our previous studies on carbon nanofom [24]. The autoclaves were filled with 0.5 M sucrose solution, and subsequently 2 mg of naphthalene was added to each container. Then,

the autoclaves were sealed and connected to the heating supply. Subsequently, one of the autoclaves was kept at 150 °C, the other at 185 °C, each for 48 h. After cooling and opening, the carbon foams which had formed in the container were extracted. Then, boiling water was applied to separate the solid carbon foam from the remaining liquid solution. After drying, the mass densities of the foams were determined using a predefined volume container and a high-precision balance.

Helium-ion microscopy

An Orion Plus (Carl Zeiss) helium-ion instrument was used. An acceleration voltage of 34.9 keV and a beam current of 0.6 pA were applied, and secondary electrons were detected to obtain the images. Since the samples were not coated with conductive layers, an electron flood gun was applied to stabilize charging. Prior to imaging, the foam material was attached to the HIM sample holder with conductive carbon pads.

The HIM induces a high brightness, low-energy spread, subnanometer-size beam of helium ions [25]. An atomic-level ion source (ALIS) is used for the production of the helium ions. In this source, the beam is formed by ionization of helium atoms at a sharp needle held at high positive voltage. Such a beam of He ions has a diameter of typically less than one atom. It is focused onto the substrate under investigation using an electro-optical lens system. The image is then provided either by ionoluminescence [26], Rutherford backscattering of the ions [27], or secondary electron emission [28]. The high resolution is given by the small subsurface ion beam spread [29]. The instrument is suitable for the imaging of low-mass elements such as carbon due to its very high brightness. In addition to imaging, elemental analysis can be achieved with the He-ion microscope [30]. In this work we chose to use the secondary electron emission setup for imaging of our samples.

Raman spectroscopy

Raman spectroscopy is a valuable method for the characterization of carbon nanofoam [24]. In these studies, Raman spectra were recorded using a micro Raman spectrometer (LabRAM ARAMIS) which was operated in the backscattering mode. As light source we used a diode laser at 473 nm, which was focused onto the sample with a 10x microscope objective. A thermoelectrically-cooled CCD detector was applied to detect the scattered photon intensity. For the measurement, the foam was mounted on conductive carbon tape.

X-ray photoelectron spectroscopy (XPS)

X-ray photoelectron spectroscopy was performed in a UHV system (Multiprobe, Omicron) at a pressure $<10^{-9}$ mbar, as applied in our previous work on carbon nanofoams [24]. The combination of monochromatic Al K α irradiation, an electron

analyzer (Sphera) with a resolution of 0.9 eV, and an emission angle of 20° was used. The deconvolution of XPS peaks was performed by consideration of a Shirley background and symmetric Voigt functions. The foam was attached to the XPS sample holder by conductive carbon tape.

In XPS, the elemental composition is obtained by measuring the binding energy of photoelectrons which are emitted when a material is irradiated by X-rays. The method is surface sensitive due to the small inelastic mean free path of the photoelectrons. With XPS, bond information can also be obtained since the core level energies are affected by the chemical environment of the atoms. For example, for carbon atoms, bonds such as C–C, C=C, C–O, and C=O can be distinguished.

A large variety of carbon materials have been investigated by XPS. In particular, XPS reveals important bonding information about carbons with nanoscale units such as carbon nanotubes [31], diamond-like carbon films [32], nanostructured carbon films [33], tetrahedral amorphous carbon films [34], amorphous carbon [35], nanoporous carbon [36], activated carbon [37], or carbon black [38]. In addition, XPS is important for the analysis of chemical structure [39], in particular, for the investigation of the sp²/sp³ hybridization ratio [35].

Results

Density

We determined the density of the foam by averaging over the densities of several foam samples. Using two different process temperatures of 160 and 185 °C in the autoclave resulted in average densities of 0.104 g·cm⁻³ and 0.278 g·cm⁻³, respectively. These densities are significantly lower than the densities of graphite (2.267 g·cm⁻³), amorphous carbon (1.8–2.1 g·cm⁻³), carbon nanotubes (1.6 g·cm⁻³) or diamond (3.515 g·cm⁻³) [40].

Various types of low-weight carbons have been reported in the literature, with densities typically between 100 and 300 mg·cm⁻³. Among these are carbon aerogels [41–43], amorphous carbon nanoparticles [44,45], nanoporous carbons [46], carbon nanotube scaffolds [47], and carbon foams [48,49]. The densities of these carbon materials are significantly lower compared to “heavy carbons” such as pristine graphite (2.26 g·cm⁻³), CVD grown carbon films (2.14 g·cm⁻³ [50]), or carbon nanotube forests (1.6 to 0.38 g·cm⁻³ [51]). Some techniques have been reported which allow the production of carbons in a wide density range (0.20 to 1.4 g·cm⁻³ [52]) when production parameters were varied.

Microscopy

Figure 1a,b shows HIM images of low-density (LD) nanofoam, and high-density (HD) nanofoams in the lower-panels (c,d). In

Figure 1a,c, relatively large-scale images are shown, with a scale bar of 50 μm , for both, (LD) (a) and HD (c). It can be seen that both foams have a granular structure composed of small spherical-like units. This is further observed in the higher-magnified images of Figure 1b,d, with a scale bar of 10 μm . The low-density foams consist of nearly monodisperse small spheres with diameters between 2 and 3 μm . These micropearls have a narrow size distribution. The sample morphology is quite uniform over large areas. Occasionally, the micropearls are grown together forming larger units. However, in most cases, the micropearls are individually separated from each other. This is different for the high-density foams, displayed in Figure 1c,d. Here, the individual carbon spheres are larger in size and show a strong tendency for coalescence. In particular, Figure 1d shows that the spheres are connected with necks formed between them. Obviously the two materials, with low or high densities, are significantly different in form and size as seen by comparison of the images in Figure 1b,d.

Raman spectroscopy

The Raman spectra for low-density and high-density nanofoams are shown in Figure 2a,b, respectively. The two prominent carbon

peaks are displayed. For the low-density foams we find the G-peak at 1890 cm^{-1} and the D-peak at 1378 cm^{-1} . Both peaks are slightly shifted to lower wavenumbers of 1587.04 cm^{-1} and 1376.63 cm^{-1} in the high-density foam, respectively (Figure 2b). This shift may be explained by the additional strain of the sp^2 network due to the formation of the neck area between spheres. In addition, the ratio of these peaks is different for the two types of foams. In the high-density foam, the D- to G-peak ratio is 0.54, slightly smaller than the value of 0.59 as determined for the low-density foam. Even though the difference in the ratio is small, it suggests that the high-density foam is of an increased graphitization stage, having a higher content of sp^2 -type carbons with extended ordered graphitic regions. Increased process temperatures, resulting in higher-density foams, obviously assists the formation of ordered graphitic wall structures. On the other hand, it also leads to extended growth of the micropearls to larger sizes and to the coalescence of the spheres.

In disordered carbon, the G- and D-peaks are usually grown together forming one broad peak. In this respect it is interesting to note that the G- and D-distributions for the nanofoams in this

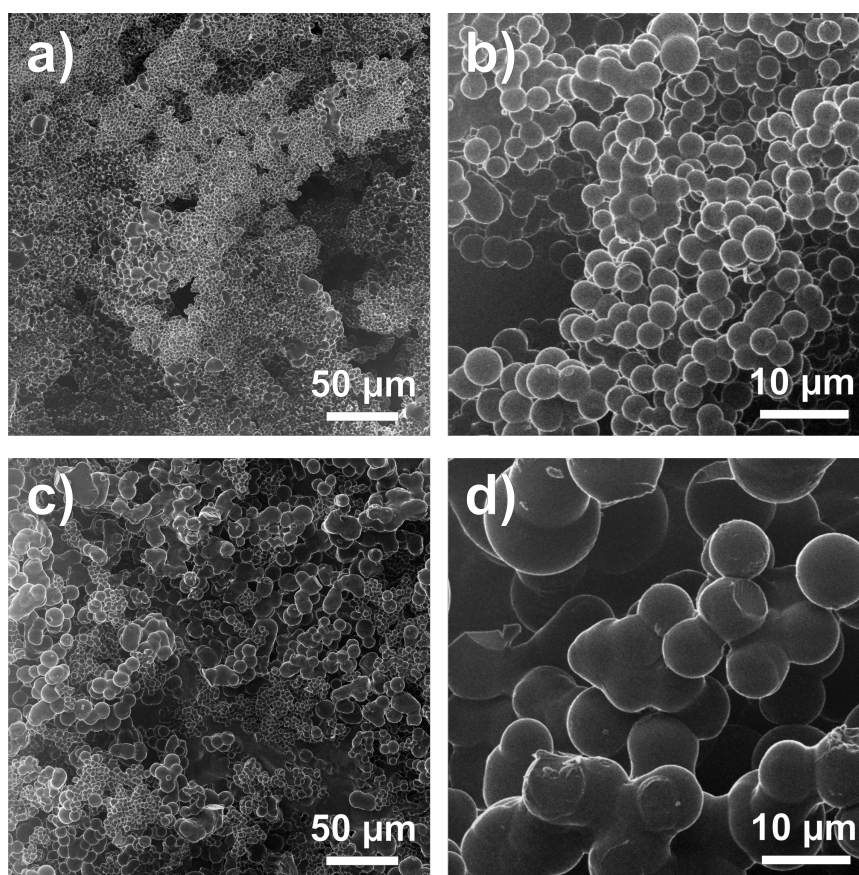


Figure 1: Helium-ion microscopy (HIM) images of low-density (a,b) and high-density (c,d) carbon nanofoams, with different magnifications.

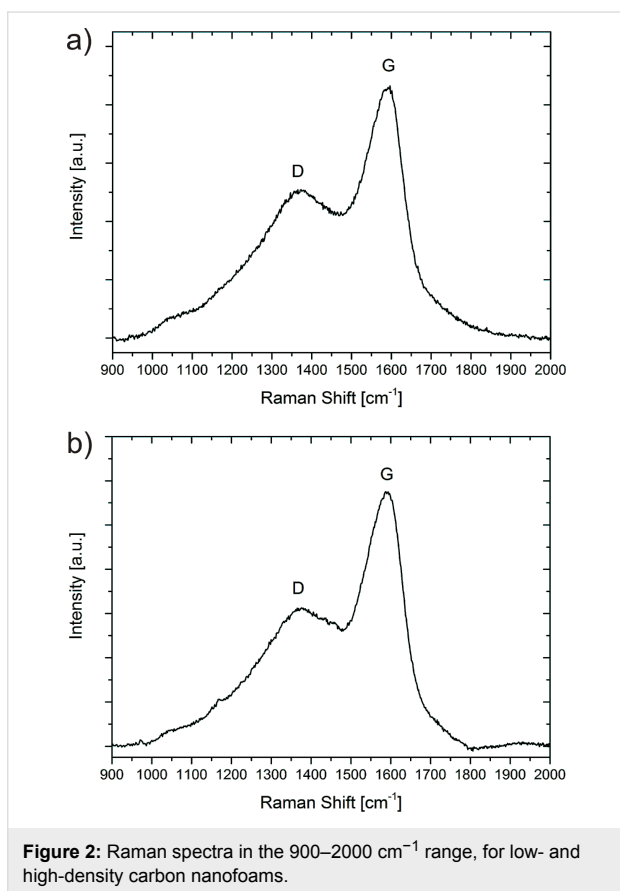


Figure 2: Raman spectra in the 900–2000 cm⁻¹ range, for low- and high-density carbon nanofoams.

study are formed by distinct peaks. This indicates that the micropearls consist of a relatively well-organized internal graphitic carbon structure.

We note that there is a gradual increase in the Raman intensity from 900 to 1376 cm⁻¹. This may be due to unidentified vibrations of various types of nanocarbons and possibly of hydrocarbons adsorbed in the foams. We note that at 1180 cm⁻¹, a peak was determined for nanocrystalline diamond films [53]. Also, two Raman features at 1180 and 1490 cm⁻¹ in addition to the G and D peaks were observed for carbon films prepared by magnetron sputtering [53]. A correlation between the 1180 cm⁻¹ peak and the sp³ content in these films was found [53]. At approximately this wavenumber, we see a small feature in the spectrum of Figure 2b. This indicates that a small diamond-like contribution is present in these foams.

XPS

In Figure 3, the XPS spectra of low- and high-density carbon nanofoams are shown. The deconvolution of the C1s peaks leads to the C1 and C2 peaks which are assigned to sp²- and sp³-type carbons, corresponding to electron binding energies of 284.4 and 285.4 eV, respectively [54]. An additional peak, C3, is detected at 288.6 and 288.5 eV, for the low- and high-density foams, respectively.

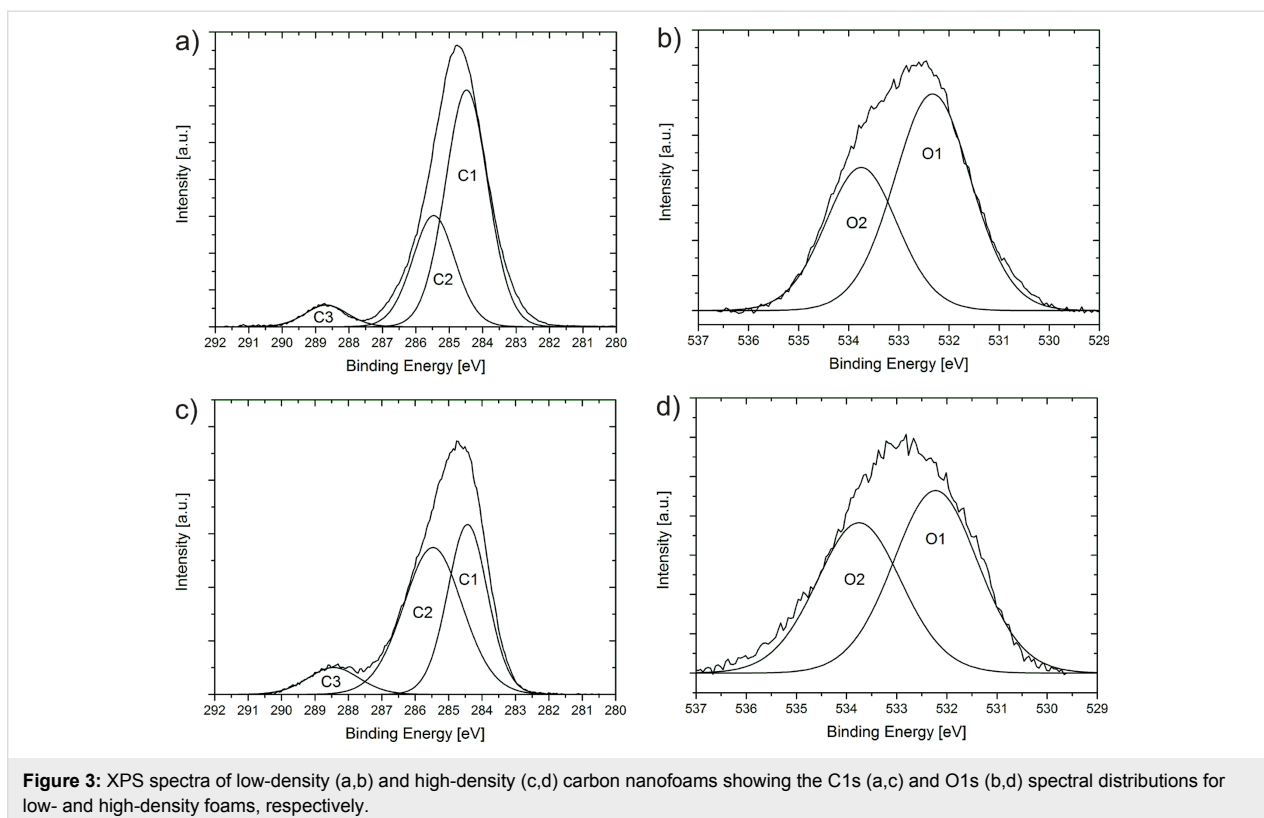


Figure 3: XPS spectra of low-density (a,b) and high-density (c,d) carbon nanofoams showing the C1s (a,c) and O1s (b,d) spectral distributions for low- and high-density foams, respectively.

Comparing the C1s distributions of Figure 3a,c for the two carbon foams we find that the shape of the C1s peak significantly changes from low to high density. In the low-density foam (a) the C1s distribution is close to that of the distribution for sp²-type carbon with a small asymmetry toward higher binding energies. The distribution is quite narrow with a FWHM of about 2 eV. When deconvoluted, we find the areas of 64% and 30% for sp² and sp³ components, respectively. The distribution in Figure 3c however shows a remarkably different sp²/sp³ ratio, with 40% and 51% for sp² and sp³ components, respectively. For the high-density sample, the sp³-content gives a strong contribution, which suggests that diamond-like regions are present.

There is an additional distribution found at about 288.5 eV which is due to various types of carbon oxides [55–58]. This peak increases from 5.9% to 8.2% for low- to high-density foams and becomes broader. This suggests that more oxygen is adsorbed in the high-density foam, and a wider variety of carbon oxide groups are present [55,59].

The O1s spectral distribution (Figure 3b,d) is also different for the two types of foams. Two-curve deconvolution for the low-density foam yields an O1 peak at 532.3 eV and an O2 peak at 533.8 eV, with corresponding relative areas of 62% and 38%. We assign these peaks to C=O and C–O bonded carbon atoms, respectively [60–62]. For the high-density foam, the O1 peak is at 532.2 eV, with 55% relative area, a small downshift from the low-density O1 peak. A significant difference between the two foams is the relative area of the O2 peak, located at 533.8 eV, which is 45% for the high-density foam. We conclude that from low- to high-density foam, the number of C=O bonded carbon atoms is reduced, and there are an increased number of C–O bonded carbon atoms in the high-density foams.

Discussion

We have demonstrated that the simultaneous existence of high pressure and high temperature in an autoclave with an aqueous solution of sucrose/naphthalene precursor leads to the formation of high-quality carbon nanofoams. The foams have uniform structure, predominantly composed of carbon microspheres. We note that our production is performed at relatively low temperatures of 150–185 °C and without a catalyst. The results show that our method leads to different carbonaceous products if the processing conditions are varied. Compared to other techniques, the hydrothermal method provides us with a mild, green, and fast technique which can easily be scaled up as a low-cost production route for large-scale applications.

In addition, the hydrothermal technique leads directly to carbon nanofoam with no further treatment necessary. This is impor-

tant since nanocarbon materials often need to be purified after synthesis. For example, production methods such as arc discharge [63] and laser ablation [64] may lead to carbon soot by-products, and additional purification is required. The nanofoam of our studies has a consistently homogeneous morphology and no such post-treatment is necessary to obtain a good-quality product.

From the HIM images we see that the carbon nanofoam consists of a conglomeration of spherical bodies. The microspheres generally have a narrow size distribution. An attractive interaction keeps the spheres together, forming the overall foam structure. We find that if other variables are kept constant, the size of the spheres is dependent on the process temperature. At higher temperatures we still find spherical micropearls but with increased diameters. This suggests that these species form by successive addition of layers added to a spherical core. Growth may occur in a concentric way leading to larger diameter spheres with increasing process temperature. In addition, a higher process temperature accelerates the growth process, facilitates the development of higher structural order and leads to a more advanced stage of carbonization. In the high-density foams, the micropearls tend to be connected to each other, with different neck-size diameters between adjacent pearls. Dangling bonds on the surface of the micropearls may lead to high surface reactivity and consequently to the aggregation of the spheres. In fact, such effects have been observed in the growth of carbon structures when the residence time in the autoclave was extended [65].

The advanced growth of the micropearls seems to be accompanied with a thickening of the walls of the graphitic scaffold. We assume that the wall structure starts with single- to few-layer graphene at the beginning of the carbonization process. Then, with further growth, additional layers of graphene are added to the wall structure. Therefore, the foams are light weight when formed in the initial stage of formation. In the experiment, this is done by using low-temperature in the hydrothermal process. At higher temperature, however, further progression of growth occurs, leading to a thickening of the wall structure and an increase in mass density. We found that the temperature used for the production of the low-density foams is close to the lower limit where foams start to form. This observation supports our assumption that there is a successive wall thickening with increasing temperature in the autoclave.

Our experiments suggest that the micropearls have an internal structure made of thin graphitic walls, which change from single-layer to multi-layer graphene with increasing progression of growth. A strictly two-dimensional graphene wall structure however does not explain the spherical shape of the micropearls. Therefore, we assume that the nanofoam scaffold rather

consists of curved graphene layers. In addition, these layers need to have a certain degree of disorder providing the porous structure of the pearls. The relatively broad Raman G and D peaks indicate that in-plane and out-of-plane Raman excitations are present.

While Raman spectroscopy probes the bulk of a sample, the information provided by XPS measurements is strongly surface related. The small (<10 nm) inelastic mean free path of the ejected photoelectrons is the crucial factor determining the surface sensitivity of XPS, which enables the quantitative estimation of the elemental composition and the chemical environment in the direct vicinity of the sample surface [66].

The XPS spectra in Figure 3 show an increased sp^3 contribution for higher-temperature-grown samples. We suggest that this originates from the neck areas between the pearls. In the neck section, the lattice structure is probably quite different from the structure in the sphere. The spherical morphology can be due to the presence of a 5/6 network with isolated pentagons surrounded by hexagons, similar to the fullerene structure. However, this structure cannot be used for the negative-curvature surfaces in the neck area. Heptagons or sp^3 -related units need to be incorporated for obtaining these areas connecting the microspheres. This may lead to the observed increase of sp^3 -character when the micropearls are connected.

Conclusion

In this study we have shown that the hydrothermal processing of sucrose with the addition of a small amount of naphthalene results in the formation of carbon nanofoam. The morphology of the obtained foam depends on the process temperature in the hydrothermal carbonization. High-quality foams with uniform structures are produced using a green method with a nontoxic precursor material. Foams with different mass densities can be produced by variation of the process temperature. Micropearls are the basic units in the low-temperature foams, while connected pearls form the high-density foams. The transition from low- to high-density foams is accompanied by a change in the graphitization degree as well as a change in the surface electronic configuration. With higher autoclave temperature, the carbonization process becomes more effective, which leads to an increase in sphere size and a thickening of the internal wall structure.

The surface sensitivity of XPS exhibits a distinct difference in the sp^3 binding contribution of the two types of foams. While higher-density foams show an increased degree of graphitization (as observed with the Raman spectra), they also reveal a significant increase of sp^3 bonded atoms (as observed with the XPS spectra). We relate this to the surface area network which

appears to be very different for the two types of foams. The formation of neck areas between the partially fused micropearls requires the inclusion of heptagons and sp^3 -type connections.

We conclude that the nanofoam materials exhibit physical properties originating from a mixture of carbon atoms with sp^2 and sp^3 hybridization. The structure in the core of the micropearls is based on a mostly sp^2 -type, three-dimensional network, whose specific property stems from the curvature and interconnection of graphitic basal planes. We assume that the low-density carbon nanofoam has the structure of a three-dimensional interconnected network of graphene. Depending on the growth conditions, the sp^2 carbon atoms can also form pentagonal and heptagonal rings with sp^3 -type interconnections built into the hexagonal network. The results show that the combination of various types of n-fold rings and hybrid sp^2 - sp^3 structures makes carbon unique among the chemical elements, and it can lead to the formation of a variety of geometrical carbon nanofoam structures.

Acknowledgements

Natalie Frese was supported during parts of this research by a scholarship from the German Academic Exchange Service (DAAD-Doktorandenstipendium).

References

- Iwu, K. O.; Lombardo, A.; Sanz, R.; Scirè, S.; Mirabella, S. *Sens. Actuators, B* **2016**, *224*, 764–771. doi:10.1016/j.snb.2015.10.109
- Gao, G.; Wu, H. B.; Ding, S.; Liu, L.-M.; Lou, X. W. *Small* **2015**, *11*, 804–808. doi:10.1002/sml.201402539
- Jo, H.; Cho, Y.-H.; Choi, M.; Cho, J.; Um, J. H.; Sung, Y.-E.; Choe, H. *Mater. Chem. Phys.* **2014**, *145*, 6–11. doi:10.1016/j.matchemphys.2014.02.009
- Rezaei, B.; Mokhtarianpour, M.; Ensafi, A. A. *Int. J. Hydrogen Energy* **2015**, *40*, 6754–6762. doi:10.1016/j.ijhydene.2015.03.122
- Jia, H.; An, J.; Guo, X.; Su, C.; Zhang, L.; Zhou, H.; Xie, C. *J. Mol. Liq.* **2015**, *212*, 763–766. doi:10.1016/j.molliq.2015.10.030
- Johnston, L. T.; Biener, M. M.; Ye, J. C.; Baumann, T. F.; Kucheyev, S. O. *J. Appl. Phys.* **2015**, *118*, 025303. doi:10.1063/1.4926738
- Naumkin, F. Y.; Wales, D. J. *Chem. Phys. Lett.* **2012**, *545*, 44–49. doi:10.1016/j.cplett.2012.07.027
- Figuerola, E.; Tramontina, D.; Gutiérrez, G.; Bringa, E. *J. Nucl. Mater.* **2015**, *467*, 677–682. doi:10.1016/j.jnucmat.2015.10.036
- Grant-Jacob, J. A.; Mills, B.; Eason, R. W. *J. Phys. D: Appl. Phys.* **2014**, *47*, 055105. doi:10.1088/0022-3727/47/5/055105
- Iino, T.; Nakamura, K. *Jpn. J. Appl. Phys.* **2009**, *48*, 07GE01. doi:10.1143/JJAP.48.07GE01
- Kurek, A.; Xalter, R.; Stürzel, M.; Mülhaupt, R. *Macromolecules* **2013**, *46*, 9197–9201. doi:10.1021/ma401971c
- Liu, J.; Zhang, L.; Yang, Q.; Li, C. *Microporous Mesoporous Mater.* **2008**, *116*, 330–338. doi:10.1016/j.micromeso.2008.04.030
- Mille, C.; Corkery, R. W. *J. Mater. Chem. A* **2013**, *1*, 1849–1859. doi:10.1039/C2TA00451H

14. Barty, A.; Marchesini, S.; Chapman, H. N.; Cui, C.; Howells, M. R.; Shapiro, D. A.; Minor, A. M.; Spence, J. C. H.; Weierstall, U.; Ilavsky, J.; Noy, A.; Hau-Riege, S. P.; Artyukhin, A. B.; Baumann, T.; Willey, T.; Stolken, J.; van Buuren, T.; Kinney, J. H. *Phys. Rev. Lett.* **2008**, *101*, 055501. doi:10.1103/PhysRevLett.101.055501
15. Sattler, K. Graphene, Fullerenes, Nanotubes, and Nanodiamonds. *Carbon Nanomaterials Sourcebook*; CRC Press: Boca Raton, FL, 2016; Vol. 1.
16. Bryning, M. B.; Milkie, D. E.; Islam, M. F.; Hough, L. A.; Kikkawa, J. M.; Yodh, A. G. *Adv. Mater.* **2007**, *19*, 661–664. doi:10.1002/adma.200601748
17. Camilli, L.; Pisani, C.; Gautron, E.; Scarselli, M.; Castrucci, P.; D'Orazio, F.; Passacantando, M.; Moscone, D.; De Crescenzi, M. *Nanotechnology* **2014**, *25*, 065701. doi:10.1088/0957-4484/25/6/065701
18. Rode, A. V.; Elliman, R. G.; Gamaly, E. G.; Veinger, A. I.; Christy, A. G.; Hyde, S. T.; Luther-Davies, B. *Appl. Surf. Sci.* **2002**, *197–198*, 644–649. doi:10.1016/S0169-4332(02)00433-6
19. Kohno, H.; Tatsutani, K.; Ichikawa, S. *J. Nanosci. Nanotechnol.* **2012**, *12*, 2844–2848.
20. Spanakis, E.; Pervolaraki, M.; Giapintzakis, J.; Katsarakis, N.; Koudoumas, E.; Vernardou, D. *Electrochim. Acta* **2013**, *111*, 305–313. doi:10.1016/j.electacta.2013.07.222
21. Faraji, S.; Stano, K. L.; Yildiz, O.; Li, A.; Zhu, Y.; Bradford, P. D. *Nanoscale* **2015**, *7*, 17038–17047. doi:10.1039/C5NR03899E
22. Rolison, D. R.; Sassin, M. B.; Long, J. W.; Wallace, J. M.; Chervin, C. N. Building energy-and size-scalable 3D energy-storage architectures with carbon nanofoam paper. In *Abstracts of papers of the American Chemical Society*, 248th ACS National Meeting and Exposition, San Francisco, CA, Aug 10–14, 2014; American Chemical Society: Washington, DC, USA; p 542.
23. Della Noce, R.; Eugénio, S.; Silva, T. M.; Carnezim, M. J.; Montemor, M. F. *J. Power Sources* **2015**, *288*, 234–242. doi:10.1016/j.jpowsour.2015.04.131
24. Mitchell, S. T.; Frese, N.; Götzhäuser, A.; Bowers, A.; Sattler, K. *Carbon* **2015**, *95*, 434–441. doi:10.1016/j.carbon.2015.08.001
25. Economou, N. P.; Notte, J. A.; Thompson, W. B. *Scanning* **2012**, *34*, 83–89. doi:10.1002/sca.20239
26. Boden, S. A.; Franklin, T. M. W.; Scipioni, L.; Bagnall, D. M.; Rutt, H. N. *Microsc. Microanal.* **2012**, *18*, 1253–1262. doi:10.1017/S1431927612013463
27. van Gastel, R.; Hlawacek, G.; Dutta, S.; Poelsema, B. *Nucl. Instrum. Methods Phys. Res., Sect. B* **2015**, *344*, 44–49. doi:10.1016/j.nimb.2014.11.073
28. Ohya, K.; Yamanaka, T. *Nucl. Instrum. Methods Phys. Res., Sect. B* **2013**, *315*, 295–299. doi:10.1016/j.nimb.2013.03.033
29. Sijbrandij, S.; Notte, J.; Sanford, C.; Hill, R. *J. Vac. Sci. Technol., B* **2010**, *28*, C6F6. doi:10.1116/1.3497012
30. Sijbrandij, S.; Thompson, B.; Notte, J.; Ward, B. W.; Economou, N. P. *J. Vac. Sci. Technol., B* **2008**, *26*, 2103–2106. doi:10.1116/1.2993262
31. Oida, S.; McFeely, F. R.; Bol, A. A. *J. Appl. Phys.* **2011**, *109*, 064304. doi:10.1063/1.3552306
32. Tagawa, M.; Ykota, K.; Kitamura, A.; Matsumoto, K.; Yoshigoe, A.; Teraoka, Y.; Kanda, K.; Niibe, M. *Appl. Surf. Sci.* **2010**, *256*, 7678–7683. doi:10.1016/j.apsusc.2010.06.030
33. Kerber, P.; Porter, L. M.; McCullough, L. A.; Kowalewski, T.; Engelhard, M.; Baer, D. *J. Vac. Sci. Technol., A* **2012**, *30*, 061407. doi:10.1116/1.4759238
34. Tay, B. K.; Shi, X.; Tan, H. S.; Chua, D. H. C. *Surf. Interface Anal.* **1999**, *28*, 231–234. doi:10.1002/(SICI)1096-9918(199908)28:1<231::AID-SIA583>3.0.CO;2-3
35. Haerle, R.; Riedo, E.; Pasquarello, A.; Baldereschi, A. *Phys. Rev. B* **2002**, *65*, 045101. doi:10.1103/PhysRevB.65.045101
36. Gordeev, S. K.; Grechinskaya, A. V.; Danishevskii, A. M.; Smorgonskaya, E. A.; Shchukarev, A. V. *Mol. Mater.* **2000**, *13*, 355–360.
37. Rao, K. V. V.; Kishore, G.; Rao, K. S.; Rao, M. N.; Rao, Y. H. *Asian J. Chem.* **2010**, *22*, 4377–4381.
38. Manickam, M.; Takata, M. *J. Power Sources* **2002**, *112*, 116–120. doi:10.1016/S0378-7753(02)00371-3
39. Takabayashi, S.; Okamoto, K.; Shimada, K.; Motomitsu, K.; Motoyama, H.; Nakatani, T.; Sakaue, H.; Suzuki, H.; Takahagi, T. *Jpn. J. Appl. Phys.* **2008**, *47*, 3376–3379. doi:10.1143/JJAP.47.3376
40. Lide, D. R. *CRC Handbook of Chemistry and Physics*; CRC Press, 2005.
41. Feng, J.; Feng, J.; Zhang, C. *J. Porous Mater.* **2012**, *19*, 551–556. doi:10.1007/s10934-011-9504-7
42. Marie, J.; Chenitz, R.; Chatenet, M.; Berthon-Fabry, S.; Cornet, N.; Achard, P. *J. Power Sources* **2009**, *190*, 423–434. doi:10.1016/j.jpowsour.2009.01.047
43. Zhou, B.; Zhang, R.; Guo, Q.-G.; Li, Z.-H.; Hu, Z.-J.; Li, J.-N.; Dong, W.-S. *New Carbon Mater.* **2011**, *26*, 117–122.
44. dos Santos, R. B.; de Brito Mota, F.; Rivelino, R. *Carbon* **2012**, *50*, 2788–2795. doi:10.1016/j.carbon.2012.02.041
45. Feng, Y.; Wang, J.; Ge, L.; Jiang, B.; Miao, L.; Tanemura, M. *J. Nanosci. Nanotechnol.* **2013**, *13*, 7012–7015. doi:10.1166/jnn.2013.8063
46. Peng, L. J.; Morris, J. R. *Carbon* **2012**, *50*, 1394–1406. doi:10.1016/j.carbon.2011.11.012
47. Shin, S. J.; Tran, I. C.; Willey, T. M.; van Buuren, T.; Ilavsky, J.; Biener, M. M.; Worsley, M. A.; Hamza, A. V.; Kucheyev, S. O. *Carbon* **2014**, *73*, 443–447. doi:10.1016/j.carbon.2014.03.006
48. Chaurasia, S.; Tripathi, S.; Munda, D. S.; Mishra, G.; Murali, C. G.; Gupta, N. K.; Dhareshwar, L. J.; Rassall, A. K.; Tallents, G. J.; Singh, R.; Kohli, D. K.; Khardekar, R. K. *Pramana* **2010**, *75*, 1191–1196. doi:10.1007/s12043-010-0205-6
49. Zani, A.; Dellasega, D.; Russo, V.; Passoni, M. *Carbon* **2013**, *56*, 358–365. doi:10.1016/j.carbon.2013.01.029
50. Urakawa, T.; Matsuzaki, H.; Yamashita, D.; Uchida, G.; Koga, K.; Shiratani, M.; Setsuhara, Y.; Sekine, M.; Hori, M. *Surf. Coat. Technol.* **2013**, *228* (Suppl. 1), S15–S18. doi:10.1016/j.surfcoat.2012.10.002
51. Sugime, H.; Esconjauregui, S.; D'Arzié, L.; Yang, J.; Makaryan, T.; Robertson, J. *ACS Appl. Mater. Interfaces* **2014**, *6*, 15440–15447. doi:10.1021/am504048h
52. Brandt, R.; Fricke, J. *J. Non-Cryst. Solids* **2004**, *350*, 131–135. doi:10.1016/j.jnoncrysol.2004.06.039
53. Schwan, J.; Ulrich, S.; Batori, V.; Ehrhardt, H.; Silva, S. R. P. *J. Appl. Phys.* **1996**, *80*, 440–447. doi:10.1063/1.362745
54. Diaz, J.; Paolicelli, G.; Ferrer, S.; Comin, F. *Phys. Rev. B* **1996**, *54*, 8064–8069. doi:10.1103/PhysRevB.54.8064
55. Hontoria-Lucas, C.; López-Peinado, A. J.; de D. López-González, J.; Rojas-Cervantes, M. L.; Martín-Aranda, R. M. *Carbon* **1995**, *33*, 1585–1592. doi:10.1016/0008-6223(95)00120-3
56. Zhou, J.-H.; Sui, Z.-J.; Zhu, J.; Li, P.; Chen, D.; Dai, Y.-C.; Yuan, W.-K. *Carbon* **2007**, *45*, 785–796. doi:10.1016/j.carbon.2006.11.019
57. Plomp, A. J.; Su, D. S.; de Jong, K. P.; Bitter, J. H. *J. Phys. Chem. C* **2009**, *113*, 9865–9869. doi:10.1021/jp900637q

58. Dreyer, D. R.; Park, S.; Bielawski, C. W.; Ruoff, R. S. *Chem. Soc. Rev.* **2010**, *39*, 228–240. doi:10.1039/B917103G
59. Kondo, H.; Nishida, Y. *Bull. Chem. Soc. Jpn.* **2007**, *80*, 1405–1412. doi:10.1246/bcsj.80.1405
60. Kostecki, R.; Schnyder, B.; Alliata, D.; Song, X.; Kinoshita, K.; Kötz, R. *Thin Solid Films* **2001**, *396*, 36–43. doi:10.1016/S0040-6090(01)01185-3
61. Boehm, H. P. *Carbon* **2002**, *40*, 145–149. doi:10.1016/S0008-6223(01)00165-8
62. Fan, L.-Z.; Qiao, S.; Song, W.; Wu, M.; He, X.; Qu, X. *Electrochim. Acta* **2013**, *105*, 299–304. doi:10.1016/j.electacta.2013.04.137
63. Hou, P.; Liu, C.; Tong, Y.; Xu, S.; Liu, M.; Cheng, H. *J. Mater. Res.* **2001**, *16*, 2526–2529. doi:10.1557/JMR.2001.0346
64. Park, T.-J.; Banerjee, S.; Hemraj-Benny, T.; Wong, S. S. *J. Mater. Chem.* **2006**, *16*, 141–154. doi:10.1039/B510858F
65. Bazargan, A.; Yan, Y.; Hui, C. W.; McKay, G. *Ind. Eng. Chem. Res.* **2013**, *52*, 12689–12702. doi:10.1021/ie4018513
66. Wepasnick, K. A.; Smith, B. A.; Bitter, J. L.; Fairbrother, D. H. *Anal. Bioanal. Chem.* **2010**, *396*, 1003–1014. doi:10.1007/s00216-009-3332-5

License and Terms


This is an Open Access article under the terms of the Creative Commons Attribution License (<http://creativecommons.org/licenses/by/4.0>), which permits unrestricted use, distribution, and reproduction in any medium, provided the original work is properly cited.

The license is subject to the *Beilstein Journal of Nanotechnology* terms and conditions: (<http://www.beilstein-journals.org/bjnano>)

The definitive version of this article is the electronic one which can be found at:
[doi:10.3762/bjnano.7.197](https://doi.org/10.3762/bjnano.7.197)

Article

Diamond-Like Carbon Nanofoam from Low-Temperature Hydrothermal Carbonization of a Sucrose/Naphthalene Precursor Solution

Natalie Frese^{1,2}, Shelby Taylor Mitchell², Amanda Bowers², Armin Götzhäuser¹ 
and Klaus Sattler^{2,*}

¹ Faculty of Physics, University of Bielefeld, D-33501 Bielefeld, Germany; natalie.frese@gmx.de (N.F.); ag@uni-bielefeld.de (A.G.)

² Department of Physics and Astronomy, University of Hawaii, 2505 Correa Road, Honolulu, HI 96822, USA; smitch22@hawaii.edu (S.T.M.); bowersa@hawaii.edu (A.B.)

* Correspondence: sattler@hawaii.edu; Tel.: +1-808-856-8941

Received: 7 June 2017; Accepted: 30 June 2017; Published: 6 July 2017

Abstract: Unusual structure of low-density carbon nanofoam, different from the commonly observed micropearl morphology, was obtained by hydrothermal carbonization (HTC) of a sucrose solution where a specific small amount of naphthalene had been added. Helium-ion microscopy (HIM) was used to obtain images of the foam yielding micron-sized, but non-spherical particles as structural units with a smooth foam surface. Raman spectroscopy shows a predominant sp^2 peak, which results from the graphitic internal structure. A strong sp^3 peak is seen in X-ray photoelectron spectroscopy (XPS). Electrons in XPS are emitted from the near surface region which implies that the graphitic microparticles have a diamond-like foam surface layer. The occurrence of separated sp^2 and sp^3 regions is uncommon for carbon nanofoams and reveals an interesting bulk-surface structure of the compositional units.

Keywords: carbon; nanomaterials; nanofoam; nanostructured; porous; ultralight materials; hydrothermal carbonization

1. Introduction

A large variety of nanomaterials can be formed from elemental carbon. Amorphous carbon materials with a high fraction of sp^2 bonds are named graphite-like carbons. When sp^3 bonds are dominating, the materials are named diamond-like carbons. Their properties depend on the relative abundance of the sp^2 - and sp^3 - hybridized carbon atoms [1]. Carbon materials with both graphite- and diamond-like bonds were realized by various synthetic methods, e.g., laser ablation, chemical vapor deposition or hydrothermal carbonization [2]. For example, a material containing graphene sheets and diamond-like structures has been observed after catalytic carbonization of wood charcoal [3]. In this study, we focus on hydrothermal carbonization (HTC) for the synthesis of carbon nanofoam with separated regions of sp^2 - and sp^3 -hybridized carbon atoms.

Hydrothermal carbonization is a promising method for the synthesis of carbon nanomaterials from biomass [4] for a wide range of applications in fields such as energy storage environment protection [5]. It has been used in industry for the production of fuels and other energetic materials [6]. The carbonization of sucrose biomass usually leads to foam-structured materials consisting of spherical micron-sized particles [7]. It has been shown that a small amount of naphthalene added to a sucrose solution acts as a nucleation seed during the HTC process leading to low density, high-quality carbon foams consisting of micropearls with internal pores [8]. The surface of these materials has been modified by chemical functionalization, and the bulk structure by introducing additional porosity [9].

A different morphology has been obtained by adding graphene oxide to biomass, which results in carbon materials with higher degree of carbonization and higher conductivity [10]. Porous carbon structures have also been produced by HTC of crude plant material, which can be up-scaled to large quantities with low cost, and these materials may have industrial applications for catalytic support and for sorption purposes [11]. Other potential applications of carbon nanofoam include hydrogen storage [12], cathodes for batteries [13,14] or composites for electrodes [15,16]. It follows that the HTC method for the synthesis of functional carbon materials can be used for a broad range of applications [2].

For this study, we produced carbon nanofoam by naphthalene-assisted hydrothermal carbonization of sucrose. We find that the amount of added naphthalene critically determines the foam morphology. At low naphthalene concentrations, the foam consists of an agglomeration of porous micropearls [8]. At higher concentration, however, the carbon nanofoam consists of micron-sized irregularly shaped particles with sponge-like surfaces as visualized by helium ion microscopy (HIM). X-ray photoelectron spectroscopy (XPS) reveals a diamond-like carbon surface. The Raman spectrum shows the D and G bands of carbon with a distinctly higher G peak. These results characterize the foam as a material consisting of species with a graphite-like core and a diamond-like shell. The density of the analyzed sample is $0.21 \text{ g}\cdot\text{cm}^{-3}$, far below the density of graphite, due to internal pores.

2. Results

2.1. Microscopy

Figure 1 displays two helium ion microscopy images of the carbon foam sample. Figure 1a shows one side of a foam particle. The particle has a diameter of about $200 \mu\text{m}$ and a uniform rough surface structure.

A higher-magnification image of the foam particle is presented in Figure 1b. It depicts the upper right part of the particle shown in Figure 1a, and it can be seen that the surface has a sponge-like and frayed character. The sponge-like surface implies a porous foamy structure, which is also indicated by the low density of $0.21 \text{ g}\cdot\text{cm}^{-3}$ of the sample. The edge resolution of the image in Figure 1b is around 15 nm , which was determined by the distance between 25% and 75% of the maximum intensity of a sharp edge [17].

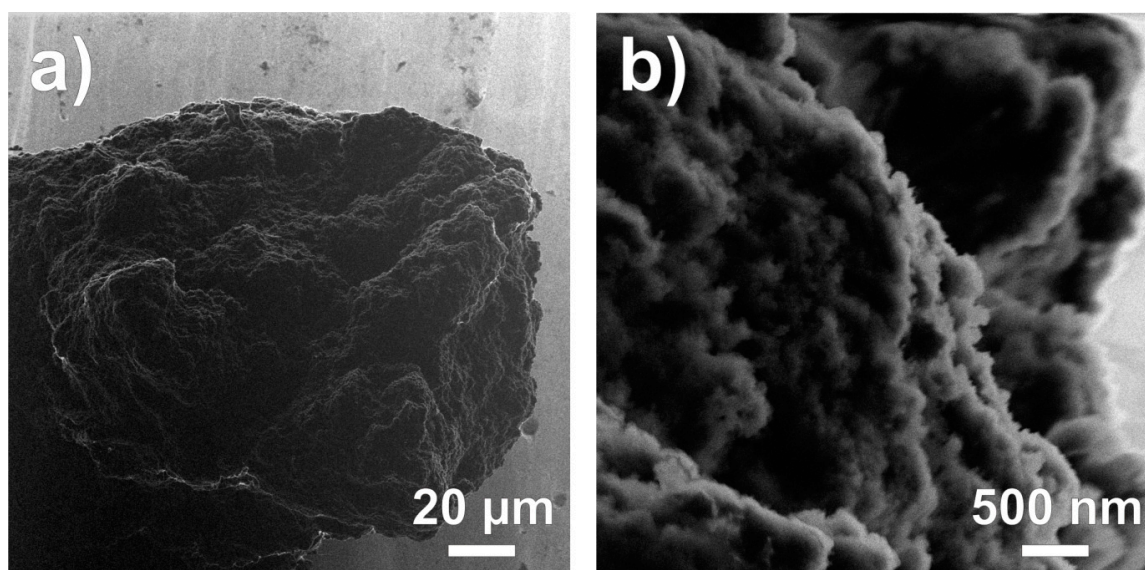


Figure 1. Helium-ion microscopy images of carbon nanofoam, (a) showing a micron-sized part of the foam and (b) showing in higher magnification the sponge-like surface of the foam.

2.2. XPS

The chemical composition of the carbon nanofoam surface was determined by XPS. Figure 2a shows the C1s and Figure 2b the O1s photoelectron signals of the foam sample. The de-convoluted carbon curve in Figure 2a consists of five peaks, labeled as C1–C5. It has been shown that the sp^3 -hybridized carbon peak is shifted around 1 eV from the sp^2 -hybridized carbon peak [18]. Therefore, the two main peaks at 284.4 eV (C1) and 285.5 eV (C2) are assigned to aromatic and aliphatic carbons, respectively. The C1 peak has an area of 28%, whereas the C2 peak has an area of 39%. Since XPS is a surface-sensitive method, it follows that the foam surface has a diamond-like composition, because the aliphatic carbons dominate in the spectrum. The remaining three peaks at 286.4 eV (19%), 287.3 eV (10%) and 289.1 eV (4%) are assigned to carbon–oxygen bonds; to hydroxyl, carbonyl and carboxylic groups, respectively [19]. Further surface groups such as carboxylic anhydride, lactone or lactol may also contribute to the carbon–oxygen peaks [20]. The feature at 289.1 eV, assigned to O=C–OH, could in part be due to π – π^* shape-up satellites associated with electron transitions between the carbon HOMO–LUMO gap. Such satellite peaks have been reported in the literature at \sim 290 eV [21], \sim 290.5 eV [22], and \sim 291 eV [23].

The O1s curve shows the presence of the oxygenated groups as seen in the C1s spectrum and can be divided into two components, C–O bonds at 533.4 eV and C=O bonds at 532.1 eV, with areas of 62% and 38%, respectively. We note that no feature is observed at about 536.0 eV, where adsorbed water would give a peak in the XPS O1s spectrum [22]. This shows that the water from the aqueous solution has entirely been removed from the samples after extracting from the autoclave and their subsequent thermal treatment. From these various results, we conclude that the surface structure of the nanofoam can be described as a diamond-like open framework decorated with oxygenated functional groups.

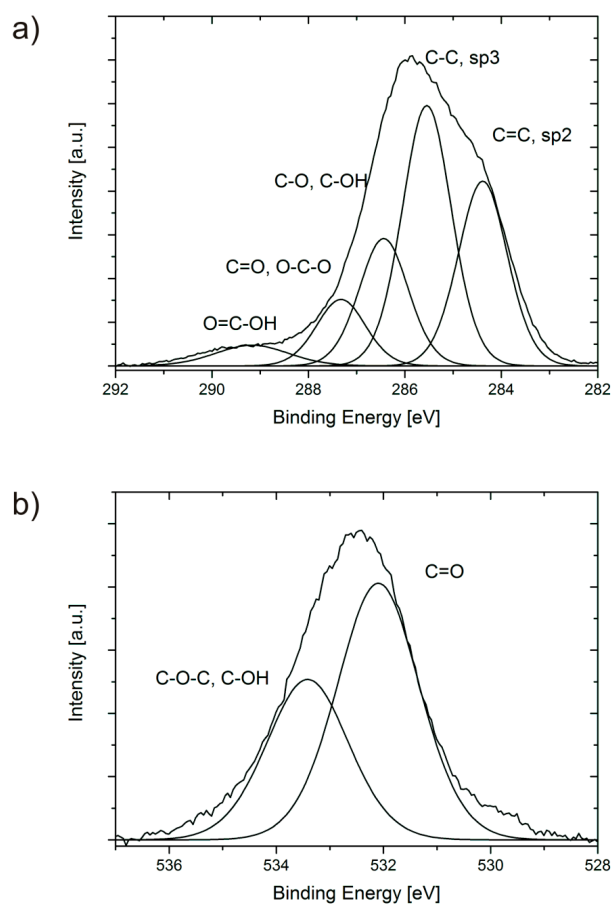


Figure 2. XP spectra of (a) C1s signals, and (b) O1s signals of the carbon nanofoam.

2.3. Raman Spectroscopy

The Raman spectrum shown in Figure 3 exhibits a pattern which is common for carbonized materials [24]. We used a Gaussian two-curve fitting to decompose the main Raman signal into two peaks. The deconvoluted G peak arises from graphite carbon bond-stretching motion and is located at around 1582 cm^{-1} . The second peak at around 1360 cm^{-1} is known as the defect-derived D peak, and is assigned to ring breathing vibrations in benzene [19]. The peak locations are in good agreement with literature values for disordered graphite, where the G peak is usually located at around 1580 cm^{-1} and the D peak at around 1350 cm^{-1} [25]. The observed G peak differs from the sharp Raman peak at 1575 cm^{-1} for perfect graphite [26]. This reveals that the material has a mixed content of aromatic and aliphatic carbons. The measured intensity of the D band relative to that of the G band is 0.52 corresponding to the values for disordered graphite, which typically lie between 0.51 and 1.1 [27]. Since the G band is broader than 45 cm^{-1} (the value for graphite), the core of the foam appears to be dominated by small aromatic clusters with sizes less than 10 \AA [28].

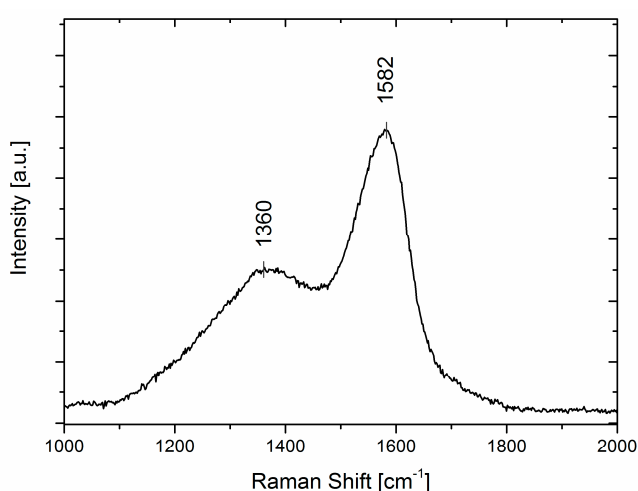


Figure 3. Raman spectrum in the wavenumber range 1000 to 2000 cm^{-1} .

3. Discussion

We have confirmed that hydrothermal carbonization is an excellent method for the production of high-quality carbon nanomaterials. It has generally been used in the past in industrial applications such as, for example, the charcoal production from raw cellulosic materials [29], mesoporous carbons from crude plant material [11], or ethanol from biomass [30]. If using natural precursor materials, excessive purification however is usually required. No such purification is necessary if synthetic hydrocarbons are used. Saccharides are among the precursor materials which are non-toxic and easily carbonized without catalysts [7,19,31]. Among these, glucose [32,33] and sucrose [8] are convenient precursors.

Many carbonization studies were performed at high temperatures and high pressures (HTHP) [34]. Serp et al. [35], for example, produced carbon nanospheres (CNS) by decomposition of methane at $1100\text{ }^{\circ}\text{C}$, Wang et al. [36] by the decomposition of benzene at $1000\text{ }^{\circ}\text{C}$. With the support of catalysts, pentane has been decomposed at 900 – $1000\text{ }^{\circ}\text{C}$ [37], anthracene at 900 – $1000\text{ }^{\circ}\text{C}$ [38] and camphor at $1000\text{ }^{\circ}\text{C}$ [39], in all these cases resulting in the synthesis of carbon nanospheres.

With solid-state precursors, process temperatures above and below the critical point of water have been used. For example, the hydrothermal carbonization was performed for cellulose in the 220 – $250\text{ }^{\circ}\text{C}$ range [40], for glucose between 170 and $500\text{ }^{\circ}\text{C}$ [19,41–44], for sucrose at $190\text{ }^{\circ}\text{C}$ [45] and for starch at $600\text{ }^{\circ}\text{C}$ [46]. Process times were typically between 4 and 12 h. For some of the materials, the graphitic nature has been improved by annealing the sample after synthesis. This typically requires temperatures of up to about $2000\text{ }^{\circ}\text{C}$ [47]. In this paper, we have shown for naphthalene-assisted

sucrose carbonization that low process temperature of only 130 °C combined with a long process time of 72 h can be used. Even at this low temperature, one obtains complete carbonization, with a high-quality product of uniform morphology and a quite high degree of graphitization.

We also like to note that our use of sucrose as precursor material, without the addition of a catalyst, is a sustainable, bio-based method for the “green” production of carbon materials. Together with the low-temperature and low-pressure process conditions, no toxic byproducts and no necessary pre- or post-purification, it provides an easy and clean way for the production of nanocarbons with promising future applications.

The morphology of the carbon nanofoam obtained in this study is unique. Carbon nanofoams usually consist of agglomerations of porous nano- or micron-sized spheres. Such so-called nano- or micro-pearls have been produced by various methods such as laser ablation [48–50], chemical vapor deposition (CVD) [39,51–60] or hydrothermal carbonization (HTC) [30–33,46,61–67]. In this paper, we show that morphologies other than micropearls can be synthesized just by changing the process parameters. In our previous study, carbon microspheres were formed by using hydrothermal carbonization of a sucrose solution with a trace amount of naphthalene [8]. In the present work, we have increased the naphthalene concentration and the process time which resulted in an entirely different foam morphology. This shows that variations in the process conditions can have a major effect on the outcome of the synthesis.

The diamond-like property of the foams in this study is unique since usually nanoporous carbon materials are rather graphitic [68] or graphenic [69] in nature. This applies to various types of materials such as nanoporous hard carbon microspheres [70], fiber-based nanoporous carbon [71], nanoporous carbon tubes [72], nanoporous carbon films [73] or activated carbon [74]. The graphitic nature, given by sp^2 hybridization, provides the large surface area in the interior of the foam scaffold. Also, the sp^2 -hybridization allows for a large variety of structures typically composed of planar aromatic sixfold rings. In addition, inclusion of pentagons leads to ring structures with positive curvature, inclusion of heptagons to areas with negative curvature. Furthermore, the aromatic graphene sheets can be curved similar to those forming the carbon nanotubes. This can lead to a large variety of graphite-like morphologies with many possible applications. For example, it is responsible for the uptake of molecules such as methane [75], CO_2 [76], proteins [77], or heavy metals [78]. Also, catalytic properties of the foam [79], as well as gas- [80] and glucose-sensing properties [81] or photoluminescence [82] are related to a graphitic or graphene-like interior of the foams. In particular, hydrogen storage, long proposed for graphitic carbon materials [83], has recently been considered for nanoporous carbons [84–86]. We note that a strong sp^3 contribution, as observed for the nanofoam in this work, will affect the general properties of these foams as well as their possible use in future technologies. New applications may be possible for such diamond-like carbon foams.

Diamond-like features of a carbon nanomaterial in Raman spectra can arise mainly from two different sources; either from sp^3 -related vibrations due to small regions of crystalline diamond (usually nanodiamonds) [87], or from regions with amorphous sp^3 -related structures [88]. It has been well documented that diamond films in Raman spectroscopy show a sharp feature at about 1332 cm^{-1} [88]. These phonon vibrations involve the sp^3 -hybridized carbon atoms in diamond. Very close to it, a band centered at about 1350 cm^{-1} is generally associated with sp^3 amorphous carbon sites and is called D-band (D standing for “disorder”). The sharp peak of crystalline diamond may be superimposed on the broader amorphous carbon band. However, for a material which contains both, amorphous and nanodiamond regions, or a hybrid combination of both, the two bands usually cannot be distinguished since the difference in location is only a few cm^{-1} . In addition, upon shrinking of the crystal to the nanoscale, major changes are observed in the Raman response of nanodiamonds: compared to bulk diamond, the nanodiamond peak is shifted to lower frequencies and appears broadened, sometimes with an asymmetry [89–91]. The phonon confinement effect is mainly considered as the physical origin for these changes [92]. In addition, the position and line shape of the Raman bands may also be affected by lattice defects in nanocrystalline areas resulting in phonon scattering as well as by

strain in the sample. For example, Shin et al. [93] found that the G peak of the Raman spectrum shifts to higher wave numbers with the increase of compressive stress. In our studies, only one band is observed in the wavenumber region where either diamond structures and/or amorphous structures would occur. This is not surprising, since both the close proximity of the sp^3 bands for diamond and of the amorphous carbon, as well as the confinement effect for small diamond clusters, leads to the observation of just one band. We conclude that the D peak in the diamond-like foam of our studies, being separated from the G peak and relatively narrow, may be due to an amorphous/nanodiamond hybrid structure.

In our studies, the sp^3 -related D-band in the Raman spectrum is measured with relatively low intensity but the C1s XPS spectrum shows a strong sp^3 -contribution. We relate these two results to the different depth of probing the sample. While Raman spectroscopy yields results for the bulk of the sample, XPS is strongly surface-sensitive. Therefore, we conclude that the bulk of the nanofoam of this study is graphitic in nature while the surface is diamond-like. In addition, both the macroscopic appearance and the HIM images reveal the foam structure of surface. In addition, we note that the low value for the mass density indicates that the core of the foam has also porous structure. The combination of the two different properties of core and surface regions may lead to exciting and valuable new applications of this material.

In the XPS O1s spectrum, various functional groups can generally be assigned to the deconvolution peaks [94–96]. In Figure 2, the peak at around 531.3 eV corresponds to C=O bonds, and the peak at around 533.5 eV corresponds to C–OH and C–O bonds. The C=O peak dominates in the de-convoluted O1s distribution. At binding energies below the C=O peak we observe a small peak which may be assigned to quinone, which is expected to give a feature at 530.7 eV [97]. We note that diamond films have been oxidized showing a strong O1s peak in the XPS [98]. The nature of the oxygen surface groups was found to depend on the oxidation process [99]. Surface morphology was found to change upon oxidation leading to lattice reconstruction at the oxygen-terminated diamond surface [100].

For diamond crystal surfaces, adsorbed oxygen exists in several functional surface groups [101]. The carbon–oxygen interaction of the diamond surface has been investigated and the oxidized diamond surface has been found to be hydrophilic [102]. We note that in our sample the C=O peak is the strongest peak in the O1s envelope. In fact, the C=O group has also been found as the dominant functional group in oxidized diamond-like carbon films [103].

At about 535.8 eV, a peak would be observed for adsorbed water. However, no feature is seen at this energy which shows that the water from the sucrose solution has successfully been removed after synthesis. For foam structures with closed cavities the water would remain in the sample. However, since no indication for water adsorption is seen in the O1s spectrum, we conclude that the foam consists of an open scaffold able to release enclosed water by heating the sample after removing from the autoclave. Also, this suggests that this material may effectively be used in adsorption applications, since the pores are open to the environment.

We conclude that the carbon nanofoams, synthesized in these studies, have a new morphology with a porous graphitic core and a diamond-like foam surface. These materials may have new and unexpected applications in various fields of technology.

4. Instruments and Methods

4.1. Hydrothermal Synthesis

A 2M sucrose solution and 9 mg of naphthalene were filled into a 130 mL stainless steel autoclave with a head space of 7 mm and heated at 130 °C. After 72 h, the formed foam was removed from the autoclave, filtered with hot water and dried at room temperature. The resulting mass density of the foam is $0.21 \text{ g}\cdot\text{cm}^{-3}$, calculated using a high-precision balance and a pre-defined volume container. We note that control experiments, where no naphthalene was added, did not result in foam formation. This suggests that naphthalene acts as a nucleation seed for starting the growth of carbon foam.

The aromatic ring structure of naphthalene induces the formation of the graphitic carbon morphology. Hydrothermal carbonization, however, is a very complex thermodynamic and chemical process with a large variety of intermediate products. From our experimental results, we find that these intermediates may also lead to diamond-like carbon formation.

Hydrothermal carbonization is a thermochemical process where hydrocarbon precursors are transformed into all-carbon materials [2,9,61]. Variables such as precursor composition, as well as autoclave temperature, pressure, and process time, critically determine the synthesized carbon morphologies and their functionalities [104]. The reaction mechanisms are complex, and the operational parameters are interconnected [105]. In addition, with higher temperature and pressure, dramatic changes in the properties of water are known to occur. The dielectric constant of water for example can be considerably lower compared to ambient conditions. The water density increases with pressure and becomes an important variable in the hydrothermal reaction process [106]. At temperatures below 300 °C, the carbon materials are mainly produced by dehydration and polymerization [2]. The mild temperature of 130 °C, applied in this work, is far below the critical point of $T = 373$ °C, and therefore provides subcritical conditions. At this mild temperature, water is considered as a reacting dehydrating agent. We note that the catalyst-free carbonization under such subcritical water conditions is more environmentally friendly than most of the other production methods for nanocarbon materials [107].

4.2. Helium Ion Microscopy

Helium ion microscopy (HIM) imaging [108] was performed with a Carl Zeiss Orion Plus [109,110]. The ion source of the HIM consists of an atomically sharp tip in helium gas, kept at high positive voltage. Field ionization at the tip of the needle combined with an electrostatic ion optics leads to a very bright He ion beam. The instrument was operated at an acceleration voltage of 34.9 keV, a beam current of 0.3 pA and a working distance of 10 mm. The images were obtained by detecting secondary electrons [111] with an Everhart–Thornley detector in the line averaging mode. Since we have used an uncoated sample, an electron flood gun was applied during imaging to stabilize charging. Prior to imaging, the foam was mounted on the sample holder with conductive carbon pads.

Compared to the scanning electron microscope (SEM), the helium ion microscope (HIM) can be applied to a smaller probe size and has a larger secondary electron yield [108]. This leads to images with stronger topographic contrast showing finer structures at the surface of the material [112]. HIM imaging is performed by a fine helium ion beam, and either the backscattered He ions or secondary electrons are detected. The exceptional contrast in the secondary electron (SE) images is due to the small surface interaction volume [113]. The escape depth for the emitted secondary electrons is typically in the range of 5–15 nm for most materials [114]. The HIM provides a stronger surface sensitivity compared to the electron microscope. The HIM also yields images with a better signal-to-noise ratio [115]. Detailed modeling of the HIM image formation with secondary electron analysis has been provided [116]. A focused spot size smaller than 0.25 nm [117] or 0.3 nm [118] has been determined for imaging with the HIM in the SE mode.

4.3. Raman Spectroscopy

Raman spectra were obtained with a micro Raman spectrometer (Labram Aramis) operated in the backscattering mode. Spectra at 473 nm were acquired with a 10× objective and a thermoelectrically-cooled charge-coupled device detector. The foam was mounted on the sample holder with conductive carbon pads.

Oscillating molecules and functional groups have vibrations which correspond to the molecular structure and the microscopic environment. Such spectroscopic fingerprints, provided by Raman spectroscopy, can be used to identify bonding configurations. Bulk crystalline, nanocrystalline, and amorphous structures can usually well be distinguished. For carbon and carbonaceous materials [119], Raman spectroscopy is a valuable method for the distinction between sp^2 - and sp^3 -related bonds as

well as sp^2/sp^3 hybrid structures. It can even differentiate between different sp^2 carbon nanostructures such as carbon nanotubes and graphene [120].

4.4. X-ray Photoelectron Spectroscopy

X-ray photoelectron spectroscopy (XPS) was performed in a multi-chamber ultra-high vacuum system (Omicron) using a monochromatic X-ray source (Al $K\alpha$) and a Sphera electron analyzer with a spectral resolution of 0.9 eV. The spectra of the foam were measured at a chamber pressure below 10^{-9} mbar and an emission angle of 20° . The foam was mounted on the sample holder with conductive carbon pads. The spectra curves were fitted with a Shirley background for C1s, a linear background for O1s and symmetrical Voigt functions for both spectra.

XPS has been successfully applied to many different carbon materials [121] such as activated carbon [122], carbon spheres [123], amorphous carbon, nanodiamonds [124], diamond-like carbon films [125], carbon nanotubes [126], or nanoporous carbons [127]. Also, it can be used to study processes such as heat and chemical treatment [128], amorphization [129], electrochemical oxidation [130], or structural deformation [131]. The use of XPS for chemical analysis [128] and bonding [127] is of particular importance for solid-state research.

A characteristic feature of XPS measurements is that the instrument provides near-surface information about a material. The mean escape depth (MED) of photoelectrons is a complex result of various factors [132]. Both elastic [133,134] and inelastic [135] scattering of the photoelectrons determine the surface sensitivity in XPS. The MEDs vary slightly for different materials and obtain values such as 2.3 nm for polycrystalline silicon [136], 1.2 nm for germanium [137], 1–3 nm for various carbon materials [138], or 1–2 nm for amorphous carbon [139]. In our studies, we detect O1s in addition to C1s photoelectrons. It has been pointed out that the escape depth of O1s electrons in photoemission is of the same order as that of C1s [140]. This suggests that the MED in our XPS experiment is 1–2 nm, for photoelectrons from both the carbon and the oxygen core levels.

Acknowledgments: Natalie Frese was supported during parts of this research by a scholarship from the German Academic Exchange Service (DAAD-Doktorandenstipendium).

Author Contributions: Klaus Sattler and Armin Gölzhäuser conceived and designed the experiments; Natalie Frese, Shelby Taylor Mitchell, Amanda Bowers and Klaus Sattler performed the experiments and analyzed the data; Klaus Sattler and Armin Gölzhäuser contributed reagents/materials/analysis tools; Natalie Frese and Klaus Sattler wrote the paper.

Conflicts of Interest: The authors declare no conflict of interest.

References

1. Robertson, J. Diamond-like amorphous carbon. *Mater. Sci. Eng. R Rep.* **2002**, *37*, 129–281. [[CrossRef](#)]
2. Hu, B.; Wang, K.; Wu, L.H.; Yu, S.H.; Antonietti, M.; Titirici, M.M. Engineering carbon materials from the hydrothermal carbonization process of biomass. *Adv Mater.* **2010**, *22*, 813–828. [[CrossRef](#)] [[PubMed](#)]
3. Hata, T.; Vystavel, T.; Bronsveld, P.; DeHosson, J.; Kikuchi, H.; Nishimiya, K.; Imamura, Y. Catalytic carbonization of wood charcoal: Graphite or diamond? *Carbon* **2004**, *42*, 961–964. [[CrossRef](#)]
4. Tekin, K.; Karagoz, S.; Bektas, S. A review of hydrothermal biomass processing. *Renew. Sustain. Energy Rev.* **2014**, *40*, 673–687. [[CrossRef](#)]
5. Titirici, M.M.; White, R.J.; Falco, C.; Sevilla, M. Black perspectives for a green future: Hydrothermal carbons for environment protection and energy storage. *Energy Environ. Sci.* **2012**, *5*, 6796–6822. [[CrossRef](#)]
6. Kruse, A.; Funke, A.; Titirici, M.M. Hydrothermal conversion of biomass to fuels and energetic materials. *Curr. Opin. Chem. Biol.* **2013**, *17*, 515–521. [[CrossRef](#)] [[PubMed](#)]
7. Titirici, M.M.; Antonietti, M.; Baccile, N. Hydrothermal carbon from biomass: A comparison of the local structure from poly- to monosaccharides and pentoses/hexoses. *Green Chem.* **2008**, *10*, 1204–1212. [[CrossRef](#)]
8. Mitchell, S.T.; Frese, N.; Golzhäuser, A.; Bowers, A.; Sattler, K. Ultralight carbon nanofoam from naphthalene-mediated hydrothermal sucrose carbonization. *Carbon* **2015**, *95*, 434–441. [[CrossRef](#)]

9. Titirici, M.M.; Antonietti, M. Chemistry and materials options of sustainable carbon materials made by hydrothermal carbonization. *Chem. Soc. Rev.* **2010**, *39*, 103–116. [[CrossRef](#)] [[PubMed](#)]
10. Krishnan, D.; Raidongia, K.; Shao, J.J.; Huang, J.X. Graphene oxide assisted hydrothermal carbonization of carbon hydrates. *ACS Nano* **2014**, *8*, 449–457. [[CrossRef](#)] [[PubMed](#)]
11. Titirici, M.M.; Thomas, A.; Yu, S.H.; Muller, J.O.; Antonietti, M. A direct synthesis of mesoporous carbons with bicontinuous pore morphology from crude plant material by hydrothermal carbonization. *Chem. Mater.* **2007**, *19*, 4205–4212. [[CrossRef](#)]
12. Blinc, R.; Arcon, D.; Umek, P.; Apih, T.; Milia, F.; Rode, A.V. Carbon nanofoam as a potential hydrogen storage material. *Phys. Status Solidi B Basic Solid State Phys.* **2007**, *244*, 4308–4310. [[CrossRef](#)]
13. Chervin, C.N.; Long, J.W.; Brandell, N.L.; Wallace, J.M.; Kucko, N.W.; Rolison, D.R. Redesigning air cathodes for metal–air batteries using mnox-functionalized carbon nanofoam architectures. *J. Power Sources* **2012**, *207*, 191–198. [[CrossRef](#)]
14. Chervin, C.N.; Wattendorf, M.J.; Long, J.W.; Kucko, N.W.; Rolison, D.R. Carbon nanofoam-based cathodes for Li–O₂ batteries: Correlation of pore solid architecture and electrochemical performance. *J. Electrochem. Soc.* **2013**, *160*, A1510–A1516. [[CrossRef](#)]
15. Long, J.W.; Chervin, C.N.; Brandell, N.L.; Wallace, J.M.; Rolison, D.R. Functionalized carbon nanofoam electrode architectures as cathodes for Zn–air and Li–air batteries. *Abstr. Pap. Am. Chem. Soc.* **2011**, *241*.
16. Spanakis, E.; Pervolaraki, M.; Giapintzakis, J.; Katsarakis, N.; Koudoumas, E.; Vernardou, D. Effect of gold and silver nanoislands on the electrochemical properties of carbon nanofoam. *Electrochim. Acta* **2013**, *111*, 305–313. [[CrossRef](#)]
17. Boden, S.A.; Asadollahbaik, A.; Rutt, H.N.; Bagnall, D.M. Helium ion microscopy of lepidoptera scales. *Scanning* **2012**, *34*, 107–120. [[CrossRef](#)] [[PubMed](#)]
18. Jackson, S.T.; Nuzzo, R.G. Determining hybridization differences for amorphous-carbon from the XPS c-1s envelope. *Appl. Surf. Sci.* **1995**, *90*, 195–203. [[CrossRef](#)]
19. Sevilla, M.; Fuertes, A.B. Chemical and structural properties of carbonaceous products obtained by hydrothermal carbonization of saccharides. *Chem. A Eur. J.* **2009**, *15*, 4195–4203. [[CrossRef](#)] [[PubMed](#)]
20. Boehm, H.P. Surface oxides on carbon and their analysis: A critical assessment. *Carbon* **2002**, *40*, 145–149. [[CrossRef](#)]
21. Darmstadt, H.; Roy, C.; Kaliaguine, S.; Choi, S.J.; Ryoo, R. Surface chemistry of ordered mesoporous carbons. *Carbon* **2002**, *40*, 2673–2683. [[CrossRef](#)]
22. Puziy, A.M.; Poddubnaya, O.I.; Socha, R.P.; Gurgul, J.; Wisniewski, M. XPS and NMR studies of phosphoric acid activated carbons. *Carbon* **2008**, *46*, 2113–2123. [[CrossRef](#)]
23. Blyth, R.I.R.; Buqa, H.; Netzer, F.P.; Ramsey, M.G.; Besenhard, J.O.; Golob, P.; Winter, M. XPS studies of graphite electrode materials for lithium ion batteries. *Appl. Surf. Sci.* **2000**, *167*, 99–106. [[CrossRef](#)]
24. Cuesta, A.; Dhamelincourt, P.; Laureyns, J.; Martinezalonso, A.; Tascon, J.M.D. Raman microprobe studies on carbon materials. *Carbon* **1994**, *32*, 1523–1532. [[CrossRef](#)]
25. Ferrari, A.C.; Robertson, J. Interpretation of Raman spectra of disordered and amorphous carbon. *Phys. Rev. B* **2000**, *61*, 14095–14107. [[CrossRef](#)]
26. Chu, P.K.; Li, L.H. Characterization of amorphous and nanocrystalline carbon films. *Mater. Chem. Phys.* **2006**, *96*, 253–277. [[CrossRef](#)]
27. Wopenka, B.; Xu, Y.C.; Zinner, E.; Amari, S. Murchison presolar carbon grains of different density fractions: A Raman spectroscopic perspective. *Geochim. Cosmochim. Acta* **2013**, *106*, 463–489. [[CrossRef](#)]
28. Schwan, J.; Ulrich, S.; Batori, V.; Ehrhardt, H.; Silva, S.R.P. Raman spectroscopy on amorphous carbon films. *J. Appl. Phys.* **1996**, *80*, 440–447. [[CrossRef](#)]
29. Guiotoku, M.; Rambo, C.R.; Hotza, D. Charcoal produced from cellulosic raw materials by microwave-assisted hydrothermal carbonization. *J. Therm. Anal. Calorim.* **2014**, *117*, 269–275. [[CrossRef](#)]
30. Kumar, S.; Kothari, U.; Kong, L.Z.; Lee, Y.Y.; Gupta, R.B. Hydrothermal pretreatment of switchgrass and corn stover for production of ethanol and carbon microspheres. *Biomass Bioenergy* **2011**, *35*, 956–968. [[CrossRef](#)]
31. Ryu, J.; Suh, Y.W.; Suh, D.J.; Ahn, D.J. Hydrothermal preparation of carbon microspheres from mono-saccharides and phenolic compounds. *Carbon* **2010**, *48*, 1990–1998. [[CrossRef](#)]
32. Li, T.; Shen, J.F.; Li, N.; Ye, M.X. Facile and novel hydrothermal preparation of functionalised carbon microspheres from glucose by using graphene sheets as a substrate. *Mater. Lett.* **2012**, *89*, 202–205. [[CrossRef](#)]

33. Liu, J.; Tian, P.; Ye, J.W.; Zhou, L.; Gong, W.T.; Lin, Y.; Ning, G.L. Hydrothermal synthesis of carbon microspheres from glucose: Tuning sphere size by adding oxalic acid. *Chem. Lett.* **2009**, *38*, 948–949. [[CrossRef](#)]
34. Bazargan, A.; Yan, Y.; Hui, C.W.; McKay, G. A review: Synthesis of carbon-based nano and micro materials by high temperature and high pressure. *Ind. Eng. Chem. Res.* **2013**, *52*, 12689–12702. [[CrossRef](#)]
35. Serp, P.; Feurer, R.; Kalck, P.; Kihn, Y.; Faria, J.L.; Figueiredo, J.L. A chemical vapour deposition process for the production of carbon nanospheres. *Carbon* **2001**, *39*, 621–626. [[CrossRef](#)]
36. Wang, P.; Wei, J.Y.; Huang, B.B.; Qin, X.Y.; Yao, S.S.; Zhang, Q.; Wang, Z.Y.; Xu, G.G.; Jing, X.Y. Synthesis and characterization of carbon spheres prepared by chemical vapour deposition. *Mater. Lett.* **2007**, *61*, 4854–4856. [[CrossRef](#)]
37. Sharon, M.; Mukhopadhyay, K.; Yase, K.; Ijima, S.; Ando, Y.; Zhao, X.L. Spongy carbon nanobeads—A new material. *Carbon* **1998**, *36*, 507–511. [[CrossRef](#)]
38. Hou, H.Q.; Schaper, A.K.; Weller, F.; Greiner, A. Carbon nanotubes and spheres produced by modified ferrocene pyrolysis. *Chem. Mater.* **2002**, *14*, 3990–3994. [[CrossRef](#)]
39. Liu, X.Y.; Huang, B.C.; Coville, N.J. The Fe(CO)₅ catalyzed pyrolysis of pentane: Carbon nanotube and carbon nanoball formation. *Carbon* **2002**, *40*, 2791–2799. [[CrossRef](#)]
40. Sevilla, M.; Fuertes, A.B. The production of carbon materials by hydrothermal carbonization of cellulose. *Carbon* **2009**, *47*, 2281–2289. [[CrossRef](#)]
41. Qi, X.H.; Lian, Y.F.; Yan, L.L.; Smith, R.L. One-step preparation of carbonaceous solid acid catalysts by hydrothermal carbonization of glucose for cellulose hydrolysis. *Catal. Commun.* **2014**, *57*, 50–54. [[CrossRef](#)]
42. Li, M.; Li, W.; Liu, S.X. Hydrothermal synthesis, characterization, and KOH activation of carbon spheres from glucose. *Carbohydr. Res.* **2011**, *346*, 999–1004. [[CrossRef](#)] [[PubMed](#)]
43. Mi, Y.Z.; Hu, W.B.; Dan, Y.M.; Liu, Y.L. Synthesis of carbon micro-spheres by a glucose hydrothermal method. *Mater. Lett.* **2008**, *62*, 1194–1196. [[CrossRef](#)]
44. Yi, Z.H.; Liang, Y.G.; Lei, X.F.; Wang, C.W.; Sun, J.T. Low-temperature synthesis of nanosized disordered carbon spheres as an anode material for lithium ion batteries. *Mater. Lett.* **2007**, *61*, 4199–4203. [[CrossRef](#)]
45. Wang, Q.; Li, H.; Chen, L.Q.; Huang, X.J. Monodispersed hard carbon spherules with uniform nanopores. *Carbon* **2001**, *39*, 2211–2214. [[CrossRef](#)]
46. Zheng, M.T.; Liu, Y.L.; Xiao, Y.; Zhu, Y.; Guan, Q.; Yuan, D.S.; Zhang, J.X. An easy catalyst-free hydrothermal method to prepare monodisperse carbon microspheres on a large scale. *J. Phys. Chem. C* **2009**, *113*, 8455–8459. [[CrossRef](#)]
47. Chang, J.C.; Tzeng, Y.F.; Chen, J.M.; Chiu, H.T.; Lee, C.Y. Carbon nanobeads as an anode material on high rate capability lithium ion batteries. *Electrochim. Acta* **2009**, *54*, 7066–7070. [[CrossRef](#)]
48. Kohno, H.; Tatsutani, K.; Ichikawa, S. Carbon nanofoam formed by laser ablation. *J. Nanosci. Nanotechnol.* **2012**, *12*, 2844–2848. [[CrossRef](#)] [[PubMed](#)]
49. Rode, A.V.; Elliman, R.G.; Gamaly, E.G.; Veinger, A.I.; Christy, A.G.; Hyde, S.T.; Luther-Davies, B. Electronic and magnetic properties of carbon nanofoam produced by high-repetition-rate laser ablation. *Appl. Surf. Sci.* **2002**, *197*, 644–649. [[CrossRef](#)]
50. Rode, A.V.; Gamaly, E.G.; Christy, A.G.; Gerald, J.F.; Hyde, S.T.; Elliman, R.G.; Luther-Davies, B.; Veinger, A.I.; Androulakis, J.; Giapintzakis, J. Strong paramagnetism and possible ferromagnetism in pure carbon nanofoam produced by laser ablation. *J. Magn. Magn. Mater.* **2005**, *290*, 298–301. [[CrossRef](#)]
51. Carrasco, J.A.; Prima-Garcia, H.; Romero, J.; Hernandez-Saz, J.; Molina, S.I.; Abellan, G.; Coronado, E. CVD synthesis of carbon spheres using NiFe-LDHs as catalytic precursors: Structural, electrochemical and magnetoresistive properties. *J. Mater. Chem. C* **2016**, *4*, 440–448. [[CrossRef](#)]
52. Levesque, A.; Binh, V.T.; Semet, V.; Guillot, D.; Fillit, R.Y.; Brookes, M.D.; Nguyen, T.P. Monodisperse carbon nanopearls in a foam-like arrangement: A new carbon nano-compound for cold cathodes. *Thin Solid Films* **2004**, *464*, 308–314. [[CrossRef](#)]
53. Ma, A.L.; Wang, X.M.; Li, T.B.; Liu, X.G.; Xu, B.S. Characteristics of carbon microspheres and study on its adsorption isotherms. *Mater. Sci. Eng. A* **2007**, *443*, 54–59.
54. Mondal, K.C.; Strydom, A.M.; Tetana, Z.; Mhlanga, S.D.; Witcomb, M.J.; Havel, J.; Erasmus, R.M.; Coville, N.J. Boron-doped carbon microspheres. *Mater. Chem. Phys.* **2009**, *114*, 973–977. [[CrossRef](#)]
55. Pradhan, D.; Sharon, M. Carbon nanotubes, nanofilaments and nanobeads by thermal chemical vapor deposition process. *Mater. Sci. Eng. B* **2002**, *96*, 24–28. [[CrossRef](#)]

56. Shi, J.L.; Peng, H.J.; Zhu, L.; Zhu, W.C.; Zhang, Q. Template growth of porous graphene microspheres on layered double oxide catalysts and their applications in lithium-sulfur batteries. *Carbon* **2015**, *92*, 96–105. [[CrossRef](#)]
57. Vieira, S.M.C.; Rego, C.A.; Birkett, P.R. Carbon spheres formed by hot filament chemical vapour deposition. *Diam. Relat. Mat.* **2008**, *17*, 100–104. [[CrossRef](#)]
58. Wang, Z.L.; Kang, Z.C. Pairing of pentagonal and heptagonal carbon rings in the growth of nanosize carbon spheres synthesized by a mixed-valent oxide-catalytic carbonization process. *J. Phys. Chem.* **1996**, *100*, 17725–17731. [[CrossRef](#)]
59. Wright, W.P.; Marsicano, V.D.; Keartland, J.M.; Erasmus, R.M.; Dube, S.M.A.; Coville, N.J. The electrical transport properties of nitrogen doped carbon microspheres. *Mater. Chem. Phys.* **2014**, *147*, 908–914. [[CrossRef](#)]
60. Zhong, Z.Y.; Chen, H.Y.; Tang, S.B.; Ding, J.; Lin, J.Y.; Tan, K.L. Catalytic growth of carbon nanoballs with and without cobalt encapsulation. *Chem. Phys. Lett.* **2000**, *330*, 41–47. [[CrossRef](#)]
61. Wohlgemuth, S.A.; Vilela, F.; Titirici, M.M.; Antonietti, M. A one-pot hydrothermal synthesis of tunable dual heteroatom-doped carbon microspheres. *Green Chem.* **2012**, *14*, 741–749. [[CrossRef](#)]
62. Chen, J.Z.; Chen, Z.H.; Wang, C.H.; Li, X.D. Calcium-assisted hydrothermal carbonization of an alginate for the production of carbon microspheres with unique surface nanopores. *Mater. Lett.* **2012**, *67*, 365–368. [[CrossRef](#)]
63. Qi, X.H.; Li, L.Y.; Tan, T.F.; Chen, W.T.; Smith, R.L. Adsorption of 1-butyl-3-methylimidazolium chloride ionic liquid by functional carbon microspheres from hydrothermal carbonization of cellulose. *Environ. Sci. Technol.* **2013**, *47*, 2792–2798. [[CrossRef](#)] [[PubMed](#)]
64. Wang, H.L.; Shi, Z.Q.; Jin, J.; Chong, C.B.; Wang, C.Y. Properties and sodium insertion behavior of phenolic resin-based hard carbon microspheres obtained by a hydrothermal method. *J. Electroanal. Chem.* **2015**, *755*, 87–91. [[CrossRef](#)]
65. Wu, Q.; Li, W.; Tan, J.; Wu, Y.J.; Liu, S.X. Hydrothermal carbonization of carboxymethylcellulose: One-pot preparation of conductive carbon microspheres and water-soluble fluorescent carbon nanodots. *Chem. Eng. J.* **2015**, *266*, 112–120. [[CrossRef](#)]
66. Zheng, M.T.; Xiao, Y.; Zhang, H.R.; Dong, H.W.; Gong, X.B.; Xu, R.C.; Lei, B.F.; Liu, Y.L.; Liu, X.T. Hydrothermal synthesis and characterization of sulfur-doped carbon microspheres. *Chin. J. Inorg. Chem.* **2013**, *29*, 1391–1399.
67. Zhou, X.; You, S.J.; Wang, X.H.; Gan, Y.; Zhong, Y.J.; Ren, N.Q. Hydrothermal synthesis of magnetic carbon microspheres for effective adsorption of CD(II) in water. *J. Chem. Technol. Biotechnol.* **2014**, *89*, 1051–1059. [[CrossRef](#)]
68. Zhang, Z.J.; Wang, Q.; Zhu, Y.Q.; Chen, X.Y. Nanoporous graphitic carbon materials: Systematic incorporation of p-/m-/o-nitroaniline as effective redox additives for largely improving the capacitive performance. *Carbon* **2016**, *100*, 564–577. [[CrossRef](#)]
69. Dyjak, S.; Kicinski, W.; Norek, M.; Huczko, A.; Labeledz, O.; Budner, S.; Polanski, M. Hierarchical, nanoporous graphenic carbon materials through an instant, self-sustaining magnesiothermic reduction. *Carbon* **2016**, *96*, 937–946. [[CrossRef](#)]
70. Jafari, S.M.; Khosravi, M.; Mollazadeh, M. Nanoporous hard carbon microspheres as anode active material of lithium ion battery. *Electrochim. Acta* **2016**, *203*, 9–20. [[CrossRef](#)]
71. Li, S.Y.; Wang, Y.; Wei, Y.; Zeng, J.; Shi, W.Y.; Wang, Y.W. Preparation and adsorption performance of palm fiber-based nanoporous carbon materials with high specific surface area. *J. Porous Mater.* **2016**, *23*, 1059–1064. [[CrossRef](#)]
72. Shrestha, L.K.; Shrestha, R.G.; Yamauchi, Y.; Hill, J.P.; Nishimura, T.; Miyazawa, K.; Kawai, T.; Okada, S.; Wakabayashi, K.; Ariga, K. Nanoporous carbon tubes from fullerene crystals as the pi-electron carbon source. *Angew. Chem. Int. Ed.* **2015**, *54*, 951–955. [[CrossRef](#)] [[PubMed](#)]
73. Jia, L.C.; Lawrence, G.; Balasubramanian, V.V.; Choi, G.; Choy, J.H.; Abdullah, A.M.; Elzatahry, A.; Ariga, K.; Vinu, A. Highly ordered nanoporous carbon films with tunable pore diameters and their excellent sensing properties. *Chem. A Eur. J.* **2015**, *21*, 697–703. [[CrossRef](#)] [[PubMed](#)]
74. Bandoz, T.J. Nanoporous carbons: Looking beyond their perception as adsorbents, catalyst supports and supercapacitors. *Chem. Rec.* **2016**, *16*, 205–218. [[CrossRef](#)] [[PubMed](#)]
75. Ortiz, L.; Kuchta, B.; Firlej, L.; Roth, M.W.; Wexler, C. Methane adsorption in nanoporous carbon: The numerical estimation of optimal storage conditions. *Mater. Res. Express* **2016**, *3*, 5. [[CrossRef](#)]

76. Rashidi, A.M.; Kazemi, D.; Izadi, N.; Pourkhalil, M.; Jorsaraei, A.; Ganji, E.; Lotfi, R. Preparation of nanoporous activated carbon and its application as nano adsorbent for CO₂ storage. *Korean J. Chem. Eng.* **2016**, *33*, 616–622. [[CrossRef](#)]
77. Puziy, A.M.; Poddubnaya, O.I.; Derylo-Marczewska, A.; Marczewski, A.W.; Blachnio, M.; Tsyba, M.M.; Sapsay, V.I.; Klymchuk, D.O. Kinetics of protein adsorption by nanoporous carbons with different pore size. *Adsorpt. J. Int. Adsorpt. Soc.* **2016**, *22*, 541–552. [[CrossRef](#)]
78. Ghiloufi, I.; Khezami, L.; El Mir, L. Nanoporous activated carbon for fast uptake of heavy metals from aqueous solution. *Desalination Water Treat.* **2015**, *55*, 935–944. [[CrossRef](#)]
79. Li, W.L.; Seredych, M.; Rodriguez-Castellon, E.; Bandosz, T.J. Metal-free nanoporous carbon as a catalyst for electrochemical reduction of CO₂ to CO and CH₄. *Chemsuschem* **2016**, *9*, 606–616. [[CrossRef](#)] [[PubMed](#)]
80. Singh, K.; Travlou, N.A.; Bashkova, S.; Rodriguez-Castellon, E.; Bandosz, T.J. Nanoporous carbons as gas sensors: Exploring the surface sensitivity. *Carbon* **2014**, *80*, 183–192. [[CrossRef](#)]
81. Zhong, C.Y.; Yuan, W.Y.; Kang, Y.J.; Xie, J.L.; Hu, F.X.; Li, C.M. Biomass-derived hierarchical nanoporous carbon with rich functional groups for direct-electron-transfer-based glucose sensing (vol 3, pg 144, 2016). *Chemelectrochem* **2016**, *3*. [[CrossRef](#)]
82. Bandosz, T.J.; Rodriguez-Castellon, E.; Montenegro, J.M.; Seredych, M. Photoluminescence of nanoporous carbons: Opening a new application route for old materials. *Carbon* **2014**, *77*, 651–659. [[CrossRef](#)]
83. Maeland, A.J.; Skjeltop, A.T. Hydrogen Storage in Carbon Material. U.S. Patent 6,290,753, 18 September 2001.
84. Geng, Z.; Zhang, C.M.; Wang, D.B.; Zhou, X.Y.; Cai, M. Pore size effects of nanoporous carbons with ultra-high surface area on high-pressure hydrogen storage. *J. Energy Chem.* **2015**, *24*, 1–8. [[CrossRef](#)]
85. Leyva-Garcia, S.; Morallon, E.; Cazorla-Amoros, D.; Beguin, F.; Lozano-Castello, D. New insights on electrochemical hydrogen storage in nanoporous carbons by in situ Raman spectroscopy. *Carbon* **2014**, *69*, 401–408. [[CrossRef](#)]
86. Ting, V.P.; Ramirez-Cuesta, A.J.; Bimbo, N.; Sharpe, J.E.; Noguera-Diaz, A.; Presser, V.; Rudic, S.; Mays, T.J. Direct evidence for solid-like hydrogen in a nanoporous carbon hydrogen storage material at supercritical temperatures. *ACS Nano* **2015**, *9*, 8249–8254. [[CrossRef](#)] [[PubMed](#)]
87. Nigmatullin, R.R.; Baleanu, D.; Povarova, D.; Salah, N.; Habib, S.S.; Memic, A. Raman spectra of nanodiamonds: New treatment procedure directed for improved Raman signal marker detection. *Math. Probl. Eng.* **2013**, *11*. [[CrossRef](#)]
88. Dychalska, A.; Popielarski, P.; Frankow, W.; Fabisiak, K.; Paprocki, K.; Szybowicz, M. Study of CVD diamond layers with amorphous carbon admixture by Raman scattering spectroscopy. *Mater. Sci. Pol.* **2015**, *33*, 799–805. [[CrossRef](#)]
89. Namba, Y.; Heidarpour, E.; Nakayama, M. Size effects appearing in the Raman-spectra of polycrystalline diamonds. *J. Appl. Phys.* **1992**, *72*, 1748–1751. [[CrossRef](#)]
90. Liu, P.; Sun, Q.; Zhu, F.; Liu, K.; Jiang, K.; Liu, L.; Li, Q.; Fan, S. Measuring the work function of carbon nanotubes with thermionic method. *Nano Lett.* **2008**, *8*, 647–651. [[CrossRef](#)] [[PubMed](#)]
91. Yoshikawa, M.; Mori, Y.; Maegawa, M.; Katagiri, G.; Ishida, H.; Ishitani, A. Raman-scattering from diamond particles. *Appl. Phys. Lett.* **1993**, *62*, 3114–3116. [[CrossRef](#)]
92. Osswald, S.; Mochalin, V.N.; Havel, M.; Yushin, G.; Gogotsi, Y. Phonon confinement effects in the Raman spectrum of nanodiamond. *Phys. Rev. B* **2009**, *80*, 075419. [[CrossRef](#)]
93. Shin, J.K.; Lee, C.S.; Lee, K.R.; Eun, K.Y. Effect of residual stress on the Raman-spectrum analysis of tetrahedral amorphous carbon films. *Appl. Phys. Lett.* **2001**, *78*, 631–633. [[CrossRef](#)]
94. Zhou, J.H.; Sui, Z.J.; Zhu, J.; Li, P.; De, C.; Dai, Y.C.; Yuan, W.K. Characterization of surface oxygen complexes on carbon nanofibers by TPD, XPS and FT-IR. *Carbon* **2007**, *45*, 785–796. [[CrossRef](#)]
95. Liu, X.; Su, D.S.; Schlogl, R. Oxidative dehydrogenation of 1-butene to butadiene over carbon nanotube catalysts. *Carbon* **2008**, *46*, 547–549. [[CrossRef](#)]
96. Desimoni, E.; Casella, G.I.; Morone, A.; Salvi, A.M. XPS determination of oxygen-containing functional-groups on carbon-fiber surfaces and the cleaning of these surfaces. *Surf. Interface Anal.* **1990**, *15*, 627–634. [[CrossRef](#)]
97. Fan, X.M.; Yu, C.; Yang, J.; Ling, Z.; Qiu, J.S. Hydrothermal synthesis and activation of graphene-incorporated nitrogen-rich carbon composite for high-performance supercapacitors. *Carbon* **2014**, *70*, 130–141. [[CrossRef](#)]
98. Mori, Y.; Kawarada, H.; Hiraki, A. Properties of metal diamond interfaces and effects of oxygen adsorbed onto diamond surface. *Appl. Phys. Lett.* **1991**, *58*, 940–941. [[CrossRef](#)]

99. Ghodbane, S.; Haensel, T.; Coffinier, Y.; Szunerits, S.; Steinmuller-Nethl, D.; Boukherroub, R.; Ahmed, S.I.U.; Schaefer, J.A. Hreels investigation of the surfaces of nanocrystalline diamond films oxidized by different processes. *Langmuir* **2010**, *26*, 18798–18805. [[CrossRef](#)] [[PubMed](#)]
100. Gajewski, W.; Huth, M.; Buth, F.; Nickel, B.; Stutzmann, M.; Garrido, J.A. Photoresponse and morphology of pentacene thin films modified by oxidized and reduced diamond surfaces. *Phys. Rev.B* **2009**, *80*, 235311. [[CrossRef](#)]
101. Makau, N.W.; Derry, T.E. Study of oxygen on the three low index diamond surfaces by XPS. *Surf. Rev. Lett.* **2003**, *10*, 295–301. [[CrossRef](#)]
102. Speranza, G.; Torrenzo, S.; Miotello, A.; Minati, L.; Bernagozzi, I.; Ferrari, M.; Dipalo, M.; Kohn, E. XPS and UPS in situ study of oxygen thermal desorption from nanocrystalline diamond surface oxidized by different process. *Diam. Relat. Mat.* **2011**, *20*, 560–563. [[CrossRef](#)]
103. Takabayashi, S.; Okamoto, K.; Motoyama, H.; Nakatani, T.; Sakaue, H.; Takahagi, T. X-ray photoelectron analysis of surface functional groups on diamond-like carbon films by gas-phase chemical derivatization method. *Surf. Interface Anal.* **2010**, *42*, 77–87. [[CrossRef](#)]
104. Shandilya, M.; Rai, R.; Singh, J. Review: Hydrothermal technology for smart materials. *Adv. Appl. Ceram.* **2016**, *115*, 354–376. [[CrossRef](#)]
105. Funke, A.; Ziegler, F. Hydrothermal carbonization of biomass: A summary and discussion of chemical mechanisms for process engineering. *Biofuels Bioprod. Biorefin. Biofpr* **2010**, *4*, 160–177. [[CrossRef](#)]
106. Gron, L.U.; LaCroix, J.E.; Higgins, C.J.; Steelman, K.L.; Tinsley, A.S. Heck reactions in hydrothermal, sub-critical water: Water density as an important reaction variable. *Tetrahedron Lett.* **2001**, *42*, 8555–8557. [[CrossRef](#)]
107. Kurniawan, A.; Effendi, C.; Ong, L.K.; Kurniawan, F.; Lin, C.X.; Angkawijaya, A.E.; Ju, Y.H.; Ismadji, S.; Zhao, X.S. Preparation of nanoporous carbon microspheres by subcritical water carbonization and electrocapacitive study. *Electrochim. Acta* **2013**, *111*, 99–107. [[CrossRef](#)]
108. Economou, N.P.; Notte, J.A.; Thompson, W.B. The history and development of the helium ion microscope. *Scanning* **2012**, *34*, 83–89. [[CrossRef](#)] [[PubMed](#)]
109. Scipioni, L.; Stern, L.A.; Notte, J.; Sijbrandij, S.; Griffin, B. Helium ion microscope. *Adv. Mater. Process.* **2008**, *166*, 27–30.
110. Scipioni, L.; Sanford, C.A.; Notte, J.; Thompson, B.; McVey, S. Understanding imaging modes in the helium ion microscope. *J. Vac. Sci. Technol. B* **2009**, *27*, 3250–3255. [[CrossRef](#)]
111. Petrov, Y.V.; Vyvenko, O.F.; Bondarenko, A.S. Scanning helium ion microscope: Distribution of secondary electrons and ion channeling. *J. Surf. Investig. X-ray Synchrotron Neutron Tech.* **2010**, *4*, 792–795. [[CrossRef](#)]
112. Sanford, C.; Notte, J.; Scipioni, L.; McVey, S.; Hill, R.; Sijbrandij, S.; Farkas, L. Advances in high resolution helium ion microscope (HIM) imaging. *Microsc. Microanal.* **2009**, *15*, 654–655. [[CrossRef](#)]
113. Bell, D.C. Contrast mechanisms and image formation in helium ion microscopy. *Microsc. Microanal.* **2009**, *15*, 147–153. [[CrossRef](#)] [[PubMed](#)]
114. Cohen-Tanugi, D.; Yao, N. Superior imaging resolution in scanning helium-ion microscopy: A look at beam-sample interactions. *J. Appl. Phys.* **2008**, *104*. [[CrossRef](#)]
115. Fox, D.; Zhou, Y.B.; O'Neill, A.; Kumar, S.; Wang, J.J.; Coleman, J.N.; Duesberg, G.S.; Donegan, J.F.; Zhang, H.Z. Helium ion microscopy of graphene: Beam damage, image quality and edge contrast. *Nanotechnology* **2013**, *24*, 33. [[CrossRef](#)] [[PubMed](#)]
116. Ohya, K.; Yamanaka, T.; Inai, K.; Ishitani, T. Comparison of secondary electron emission in helium ion microscope with gallium ion and electron microscopes. *Nucl. Instrum. Methods Phys. Res. Sect B Beam Interact. Mater. At.* **2009**, *267*, 584–589. [[CrossRef](#)]
117. Ward, B.W.; Notte, J.A.; Economou, N.P. Helium ion microscope: A new tool for nanoscale microscopy and metrology. *J. Vac. Sci. Technol. B* **2006**, *24*, 2871–2874. [[CrossRef](#)]
118. Sijbrandij, S.; Notte, J.; Sanford, C.; Hill, R. Analysis of subsurface beam spread and its impact on the image resolution of the helium ion microscope. *J. Vac. Sci. Technol. B* **2010**, *28*, C6F6–C6F9. [[CrossRef](#)]
119. Chipara, D.M.; Chipara, A.C.; Chipara, M. Raman spectroscopy of carbonaceous materials: A concise review. *Spectroscopy* **2011**, *26*, 42–47.
120. Dresselhaus, M.S.; Jorio, A.; Hofmann, M.; Dresselhaus, G.; Saito, R. Perspectives on carbon nanotubes and graphene Raman spectroscopy. *Nano Lett.* **2010**, *10*, 751–758. [[CrossRef](#)] [[PubMed](#)]

121. Retzko, I.; Unger, W.E.S. Analysis of carbon materials by X-ray photoelectron spectroscopy and X-ray absorption spectroscopy. *Adv. Eng. Mater.* **2003**, *5*, 519–522. [[CrossRef](#)]
122. Lennon, D.; Lundie, D.T.; Jackson, S.D.; Kelly, G.J.; Parker, S.F. Characterization of activated carbon using X-ray photoelectron spectroscopy and inelastic neutron scattering spectroscopy. *Langmuir* **2002**, *18*, 4667–4673. [[CrossRef](#)]
123. Ray, S.C.; Tetana, Z.N.; Erasmus, R.; Mathur, A.; Coville, N.J. Carbon spheres for energy applications: Raman and X-ray photoemission spectroscopy studies. *Int. J. Energy Res.* **2014**, *38*, 444–451. [[CrossRef](#)]
124. Petit, T.; Arnault, J.C.; Girard, H.A.; Sennour, M.; Bergonzo, P. Early stages of surface graphitization on nanodiamond probed by X-ray photoelectron spectroscopy. *Phys. Rev. B* **2011**, *84*, 233407. [[CrossRef](#)]
125. Takabayashi, S.; Okamoto, K.; Shimada, K.; Motomitsu, K.; Motoyama, H.; Nakatani, T.; Sakaue, H.; Suzuki, H.; Takahagi, T. Chemical structural analysis of diamondlike carbon films with different electrical resistivities by X-ray photoelectron spectroscopy. *Jpn. J. Appl. Phys.* **2008**, *47*, 3376–3379. [[CrossRef](#)]
126. Abbas, M.; Wu, Z.Y.; Zhong, J.; Ibrahim, K.; Fiori, A.; Orlanducci, S.; Sessa, V.; Terranova, M.L.; Davoli, I. X-ray absorption and photoelectron spectroscopy studies on graphite and single-walled carbon nanotubes: Oxygen effect. *Appl. Phys. Lett.* **2005**, *87*. [[CrossRef](#)]
127. Gordeev, S.K.; Grechinskaya, A.V.; Danishevskii, A.M.; Smorgonskaya, E.A.; Shchukarev, A.V. Study of bonding in nanoporous carbon by X-ray photoelectron spectroscopy. *Mol. Mater.* **2000**, *13*, 355–360.
128. Yang, D.; Velamakanni, A.; Bozoklu, G.; Park, S.; Stoller, M.; Piner, R.D.; Stankovich, S.; Jung, I.; Field, D.A.; Ventrice, C.A.; et al. Chemical analysis of graphene oxide films after heat and chemical treatments by X-ray photoelectron and micro-Raman spectroscopy. *Carbon* **2009**, *47*, 145–152. [[CrossRef](#)]
129. Takahiro, K.; Terai, A.; Oizumi, S.; Kawatsura, K.; Yamamoto, S.; Naramoto, H. Amorphization of carbon materials studied by X-ray photoelectron spectroscopy. *Nucl. Instrum. Methods Phys. Res. Sect. B Beam Interact. Mater. At.* **2006**, *242*, 445–447. [[CrossRef](#)]
130. Achour, A.; Vizireanu, S.; Dinescu, G.; Le Brizoual, L.; Djouadi, M.A.; Boujtita, M. Electrochemical anodic oxidation of nitrogen doped carbon nanowall films: X-ray photoelectron and micro-Raman spectroscopy study. *Appl. Surf. Sci.* **2013**, *273*, 49–57. [[CrossRef](#)]
131. Barty, A.; Marchesini, S.; Chapman, H.N.; Cui, C.; Howells, M.R.; Shapiro, D.A.; Minor, A.M.; Spence, J.C.H.; Weierstall, U.; Ilavsky, J.; et al. Three-dimensional coherent X-ray diffraction imaging of a ceramic nanofoam: Determination of structural deformation mechanisms. *Phys. Rev. Lett.* **2008**, *101*, 055501. [[CrossRef](#)] [[PubMed](#)]
132. Jablonski, A.; Tilinin, I.S.; Powell, C.J. Mean escape depth of signal photoelectrons from amorphous and polycrystalline solids. *Phys. Rev. B* **1996**, *54*, 10927–10937. [[CrossRef](#)]
133. Jablonski, A. Elastic photoelectron scattering effects in the XPS analysis of stratified samples. *J. Phys. D Appl. Phys.* **2012**, *45*, 31. [[CrossRef](#)]
134. Nefedov, V.I. Photoelectron elastic scattering effects in XPS. *J. Electron Spectrosc. Relat. Phenom.* **1999**, *100*, 1–15. [[CrossRef](#)]
135. Jablonski, A.; Powell, C.J. Relationships between electron inelastic mean free paths, effective attenuation lengths, and mean escape depths (vol 100, pg 137, 1999). *J. Electron Spectrosc. Relat. Phenom.* **2000**, *107*, 201. [[CrossRef](#)]
136. Tilinin, I.S.; Jablonski, A.; Lesiakorłowska, B. Mean escape depth of signal photoelectrons from amorphous and polycrystalline solids. *Acta Phys. Pol. A* **1994**, *86*, 845–852. [[CrossRef](#)]
137. Hovis, J.S.; Hamers, R.J.; Greenlief, C.M. Preparation of clean and atomically flat germanium(001) surfaces. *Surf. Sci.* **1999**, *440*, L815–L819. [[CrossRef](#)]
138. Wang, B.; Ma, Y.F.; Wu, Y.P.; Li, N.; Huang, Y.; Chen, Y.S. Direct and large scale electric arc discharge synthesis of boron and nitrogen doped single-walled carbon nanotubes and their electronic properties. *Carbon* **2009**, *47*, 2112–2115. [[CrossRef](#)]
139. Reinke, P.; Francz, G.; Oelhafen, P.; Ullmann, J. Structural changes in diamond and amorphous carbon induced by low-energy ion irradiation. *Phys. Rev. B* **1996**, *54*, 7067–7073. [[CrossRef](#)]
140. Onoe, J.; Nakao, A.; Takeuchi, K. XPS study of a photopolymerized c-60 film. *Phys. Rev. B* **1997**, *55*, 10051–10056. [[CrossRef](#)]



Literature

- [1] H. S. Stoker: *General, Organic, and Biological Chemistry: 4th Edition*. Cengage Learning (2007) Page 294
- [2] K. D. Sattler: *Carbon Nanomaterials Sourcebook*. CRC Press (2016)
- [3] G. Benedek, P. Milani, V. G. Ralchenko: *Nanostructured Carbon for Advanced Applications*. Kluwer Academic Publishers (2000) Pages 3-5
- [4] S. A. Boden, A. Asadollahbaik, H. N Rutt, D. M. Bagnall: *Helium ion microscopy of Lepidoptera scales*. Scanning Vol. 34 (2012) Pages 107-120
- [5] H. R. Horton, L. A. Moran, K. G. Scrimgeour, M. D. Perry, J. D. Rawn: *Biochemie*. Pearson Education Deutschland GmbH (2008) Pages 170-173
- [6] C. Dart: *Lipid microdomains and the regulation of ion channel function*. The Journal of Physiology Vol. 588 (2010) Pages 3169-3178
- [7] N. Frese: *Abbildung biologischer Zellen mittels Helium-Ionen-Mikroskopie*. Master thesis, Bielefeld University, Bielefeld (2013)
- [8] I. B. Levitan, L. K. Kaczmarek: *The Neuron: Cell and Molecular Biology*. Oxford University Press (2002) Pages 9-11
- [9] J. R. Buitenweg, W. L. C. Rutten, E. Marani: *Geometry-based finite-element modeling of the electrical contact between a cultured neuron and a microelectrode*. IEEE transactions on bio-medical engineering Vol. 50 (2003) Pages 501-509
- [10] A. Turchanin, A. Götzhäuser: *Carbon Nanomembranes*. Advanced Materials Vol. 28 (2016) Pages 6075-6103
- [11] R. Henderson, P. N. T. Unwin: *Three-dimensional model of purple membrane obtained by electron microscopy*. Nature Vol. 257 (1975) Pages 28-32
- [12] D. Rhinow, J. Vonck, M. Schranz, A. Beyer, A. Götzhäuser, N. Hampp: *Ultrathin conductive carbon nanomembranes as support films for structural analysis of biological specimens*. Physical Chemistry Chemical Physics Vol. 12 (2010) Pages 4345-4350
- [13] D. Oesterhelt, W. Stoerkenius: *Functions of a New Photoreceptor Membrane*. Proceedings of the National Academy of Sciences of the United States of America Vol. 70 (1973) Pages 2853-2857
- [14] L. Keszthelyi: *Orientation of membrane fragments by electric field*. Biochimica et Biophysica Acta 598 Vol. 70 (1980) Pages 429-436

- [15] J. Sasaki, L. S. Brown, Y. S. Chon, H. Kandori, A. Maede, R. Needleman, J. K. Lanyi: *Conversion of bacteriorhodopsin into a chloride pump*. Science Vol. 269 (1995) Pages 73-75
- [16] A. Turchanin, A. Tinazli, M. El-Desawy, H. Grossmann, M. Schnietz, H. H. Solak, R. Tampe, A. Götzhäuser: *Molecular self-assembly, chemical lithography, and biochemical tweezers: a path for the fabrication of functional nanometer-scale protein arrays*. Advanced Materials Vol. 20 (2008) Pages 471-477
- [17] M. M. Titirici, R. J. White, C. Falco, M. Sevilla: *Black perspectives for a green future: hydrothermal carbons for environment protection and energy storage*. Energy and Environmental Science Vol. 5 (2012) Pages 6796-6822
- [18] W. L. Rice, A. N. Van Hoek, T. G. Paunescu, C. Huynh, B. Goetze, B. Singh, L. Scipioni, L. A. Stern, D. Brown: *High Resolution Helium Ion Scanning Microscopy of the Rat Kidney*. PLOS ONE Vol. 8 (2013) Pages 1-9
- [19] W. S. Vanden Berg-Foels, L. Scipioni, C. Huynh, X. Wen: *Helium ion microscopy for high-resolution visualization of the articular cartilage collagen network*. Journal of Microscopy Vol. 246 (2012) Pages 168-176
- [20] D. C. Bell, M. C. Lemme, L. A. Stern, J. R. Williams, C. M. Marcus: *Precision cutting and patterning of graphene with helium ions*. Nanotechnology Vol. 20 (2009) Pages 455301-455305
- [21] D. C. Bell: *Contrast mechanisms and image formation in helium ion microscopy*. Microscopy and Microanalysis Vol. 15 (2009) Pages 147-153
- [22] *Helium Ion Microscope Operation Training Manual*. Carl Zeiss SMT Oberkochen (2010)
- [23] N. P. Economou, J. A. Notte, W. B. Thompson: *The history and development of the helium ion microscope*. Scanning Vol. 34 (2011) Pages 1-7
- [24] K. Jopp: *Scharfes Auge für die Nanowelt*. Innovation Vol. 19 (2008) Pages 34, 35
- [25] J. Morgan, J. Notte, R. Hill, B. Ward: *An introduction to the helium ion microscope*. Microscopy Today Vol. 14 (2006) Pages 24-31
- [26] R. Ramachandra: *A Study of Helium Ion Induced Secondary Electron Production*. Dissertation, University of Tennessee, Knoxville (2009)
- [27] K. W. Kim: *Biological Applications of Helium Ion Microscopy*. Applied Microscopy Vol. 34 (2013) Pages 9-13
- [28] L. Scipioni, C. A. Sanford, J. Notte, B. Thompson, S. McVey: *Understanding imaging modes in the helium ion microscope*. Journal Vacuum Science and Technology B Vol. 27 (2009) Pages 3250-3255

- [29] R. Ramachandra, B. Griffin, D. Joy: *A model of secondary electron imaging in the helium ion scanning microscope*. Ultramicroscopy Vol. 109 (2009) Pages 746-757
- [30] B. W. Ward, J. A. Notte, N. P. Economou: *Helium ion microscope: A new tool for nanoscale microscopy and metrology*. Journal Vacuum Science and Technology B Vol. 24 (2006) Pages 2671-2874
- [31] B. J. Griffin: *A Comparison of Conventional Everhart-Thornley Style and In-Lens Secondary Electron Detectors - A Further Variable in Scanning Electron Microscopy*. Scanning B Vol. 33 (2011) Pages 162-173
- [32] M. T. Postek, A. E. Vladar: *Helium ion microscopy and its application to nanotechnology and nanometrology*. Scanning Vol. 30 (2008) Pages 457-462
- [33] A. E. Vladar, M. T. Postek, B. Ming: *On the Sub-Nanometer Resolution of Scanning Electron and Helium Ion Microscopes*. Microscopy Today Vol. 17 (2009) Pages 6-13
- [34] D. Bazou, G. Behan, C. Reid, J. Boland, H. Zhang: *Imaging of human colon cancer cells using He-Ion scanning microscopy*. Journal of Microscopy Vol. 242 (2010) Pages 290-294
- [35] L. Scipioni, D. Pickard: *Working with Uncoated Biological Specimens*. Application Note, Carl Zeiss SMT (2009) Pages 1-6
- [36] G. Binnig, C. Quate, C. Gerber: *Atomic Force Microscope*. Physical Review Letters Vol. 56 (1986) Pages 930-933
- [37] N. Frese: *Optimierung der Sputterparameter zur Reinigung von nc-AFM-Spitzen in einem UHV-AFM*. Bachelor thesis, Bielefeld University, Bielefeld (2012)
- [38] F. Giessibl: *Atomic Resolution of the Silicon (111)-(7x7) Surface by Atomic Force Microscopy*. Science Vol. 267 (1995) Pages 68-71
- [39] O. Marti, B. Drake, P. Hansma: *Atomic force microscopy of liquid-covered surfaces: Atomic resolution images*. Applied Physics Letters Vol. 51 (1987) Page 484
- [40] H.-J. Butt, B. Cappella, M. Kappl: *Force measurements with the atomic force microscope: Technique, interpretation and applications*. Surface Science Reports Vol. 59 (2005) Pages 1-152
- [41] P. Girard: *Electrostatic force microscopy: principles and some applications to semiconductors*. Nanotechnology Vol. 12 (2001) Pages 485-490
- [42] A. Brechling: *Charakterisierung von Phospholipid Mono-, Bi- und Multilayern auf funktionalisierten Alkylsiloxan Self-Assembled Monolayern auf Si(100) Substraten*. Dissertation, Bielefeld University, Bielefeld (2003)

- [43] P. van der Heide: *X-ray Photoelectron Spectroscopy: An introduction to Principles and Practices*. Wiley (2011)
- [44] D. Briggs, J. T. Grant: *Surface Analysis by Auger and X-Ray Photoelectron Spectroscopy*. IM Publications (2003)
- [45] S. Hofmann: *Auger- and X-Ray Photoelectron Spectroscopy in Materials Science: A User-Oriented Guide*. Springer Science and Business Media (2012)
- [46] C. V. Raman, K. S. Krishnan: *A new type of secondary radiation*. Nature Vol. 121 (1928) Pages 501, 502
- [47] E. Smith, G. Dent: *Modern Raman Spectroscopy: A Practical Approach*. Wiley (2005)
- [48] L. Favor: *Eukaryotic and Prokaryotic Cell Structures: Understanding Cells With and Without a Nucleus*. The Rosen Publishing Group, Inc (2004) Pages 5-7
- [49] C. Becker: *Lokalisation von Proteinen im Kernmembranbereich mit der SDS-Gefrierbruch-Immunzytochemie*. Dissertation, Westfälische Wilhelms-Universität Münster (2004) Pages 1-5
- [50] N. Ulfig: *Bewegungsapparat: Lehrbuch der allgemeinen und speziellen Anatomie*. Karger, Basel (2002)
- [51] G. M. Cooper: *The Cell. A molecular approach*. ASM Press, Washington (1997)
- [52] H. Lodish: *Molekulare Zellbiologie*. Walter de Gruyter, Berlin (1996)
- [53] B. Alberts: *Molecular Biology of the Cell*. Garland Science, New York (2002)
- [54] H. M. Berman: *The Protein Data Bank*. Nucleic Acids Research Vol. 28, Oxford University Press (2000) Pages 235-242
- [55] D. U. Silverthorn: *Physiologie*. Pearson Studium, München (2009)
- [56] R. G. Parton, K. Simons: *Digging into caveolae*. Science Vol. 269 (1995) Pages 1398-1400
- [57] L. J. Pike: *The challenge of lipid rafts*. Journal of lipid research Vol. 50 (2009) Pages 323-328
- [58] S. Neuss-Stein: *Untersuchungen zur Bedeutung mesenchymaler Stammzellen in der Geweberegeneration*. Dissertation, RWTH Aachen (2004) Pages 1-5
- [59] J. F. W. Greiner, S. Hauser, D. Widera, J. Müller, F. Qunneis, C. Zander, I. Martin, J. Mallah, D. Schuetzmann, C. Prante, H. Schwarze, W. Prohaska, A. Beyer, K. Rott, A. Hütten, A. Gölzhäuser, H. Sudhoff, C. Kaltschmidt, B. Kaltschmidt: *Efficient animal-serum*

- free 3D cultivation method for adult human neural crest-derived stem cell therapeutics.* European Cells and Materials Vol. 22 (2011) Pages 403-419
- [60] <http://web.biologie.uni-bielefeld.de/cellbiology/index.php/research/neural-crest-derived-stem-cells>
- [61] B. Alberts, A. Johnson, J. Lewis, M. Raff, K. Roberts, P. Walter: *Molekularbiologie der Zelle.* Neuroforum Vol. 1 (2011) Pages 12-20
- [62] J. S. Wiegert, T. G. Oertner: *Dendritische Spines: Dynamische Bausteine des Gedächtnisses.* Stem Cells and Development Vol. 21 (2012) Pages 742-756
- [63] M. Schürmann, N. Frese, A. Beyer, P. Heimann, D. Widera, V. Mönkemöller, T. Huser, B. Kaltschmidt, C. Kaltschmidt, A. Götzhäuser: *Helium ion microscopy visualizes lipid nanodomains in mammalian cells.* Small Vol. 11 (2015) Pages 5781-5789
- [64] M. Schürmann, N. Shephard, N. Frese, K. Geishendorf, H. Sudhoff, A. Götzhäuser, U. Rückert, C. Kaltschmidt, B. Kaltschmidt, A. Thomas: *Technical feasibility study for production of tailored multielectrode arrays and patterning of arranged neuronal networks.* Plos One Vol. 13 (2018)
- [65] W. Dai, F. Shao, J. Szczerbinski, R. McCaffrey, R. Zenobi, Y. Jin, A. D. Schlüter, W. Zhang: *Synthesis of a Two-Dimensional Covalent Organic Monolayer through Dynamic Imine Chemistry at the Air/Water Interface.* Angewandte Chemie International Edition Vol. 55 (2016) Pages 213-217
- [66] P. Angelova, H. Vieker, N.-E. Weber, Dan Matei, O. Reimer, I. Meier, S. Kurasch, J. Biskupek, D. Lorbach, K. Wunderlich, L. Chen, A. Terfort, M. Klapper, K. Müllen, U. Kaiser, A. Götzhäuser: *A Universal Scheme to Convert Aromatic Molecular Monolayers into Functional Carbon Nanomembranes.* ACS Nano Vol. 7 (2013) Pages 6489-6497
- [67] M. Woszczyzna, A. Winter, M. Grothe, A. Willunat, S. Wundrack, R. Stosch, T. Weimann, F. Ahlers, A. Turchanin: *All-Carbon Vertical van der Waals Heterostructures: Non-destructive Functionalization of Graphene for Electronic Applications.* Advanced Materials Vol. 26 (2014) Pages 4831-4837
- [68] Y. Yang, P. Dementyev, N. Biere, D. Emmrich, P. Stohmann, R. Korzetz, X. Zhang, A. Beyer, S. Koch, D. Anselmetti, A. Götzhäuser: *Rapid Water Permeation Through Carbon Nanomembranes with Sub-Nanometer Channels.* ACS Nano Vol. 12 (2019) Pages 4695-4701
- [69] M. Wortmann, A. Hoffmann, N. Frese, A. Heide, J. Brikmann, N. Brandt, M. Menzel, A. Götzhäuser, E. Moritzer, B. Hüsgen: *Advanced Output of Silicone Molds in Vacuum Casting Processes by Polyamide 12 Powder Supplementation.* Polymer-Plastics Technology and Materials (2019) accepted

- [70] W. Eck, A. Küller, A. und M. Grunze, B. Völkel, A. Gözlhäuser: *Free-standing nanosheets from cross-linked biphenyl self-assembled monolayers*. *Advanced Materials* Vol. 17 (2005) Pages 2583-2587
- [71] A. Turchanin, A. Tinazli, M. El-Desawy, H. Großmann, M. Schnietz, H.H. Solak, R. Tampé, A. Gözlhäuser: *Molecular self-assembly, chemical lithography, and biochemical tweezers: A path for the fabrication of functional nanometer-scale protein arrays*. *Advanced Materials* Vol. 20 (2008) Pages 471-477
- [72] Z. Zheng, C. T. Nottbohm, A. Turchanin, H. Muzik, A. Beyer, M. Heilemann, M. Sauer, A. Gözlhäuser: *Janus nanomembranes: A generic platform for chemistry in two dimensions*. *Angewandte Chemie International Edition* Vol. 49 (2010) Pages 8493-8497
- [73] N. Frese, J. Scherr, A. Beyer, A. Terfort, A. Gözlhäuser, N. Hampp, D. Rhinow: *Multicomponent patterned ultrathin carbon nanomembranes by laser ablation*. *Applied Surface Science* Vol. 427 (2018) Pages 126-130
- [74] D. Oesterhelt, W. Stoeckenius: *Rhodopsin-like Protein from the Purple Membrane of Halobacterium halobium*. *Nature New Biology* Vol. 233 (1971) Pages 149-152
- [75] J. S. Jubb, D. L. Worcester, H. L. Crespi, G. Zaccai: *Retinal location in purple membrane of Halobacterium halobium: a neutron diffraction study of membranes labelled in vivo with deuterated retinal*. *The EMBO Journal* Vol. 3 (1984) Pages 1455-1461
- [76] D. Oesterhelt: *Bacteriorhodopsin as a light-drive ion exchanger?* *FEBS Letters* Vol. 64 (1976) Pages 20-22
- [77] J. Sasaki, L. S. Brown, Y. S. Chon, H. Kandori, A. Maeda, R. Needleman, J. K. Lanyi: *Conversion of bacteriorhodopsin into a chloride ion pump*. *Science* Vol. 269 (1995) Pages 73-75
- [78] S. T. Mitchell, N. Frese, A. Gözlhäuser, A. Bowers, K. Sattler: *Ultralight carbon nanofoam from naphthalene-mediated hydrothermal sucrose carbonization*. *Carbon* Vol. 95 (2015) Pages 434-441
- [79] N. Frese, S. T. Mitchell, C. Neumann, A. Bowers, A. Gözlhäuser, K. Sattler: *Fundamental properties of high-quality carbon nanofoam: from low to high density*. *Beilstein Journal of Nanotechnology* Vol. 7 (2016) Pages 2065-2073
- [80] N. Frese, S. T. Mitchell, A. Bowers, A. Gözlhäuser, K. Sattler: *Diamond-Like Carbon Nanofoam from Low-Temperature Hydrothermal Carbonization of a Sucrose/Naphthalene Precursor Solution*. *C* Vol. 3 (2017) Pages 23-37

- [81] S. Leyva-Garcia, E. Morallón, D. Cazorla-Amorós, F. Béguin, D. Lozano-Castelló: *New insights on electrochemical hydrogen storage in nanoporous carbons by in situ Raman spectroscopy*. Carbon Vol. 69 (2014) Pages 401-408
- [82] R. S. Kalubarme, C. J. Park, P. M. Shirage: *Two-Dimensional Mesoporous Carbon Electrode for High Energy Density Electrochemical Supercapacitors*. Journal of Nanoscience and Nanotechnology Vol. 15 (2015) Pages 1253-1260
- [83] M. Sevilla, A. B. Fuertes: *Chemical and structural properties of carbonaceous products obtained by hydrothermal carbonization of saccharides*. Chemistry-A European Journal Vol. 15 (2009) Pages 4195-4203

Acknowledgement

Diese Arbeit entstand am Lehrstuhl für Physik supramolekularer Systeme und Oberflächen der Universität Bielefeld. Dem Leiter, Herrn Prof. Dr. Armin Götzhäuser, danke ich für die herzliche Aufnahme in die Arbeitsgruppe, die interessante Aufgabenstellung und die Betreuung während der Arbeit.

Außerdem danke ich der gesamten D0 Forschungsgruppe und den Mitarbeitern von CNM Technologies.

Martin und Klaus danke ich für die gute Zusammenarbeit und Unterstützung.

Andrea danke ich für Forschungsk Kooperationen und die Begutachtung dieser Arbeit.

Besonderer Dank gilt meinen Eltern.